

Online optimisation of the CLIC Drive Beam bunch
train recombination at CTF3

Davide Gamba
Jesus College, Oxford

Thesis submitted in fulfilment of the requirements for the degree of Doctor
of Philosophy at the University of Oxford

Trinity Term, 2016

Abstract

The Compact Linear Collider (CLIC) design is the leading alternative for a future multi-TeV e^+e^- linear collider. One of the key aspects of the design is the use of a Drive Beam as power source for the acceleration of the colliding beams. This work is focused on the optimisation of the set-up and the operations of the CLIC Drive Beam recombination at the CLIC Test Facility (CTF3) at CERN.

The main effects that may affect the beam quality during the recombination are studied, with emphasis on orbit, transverse dynamics and beam energy effects. A custom methodology is used to analyse the problem, both from a theoretical and a numerical point of view. The aim is to provide first-order orbit and transverse optics constraints, which can be used as guidelines during the set-up of the beam recombination process. The developed techniques are applied at the CTF3, and the results are reported. The non-linear beam energy effects have been investigated by means of MAD-X simulations. The results show that these effects might be critical for the quality of the recombined beam. A proper non-linear correction turns out to be necessary, especially in the Delay Loop (DL). An alternative DL optics is proposed to mitigate the non-linear energy effects using only linear elements, in contrast with the original design, which relies on sextupoles.

A set of tools for the online control and optimisation of the beam orbit and dispersion has been implemented, deployed and used for the optimisation of the Drive Beam production at CTF3. Particular effort was put into the development of a generic linear feedback application, which is presented in this work. Thanks to the generality of the problem and its implementation, the feedback has been successfully used for a series of optimisations of the beam at CTF3. A collection of experimental results, focused on the Drive Beam recombination process, is presented and discussed.

Per impiombà 'l röhca e 'ngöhàh gacc tacolér,
mè ì patömàt a branda 'n dol hgorlér
e ì fracàt dò co i cröhch röhca a brandöh¹.
Ol Baldro Rago

¹In order to learn the art and to claim oneself to be an expert sheep herder / one has to bivouac many nights in the grass / and consume salt in abundance at the shepherd's table.

Acknowledgements

I would like to acknowledge my CERN supervisor Frank Tecker and my Oxford University supervisor Philip Burrows. They offered me the unique opportunity to work for two of the most prestigious academic institutions in the world. Their invaluable guidance not only made this work possible, but it generated an important building block of my education and career as an accelerator physicist. I am grateful to the John Adams Institute (JAI) and FONT group members at the Oxford University for their support and assistance, specially to Andrei Seryi for inspiring discussions.

My research was conducted mainly at CERN, more precisely in the CTF3 control room where I spent most of my time. There I had the opportunity to work with outstanding physicists, engineers and technicians, all willing to share their experiences and propose new ideas. I would like to particularly thank Ben Constance for the late evening discussions, Guido Sterbini for the continual inspiring ideas, Piotr Skowronsky for his strength and determination in achieving results, Roberto Corsini for his invaluable experience, Steffen Doebert for his pragmatism, Wilfrid Farabolini for his genial creativity and determination. For the experimental results I obtained and the experience I gained via the operation of the facility I should thank the machine itself for resisting to my demanding requests. Clearly this was possible only thanks to Alan Chauchet, Andrew Bruton, Aurelie Goldblatt, Christoph Hessler, Eric Chevallay, Esa Paju, Gerard McMonagle, Luca Timeo, Stefano Mazzoni, Stephane Burger, Stephane Curt, Stephane Rey, and all other staff and technicians who with passion and dedication keep CTF3 alive. From them also I learned inestimable practical experience that would have been difficult to get anywhere else. Learning is rarely a lonely process. At CERN I had the opportunity to meet brilliant researchers from all over the world. It was my great pleasure to share the last few years with Alexey Dubrovskiy, Andrea Palaia, Davide Lanaia, Irene Martini, Irina Shreyber, Jack Roberts, Jacobo Montaño, Luis Navarro, Lukas Malina, Maria Kastriotou, Mikhail Martyanov, Mohsen Kelisani, Tobias Persson and all the other students and fellows that with me took their first steps at CERN. All of them contributed to expanding the horizons in my professional and personal lives.

Above all, it is thanks to the continuous support and encouragement of my parents, Emilio and Maria, and to the stimulation of my brother Mirko that this work was possible. They are just the peak of the mountain of relatives and friends that constitute the “Valbosana family”. Thanks to all of them for their continuous support and for giving me the talent and the opportunity to arrive here.

Last but not least, special thanks to my partner Julia for being next to me all the way through this wonderful journey. She is the light and the guide that kept me on the right path.

Contents

1	Introduction	1
1.1	Recent achievements in High Energy Physics	2
1.2	Needs for electron-positron colliders	4
1.3	CLIC	6
1.3.1	Drive Beam recombination	7
1.3.2	The CLIC Test Facility at CERN	9
2	Transverse Beam Dynamics	13
2.1	Common definitions	14
2.2	First Order Transverse Beam Optics	17
2.3	Higher Order Representation	20
2.4	Energy Dependence	20
3	Software Tools	25
3.1	Data Acquisition with MATLAB	25
3.2	Dispersion measurement tool	27
3.2.1	Common notions for dispersion measurement	28
3.2.2	Dispersion measurement via PCA	31
3.2.3	Non-linear dispersion measurement	33
3.2.4	Application features	35
3.3	A generic slow-feedback implementation	36
3.3.1	Details of the linearFeedback implementation	38
3.3.2	linearFeedback interface and use	40
3.4	Quadrupole scan	42
3.4.1	Phase-space distribution: Tomography	45
4	DBRC Optics Verification and Optimisation	48
4.1	Simulations with MAD-X	49
4.1.1	Note on the definition of emittance	51
4.2	Drive Beam Recombination at CTF3	53
4.2.1	Main emittance growth contributions	55
4.2.2	Monochromatic effects after the Delay Loop	64
4.2.3	Monochromatic effects at the Combiner Ring	66
4.3	Energy spread effects	71
4.4	Possible cure of non-linear dispersion in DL	85
4.4.1	Design solution using sextupoles	89

4.4.2	Optimisation using linear elements	92
4.4.3	Summary on the studied non-linear chromatic effects	97
5	Transverse dynamics optimisation at CTF3	106
5.1	Device naming conventions	107
5.2	Dispersion Free Steering	108
5.3	Commissioning of a new Delay Loop optics	112
5.4	Matching between delayed and bypassing bunches	118
5.4.1	Horizontal and vertical orbit matching	118
5.4.2	Horizontal and vertical dispersion matching	120
5.4.3	Transverse optics matching	122
5.5	Matching between different turns in CR	125
5.5.1	Measurement of the transverse matching	125
5.5.2	Orbit matching	127
5.5.3	Dispersion Target Steering in the CR	130
5.6	Latest beam quality	134
5.7	Other Applications of the Generic Feedback	137
5.7.1	Optimisation of the Bunching System	137
5.7.2	Energy Stabilisation Along the Pulse	138
5.7.3	Injection bump closure at the CERN Proton Synchrotron	139
6	Conclusions	143
6.1	Summary	143
6.2	Suggestions for further work	145
A	Periodic Lattice Solution	146
B	Verification of the main assumptions	149
B.1	Ideal, Gaussian initial beam	149
B.2	Synchrotron radiation	149
B.3	Betatron linearity	150
C	Useful Taylor Series	152
D	Combining Covariance Matrices	153
	Bibliography	154

Chapter 1

Introduction

The use of particles to probe the inner structure of matter started with Rutherford's experiments at the beginning of the 20th century. It was Rutherford himself who afterwards in the late 1920s suggested the path to particle physics investigation, by asking the scientific community to look into accelerator technology as a fundamental tool for future studies. The need for accelerated particles as a probe for studying the constituents of matter can be understood by simple dimensional consideration. Visible light has a wavelength of the order of 10^{-7} m, which characterises its spatial resolution limit. The Bohr radius, i.e. approximately the distance between the proton and the electron in a hydrogen atom, is of the order of 10^{-11} m, and so it cannot be studied with visible light. However to a particle with momentum p one can associate an equivalent De Broglie wavelength, $\lambda = h/p$, where h is the Planck constant. By using particles with higher and higher momentum one can then study smaller and smaller structures. Unfortunately the higher the energy scale, the bigger and/or more complex particle accelerators become. The largest and most powerful existing accelerator to date is the Large Hadron Collider (LHC) [1] at CERN, which is a 27 km long storage ring, where protons and heavy ions are stored and accelerated up to 7 TeV (protons) or 2.76 TeV per nucleon (heavy ions). The remarkable size and cost of such machines make the scientific community wonder if smaller alternatives could be found. This leads to a growing interest in new particle acceleration technology, like laser-driven or beam-driven plasma acceleration. On the other hand the state of the art of such technologies is not yet ready to make them compete with most future collider designs, which are still based on conventional acceleration techniques. Examples are the Future Circular Collider (FCC) [2], the Compact Linear Collider (CLIC) [3] and the International Linear Collider (ILC) [4] studies.

One of the biggest challenges of accelerator physics it is to gain an understanding of the link between theoretical predictions and simulations and what is observed in real experimental facilities. This is not surprising: with thousands of different components, it is sometimes impossible to have them all under full control. Long and rigorous work is needed before being able to formulate a clear statement about the agreements between theory and practice. Moreover, the required knowledge of the experimental set-up is so vast and the resources available are often so little, that the experimental accelerator physicist needs to identify and concentrate on a few main points.

The work presented here is focused on the CLIC design and in particular on the study and optimisation of the so called Drive Beam Recombination Complex, which is being tested at the CLIC Test Facility (CTF3) [5] at CERN. The aim of this work is to investigate the leading effects that might affect the Drive Beam quality during the recombination process at CTF3, and to develop the necessary tools to keep it under control. The results which are presented in this thesis are not meant to be a measurement of the quality of CLIC Drive Beam recombination, but to represent the current understanding of the process and to show the state of our ability to control it. This is the first necessary step to achieve the specification required by the CLIC Drive Beam design.

This thesis consists of three main parts: the first part is theoretical where methods and tools used are presented, the second part focuses on simulations and the final part on experimental results. Following some general introduction, a recap of transverse beam dynamics is presented in Chapter 2. The accent is put on the generic and simple concepts that have been used in later chapters. The software tools that have been developed to perform the studies will be presented in Chapter 3. In Chapter 4 simulations with MAD-X [6] of the Drive Beam recombination at CTF3 are presented, while the experimental results are described in Chapter 5. Finally, Chapter 6 summarises the achievements resulting from the work presented in this thesis.

1.1 Recent achievements in High Energy Physics

The Standard Model (SM) of particle physics [7] is one of the greatest achievements of 20th century science. This model attempts to describe the known subatomic particles and their interactions by means of a few fundamental particles: fermions (listed in Table 1.1) which are the basic constituents of matter and bosons (listed in Table 1.2). Moreover, the Standard Model predicts for each fermion an equivalent anti-matter particle with opposite charge.

Generation	Leptons		Quarks	
1	Electron e^-	Electron neutrino ν_e	Up u	Down d
2	Muon μ^-	Muon neutrino ν_μ	Charm c	Strange s
3	Tau τ^-	Tau neutrino ν_τ	Top t	Bottom b

Table 1.1: The fundamental fermions of the Standard Model.

Boson	Function
Photon γ	Electromagnetic force
Weak bosons W^\pm, Z^0	Weak force
Gluon g	Strong force
Higgs boson h	Electroweak symmetry breaking.

Table 1.2: The fundamental bosons of the Standard Model.

The matter is mainly made of compounds of particles of the first generation. The strong interaction, mediated by gluons, keeps quarks and antiquarks bounded in pairs, named mesons, or triplets, named baryons. Theoretically a third possible combination could be made of 4 quarks and one anti-quark, which would form an “exotic baryon” or pentaquark [8]. Recent observations from the LHCb collaboration [9] may have confirmed their existence.

The proton and the neutron are baryons. Under the right circumstances they can be bound together by residual strong forces to form atomic nuclei. The electromagnetic force plays its role in binding nuclei with electrons to form atoms. The process continues with the residual electromagnetic force which is then able to bind atoms to form molecules, and so the form of macroscopic matter that we are used to interacting with.

In the general framework of the Standard Model, the electromagnetic and weak forces are unified. However this unification implies that all the particles would be massless. In order to give mass to the particles as we observe them, the Brout-Englert-Higgs mechanism was introduced [10, 11, 12]. This is based on the existence of the Higgs field which permeates the entire Universe, and it interacts with all the particles of the Standard Model giving them mass. Moreover by spontaneous symmetry breaking the weak bosons W^\pm and Z^0 are massive, and the photon is massless. The quantum of the Higgs field is the Higgs boson. After the first few years of operation of the LHC a new particle was experimentally observed by both ATLAS and CMS experiments [13, 14], which has been associated with the Higgs boson.

The Higgs is the last “piece” of the Standard Model jigsaw puzzle. Unfortunately the Standard Model is not enough to describe a series of effects that have been observed in nature. It completely ignores the existence of the gravitational force. In addition, astronomical observations have led to the need to introduce the existence of Dark Matter: a new kind or state of matter which has not yet been understood. Many experiments with neutrinos observed that are not massless. They are actually linear combinations of quantum mechanical states, and can spontaneously change flavour: the so called neutrino oscillations. These are properties that are not predicted by the Standard Model. Theorists have still open questions on the Standard Model itself. The fact that fundamental fermions come in three generations, or the hopes of a Grand Unified Theory, in which the strong, electromagnetic and weak forces may be considered as low-energy expressions of a single unified force. Over the last decades several models are trying to fit all the observed effects. An important class are the supersymmetric theories, which postulate the existence of a super-symmetric partner of each particle of the Standard Model, which might have masses at the Terascale.

Although no strong experimental evidence has been observed for new particles, searches continue. Some hint of a possible new particle at about 750 GeV were announced in [15, 16], but recently discarded as statistical fluctuation in [17, 18].

1.2 Needs for electron-positron colliders

The likelihood of a certain particle interaction A to occur in a beam-beam collision is given by

$$P(A) = \mathcal{L}\sigma(A) \quad (1.1)$$

where $\sigma(A)$ is the *cross section* of the interaction and \mathcal{L} the luminosity, which is defined as:

$$\mathcal{L} = H \frac{f_{col} N^2}{4\pi\sigma_x\sigma_y} \quad (1.2)$$

where σ_x and σ_y are the beam transverse sizes, N is the number of particles in the interacting bunch, f_{col} is the frequency of the collisions and H is an enhancement factor which accounts for electromagnetic effects at the interaction point. Clearly the higher the collision frequency or the denser the beams, the more events one can observe.

The LHC collides two proton beams, which turn in opposite directions in a 27 km storage ring. Protons are first injected into the ring, accelerated to the desired energy, and then brought to collision. The same beams keep circulating nearly at the speed of light and they collide with each other for typically 20 hours. Given the geometry of the machine and the presence of four interaction points (ALICE, ATLAS, CMS and LHCb experiments), each proton has a high probability to take part in a collision with another proton circulating in the opposite direction. The high collision frequency and bunch density make the LHC the most powerful, currently running machine for exploring the high energy frontier. The energy limit of such machines is mainly given by the limited magnetic field reachable in bending magnets. The fundamental relationship here is the so called rigidity: $B\rho \approx 3.3p$ where B is the magnetic field in T/m and p is particle momentum in GeV/c.

Protons are composite particles. This means that the collisions take place between their constituent quarks and gluons, but there is no a-priori knowledge of which particles collide and at which energy. Moreover quarks and gluons take part in the strong interaction, which results in large numbers of background particles, which add complexity to the detector design and data reconstruction. In this sense building a lepton collider gives much more control of the interaction: the energy of the collision can be controlled and varied at convenience, and the interacting particles can be produced with a high degree of polarisation. Electrons and positrons are the most natural choice for lepton colliders.

Historically both electron and proton colliders have been realised. According to the European Strategy for Particle Physics [19], one of the main priorities is to undertake design studies for the post-LHC era. Due to the discovery of the Higgs boson, a strong interest in electron-positron collider designs is expressed in [19].

At the TeV scale the limiting factor for electron-positron machines is the synchrotron radiation. The power P radiated by a single particle is proportional to:

$$P \propto \frac{1}{\rho^2} \frac{E^4}{m_0^4} \quad (1.3)$$

where ρ is the bending radius, E the particle energy and m_0 its rest mass. Electrons have a mass which is approximately 2000 times smaller than protons, which has a huge impact on Eq. 1.3. The LEP [20] collider, installed in the same tunnel as LHC, was limited by synchrotron radiation at about 100 GeV. It is then unimaginable to reach the TeV scale with electron-positron circular colliders. Muons on the other hand have a rest mass which is only 10 times smaller than protons, which makes them more appealing. R&D studies in this direction are ongoing, but many technological challenges still need to be addressed [21].

To reduce the synchrotron radiation in electron-positron colliders the only way is to increase the bending radius ρ in Eq. 1.3. This is the basis, for example, of FCC-ee [22]: an electron-positron circular collider that could be installed in a hypothetical 80 to 100 km long ring that could later host FCC-hh [2], another hadron collider. Even if the average design radius of the FCC-ee ring is almost double that of the LHC, the design beam energy is at most 175 GeV: still far away from the TeV scale. The same strategy is adopted by the CEPC-SPPC design study [23]: a 54 km long ring could host first an electron-positron collider (CEPC) with beam energy up to 120 GeV and later a proton collider (SPPC) with beam energy up to 35 TeV. The ideal extreme would be the limit $\rho \rightarrow \infty$, i.e. a linear collider. In this case one of the main concerns is the efficiency: the acceleration process in a circular machine can be slow, i.e. a small acceleration repeated for many turns, and once accelerated the beam can stay in collision for several minutes or hours. In a linear collider instead each beam is generated, accelerated, and collided only once. Particles that did not collide are lost, as is their energy. In a circular collider the repetition rate of the collisions is given by the revolution frequency of the ring, which is typically of the order of a few kHz. It is difficult to imagine competing with such a number in a linear machine, so in order to be competitive in terms of luminosity, Eq. 1.2, a linear collider design has to have extremely small beam size.

There are currently two realistic designs for future linear e^+e^- colliders: CLIC [3] and ILC [4]. The ILC design is meant to fulfil the recommendation given by International Technology Recommendation Panel (ITRP), which was formed by the International Committee for Future Accelerators (ICFA). In the ITRP report of 2004 [24] the recommendation was to opt for superconducting technology as the basis for a future linear collider with centre-of-mass energies up to 500 GeV, with a possible upgrade to 1 TeV. The CLIC design is an alternative proposal using normal conducting technology that allows one to extend the maximum energy scale up to 3 TeV.

Table 1.3 lists some of the main parameters of ILC and CLIC, which can be compared with the preliminary parameters for FCC-ee and CEPC at their maximum design energies. The four projects are very different with respect to each other in design and technology. Since the present work is a contribution to the CLIC design, this will be more extensively described in the following section.

Parameter	ILC	CLIC		FCC-ee	CEPC
Center of mass energy [GeV]	500	500	3000	350	240
Peak Luminosity [$\text{cm}^{-2} \text{s}^{-1} \times 10^{34}$]	1.8	2.3	5.9	1.8	1.8
Accelerator length [km]	31	13.0	48.3	100	53.6
Acc. gradient loaded [MV/m]	31.5	80	100	10 - 20	15.6
Particles per bunch [10^9]	20	6.8	3.72	140	371
Bunch separation [ns]	554	0.5	0.5	-	-
Number of bunches	1312	354	312	98	50
Repetition rate [Hz]	5	50	50	≈ 3000	≈ 5600
Hor./vert. norm. emitt. [μm]/[nm]	10/35	2.4/25	0.66/20	0.68/0.68	1.6/4.8
Hor./vert. IP beam size [nm]	474/5.9	202/2.3	40/1	45000/45	73700/160
AC Power consumption [MW]	163	271	582	≈ 300	≈ 500

Table 1.3: ILC and CLIC main parameters [3, 4, 25], in comparison with equivalent parameters for FCC-ee [26, 27] and CEPC [23].

1.3 CLIC

The CLIC study [3, 28] aims to design a linear electron-positron collider with a collision energy at centre of mass up to 3 TeV. In order to reach such high beam energy, while keeping the length of the accelerator “compact”, a 100 MV/m accelerating gradient was chosen, which means a total length of about 30 km of accelerating structures, plus the needed space for focusing elements. Superconducting cavities are not able to support such high gradients, so the choice fell onto normal-conducting cavities. The optimisation of costs, geometric tolerances and the studies on RF breakdown rate resulted in the choice of 12 GHz RF and a beam pulse length of 240 ns [3]. The main limiting factor is the breakdown rate (BDR), which follows the empirical scaling law $BDR \propto E^{30}\tau^5$ where E is the accelerating gradient and τ is the RF pulse length [29]. According to the latest design [3] the RF power needed is calculated to be about 61 MW per 23 cm long accelerating structure. Klystrons are the conventional sources for RF, but the required RF-pulse specifications, and the number of units needed, make this solution especially inefficient. Instead, the CLIC design makes use of a novel two-beam acceleration scheme: a high intensity (100 A), low energy (2.4 GeV) Drive Beam is used to store, compress and transport the energy to the Power Extraction and Transport Structures (PETS) which run parallel to the main colliding beam. In the PETS the Drive Beam is *decelerated* and the extracted RF power is used to feed the accelerating structures of the Main Beam.

The latest layout of the full complex is shown in Figure 1.1. From the collider point of view the interesting part is the bottom of the layout: the main, colliding, beams are generated in dedicated electron and positron injectors; their emittance is reduced in damping rings taking advantage of synchrotron radiation effects; their energy is increased up to 9 GeV by a common booster; they are transported to the far ends of the main linacs; they are accelerated by the 100 MV/m gradient along the main linacs up to the nominal energy and

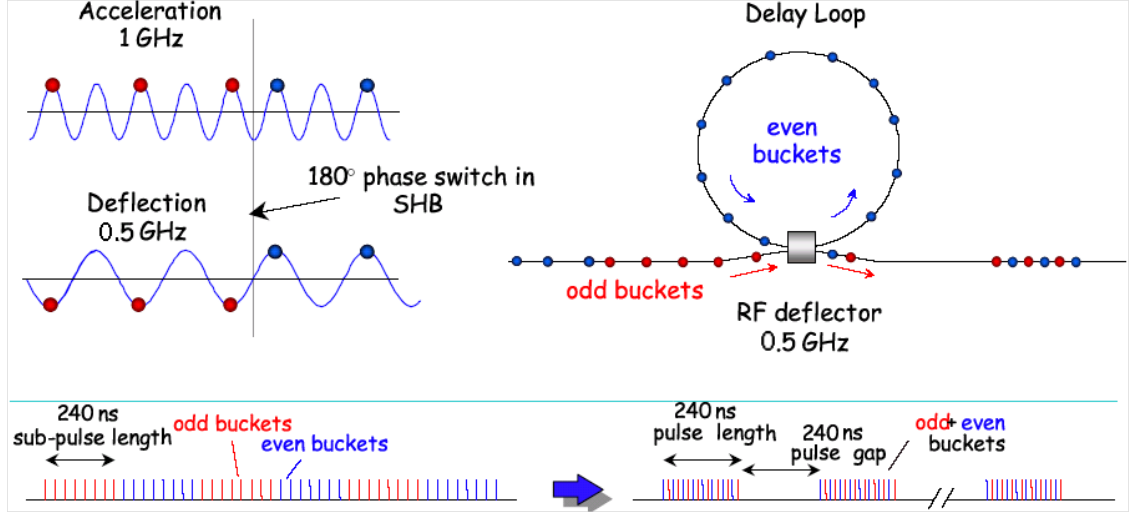


Figure 1.2: Schematic diagram of the factor-2 bunch recombination at the Delay Loop [3].

is performed with a Delay Loop, as depicted in the schematic of Figure 1.2. A 0.5 GHz transverse deflector is used to kick the even bunches inside the delay line, while the odd bunches are kicked to take the shortest path. The difference in length of the two paths is about 240 ns, and tuned at the ps-level such that the two trains of bunches can merge together, forming several 240 ns-long trains with bunching frequency at 1 GHz, separated by 240 ns of empty space.

A similar technique is used in the following Combiner Rings (CR1 and CR2) to merge 12 such trains to form the final 24 trains of 12 GHz bunches, which are needed in the decelerator sections. In CR1 and CR2 the bunching frequency is increased by a factor 3 and 4 respectively. Figure 1.3 shows a schematic of the recombination in CR2. Two RF deflectors are used to generate local closed bumps in the injection section. The frequency of these deflectors is the same as that of the incoming bunches. At injection (top-left) only the second deflector is seen by the incoming beam, and it is used to inject the bunches on the closed orbit solution of the ring after the injection septum. The ring length is tuned such that after one turn the circulating bunches arrive at the deflecting cavities with a delay of one quarter the RF wavelength, i.e. at zero crossing and so not receiving any kick. At the same time another train of bunches is injected as shown in Figure 1.3 (top-right). After another turn (bottom-left) the first injected bunches are kicked by the first deflector. The generated orbit bump is opposite with respect to the injection septum. The orbit bump is then closed by the second deflector, while other bunches are injected. Finally after three turns (bottom-right) the initial bunches arrive again at zero crossing, the second injected bunches follow the orbit bump opposite the septum, the third injected bunches are also at zero crossing and a final train of incoming bunches is injected. The final beam bunch train has 4 times the initial bunching frequency and pulse current. By carefully adjusting the ring length one can achieve other recombinations, like the factor 3 required in CR1, or even a factor 5 recombination which was employed in an earlier design of CLIC [31].

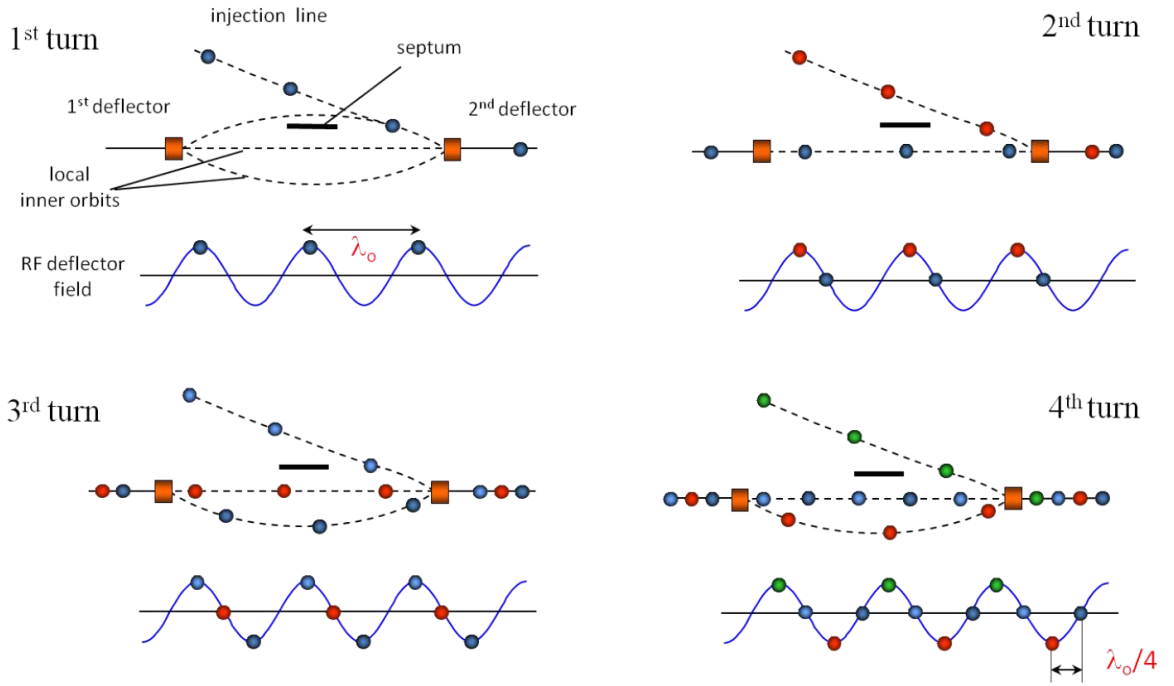


Figure 1.3: Schematic diagram of the factor-4 bunch recombination in the second Combiner Ring (CR2) [3].

1.3.2 The CLIC Test Facility at CERN

At CERN, the CLIC Test Facility (CTF3) [5] has been designed and commissioned to demonstrate the feasibility of the key technologies of CLIC. There are two main aims of the facility:

1. To demonstrate the feasibility of the high-current Drive Beam production by means of the bunch recombination described in the previous section.
2. To demonstrate the possibility to efficiently extract the power from the Drive Beam, and to validate the two-beam acceleration scheme by accelerating a witness electron beam provided by a dedicated injector.

The beam parameters have been scaled with respect to the CLIC design. For the Drive Beam a comparison between CLIC and CTF3 is presented in Table 1.4.

Figure 1.4 shows a layout of the facility and its beamlines. A thermionic electron gun generates the initial $1.4 \mu\text{s}$ -long DC beam, with an intensity of 4 A. The bunching can be performed in two ways: either using three sub-harmonic bunchers (SHBs) at 1.5 GHz powered by Traveling Wave Tube amplifiers (TWT); or using a 3 GHz standing wave pre-buncher followed by a 3 GHz traveling wave buncher powered by a normal klystron. In the first case, the fast phase-switch time of TWTs and SHBs allows production of the odd and even 1.5 GHz bunch trains with the pattern required for the beam recombination. In the second case a constant 3 GHz bunch train is produced. In this case the TWTs are turned off, and the SHBs do not have any function.

Parameter [Units]	CLIC	CTF3 (design)	CTF3 (achieved)
E [GeV]	2.4	0.15	0.135
E spread r.m.s. $\Delta E/E_0$ [%]	≈ 1	≈ 1	< 1
I [A]	100	30	28
Norm. emitt. r.m.s. [μm]	≤ 150	≤ 150	≈ 150 (x4 recomb.)
T_{pulse} initial [μs]	140	1.4	1.4
T_{pulse} final [ns]	240	140 (240)	140 (240)
Bunch length [mm]	≤ 1	≤ 1	≤ 2
Bunch frequency [GHz]	12	12	12

Table 1.4: Main CLIC and CTF3 Drive Beam parameters after recombination [3, 5]. For CTF3, the specifications for a 3 GHz beam instead of the nominal 1.5 GHz beam are shown in parenthesis.

After a first acceleration, the bunches are compressed in a small magnetic chicane, and then they are accelerated in fully-loaded accelerating structures [32] along the linac, up to the nominal energy of about 130 MeV. The RF frequency is 3 GHz. With slightly different beam parameters the Dogleg experiment [33] is set-up in the middle of the linac. A stretching chicane (the ‘‘Frascati chicane’’ [34]) can be used to stretch the bunch length before it enters the DBRC. The Frascati chicane was introduced to avoid coherent synchrotron radiation (CSR) in the following DBRC. This could be an issue for the short bunches required by the initial 30 GHz CLIC design [31], but it turned out not to be for the current 12 GHz design. Recently a bypass has been installed and the chicane is not used anymore.

In the DBRC the first ring encountered is the Delay Loop (DL). This is used for the first factor-2 recombination of the Drive Beam, but it is in use only with the 1.5 GHz injector bunching scheme. For CTF3 the recombined pulse length is only 140 ns instead of 240 ns for CLIC. The DL is then shorter than the CLIC one, and it is based on a single transverse RF cavity operating at 1.5 GHz, which is crossed twice by the delayed beam. The DL can be bypassed simply by switching off the transverse deflector. If needed one can also make the full beam circulate in the DL using static correctors. Clearly no recombination is possible in these cases. The DL bypass is the normal condition when operating with an incoming 3 GHz beam. In the case of 1.5 GHz operations, 4 trains of 3 GHz bunches are produced after the DL. Each 140 ns-long train is separated by 140 ns of empty space¹.

The transfer line TL1 takes the beam to the single Combiner Ring (CR) of CTF3, which performs the factor-4 recombination as explained in the previous section. Two 3 GHz deflecting structures are installed at the side of the injection septa. The length of the CR is double that of the DL. The recombination in the CR is possible with both 1.5 GHz and 3 GHz set-ups of the injector. In the first case the total recombination is $2 \times 4 = 8$, while in the second it is only possible to obtain the factor-4 recombination of the CR. The combined

¹It is actually true that the 1.5 GHz bunching may leave some electrons in the buckets that are meant to be empty. Those are referred as ‘‘satellites’’, and in the CLIC design they are supposed to be removed in a dedicated section. At CTF3 there is no cleaning section, so even satellites combine with each other and finally result in undesired trains of small intensity after the main combined pulse.

beam is extracted from the CR by a fast-rising electrostatic kicker installed in the ring. In the case of a factor-8 recombination the beam circulating in the ring is only 140 ns-long, i.e. filling half the ring. The empty half gives enough time to the extraction kicker to rise at nominal voltage. In case of a 3 GHz set-up from the injector, with the factor-4 recombination all the CR is filled. No time is given for the extraction kicker to rise, which leads to the loss of the head or tail of the combined pulse. For some special set-ups the CR can be bypassed by only performing half a turn. In this case the RF deflector used for the injection and the extraction kicker can be substitute by static magnetic correctors.

After the CR the beam can be transported to the CLIC Experimental area (CLEX) via the transfer line TL2. TL2 hosts the Phase-Feed-Forward experiment [35, 36], which aims to stabilise the bunch phase stability to provide stable RF production in the decelerator.

In CLEX the Drive Beam can be used for two main experiments: in the Test Beam Line (TBL) the beam is decelerated by a series of PETS, and the extracted RF power is measured and characterised. In the Two Beam Module (TBM) the power extracted from the beam is directly used to accelerate a witness beam that is generated by the CALIFES (Concept d'Accélérateur Linéaire pour Faisceau d'Electrons Sonde) injector [37].

The full experimental program of CTF3 is extremely rich and only a few main experiments have been mentioned in the above description. For most of the initial goals a proof-of-principle has been achieved, in particular for the Drive Beam generation and the Two-Beam acceleration. However a few stability and beam quality results are still missing. One of the objectives required by the CLIC Design Report [3] is to obtain at CTF3 a factor-8 recombined beam with normalised emittances below $150 \mu\text{m}$ in both planes. Unfortunately this requirement has not yet been fulfilled at CTF3, even after many years of operation. This triggered the necessity of a more careful study of the dynamics and effects that may spoil the recombination. The presented thesis forms such a study.

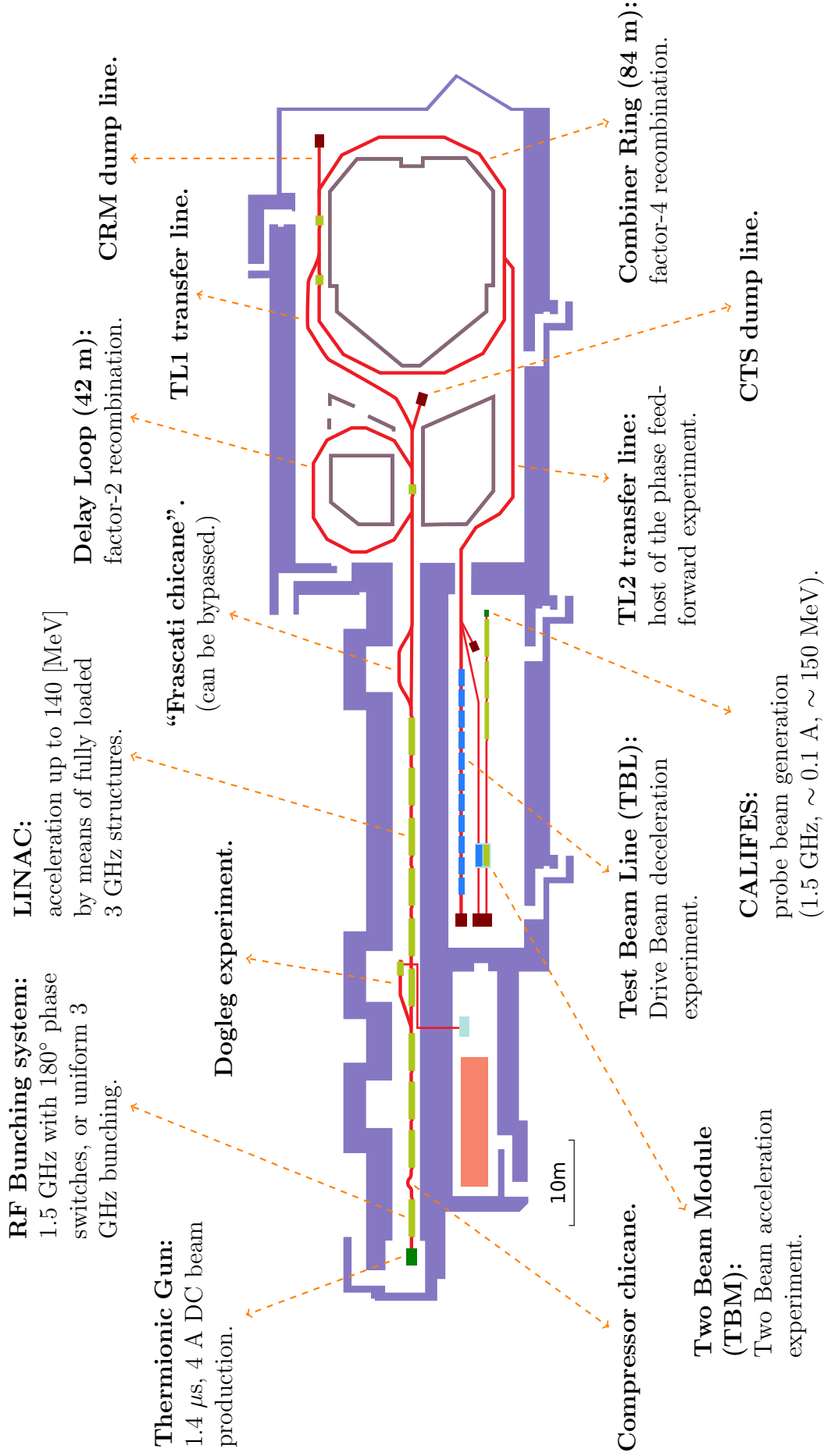


Figure 1.4: Layout of the CLIC Test Facility at CERN (CTF3) showing the main parts. The beam path is identified by solid red lines. Accelerating structures, both longitudinal and transverse, are identified by a green block on the beam path, while blue blocks represent decelerating structures.

Chapter 2

Transverse Beam Dynamics

A complete and comprehensive theory of the dynamics of particle accelerators is covered in detail by many specialised books (e.g. [38, 39, 40, 41]). This chapter is meant to recapitulate some basic concepts of transverse beam dynamics, in order to derive and to understand the techniques used to obtain the results presented in this work.

A common starting point in many specialised books is the introduction of the electromagnetic fields and their effect on charged particles. It normally follows the description of single particle motion by means of the Lagrangian and Hamiltonian formalism. Finally the matrix formalism is introduced to describe the transport of the beam and the *betatron functions* are defined to describe the properties of the *lattice* of an accelerator. This is not the path that will be followed here. The starting point will be the matrix formalism, from which a consistent “theory” will be derived, by adopting a statistical approach more than single particle dynamics. The effort of building such a theory will provide an easy to use formalism to treat orbit, dispersion and emittance growth issues in generic transfer lines as they have been treated at CTF3. The formalism presented is also an attempt to separate the description of the beamline itself from the properties of the incoming beam, allowing to optimise the first without a-priori knowledge of the second.

One should stress from the beginning that the present work is about linear accelerators. To be more precise, this work is about transfer lines for ultra-relativistic electron beams. In fact the whole CLIC Drive Beam Recombination Complex (DBRC) can be seen as a long and complex transfer line, where no *longitudinal* acceleration is performed on the beam. This first consideration is reflected in the description of beam dynamics presented in this chapter, which relies on “strong hypotheses” that might not be true for storage rings, nor for low-energy beams. These assumptions are:

- This work mainly covers transverse effects in the DBRC, so the developed theory is focused on the transverse dynamics of the beam.
- The simulated transfer lines are assumed to contain only linear magnetic elements (i.e. dipoles and quadrupoles). In some cases, sextupoles will be introduced: the assumption is that they can be treated as special quadrupoles, whose strengths are dependent on the incoming mean beam position.

- The dynamics of the particles transported in a lattice element is expressed by a Hamiltonian, which normally is the case for linear machines.
- Particle-particle interactions are neglected, both within the same bunch (e.g. space-charge effects, intra-bunch effects) and within the same pulse (e.g. inter-bunch wake-fields).
- There are no effects such as synchrotron radiation which may alter the particles' momentum along the direction of motion.

The justification for such hypotheses is mainly due to the length of the machine under study: the DBRC at CTF3 (as well as in CLIC) is typically a few hundred metres long, and is traversed by the beam in a single passage. Some more thoughts on the assumptions can be found in appendix B. There could be other effects that may drastically spoil the beam quality. For example in the early stage of CTF3 an instability in the RF deflector of the CR was observed and this was the main limitation for achieving the first beam recombination. A new deflecting cavity was then designed that cured the issue [42]. The assumption in this work is that no such hardware-related issues are still dominant, and the attempt is to investigate more conceptual issues that are indeed revealed in the following chapters.

2.1 Common definitions

Before going into the details of the beam dynamics, one needs to define a reference system and the relative coordinate variables. This work follows similar conventions of the well-known tool MAD-X [43]. In particular, the reference system is a moving reference along the so called *reference orbit*, i.e. the theoretical trajectory of an ideal particle with design momentum travelling through the center of all the ideally-placed magnetic elements. At each location along the lattice a right-handed coordinate system $(\hat{x}; \hat{y}; \hat{s})$ is placed such that the coordinate \hat{s} is tangent to the reference orbit and \hat{y} is perpendicular to the plane of the accelerator, which one can assume for simplicity to be lying in the horizontal plane. With such a coordinate system, the canonical variables describing the transverse orbit of a single particle are the two pairs $(x; p_x)$, $(y; p_y)$, where x and y are the transverse displacement in metres of the particle, p_x and p_y are the transverse momenta normalised by the design momentum p_0 . For the longitudinal plane, neglected here, the pair $(t, \Delta p/p_0)$ can be considered, where t is the longitudinal displacement in metres, and $\Delta p/p_0$ is the momentum deviation of the considered particle with respect to the design momentum particle¹.

One can see a beam as an ensemble of n particles, and each particle i can be represented in phase space by its canonical coordinates, i.e. $(x_i; p_{x_i}; y_i; p_{y_i})$. A complete description of the ensemble can be achieved by listing these coordinates in a matrix, where each column

¹For the longitudinal plane MAD-X ([43]) uses a slightly different definition of the momentum deviation, but the differences are normally negligible for ultra-relativistic beams.

contains the phase-space coordinates of a single particle:

$$\text{beam} := \begin{bmatrix} \mathbf{x} \\ \mathbf{p}_x \\ \mathbf{y} \\ \mathbf{p}_y \end{bmatrix} = \begin{bmatrix} x_1 & x_2 & \cdots & x_n \\ p_{x1} & p_{x2} & \cdots & p_{xn} \\ y_1 & y_2 & \cdots & y_n \\ p_{y1} & p_{y2} & \cdots & p_{yn} \end{bmatrix} \quad (2.1)$$

In general a beamline lattice is made of a series of magnetic elements that change the coordinates of each particle by some non-linear function of the initial coordinates. In practice the main magnetic elements installed in a beamline are quasi-linear so the first-order approximation is generally a good starting point. In this view, each i^{th} -particle is transported through the machine elements by a linear map of the initial phase-space coordinates:

$$\begin{bmatrix} \mathbf{x} \\ \mathbf{p}_x \\ \mathbf{y} \\ \mathbf{p}_y \end{bmatrix}_S = \mathbf{R}_{0S} \begin{bmatrix} \mathbf{x} \\ \mathbf{p}_x \\ \mathbf{y} \\ \mathbf{p}_y \end{bmatrix}_0 \quad (2.2)$$

where \mathbf{R}_{0S} is the square matrix that represents the beamline lattice from a reference position 0 until the position S . In this linear approximation, for a beam lattice made of N elements (e.g. quadrupoles, dipoles, drifts), \mathbf{R}_{0S} is the result of the matrix multiplication of the N matrices \mathbf{R}_i representing each lattice element:

$$\mathbf{R}_{0S} = \mathbf{R}_N \cdots \mathbf{R}_3 \mathbf{R}_2 \mathbf{R}_1. \quad (2.3)$$

It should be noted in Eq. 2.3 that the matrix \mathbf{R}_1 represents the first element encountered by the beam, so it has to be the rightmost matrix in the multiplication. Similarly if \mathbf{R}_{0S} represents the lattice of one turn in a ring or a periodic lattice, then the matrix representing the evolution of N turns is simply \mathbf{R}_{0S}^N .

Instead of *tracking* all the particles, one might want to track the overall behaviour or envelope of the beam, i.e. mainly its size and divergence. This information can be represented by the covariance matrix Σ :

$$\Sigma = \text{cov}(\text{beam}) \quad (2.4)$$

$$= \begin{bmatrix} \sigma(\mathbf{x}, \mathbf{x}) & \sigma(\mathbf{x}, \mathbf{p}_x) & \sigma(\mathbf{x}, \mathbf{y}) & \sigma(\mathbf{x}, \mathbf{p}_y) \\ \sigma(\mathbf{p}_x, \mathbf{x}) & \sigma(\mathbf{p}_x, \mathbf{p}_x) & \sigma(\mathbf{p}_x, \mathbf{y}) & \sigma(\mathbf{p}_x, \mathbf{p}_y) \\ \sigma(\mathbf{y}, \mathbf{x}) & \sigma(\mathbf{y}, \mathbf{p}_x) & \sigma(\mathbf{y}, \mathbf{y}) & \sigma(\mathbf{y}, \mathbf{p}_y) \\ \sigma(\mathbf{p}_y, \mathbf{x}) & \sigma(\mathbf{p}_y, \mathbf{p}_x) & \sigma(\mathbf{p}_y, \mathbf{y}) & \sigma(\mathbf{p}_y, \mathbf{p}_y) \end{bmatrix} \quad (2.5)$$

One of the properties of the covariance matrix is that

$$\text{cov}(\mathbf{A}\mathbf{X} + \mathbf{a}) = \mathbf{A} \text{cov}(\mathbf{X}) \mathbf{A}^T \quad (2.6)$$

where \mathbf{A} and \mathbf{a} are respectively a transformation matrix and an offset vector with the proper dimensions. For our purposes Eq. 2.6 implies:

$$\Sigma_S = \mathbf{R}_{0S} \Sigma_0 \mathbf{R}_{0S}^T \quad (2.7)$$

where Σ_0 and Σ_S are respectively the covariance matrices at the reference location and at position S along the lattice.

It is important to note the evolution of the determinant of the Σ matrix:

$$\det(\Sigma_S) = \det(\mathbf{R}_{0S} \Sigma_0 \mathbf{R}_{0S}^T) = \det(\mathbf{R}_{0S})^2 \det(\Sigma_0). \quad (2.8)$$

The matrix \mathbf{R}_{0S} represents a canonical transformation, i.e. it is symplectic. For linear transformations, the symplecticity implies that the determinant of the transformation matrix \mathbf{R}_{0S} is ± 1 . Then by Eq. 2.8 it follows that in a transfer line the quantity $\det(\Sigma_0)$ is conserved. The square root of this quantity is the *statistical emittance* of the beam.

$$\epsilon_\Sigma = \sqrt{\det(\Sigma_0)} \quad (2.9)$$

The beam envelope description might not be complete without the information of the average beam position, that can be computed by the linearity of Eq. 2.2:

$$\begin{bmatrix} \langle \mathbf{x} \rangle \\ \langle \mathbf{p}_x \rangle \\ \langle \mathbf{y} \rangle \\ \langle \mathbf{p}_y \rangle \end{bmatrix}_S = \mathbf{R}_{0S} \begin{bmatrix} \langle \mathbf{x} \rangle \\ \langle \mathbf{p}_x \rangle \\ \langle \mathbf{y} \rangle \\ \langle \mathbf{p}_y \rangle \end{bmatrix}_0 \quad (2.10)$$

In a real machine one has to consider also kicks due to misalignments and magnetic field errors. In a first-order approximation we can imagine all these errors like “virtual” dipoles magnets, i.e. kicks to the beam proportional to the magnet current (e.g. a dipole field error or an orbit corrector) or to the misalignment (e.g. a misaligned quadrupole). A more generic representation with respect to Eq. 2.10 is then:

$$\begin{bmatrix} \langle \mathbf{x} \rangle \\ \langle \mathbf{p}_x \rangle \\ \langle \mathbf{y} \rangle \\ \langle \mathbf{p}_y \rangle \\ I_i \\ \vdots \\ \Delta x_j \\ \vdots \end{bmatrix}_S = \begin{bmatrix} & & & & & r_{x,I_i} & \cdots & r_{x,\Delta x_j} & \cdots \\ & & & & & r_{p_x,I_i} & \cdots & r_{p_x,\Delta x_j} & \cdots \\ & & & & & r_{y,I_i} & \cdots & r_{y,\Delta x_j} & \cdots \\ & & & & & r_{p_y,I_i} & \cdots & r_{p_y,\Delta x_j} & \cdots \\ \mathbf{R}_{0S} & & & & & 1 & 0 & 0 & 0 \\ 0 & 0 & 0 & 0 & 0 & 0 & \ddots & 0 & 0 \\ 0 & 0 & 0 & 0 & 0 & 0 & 0 & 1 & 0 \\ 0 & 0 & 0 & 0 & 0 & 0 & 0 & 0 & \ddots \end{bmatrix} \begin{bmatrix} \langle \mathbf{x} \rangle \\ \langle \mathbf{p}_x \rangle \\ \langle \mathbf{y} \rangle \\ \langle \mathbf{p}_y \rangle \\ \vdots \\ I_i \\ \vdots \\ \Delta x_j \\ \vdots \end{bmatrix}_0 \quad (2.11)$$

In Eq. 2.11 one can identify 4 main block matrices. The top-left matrix is the initial \mathbf{R}_{0S} . The bottom-left and bottom-right are trivial, and are only needed to keep the square form of the transport matrix. The coefficients $r_{i,j}$ of the top-right matrix are responsible for describing the linear effects on the beam mean orbit due to misalignments, steerers and/or dipole errors. One often refers to this latest block as the *response matrix*. It has to be noticed that by construction the top-left block is not influenced by the right side of the matrix. Indeed the covariance matrix representing the beam envelope does not depend on

the mean values of particle coordinates: e.g. a dipole corrector kicks all the particles in the same way (at first order), corresponding in phase space to a rigid translation of the particle distribution without affecting its shape. That is why when speaking about *beam optics* one normally considers only the \mathbf{R}_{0S} matrix, which evolves on its own according to Eq. 2.3. The coefficients on the top-right block are instead influenced by \mathbf{R}_{0S} while evolving along the lattice, so the full response matrix can only be evolved by considering the full matrix in Eq. 2.11.

2.2 First Order Transverse Beam Optics

A common formalism to describe the transverse beam dynamics is by using the Twiss parameters² α , β , γ and the emittance ϵ . Such formalism is normally used to treat the special case of uncoupled, monochromatic, gaussian beams. Under these additional assumptions one can study the two transverse planes $(x; p_x)$ and $(y; p_y)$ independently. Moreover, considering for example the horizontal phase space $(x; p_x)$, the beam is a bi-Gaussian distribution enclosed in an ellipse whose equation is:

$$\epsilon = \gamma x^2 + 2\alpha x p_x + \beta p_x^2; \quad (2.12)$$

$$\text{where } \gamma = \frac{1 + \alpha^2}{\beta}. \quad (2.13)$$

The relation with the covariance matrix of such a representation is expressed as [45]:

$$\Sigma = \begin{bmatrix} \sigma(\mathbf{x}, \mathbf{x}) & \sigma(\mathbf{x}, \mathbf{p}_x) \\ \sigma(\mathbf{p}_x, \mathbf{x}) & \sigma(\mathbf{p}_x, \mathbf{p}_x) \end{bmatrix} \quad (2.14)$$

$$= \epsilon \begin{pmatrix} \beta & -\alpha \\ -\alpha & \gamma \end{pmatrix}. \quad (2.15)$$

By the definitions of Eq. 2.13 and Eq. 2.15 one can note that the determinant of the Σ matrix, which is conserved in a transfer line due to Eq. 2.8, is the Twiss emittance ϵ square:

$$\begin{aligned} \det(\Sigma) &= \epsilon^2(\beta\gamma - \alpha^2) \\ &= \epsilon^2. \end{aligned} \quad (2.16)$$

Equation 2.16 is consistent with the definition of statistical emittance, Eq. 2.9. Here the Twiss emittance has also a geometrical meaning: multiplied by π it represents the area of the ellipse enclosing 68.7% of the beam particles, as in Eq. 2.12.

Following the same formalism of Eq. 2.7, one can then write the evolution of the Twiss parameters along a transfer line as:

$$\begin{pmatrix} \beta_s & -\alpha_s \\ -\alpha_s & \gamma_s \end{pmatrix} = \begin{pmatrix} A_{0S} & B_{0S} \\ C_{0S} & D_{0S} \end{pmatrix} \begin{pmatrix} \beta_0 & -\alpha_0 \\ -\alpha_0 & \gamma_0 \end{pmatrix} \begin{pmatrix} A_{0S} & C_{0S} \\ B_{0S} & D_{0S} \end{pmatrix} \quad (2.17)$$

²Also called Courant-Snyder notation, introduced in [44]

where

$$\begin{pmatrix} A_{0S} & B_{0S} \\ C_{0S} & D_{0S} \end{pmatrix} = \mathbf{R}_{0S}; \quad (2.18)$$

$$\det(\mathbf{R}_{0S}) = 1. \quad (2.19)$$

Equation 2.17 is actually linear in terms of the initial Twiss parameters, so by simple algebra one can finally rewrite it as:

$$\begin{pmatrix} \beta_s \\ \alpha_s \\ \gamma_s \end{pmatrix} = \begin{pmatrix} A_{0S}^2 & -2A_{0S}B_{0S} & B_{0S}^2 \\ -A_{0S}C_{0S} & A_{0S}D_{0S} + B_{0S}C_{0S} & -B_{0S}D_{0S} \\ C_{0S}^2 & -2C_{0S}D_{0S} & D_{0S}^2 \end{pmatrix} \begin{pmatrix} \beta_0 \\ \alpha_0 \\ \gamma_0 \end{pmatrix} \quad (2.20)$$

Equation 2.20 shows that a given lattice, a priori, can be described by knowing the coefficients of \mathbf{R}_{0S} along the lattice, i.e. $(A_{0S}; B_{0S}; C_{0S}; D_{0S})$, without necessarily specifying the initial Twiss conditions $(\beta_0; \alpha_0; \gamma_0)$. However in storage rings, where this formalism was first introduced [44], the closed geometry identifies a closed solution, i.e. the Twiss parameters which do not change after one turn in the ring³. In such cases it is more interesting to track the Twiss functions $(\beta_s; \alpha_s; \gamma_s)$ all along the lattice, and so to see the β function as the modulation of the transverse beam size along the lattice according to Eq. 2.15:

$$\sigma_x(s) = \sqrt{\sigma(\mathbf{x}, \mathbf{x})(s)} = \sqrt{\beta(s)\epsilon} \quad (2.21)$$

So far one can make some important observations:

- Equation 2.21 underlines that ϵ can be seen as a figure of merit of the beam quality, independent of the lattice under consideration.
- The Twiss functions can be seen as a figure of merit of the lattice quality, even though they depend on the initial Twiss parameters, i.e. on the injected or circulating beam.
- While optimising a transfer line one might have some freedom in the initial Twiss parameters, so it might be useful to directly optimise the behaviour of the coefficients of \mathbf{R}_{0S} instead of the Twiss functions.

Given some initial Twiss parameters, and so the Twiss functions along a transfer line, one can rewrite [39, 44] the transport matrix 2.18 as:

$$\mathbf{R}_{0S} = \begin{pmatrix} A_{0S} & B_{0S} \\ C_{0S} & D_{0S} \end{pmatrix} = \begin{pmatrix} \sqrt{\frac{\beta_s}{\beta_0}}(\cos \mu_s + \alpha_0 \sin \mu_s) & \sqrt{\beta_s \beta_0} \sin \mu_s \\ \frac{\alpha_0 - \alpha_s}{\sqrt{\beta_s \beta_0}} \cos \mu_s - \frac{1 + \alpha_s \alpha_0}{\sqrt{\beta_s \beta_0}} \sin \mu_s & \sqrt{\frac{\beta_0}{\beta_s}}(\cos \mu_s - \alpha_s \sin \mu_s) \end{pmatrix} \quad (2.22)$$

where μ is the *phase-advance* and is defined as

$$\mu_s = \int_0^s \frac{1}{\beta(s)} ds. \quad (2.23)$$

³Details on how to find the closed solution of a given lattice are described in appendix A.

From this particular form, can observe that the matrix in Eq. 2.22 can be rewritten as:

$$\mathbf{R}_{0s} = \begin{pmatrix} \sqrt{\beta_s} & 0 \\ -\frac{\alpha_s}{\sqrt{\beta_s}} & \frac{1}{\sqrt{\beta_s}} \end{pmatrix} \begin{pmatrix} \cos \mu_s & \sin \mu_s \\ -\sin \mu_s & \cos \mu_s \end{pmatrix} \begin{pmatrix} \frac{1}{\sqrt{\beta_0}} & 0 \\ \frac{\alpha_0}{\sqrt{\beta_0}} & \sqrt{\beta_0} \end{pmatrix} \quad (2.24)$$

where the middle matrix of Eq. 2.24 is a simple clock-wise rigid rotation of the angle μ_s . This expression suggests the introduction of the so called *normalised phase space*. Given the Twiss parameters at some location, instead of using the canonical coordinate $(x; p_x)$, one can apply the following transformation:

$$\begin{pmatrix} x_N \\ p_{Nx} \end{pmatrix} = \begin{pmatrix} \frac{1}{\sqrt{\beta}} & 0 \\ \frac{\alpha}{\sqrt{\beta}} & \sqrt{\beta} \end{pmatrix} \begin{pmatrix} x \\ p_x \end{pmatrix} \quad (2.25)$$

or its inverse:

$$\begin{pmatrix} x \\ p_x \end{pmatrix} = \begin{pmatrix} \sqrt{\beta} & 0 \\ -\frac{\alpha}{\sqrt{\beta}} & \frac{1}{\sqrt{\beta}} \end{pmatrix} \begin{pmatrix} x_N \\ p_{xN} \end{pmatrix} \quad (2.26)$$

where the N subscript indicates the new *normalised* coordinates. In view of this transformation one can then see Eq. 2.24, from right to left, as the operation of going to the normalised phase space at $s = 0$; operate a simple rotation of angle μ_s ; finally go back to the real phase-space coordinates. The same transformations can be defined for the Twiss matrix:

$$\begin{pmatrix} \beta_N & -\alpha_N \\ -\alpha_N & \gamma_N \end{pmatrix} = \begin{pmatrix} \frac{1}{\sqrt{\beta_T}} & 0 \\ \frac{\alpha_T}{\sqrt{\beta_T}} & \sqrt{\beta_T} \end{pmatrix} \begin{pmatrix} \beta_R & -\alpha_R \\ -\alpha_R & \gamma_R \end{pmatrix} \begin{pmatrix} \frac{1}{\sqrt{\beta_T}} & \frac{\alpha_T}{\sqrt{\beta_T}} \\ 0 & \sqrt{\beta_T} \end{pmatrix} \quad (2.27)$$

$$\begin{pmatrix} \beta_R & -\alpha_R \\ -\alpha_R & \gamma_R \end{pmatrix} = \begin{pmatrix} \sqrt{\beta_T} & 0 \\ -\frac{\alpha_T}{\sqrt{\beta_T}} & \frac{1}{\sqrt{\beta_T}} \end{pmatrix} \begin{pmatrix} \beta_N & -\alpha_N \\ -\alpha_N & \gamma_N \end{pmatrix} \begin{pmatrix} \sqrt{\beta_T} & -\frac{\alpha_T}{\sqrt{\beta_T}} \\ 0 & \frac{1}{\sqrt{\beta_T}} \end{pmatrix} \quad (2.28)$$

where the subscript N and R indicate respectively the coordinate in normalised and real phase space, while T indicates the Twiss parameters with respect to which the transformation is performed. Clearly if the transformation 2.27 is performed with respect to the same Twiss parameters as the real phase space one, then in normalised phase space the transverse matrix simply becomes the identity matrix. In this case the representation of the beam in *normalised* phase space from the ellipse of Eq. 2.12 is a circle:

$$\epsilon = x_N^2 + p_{xN}^2 \quad (2.29)$$

whose area is $\epsilon\pi$.

The representation of the beam in normalised phase space is often very handy, because Eq. 2.17 becomes a simple rotation:

$$\begin{pmatrix} \beta_{Ns} & -\alpha_{Ns} \\ -\alpha_{Ns} & \gamma_{Ns} \end{pmatrix} = \begin{pmatrix} \cos \mu_s & \sin \mu_s \\ -\sin \mu_s & \cos \mu_s \end{pmatrix} \begin{pmatrix} \beta_{N0} & -\alpha_{N0} \\ -\alpha_{N0} & \gamma_{N0} \end{pmatrix} \begin{pmatrix} \cos \mu_s & -\sin \mu_s \\ \sin \mu_s & \cos \mu_s \end{pmatrix} \quad (2.30)$$

The use of the Twiss function formalism, Eq. 2.22 and 2.24, will be limited in this work. This is because in an open transfer line the initial Twiss conditions might not always be

well defined. However the Twiss formalism to represent the phase-space evolution in real or normalised phase space is such a powerful tool that it is not possible to avoid using it. This formalism remains valid also for non-Gaussian beams. In this case one needs to be careful not to imagine the beam as fully enclosed in the ellipse of Eq. 2.12, as to interpret Eq. 2.21 as the standard deviation of the size of the beam, but just as the square root of the variance of the beam distribution.

2.3 Higher Order Representation

So far only the simplest case of linear transport has been considered, i.e. each component of a beamline is modelled as a simple matrix that transforms the initial particle coordinates into the final one. In reality a beamline can include higher order magnetic elements (e.g. sextupoles), or in general linear elements, as quadrupoles, might have non-linear effects. Considering again the MAD-X formalism [43], one could extend the beam dynamics representation up to the second order of each element as:

$$\begin{bmatrix} \mathbf{x} \\ \mathbf{p}_x \\ y \\ \mathbf{p}_y \\ c t \\ \Delta \mathbf{p}/p_0 \end{bmatrix}_S = \mathbf{R}_{0S} \begin{bmatrix} \mathbf{x} \\ \mathbf{p}_x \\ y \\ \mathbf{p}_y \\ c t \\ \Delta \mathbf{p}/p_0 \end{bmatrix}_0 + \mathbf{T}_{0S} \left(\begin{bmatrix} \mathbf{x} \\ \mathbf{p}_x \\ y \\ \mathbf{p}_y \\ c t \\ \Delta \mathbf{p}/p_0 \end{bmatrix}_0, \begin{bmatrix} \mathbf{x} \\ \mathbf{p}_x \\ y \\ \mathbf{p}_y \\ c t \\ \Delta \mathbf{p}/p_0 \end{bmatrix}_0 \right) \quad (2.31)$$

In Eq. 2.31 \mathbf{T}_{0S} is a tensor-like object that defines the coefficients of all the second-order terms. For example \mathbf{T}_{0S136} is the coefficient of the contribution to x_{iS} due to the second-order term $y_{i0} \Delta p_i/p_0$. On the other hand the representation of Eq. 2.31 turns out to be impractical for studying higher than second-order effects because of the exponential growth on the number of terms. For this MAD-X [6, 46] introduced the PTC symplectic integrator [47] that can be used to study the non-linear dynamics at any desired order mainly by means of particle tracking.

The use of PTC_TRACKING techniques to study non-linear dynamics is the standard tool used at CERN for optimising the main accelerator complex (e.g. PS, SPS, LHC). For the present work the use of PTC_TRACK is not the most efficient way to disentangle the different effects. Moreover this work is mainly focused on non-linear effects due to terms in $\Delta p/p_0$. To clearly emphasise the energy dependence of the final beam parameters, the formalism used in the present work is described in the following section.

2.4 Energy Dependence

To first approximation the energy dependence on the single i -th particle trajectory is treated as linear in $\Delta p_i/p_0$, where p_i is the particle momentum and p_0 is the design momentum of

the line under consideration. This dependence comes from the linearisation of the inverse of the particle momentum p_i that arises in nearly any magnetic element of a beamline. The kick ($\Delta\alpha$) experienced by a particle crossing a thin magnet can be expressed as:

$$\Delta\alpha = \frac{K}{p_i} \quad (2.32)$$

$$= \frac{K}{p_0(1 + \Delta p_i/p_0)} \quad (2.33)$$

$$= \frac{K}{p_0} [1 - \Delta p_i/p_0 + (\Delta p_i/p_0)^2 - (\Delta p_i/p_0)^3 + O((\Delta p_i/p_0)^4)] \quad (2.34)$$

$$= \frac{K}{p_0} \Lambda, \quad (2.35)$$

where K is some constant dependent on the type, geometry, strength of the magnet, and on the incoming particle orbit. The newly introduced variable Λ is defined as $1/(1 + \Delta p_i/p_0)$, or its Taylor expansion⁴, and carries the energy dependence to any desired order.

In order to better emphasise the effects of the momentum dependence, as in Eq. 2.34, on the single particle trajectory one can consider an even more simplified formalism by adding some assumptions:

- The two transverse planes are independent, i.e. there is no coupling between them. For reference only the horizontal plane will be considered in the following.
- There is no incoming *dispersion*, i.e. there is no dependence on $\Delta p/p_0$ of the incoming coordinates (x_0, p_{x_0}) .
- The lattice is made of *thin-lens* elements: zero-length devices that kick the beam sharply. Note that this will make the beam trajectory not smooth.
- Only linear elements in the incoming coordinates x and p_x are considered.
- No acceleration is performed in the modelled beamline. More generally, any effect that might change the momentum of a single particle (expressed by $\Delta p_i/p_0$) are neglected, e.g. synchrotron radiation.

The main components of such a beamline are drifts and quadrupoles, whose transfer matrices are:

$$\mathbf{R}_{\text{quadrupole}} = \begin{bmatrix} 1 & 0 \\ k_Q I_Q & 1 \end{bmatrix} \quad (2.36)$$

$$\mathbf{R}_{\text{drift}} = \begin{bmatrix} 1 & L \\ 0 & 1 \end{bmatrix} \quad (2.37)$$

where k_Q is some constant proper of the quadrupole geometry and the reference beam energy; I_Q is the current set to the quadrupole; L is the length of the drift. To the standard definition

⁴The general form of this series expansion is available in appendix C, Eq. C.1.

of Eq. 2.36 and 2.37 one needs to add the dependence on the energy deviation with respect to the nominal. This can be done multiplying by Λ (from Eq. 2.35) every time a kick is applied to the incoming particle. Moreover one might want to treat the presence of correctors, dipoles and quadrupoles misalignments. Those elements, in first approximation, do not take part in the pure transverse optics behaviour, so one needs to introduce a third column (and a third row, which is trivial) to accommodate their effect on the beam. It is then straightforward to arrive at the following transport matrices:

$$\mathbf{x}_0 = \begin{bmatrix} x_0 \\ p_{x_0} \\ 1 \end{bmatrix} \quad (2.38)$$

$$\mathbf{R}_{\text{drift}} = \begin{bmatrix} 1 & L & 0 \\ 0 & 1 & 0 \\ 0 & 0 & 1 \end{bmatrix} \quad (2.39)$$

$$\mathbf{R}_{\text{corrector}} = \begin{bmatrix} 1 & 0 & 0 \\ 0 & 1 & k_C I_C \Lambda \\ 0 & 0 & 1 \end{bmatrix} \quad (2.40)$$

$$\mathbf{R}_{\text{bending}} = \begin{bmatrix} 1 & 0 & 0 \\ 0 & 1 & k_D I_D (\Lambda - 1) + \delta I_D k_D I_D \Lambda \\ 0 & 0 & 1 \end{bmatrix} \quad (2.41)$$

$$\mathbf{R}_{\text{quadrupole}} = \begin{bmatrix} 1 & 0 & 0 \\ k_Q I_Q \Lambda & 1 & \Delta x_Q k_Q I_Q \Lambda \\ 0 & 0 & 1 \end{bmatrix} \quad (2.42)$$

where I_C is the corrector current, I_D is the nominal dipole current and $\delta I_D = \Delta I_D / I_D$ is a *scaling error* of the bending magnet. $K_Q; K_D; K_C$ are constants which depend on the static properties of each element and on the reference beam energy. By construction the elements of the third column are never multiplied with each other while composing the transport matrix of a multi-element lattice. This means that indeed one can make independent any parameter that appears uniquely in this column, i.e. correctors current, quadrupole misalignment and dipole errors as in the formalism of Eq. 2.11. Note that the factor Λ has been introduced for every term that kicks the beam, with the exception of the bending magnet, which has a $(\Lambda - 1)$ factor. The case of the bending magnet is very special: if there is no scaling error (i.e. $\delta I_D = 0$), and a particle with design momentum is considered (i.e. $\Delta p_i / p_0 = 0$), then the transport matrix (Eq. 2.41) becomes trivial. The bending magnet is still kicking the particle, but it is also “bending” the reference system by the same amount, such that the effects on the particle coordinate is null. Another important observation is that for the quadrupole element, Eq. 2.42, the kick appears in the first column. This means that such kick will get multiplied by the strength of all the other elements while composing the transfer matrix of a multi-element transfer line. In terms of energy dependence, the combined transfer matrix describing a multi-element beamline will contain elements expressed as a polynomial in Λ up to Λ^n or $(\Lambda - 1)\Lambda^n$, where n is the number of quadrupole elements present in the line, and the terms in $(\Lambda - 1)$ are associated to the effects of a single bending magnet encountered by

the beam. A generic form of a final transport matrix would be:

$$\mathbf{R}_{\text{lattice}} = \begin{bmatrix} \sum_{i=1}^n a_i \Lambda^i & \sum_{i=1}^n b_i \Lambda^i & I_{D_i}(\Lambda - 1) \sum_{i=1}^n c_i \Lambda^i + I_{C_i} \Lambda \sum_{i=1}^n d_i \Lambda^i + \dots \\ \dots & \dots & \dots \\ 0 & 0 & 1 \end{bmatrix} \quad (2.43)$$

where a_i, b_i, c_i, d_i are coefficients that depend only on quadrupole strengths and lattice design geometry. In the third column of the full transport matrix in Eq. 2.43 there is a linear combination of the different effects that uniformly kick the centroid of the beam. For clarity, in Eq. 2.43 only bending magnets (I_{D_i}) and correctors (I_{C_i}) are reported. Quadrupoles misalignments and errors or variation of the bending currents are similar to the corrector case.

Typically, one refers to chromatic effects or *chromaticity* when beam energy variation affects the pure *optics*, i.e. the top left 2×2 sub-matrix of $\mathbf{R}_{\text{lattice}}$. *Dispersion* is instead the effect of beam energy on the *orbit* of the beam.

The currents of correctors and bending magnets have been explicitly kept in Eq. 2.43, such that one can imagine them as knobs that can be varied. One can also introduce another scaling factor for the *optics* of the lattice, i.e. imagine that all the quadrupoles can be scaled by some amount. By looking at Eq. 2.42, one could rewrite I_Q as $I_{0Q}(1 + \Delta I_Q/I_{0Q}) = I_{0Q}\Gamma$, where I_{0Q} is the ‘‘nominal’’ quadrupole current. By defining $\Gamma = (1 + \Delta I_Q/I_{0Q})$, one can finally rewrite the generic ingredients of matrix $\mathbf{R}_{\text{lattice}}$ as:

$$\sum_{i=1}^n a_i \Lambda^i = \sum_{i=1}^n a_{0,i} \Lambda^i \Gamma^i \quad (2.44)$$

$$I_{D_i}(\Lambda - 1) \sum_{i=1}^n c_i \Lambda^i = -\frac{\Delta p_i}{p_0} I_{D_i} \sum_{i=1}^n c_{0,i} \Lambda^{i+1} \Gamma^i \quad (2.45)$$

$$I_{C_i} \Lambda \sum_{i=1}^n d_i \Lambda^i = I_{C_i} \sum_{i=1}^n d_{0,i} \Lambda^{i+1} \Gamma^i \quad (2.46)$$

Together with the Taylor expansion of Λ^n and Γ^n , one has all the elements to make some operational observation on the behaviour of a lattice as a function of the beam energy⁵⁶:

- The chromatic effect of varying energy is equivalent, at first order *only*, to scale of the same amount, but opposite sign, the quadrupoles strength. In fact for the nominal energy one can write:

$$\sum_{i=1}^n a_{0,i} \Gamma^i = \sum_{i=1}^n a_{0,i} \left(1 + i \frac{\Delta I_Q}{I_{0,Q}} + \frac{i(i-1)}{2} \left(\frac{\Delta I_Q}{I_{0,Q}} \right)^2 + \dots \right) \quad (2.47)$$

while for nominal quadrupole strengths, and so expanding the energy dependence, it becomes:

$$\sum_{i=1}^n a_{0,i} \Lambda^i = \sum_{i=1}^n a_{0,i} \left(1 - i \frac{\Delta p_i}{p_0} + \frac{i(i+1)}{2} \left(\frac{\Delta p_i}{p_0} \right)^2 + \dots \right). \quad (2.48)$$

Clearly the two expressions are not easily comparable at orders higher than the first.

⁵In order to obtain Eq. 2.45, one can use the fact that $1/(1+x) - 1 = -x/(1+x)$.

⁶For convenience, the generic Taylor expansions of such expressions are reported in appendix C.

- All the elements of matrix $\mathbf{R}_{\text{lattice}}$ contribute to orbit and dispersion. However in an ideal aligned machine, with zero incoming beam orbit and no correctors, only the third column of matrix $\mathbf{R}_{\text{lattice}}$ is relevant, and its non-zero terms are in the form of Eq. 2.45. This means that, in an ideal machine, only the bending magnets create dispersion.
- The first observation is valid also for dispersive effects: scaling *all* the magnetic elements is equivalent *only at first order* to changing, with opposite sign, the energy of the beam.
- The contribution to dispersion of a corrector, as well as other imperfections, comes from the expansion of Eq. 2.46:

$$I_{C_i} \sum_{i=1}^n d_{0,i} \Lambda^{i+1} = I_{C_i} \sum_{i=1}^n d_{0,i} \left(1 - (i+1) \frac{\Delta p_i}{p_0} + \frac{(i+1)(i+2)}{2} \left(\frac{\Delta p_i}{p_0} \right)^2 + \dots \right). \quad (2.49)$$

Note that, by construction, the dispersion contribution of a corrector is linear in the corrector current and strictly related to its orbit response, but the relation between the two is not trivial.

- Following the assumed transfer matrix of bending magnets, Eq. 2.41, one can write the *orbit* response due to bending magnet scaling, i.e. due to the term in δI_D , as:

$$\delta I_D I_D \sum_{i=1}^n c_{0,i} \Lambda^{i+1} \Gamma^i. \quad (2.50)$$

Note that the response to orbit by scaling a bending magnet is equal to the *linear* dispersion contribution of that magnet, Eq. 2.45. This means that operationally one can measure the *nominal* (without being affected by correctors and quadrupoles misalignments) dispersion in a line, with opposite sign, by measuring the *orbit response* by scaling of the bending magnets. Of course this by itself will *not* give the information about the dispersion contribution of a bending scaling error that, similarly to correctors, has a dependence similar to Eq. 2.49, but it is a powerful method to measure the expected nominal dispersion, verify the optics, and to have an indirect calibration of any dispersive Beam Position Monitors (BPM), i.e. monitors that are installed where dispersion is by design non zero.

This thesis aims to study in detail the non-linear energy dependence of $\mathbf{R}_{\text{lattice}}$. From the formalism introduced so far, and in particular by the expansions of Eq. 2.43, one could make the attempt to extract the leading orders of non-linear effects. On the other hand the pragmatic approach used in this work is to numerically and experimentally probe $\mathbf{R}_{0\mathbf{s}}$ with different beam energies ($\Delta p/p_0$), and so represent the beam evolution as:

$$\begin{bmatrix} \mathbf{x} \\ \mathbf{p}_x \\ \mathbf{y} \\ \mathbf{p}_y \\ c \mathbf{t} \end{bmatrix}_S = \overline{\mathbf{R}_{0\mathbf{s}}}(\Delta p/p_0) \begin{bmatrix} \mathbf{x} \\ \mathbf{p}_x \\ \mathbf{y} \\ \mathbf{p}_y \\ c \mathbf{t} \end{bmatrix}_0 \quad (2.51)$$

This is the basis of the simulations that will be presented in Chapter 4.

Chapter 3

Software Tools

The main hardware components of any modern accelerator are: charged particle sources, magnets to steer and focus the beam in the transverse plane, radio-frequency source and cavities to accelerate and focus the beam in the longitudinal direction, and beam instrumentation to measure the beam properties and quality. Thanks to computer technology most of the signals and knobs can be handled from a single console that has in principle access to all the signals and the parameters of the equipment. However more options and signals, and hence information available is not necessarily a plus by itself. One might easily get lost in the zoo of signals, and eventually concentrate on a “wrong” sub-set of them. In order to make order and extract the necessary intelligible information, one needs to take into account additional, complementary work to design, write and debug different kinds of software and tools.

This chapter describes the main tools which have been developed in order to achieve the results presented in the following chapters. The emphasis will be put on the main mathematical concepts and procedures implemented into the tools, more than the implementation itself which is of less interest. The described tools and procedures have to be considered as the working state of the art at the time of writing. As with any software, the developed tools are dynamic systems that are continually updated and improved to address the requests that arise on a daily basis while studying the behaviour of the accelerator. For this a large amount of resources and time have been invested to implement the tools so as to be as generic as possible from the beginning. The results presented in Chapter 5 are indicative of the success of this approach: the same few tools have been used to tackle a variety of diverse problems.

3.1 Data Acquisition with MATLAB

The keys for the success of any experiment are first the quality of the available instrumentation, and a reliable and flexible system of data acquisition and data processing. At CERN a complex network of front ends is responsible for the digitisation and distribution of the data, which are normally available in quasi-realtime to the experimentalists via the JAPC

Java API¹ [48]. The choice of the Java programming language allows one to have a single API for the different platforms normally used at CERN (mainly Scientific Linux and Microsoft Windows). On the other hand Java does not provide a satisfactory mathematical environment, and any development of new software is time consuming. As a result, different communities at CERN developed over the years a series of monolithic Java applications to perform common tasks or monitor beam properties and equipment status. This framework is very appropriate for machine operations, but it can be restrictive for machine development: accelerator physicists are left with very few generic tools to acquire and save signals, which need to be post-processed by third-party applications. It is worthwhile to mention Oasis [49]: a virtual scope that allows one to remotely connect, configure and obtain digitised signals from most of the ADCs installed around the CERN Accelerator Complex, and that replaced older applications like the Sampler [50] that is still in use for some particular applications. At CTF3 a few custom Java applications have been developed, for instance a generic signal monitor [51, 52] used to keep track of signal references and to detect hardware drifts, and many software feedbacks to stabilise mainly the Radio Frequency (RF) power used to accelerate the beam [53, 54].

An alternative to the pure Java approach was to use another computing environment that can be interfaced directly or indirectly to the CERN accelerator control system. The choice at CTF3 has been to use MATLAB [55]. MATLAB is a well developed multi-platform computing environment, which is currently available at CERN both on Windows and Linux consoles. It is very powerful; it has many advanced libraries available (most of the toolboxes are available within the CERN installation); it has a big user community inside and outside CERN; it has an easy to learn syntax (adopted also by other computing environments); it is a weakly typed programming language (i.e. a few lines of code are enough to perform advanced calculations and produce publication-ready plots), and, very importantly, it supports the loading of external Java libraries. Since most of the APIs available at CERN are written in Java, it was natural to choose a programming language that could make use of these APIs and at the same time allow fast development for all the studies and applications that require high flexibility, rich mathematical libraries and easy to produce results and plots.

MATLAB libraries to *get* signals and *set* equipment parameters have been developed by the CTF3 community over the past years. This made possible many different studies at CTF3. Unfortunately these libraries were not sufficient for most of the studies presented in this work. In particular there was no simple way to ensure the synchronisation between the signals acquired from different devices, and to systematically collect the signals for each beam produced in the facility. The step forward was then to profit from the *monitoring* capabilities normally provided by the JAPC API, but never implemented in MATLAB before. This triggered a full re-styling of the old libraries and the implementation of a generic library known as *matlabJapc*, which made possible most of the experimental work presented here and many more studies in other departments at CERN.

Just as a practical example, the following MATLAB code is enough to monitor a BPM signal (identified by the JAPC parameter “CL.STBPM0402S/Samples#samples”):

¹Application Programming Interface.


```
1 % create a matlabJapcMonitor object:
2 myMonitorObject = matlabJapcMonitor('SCT.USER.SETUP', ...
   {'CL.STBPM0402S/Samples#samples'}, @(data) ...
   plot(data.CL_STBPM0402S.Samples.samples.value));
3 % start the acquisition:
4 myMonitorObject.start();
5 %% ... after some time one might want to stop the acquisition:
6 myMonitorObject.stop();
```

Each time a new beam is produced at CTF3 under the so called *machine-cycle* or *user* “SCT.USER.SETUP” the monitor object receives the digitised signal from the BPM, and it plots it.

The details of the implementation and the features of the *matlabJapc* library are beyond the scope of this work, but it is worth mentioning the main lesson learned by the experience of its development: for machine development the key to success is to have a reliable, easy and fast way to combine the information from all the signals available in real-time. A natural environment can be any *scripting* environment with *rich mathematical capabilities*, a *reasonable user community* and the ability to easily interact with the control system via *simple* and at the same time *flexible* libraries. This is confirmed by the fact that, also thanks to our successful experience, other communities at CERN started to use our libraries and to develop similar ones for other scripting environments (e.g. Python, Mathematica). All these experiences triggered discussions between the “beam experts” and the CERN Controls group (BE/CO), which might contribute to the future development of the CERN controls infrastructure.

3.2 Dispersion measurement tool

The most commonly available observable for the operator to set-up a beamline is the centroid beam position and the beam intensity along the beamline, i.e. the beam orbit and transmission. At CTF3 this is mainly measured by Beam Position Monitors (BPMs) installed in the different lines. At start-up, the hope of the operator is that the transverse optics and the beam quality are good enough to be able to transport the beam all the way without major beam losses. This is normally achieved after a few empirical iterations acting on orbit corrector magnets to steer the beam close to the centre of BPMs and, if necessary, slightly adjusting the quadrupoles’ strength.

Once the beam is transported all the way on a “reasonable” orbit, a useful verification of the quality of the set-up can be achieved by means of dispersion measurements, i.e. the orbit deviation of a particle due to its energy deviation with respect to the design energy. This is specially important in lines where dispersion is non-zero by design, like in the Drive Beam Recombination Complex (DBRC). An uncontrolled dispersion may easily increase the transverse beam size, leading to heavy beam losses and degraded stability. At CTF3 a MATLAB application has been developed to perform *online* dispersion measurements in the different beamlines. The final functionalities and design of this application is the result of various iterations to respond to the needs raised during daily CTF3 operations. Before

describing the main features and use of the application the basic concepts and techniques used for these measurements are discussed.

3.2.1 Common notions for dispersion measurement

Some theoretical details about transverse phase-space energy dependence have been treated in Section 2.4, to which we will refer in the following paragraph. By definition [56] the dispersion is the variation of the orbit of a single off-energy particle, with respect to the orbit of a particle with nominal energy. In the most general case the dispersion is a non-linear multi-dimensional function of the phase-space coordinates in terms of the momentum offset ($x = D(\Delta p/p_0)$). In the simpler linear case it is the linear coefficient D_x in the relation:

$$\Delta x_i = D_x \frac{\Delta p_i}{p_0} \quad (3.1)$$

where Δx_i is the orbit displacement of the i^{th} particle due to its energy offset $\Delta p_i/p_0$. In first approximation one can see the full beam as a single particle with energy equal to its mean energy. In order to measure the dispersion in a transfer line, experimentally one has to change the energy of the beam with respect to the nominal energy for which the line is tuned, and so measure the effect on the mean beam orbit. At CTF3 this can be accomplished in different ways:

- By scaling all the magnetic elements of the transfer line under consideration. This does not change the properties of the beam, but the scaled strength of the magnetic elements will give the same effect as an inverse change in the energy of the beam. Note that this method will not reveal a possible incoming dispersion if the scaling is performed only on a section of the line. Moreover, as shown in Section 2.4, this method is valid only for measuring the first-order dispersion.
- By scaling the beam current at the source. Since the Drive Beam linac relies on fully loaded acceleration, any change in beam current is translated in an effective mean energy variation² that can be assumed to be linear [5].
- By moving the RF phase and/or power of one accelerating structure. This will simply lead to a smaller acceleration at one location of the linac, and so a final variation of beam energy. This measurement would start only from the chosen structure onward, and normally one could obtain slightly different results depending on the chosen structure.
- Parasitically, by watching the natural shot-to-shot beam-energy jitter due to RF phase, RF power jitter and/or beam current jitter.

²By scaling the beam current one might also induce some other intensity-related orbits effect, like wake fields kicks. This has been used for Wakefield Free Steering (WFS) in [57, 58].

From a mathematical point of view all these methods are similar and can be described by a simple matrix formalism:

$$\vec{a} = (a_1; a_2; a_3; \dots; a_n) \quad (3.2)$$

$$\mathbf{M} = \begin{bmatrix} b_{1,1} & b_{1,2} & b_{1,3} & \dots & b_{1,n} \\ b_{2,1} & b_{2,2} & b_{2,3} & \dots & b_{2,n} \\ b_{3,1} & b_{3,2} & b_{3,3} & \dots & b_{3,n} \\ \vdots & \vdots & \vdots & \dots & \vdots \\ b_{m,1} & b_{m,2} & b_{m,3} & \dots & b_{m,n} \end{bmatrix} \quad (3.3)$$

where \mathbf{M} contains the beam position *variation* $b_{i,j}$ as measured at m BPMs with respect to the unexcited orbit, for n different shots. The vector \vec{a} contains the information on the beam momentum variation imposed at each shot. Normally it would be:

$$\frac{\Delta p_i}{p_0} = k a_i \quad (3.4)$$

where i indicates the i^{th} shot and k is a constant of proportionality that depends on the way one decided to excite the relative energy variation $\Delta p_i/p_0$. The beamline *linear* dispersion at the BPMs location would then be the array of the linear fit coefficients between \vec{a} and each row of \mathbf{M} :

$$k \begin{pmatrix} D_1 \\ D_2 \\ D_3 \\ \vdots \\ D_m \end{pmatrix} \begin{pmatrix} a_1 & a_2 & a_3 & \dots & a_n \end{pmatrix} = \begin{bmatrix} b_{1,1} & b_{1,2} & b_{1,3} & \dots & b_{1,n} \\ b_{2,1} & b_{2,2} & b_{2,3} & \dots & b_{2,n} \\ b_{3,1} & b_{3,2} & b_{3,3} & \dots & b_{3,n} \\ \vdots & \vdots & \vdots & \dots & \vdots \\ b_{m,1} & b_{m,2} & b_{m,3} & \dots & b_{m,n} \end{bmatrix} \quad (3.5)$$

where \vec{D} is the dispersion for the different BPMs.

Equation 3.5 can be easily solved in least-square terms by multiplying on the right of both sides of the equation by the column vector \vec{a} divided by its square norm:

$$k \begin{pmatrix} D_1 \\ D_2 \\ D_3 \\ \vdots \\ D_m \end{pmatrix} = \begin{bmatrix} b_{1,1} & b_{1,2} & b_{1,3} & \dots & b_{1,n} \\ b_{2,1} & b_{2,2} & b_{2,3} & \dots & b_{2,n} \\ b_{3,1} & b_{3,2} & b_{3,3} & \dots & b_{3,n} \\ \vdots & \vdots & \vdots & \dots & \vdots \\ b_{m,1} & b_{m,2} & b_{m,3} & \dots & b_{m,n} \end{bmatrix} \begin{pmatrix} a_1 \\ a_2 \\ a_3 \\ \vdots \\ a_n \end{pmatrix} \frac{1}{\sum_i a_i^2} \quad (3.6)$$

The only missing information to finally extract the dispersion pattern in natural units is the value of k , which depends on the way the measurement was performed:

All magnets scaling. In linear approximation scaling 1% *up* all the magnetic elements of a lattice (or a sub-section of it) is equivalent to injecting a beam with 1% *less* energy. In this case $k = -1$.

Bending scaling. As shown in Section 2.4, scaling one or all the bending magnets is equivalent to measure, with opposite sign, the *nominal linear* dispersion induced by these magnet. Also in this case $k = -1$.

Beam current scaling. In theory by knowing the effective RF power delivered to the accelerating structures and their beam loading one could estimate the energy variation due to a change in beam current [5]. In practice the real dependence might not be easily accessible. As a generic alternative one can consider a reference BPM in a (high) dispersion region as an energy meter: at first order the beam position at such a BPM is proportional to the energy variation as in Eq. 3.1 where D_x is the dispersion at that BPM. So in Eq. 3.6 it would be $k = 1/D_x$, and \vec{a} the measured orbits at the reference BPM. Clearly one has to assume that one precisely knows the dispersion at that location, as well as the BPM calibrations, misalignments and incoming orbit. In practice by choosing the first BPM right after the first bending magnet encountered by the beam, one can easily compute and measure the dispersion with good precision just by knowing the bending angle³. Even not knowing precisely the “reference” dispersion value D_x one can always assume it fixed to a reasonable value, and so obtain at least a dispersion *pattern*. This can always be useful for example to verify areas where dispersion is expected to be zero.

Other beam energy variation. As for the beam current scaling, one might not have clear information on the shot-to-shot energy variation. In these cases it is always possible to refer to a reference dispersive BPM as an energy meter as in the previous case.

The described method to measure dispersion is extremely simple and robust, but one has to be careful in interpreting the obtained pattern: if the induced beam energy variation is too small one might be measuring other source of correlations, e.g. a jittering power supply. For this reason it turned out to be practical to add an error bar on each measurement point. This is defined as the r.m.s. of the residuals, normalised by the excitation norm:

$$\begin{pmatrix} \sigma_{D_1} \\ \sigma_{D_2} \\ \vdots \\ \sigma_{D_m} \end{pmatrix} = \sqrt{\frac{\sum_{row} \left(\begin{bmatrix} b_{1,1} & b_{1,2} & \dots & b_{1,n} \\ b_{2,1} & b_{2,2} & \dots & b_{2,n} \\ \vdots & \vdots & \dots & \vdots \\ b_{m,1} & b_{m,2} & \dots & b_{m,n} \end{bmatrix} - k \begin{pmatrix} D_1 \\ D_2 \\ \vdots \\ D_m \end{pmatrix} \begin{pmatrix} a_1 & a_2 & \dots & a_n \end{pmatrix} \right)^2}{(n-1) \sum_i a_i^2}} \quad (3.7)$$

The error bar computed with Eq. 3.7 increases both if there is no good correlation between energy excitations a_i and beam position $b_{m,i}$, and in the case where the energy excitation used is too small.

³This is particularly easy if there is no other elements between the bending and the BPM, but only a reasonably long drift.

3.2.2 Dispersion measurement via PCA

In some cases one has no knowledge about the energy variations experienced by the beam from shot to shot, i.e. no means to determine the vector \vec{a} . One can still attempt to compute the dispersion by means of Principal Component Analysis (PCA) [59, 60] of the matrix \mathbf{M} . If one assumes that the only source of beam position variation is due to a mean energy variation, i.e. there are no other betatron sources like a jittering power supply, then the strongest component of PCA is the dispersion pattern.

The dispersion monitor application developed at CTF3 implements PCA analysis of the acquired orbits. This can be useful not only to measure the dispersion pattern, but also to identify other sources of beam jitter. The steps used for the analysis are:

- Apply so-called *mean normalisation* to the matrix \mathbf{M} . In practice this means removing the mean beam position at each BPM. This should be automatic via the definition of the matrix \mathbf{M} as a differential orbit measurement with respect to a stable position, i.e. the mean orbit. This step is very important: a residual mean offset of the acquired beam positions might lead the analysis to detect not the main source of jitter, but simply the mean orbit of the beam.
- Perform so-called “scaling normalisation”. The main idea behind PCA is to find the correlated pattern that explains most of the jitter measured in \mathbf{M} . If one of the pickups measures a significantly higher jitter, then PCA would tend to be biased towards mainly explaining that oscillation, without really correlating it with other pickups. By assuming that the jitter observed is Gaussian distributed, it is then reasonable to scale each row of \mathbf{M} by the r.m.s. of the row itself.
- Compute the Singular Value Decomposition (SVD) of \mathbf{M} :

$$[\mathbf{U}, \mathbf{S}, \mathbf{V}] = \text{svd}(\mathbf{M}) \quad (3.8)$$

By construction the obtained decomposition is such that matrices \mathbf{U} and \mathbf{V} are orthogonal, while \mathbf{S} is diagonal, and it holds that $\mathbf{M} = \mathbf{USV}^T$.

- The dispersion pattern, in arbitrary units, is the first column of matrix \mathbf{U} rescaled by the inverse of the “scaling normalisation” factors applied at the beginning. This a fair assumption only if one is sure that the energy variation is the biggest source of orbit variation.
- The information of how much the energy was varying from shot to shot is available, in arbitrary units, in the first column of matrix \mathbf{V} .

In order to scale the dispersion pattern found to its natural units, one has to make additional assumptions. Once again the simplest and probably most reasonable method is to scale the pattern such that it fits the design dispersion at a reference location chosen within the acquired BPMs. An alternative method is to make some assumptions on the amplitude of the energy jitter one is expecting while performing the measurement. The typical beam-energy

jitter measured at CTF3 is of the order of $\sigma_{\Delta p/p_0} \approx 10^{-3}$. Since the BPM measurement is acquired in millimetres, and given that according to Eq. 3.1 it is $\sigma_{\Delta x} = D_x \sigma_{\Delta p/p_0}$, then it turns out that a reasonable estimation of the dispersion pattern in metres is the first column of \mathbf{U} scaled by $\mathbf{S}_{1,1}/\sqrt{n}$ where n is the number of beam shots acquired.

The PCA/SVD analysis provides another way of judging the quality of the measurement. One should always look at the spectrum of the singular values extracted from the SVD, which are the elements on the diagonal of matrix \mathbf{S} in Eq. 3.8. If a single source of orbit jitter is present, then one should see only one outstanding singular value ($\mathbf{S}_{1,1}$), while all the other singular values should lie on a lower decaying plateau, and they should represent the noise of the BPMs. In order to quantify this aspect, one can compute the ratio between the first singular value and the sum of all singular values ($\mathbf{S}_{1,1}/\sum_i \mathbf{S}_{i,i}$). This indicates how much *variance* is *retained* in terms of PCA by the first singular value and the associated singular direction (first column of matrix \mathbf{U}). If the ratio of the retained variance is above a certain threshold (for example $> 80\%$), then one can be confident that the found pattern is a good measurement of dispersion, given of course that the energy jitter from shot to shot is the main source of beam position jitter.

Moreover if the retained variance is lower than the expectation, which normally means that n singular values stand out above the “noise plateau”, then this means that there are n sources of beam orbit jitter, and no statement can be made on which could be the dispersion pattern using PCA techniques. The actual dispersion pattern could in fact be any linear combination of the first n columns of the matrix \mathbf{U} . However in these cases one could still extract precious information from this kind of analysis, for example to identify beam jitter sources. If the n sources of jitter are independent, and their effects on the beam orbit are orthogonal, then the first n columns of the matrix \mathbf{U} turn out to be the orbit effects of each single source, one of which could indeed be the energy.

Figure 3.1 shows a real example. In the middle of the CTF3 run of 2015 there was the suspicion that some magnetic element near the injection point of the Combiner Ring (CR) was jittering. After collecting about 100 beam orbits affected by the natural beam orbit jitter, the SVD analysis gave the spectrum presented in Figure 3.1(b). The presence of two main sources of jitter is clearly visible, and the two associated singular directions are plotted in Figure 3.1(a). These have to be compared with the measured orbit response from either enhancing the energy jitter (by scaling the beam current) or the septa jitter (by manually varying its current), which are also reported in Figure 3.1(a). The agreement between the first two singular directions and the two independently measured energy and magnetic responses is clear. This led to further investigation on the power supply of the septa, which was eventually fixed.

It is clear that PCA can be a powerful method to measure and cross-check the dispersion pattern, as well as to identify other possible sources of orbit jitter. This method has been implemented and successfully used in the dispersion monitor tool developed at CTF3.

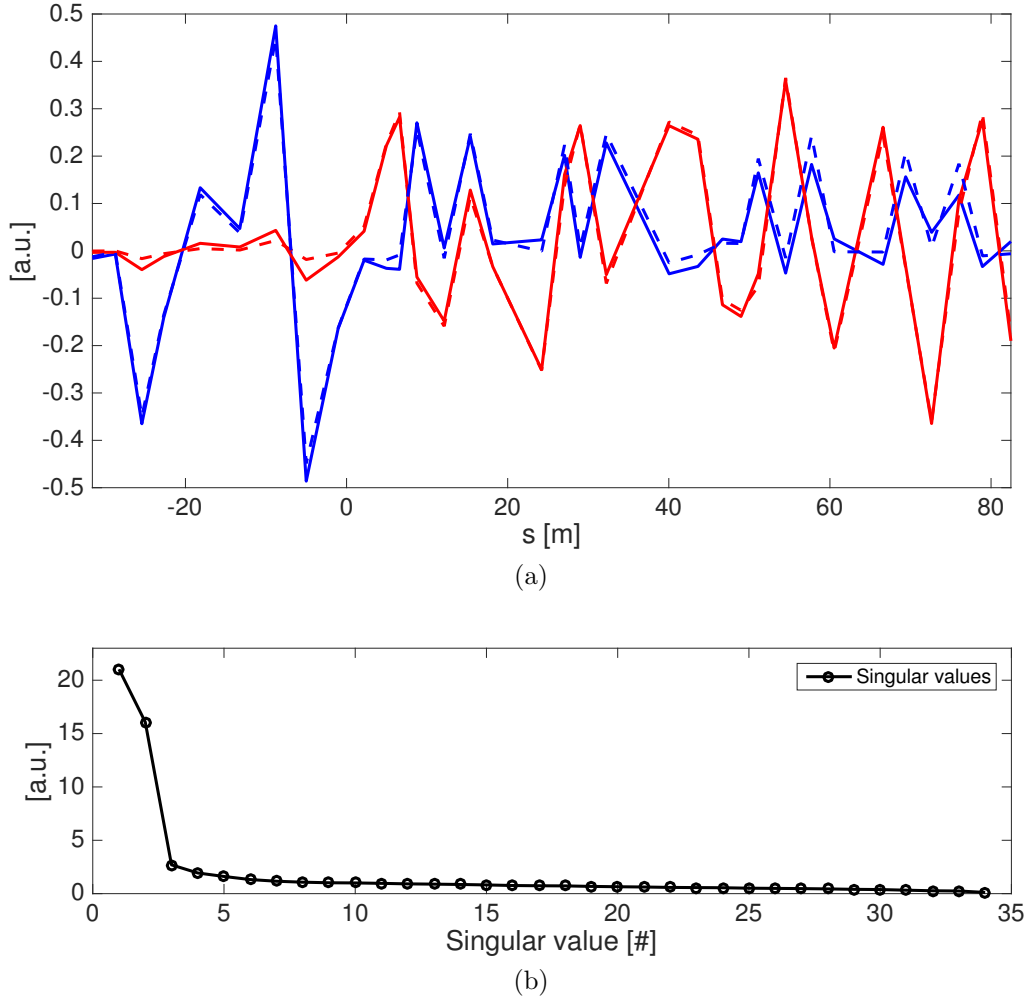


Figure 3.1: Example of jitter identification near the CR injection septa at CTF3. (a) on the horizontal axis is the position of the available BPMs in the area with respect to the septa position ($s = 0$ m). On the vertical axis is the normalised transverse orbit response under the effects of septa variation (dashed-red line) and beam-energy variation (dashed-blue line). The blue and red solid lines are the first and second singular directions of the SVD/PCA analysis conducted on 100 consecutive beam orbits. (b) the singular values spectrum of the associated SVD decomposition.

3.2.3 Non-linear dispersion measurement

In general one assumes that the beam orbit is linearly dependent on energy variations, and practically this is most of the time a fair assumption. Actually one should expect an inversely proportional dependence on the energy of the beam (to some power), which is due to the kicks given to the beam from the magnetic elements of the lattice (see Section 2.4). This means that for high energy variation and strong optics (like in CTF3) one might expect non-linearities. One might then wonder how the natural energy spread of the beam could interfere with the measurement of the beam position, and so with the dispersion measurement as a difference between two beam positions readings. If one assumes that the beam has a Gaussian energy distribution, then when the beam is crossing a location affected by a generic

non-linear dispersion the average beam position is defined as:

$$\langle x \rangle = \int_{-\infty}^{\infty} d\frac{\Delta p}{p_0} \left[D_x \frac{\Delta p}{p_0} + DD_x \left(\frac{\Delta p}{p_0} \right)^2 + DDD_x \left(\frac{\Delta p}{p_0} \right)^3 + \dots \right] \times \frac{1}{\sqrt{2\pi}\sigma_{\Delta p/p_0}} \exp\left(-\frac{1}{2} \left(\frac{\Delta p/p_0 - \langle \Delta p/p_0 \rangle}{\sigma_{\Delta p/p_0}} \right)^2\right) \quad (3.9)$$

where D_x, DD_x, \dots are the linear and non-linear coefficients of the dispersion. All integrals in Eq. 3.9 are the non-central moments of the Gaussian distribution. This leads to:

$$\langle x \rangle = D_x \langle \frac{\Delta p}{p_0} \rangle + DD_x \left(\langle \frac{\Delta p}{p_0} \rangle^2 + \sigma_{\Delta p/p_0}^2 \right) + DDD_x \left(\langle \frac{\Delta p}{p_0} \rangle^3 + 3 \langle \frac{\Delta p}{p_0} \rangle \sigma_{\Delta p/p_0}^2 \right) + \dots \quad (3.10)$$

Equation 3.10 clearly shows that indeed the average beam position is affected by the beam-energy spread in the case of non-linear dispersion. For the dispersion measurement one actually needs the orbit difference between two beams with different energies, which turns out to be:

$$\Delta \langle x \rangle = D_x \Delta \langle \frac{\Delta p}{p_0} \rangle + (DD_x + 3DDD_x \sigma_{\Delta p/p_0}^2) \Delta \left(\langle \frac{\Delta p}{p_0} \rangle^2 \right) + (DDD_x + \dots) \Delta \left(\langle \frac{\Delta p}{p_0} \rangle^3 \right) + \dots \quad (3.11)$$

Similarly to the procedures described in Section 3.2.1 one can then collect a series of orbit differences under the effect of measurable energy variations, and fit the *linear* coefficients of Eq. 3.11 with respect to the *powers* of the energy variations and extract the linear dispersion coefficient D_x , which is *not* affected by higher order dispersion and/or by the *Gaussian* energy spread $\sigma_{\Delta p/p_0}$. Equation 3.11 highlights also other observations. If for example the third order dispersion DDD_x is negligible, then also the second order dispersion is accessible with reasonable precision. However the higher order the non-linear term, the more the energy spread of the beam might affect the measurement.

At CTF3 the non-linear behaviour of the dispersion can be visible in areas with high dynamic aperture, for example at the end of the linac after the ‘‘Frascati’’ chicane (see Figure 1.4). Figure 3.2(a) shows the expect non-linear dispersion at three BPMs after the Frascati chicane, which is normally set with a strong optics ($R_{56} = 0$ optics). The simulation is performed by considering a random displacement of the quadrupoles in the line of the order of $100\mu m$, which is the typical alignment precision of CTF3. Figure 3.2(b) shows a real measurement performed in 2014: the beam energy variation on the x axis is computed from the horizontal beam position at the first dispersive BPM in the Frascati chicane. Even though the two plots in Figure 3.2 have different vertical axis scales, the non-linear behaviour of the orbit dependence on the beam energy is extremely similar between measurement and simulation. The factor 2 scaling difference between the two plots is not justified by the effect presented in Eq. 3.11, but it could be attributed to calibration error of the BPMs, which was suspected but never verified. Still one can state that at CTF3 non-linear energy effects are present and at least qualitatively measurable.

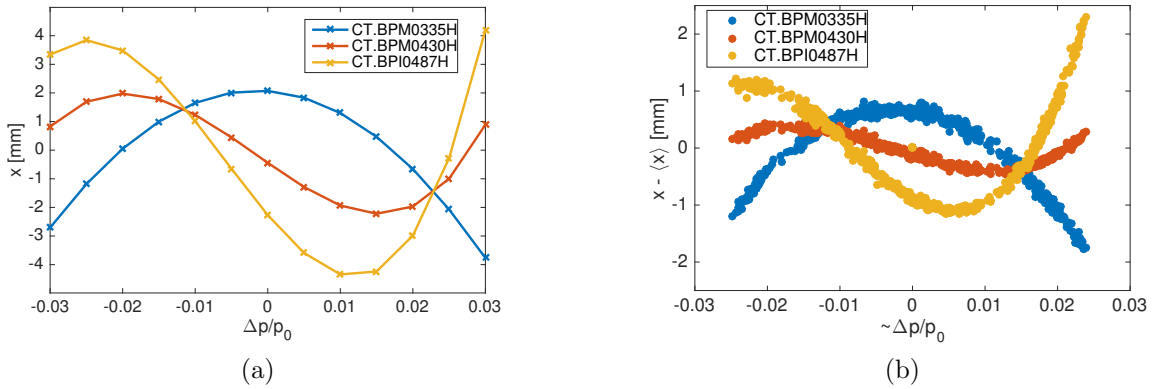


Figure 3.2: Example of non-linear dispersion measurement at the end of the linac at CTF3. (a) the MAD-X simulation of the single particle horizontal position as a function of the momentum error at three different BPMs installed in the area, and whose name is specified in the legend. (b) a measurement of the average beam momentum as a function of the beam-momentum error. The measurement has been performed at the same BPMs simulated in (a). For each BPM the total mean position has been subtracted.

3.2.4 Application features

The *onlineDispersion* MATLAB application developed at CTF3 implements all the measurements described in the previous sections. The common ingredient for all these measurement is to collect a certain number of consecutive orbits. At each new beam shot a new orbit is collected, stored in a circular buffer of the desired size, and the dispersion calculation is performed on the stored data and the Graphical User Interface (GUI) is updated. It turned out that the “online” approach adopted is very useful to obtain an immediate feedback on the quality of the measurement even after only a few shots. A full list of the application features implemented can be summarised as follows:

- Measurement and history of the estimated energy error ($\Delta p_i/p_0$) as the beam position at a reference (dispersive) BPM, normalised by the nominal dispersion expected at that location.
- Ability to wiggle the beam current and/or a set of selected magnets with definable amplitudes and steps.
- Fit of the dispersion as the linear (or non-linear) correlation of each BPM’s data with respect to: the energy as measured at the reference BPM, or the beam current as measured at the exit of the Drive Beam injector, or the scaling of the specified magnets.
- PCA analysis of the acquired orbits and the singular value spectrum is always visible on the application GUI.
- Detailed view of a generic SVD analysis (Eq. 3.8) of the acquired orbits, including the display of the weighted singular directions in the orbit space (columns of matrix \mathbf{U}) and time space (columns of matrix \mathbf{V}).

- Detailed view, by scatter plot, of the correlation between a selected BPM and either the reference BPM or the magnet scaling or the beam current scaling.
- Measurement and history of the “dispersive” component of the mean beam orbit. This is computed simply by operating the scalar product between the measured dispersion and the mean orbit as measured by the BPMs. A dispersive component different from zero might be a sign that the optics is not matched to the mean energy of the beam.

The main graphical interface of the application is illustrated in Figure 3.3. The final implementation consists of a MATLAB compiled executable that loads a user-editable XML⁴ configuration file. In this way the same application can be used to measure the dispersion in any desired beamline of CTF3. The XML configuration file contains mainly the list of BPMs to monitor and the list of magnets to use for the magnet-scaling measurement type. All the details of the implementation and possible options and setup of the application are beyond the scope of the present work. It is worth mentioning that a separate GUI, not shown here, can display the detailed SVD analysis of the acquired orbits. This last GUI turned out to be extremely useful when more than one outstanding singular value is detected: by looking at the detected singular direction in the observable space one has some hints on the source of additional orbit jitter that is not correlated to the beam energy variation.

3.3 A generic slow-feedback implementation

From the operator point of view, operating an accelerator means to act on some parameters of the accelerator components in order to control the quality of the beam as it is measured by the beam instrumentation. With a further simplification one might expect that *small-enough* changes of some parameters correspond to *small, linear* changes of the beam properties. Clearly the assumption of *linearity* it is not always applicable, but even in the cases where it is, one might have many linear parameters to be optimised to reach the desired beam specification. To overcome this complexity a generic feedback library has been developed: *linearFeedback* is a MATLAB class developed to easily implement feedbacks to steer any *observable* parameter available in the CERN control system (i.e. reachable via JAPC [48]) that linearly (or quasi-linearly) responds to the excitation of some *steerer* that is reachable via the CERN control system. There is no need to know the linear response between observable and steerers: *linearFeedback* is able to measure that by exciting the specified steerers and by measuring the response of the observables. The natural use of this tool, which also triggered its development, is the beam orbit steering. Here the beam orbit (observable) is steered by actioning on dipole correctors (steerers). Often the response matrix is known by the optics model of the line, but there might be issues and errors that make it interesting, if not necessary, to measure the response matrix on the live machine. In the following paragraph the main mathematical details of the implementation are presented, followed by some details of the state of the art of the interface and its use.

⁴eXtensible Markup Language.

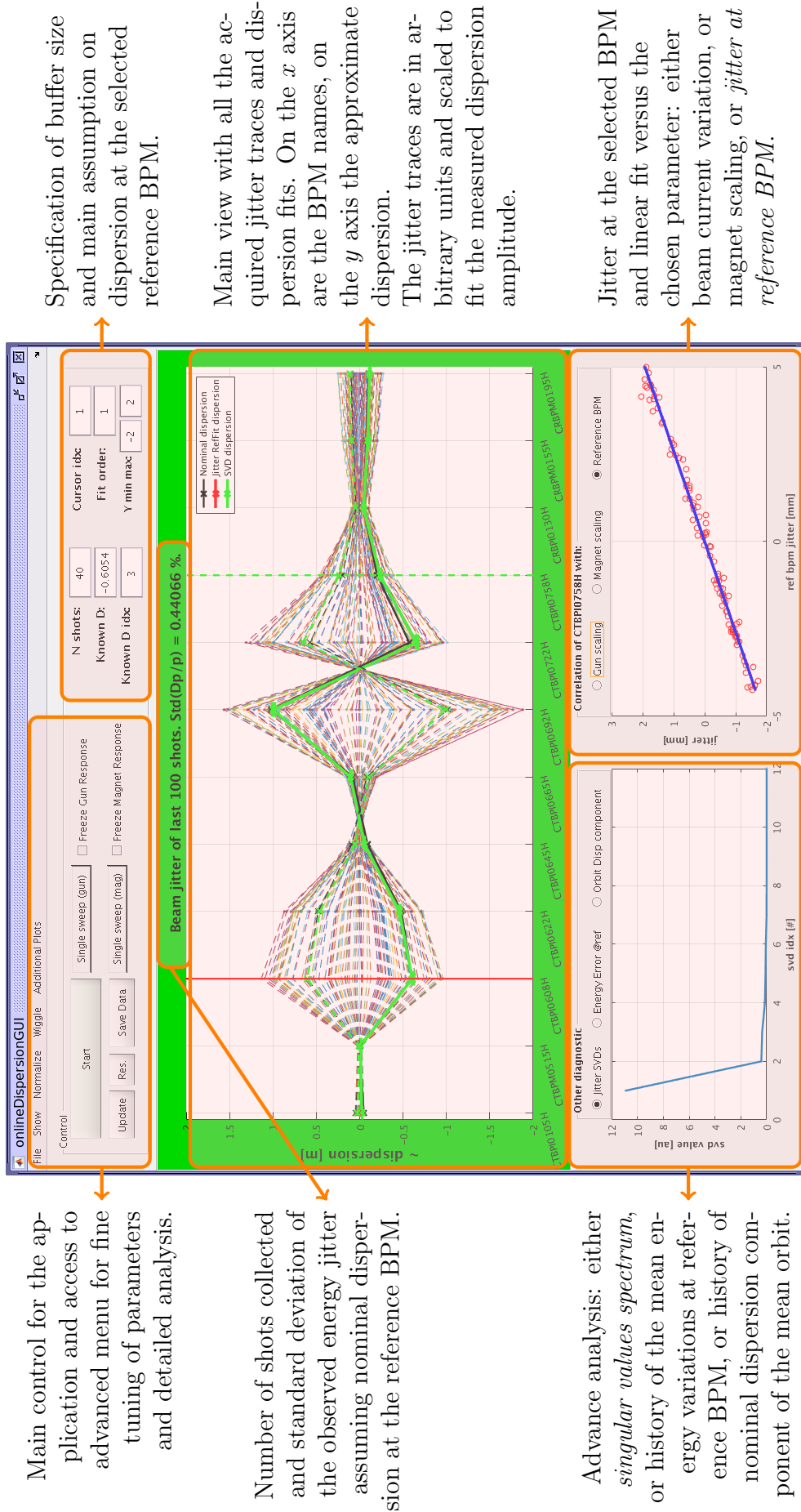


Figure 3.3: Online dispersion monitor. Main graphical interface.

3.3.1 Details of the linearFeedback implementation

Formally the goal of *linearFeedback* is to help the user to solve a problem that can be described by a system of equations:

$$\Delta \mathbf{o}_{\text{desired}} = \mathbf{M} \Delta \mathbf{s}_{\text{needed}} \quad (3.12)$$

where $\Delta \mathbf{o}_{\text{desired}}$ is a vector of the desired variation of a set of *observables*, which are known to be linearly dependent on the variation of a set of *steerers*, $\Delta \mathbf{s}_{\text{needed}}$. The matrix \mathbf{M} contains linear coefficients that link observables and steerers. Per se the problem is trivial and it only requires to invert the matrix \mathbf{M} . The challenge appears when the components of Eq. 3.12 are not well defined, for example:

- The observables have measurements errors⁵.
- The system is either over-determined (more independent observables than steerers) or under-determined (more independent steerers than observables).
- There are hardware limitations on the possible settings of the steerers.
- The elements of the matrix \mathbf{M} are not explicitly known.
- The linearity of the response is ensured only for a sub-space of the steerers/observables spaces.

The implementation of *linearFeedback* tries to overcome the listed limitations by simple precautions. The system is always made over-determined: the problem is extended such that the feedback tries not only to find the steerer settings that produce the wanted observation, but also such that the new settings are not *too* far from a desired configuration. Moreover independent weights can be specified for each of the observables. These could be specified as inversely proportional to the error in measuring the particular observable, or according to the user experience or needs. Equation 3.12 has to be rewritten as:

$$\mathbf{W} \begin{bmatrix} \Delta \mathbf{o}_{\text{desired}} \\ \Delta \mathbf{s}_{\text{desired}} \end{bmatrix} = \mathbf{W} \begin{bmatrix} \mathbf{M} \\ \mathbf{1} \end{bmatrix} \Delta \mathbf{s}_{\text{needed}} \quad (3.13)$$

where $\mathbf{1}$ is the identity matrix of the appropriate size, $\Delta \mathbf{s}_{\text{desired}}$ is the desired variation of the steerer settings, eventually zero, and \mathbf{W} is the weight diagonal matrix. The solution of such a system in a *least-squares* sense is well known [61]:

$$\Delta \mathbf{s}_{\text{needed}} = \left(\begin{bmatrix} \mathbf{M} \\ \mathbf{1} \end{bmatrix}^T \mathbf{W} \begin{bmatrix} \mathbf{M} \\ \mathbf{1} \end{bmatrix} \right)^{-1} \begin{bmatrix} \mathbf{M} \\ \mathbf{1} \end{bmatrix}^T \mathbf{W} \begin{bmatrix} \Delta \mathbf{o}_{\text{desired}} \\ \Delta \mathbf{s}_{\text{desired}} \end{bmatrix} \quad (3.14)$$

⁵In the current implementation of *linearFeedback* the assumption is made that the steerers are well known and controllable, i.e. the error in measuring the state \mathbf{s}_0 of the steerers, at any time, is negligible.

such that the solution minimises the euclidean norm of the weighted residuals:

$$\Delta \mathbf{s}_{\text{needed}} = \mathbf{x} : \min_{\mathbf{x}} \left\| \mathbf{W}^{1/2} \left(\begin{bmatrix} \Delta \mathbf{o}_{\text{desired}} \\ \Delta \mathbf{s}_{\text{desired}} \end{bmatrix} - \begin{bmatrix} \mathbf{M} \\ \mathbf{1} \end{bmatrix} \mathbf{x} \right) \right\|^2. \quad (3.15)$$

The actual implementation of *linearFeedback* does not make use of the solution provided by Eq. 3.14. Instead the MATLAB *lsqlin* function [62] is used. This allows one to specify boundary conditions on the strength of the available steerers. The details of the implementation of this function are outside of the scope of this thesis. The use of the *lsqlin* function has been initially introduced by the attempt to constrain the steerers not only within their hardware limitation, but also to give the user the possibility of constraining the strength of each steerer, and eventually force the system not to move some of the steerers. An alternative approach to obtain a similar result is to operate a Singular Value Decomposition (SVD) of the matrix \mathbf{M} , and apply a cut-off on its singular values. In the literature (e.g. [63]) one can find many different ways to choose the SVD cut-off, but one has to make some assumption on the system under correction. From experience at CTF3 it turned out that the most generic approach is still to add tuneable weights, by means of the matrix \mathbf{W} , to the desired correction ($\Delta \mathbf{s}_{\text{desired}}$). A similar approach was also applied in [57, 58].

The *linearFeedback* implementation also allows one to compute and see the strength of the correction and its effect on the observables before applying it. This allows the user to adjust as desired the weights of observables and steerers before taking any real action. Only when the proposed correction and its effect are satisfactory, can the user then apply the correction with a given gain to (hopefully) approach the solution. The use of the *lsqlin* function has been preserved for flexibility, but if the steerer weights are sufficiently large the proposed correction can be made always within the desired steerers limits.

In order to address the case where no trustworthy information is available about the matrix \mathbf{M} , the *linearFeedback* implements system identification techniques. The procedure used to measure the response matrix can be derived from Eq. 3.12:

$$\mathbf{M} = \begin{bmatrix} \Delta \mathbf{s}_1 & \Delta \mathbf{s}_2 & \cdots & \Delta \mathbf{s}_n \end{bmatrix}^{-1} \begin{bmatrix} \Delta \mathbf{o}_1 & \Delta \mathbf{o}_2 & \cdots & \Delta \mathbf{o}_n \end{bmatrix} \quad (3.16)$$

where $\Delta \mathbf{s}_i$ are a complete set of experimental settings that span the whole linear space of the steerers, while $\Delta \mathbf{o}_i$ are the measured variations obtained on the observables. In the *linearFeedback* different strategies to probe the full space of the steerer settings are implemented:

- Excite each single steerer one after the other. This is equivalent to measuring one by one the columns of matrix \mathbf{M} .
- Randomly (or quasi-randomly) add some controlled noise to the steerers.
- Knowing an approximate version of the response matrix \mathbf{M} , apply an excitation to the steerers such that a desired variation of the observables is performed (e.g. local bumps).

The first method is of course the cleanest. However in some cases it is more interesting or necessary to excite many steerers at the same time. The last method is instead the best choice for a final tuning of the response matrix and to update it in case of slow non-linear drifts of the system. In the implementation of *linearFeedback* the user can choose the most suitable technique. Moreover, while performing an actual correction, one can decide to use the outcome of each correction step to keep the response matrix up-to date. In this case a selectable gain can be used to tune how fast the matrix \mathbf{M} is updated if the outcome of a correction is far from the prediction.

3.3.2 linearFeedback interface and use

A priori the *linearFeedback* does not need a Graphical User Interface (GUI), but this turned out to be necessary for daily operations as well as for machine development. A considerable amount of time has been invested in the development a general purpose GUI, with the possibility to quickly analyse the data history via the same interface. The developed GUI is illustrated in Figure 3.4. This single interface has all the information needed and the means to set-up efficiently the feedback and control its operation. Other *expert* settings and diagnostic tools are hidden behind the top main menu.

The *linearFeedback* is by itself a library, and not a tool usable out of the box, but it provides a generic framework that can be applied to nearly any linear system. *LinearFeedback* also takes care of the interface with the CERN control system via the developed MATLAB/JAPC library described in Section 3.1. To be practically usable one needs only to implement a function to translate the signals coming from the CERN infrastructures into proper observables and settings, and a function to translate the steerer settings suggested by the feedback to proper commands understandable by the steerer hardware. What triggered the development of such infrastructure was the necessity to have an easy and flexible way to keep under control orbits and dispersion in the DBRC. For this specific use an additional *orbitCorrection* tool has been implemented. *OrbitCorrection* is just a specialised “MATLAB subclass” of *linearFeedback*. Its main task is to implement the concept of beam orbit and dispersion as observables, and a function to directly act on the dipole correctors installed in the CTF3 beamlines. For further flexibility the *orbitCorrection* was compiled as a standalone application that requires an XML configuration file. This is user-editable, and it contains mainly the signals of the BPMs to use as simple orbit or as dispersion measurement points, and the list of corrector magnets. The “beam dispersion” definition implemented in the *orbitCorrection* tool is a linear fit of the beam jitter at each BPM location with respect to a reference BPM where the dispersion is assumed to be known and constant. This turned out to be the most reliable and generic dispersion measurement of the ones described in Section 3.2.

The *orbitCorrection* is only an example of use of the *linearFeedback* library. The use of *linearFeedback* has been applied also to solve different problems than the orbit steering. Some of these results will be presented in Section 5.7.

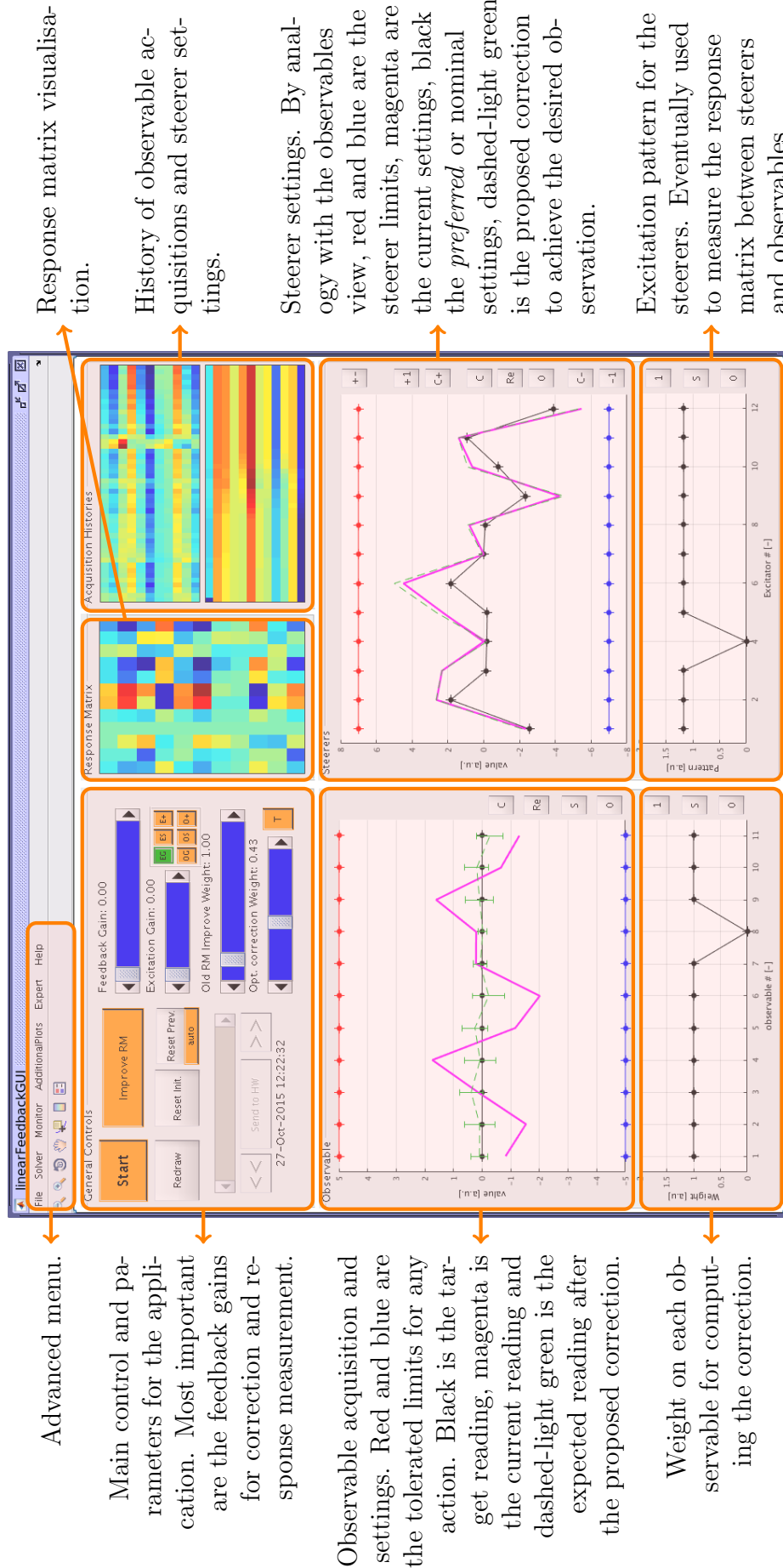


Figure 3.4: linearFeedback main graphical interface.

3.4 Quadrupole scan

For the study of the linear transverse dynamics it is often important to measure the Twiss parameters of the beam at a given location in a transfer line. A common way to do so in transfer lines is by means of a *quadrupole scan* (e.g. in [64]), often contracted as *quadscan*. For this technique one needs some beam instrumentation device able to measure the beam size in real-space, for example a screen, and the possibility to change the beam size by varying upstream quadrupole magnets. By recording the beam sizes and the quadrupole strength variations, one is then able to fit the initial Twiss parameters. The full procedure normally assumes that the beam can be represented in phase space as a bi-Gaussian distribution both in the horizontal and vertical planes. Normally one would consider the two planes as uncoupled, but in the literature 4D measurement of coupled beams have been studied, e.g. in [65].

At CTF3 a MATLAB application was already developed and successfully used for many years for the commissioning and optimisation of the accelerator complex [66, 67, 68]. The mathematics behind it is conceptually simple. Following the formalism of Eq. 2.20 one can write the beam *variance* in real-space at the screen location as:

$$\sigma_s^2 = \beta_s \epsilon = \begin{pmatrix} A^2 & -2AB & B^2 \end{pmatrix} \begin{pmatrix} \beta_0 \\ \alpha_0 \\ \gamma_0 \end{pmatrix} \epsilon \quad (3.17)$$

where $\beta_0, \alpha_0, \gamma_0$ are the Twiss parameters one would like to measure at some location, A, B are the relevant coefficients of the transfer matrix from the Twiss parameters measurement location up to the screen location, and ϵ is the emittance that is assumed to be preserved during the transport of the beam. By varying the strength of the quadrupoles in the lattice, and so by modifying in a controlled manner the coefficients A, B , one can record for $n > 3$ consecutive shots the different settings and the measured variances:

$$\begin{pmatrix} \beta_{s,1} \\ \beta_{s,2} \\ \vdots \\ \beta_{s,n} \end{pmatrix} \epsilon = \begin{pmatrix} A_1^2 & -2A_1B_1 & B_1^2 \\ A_2^2 & -2A_2B_2 & B_2^2 \\ \vdots & \vdots & \vdots \\ A_n^2 & -2A_nB_n & B_n^2 \end{pmatrix} \begin{pmatrix} \beta_0 \\ \alpha_0 \\ \gamma_0 \end{pmatrix} \epsilon \quad (3.18)$$

The initial covariance matrix, defined by $\beta_0\epsilon, \alpha_0\epsilon, \gamma_0\epsilon$ (see Eq. 2.15), can be computed by inverting the linear system of Eq. 3.18. The emittance ϵ can finally be extracted as the square root of the determinant of the covariance matrix, Eq. 2.16, and so one can fully determine the Twiss parameters at the beginning of the line. It has to be stressed that the emittance measured is the *geometric* emittance. This is then generally transformed into the *normalised* emittance ϵ_N by multiplying with the relativistic γ of the beam.

The operational challenge of this technique is in the choice of an appropriate set of quadrupoles and relative strengths to perform the measurement. The simplest strategy is to use only a couple of quadrupoles in the vicinity of a screen, and to vary a single quadrupole such that the beam variance measured at the screen is passing a minimum, i.e.

the beam waist. In phase space this turns out to be equivalent to a rotation of the phase-space distribution from a positive covariance, σ_{x,p_x} , to a negative one. Another interesting approach is described in [69], which is based on a work done [70, 71] at the previous CLIC Test Facility 2 (CTF2). In this latter case the idea is not to move only one quadrupole at a time, but to move many quadrupoles to keep the beam size at the screen constant, i.e. only changing the phase advance between the Twiss-parameter measurement point and the screen location. This technique has been implemented recently within the general quadrupole scan application available at CTF3, but not used for the results presented in this thesis.

In general special care should be taken while performing this kind of measurement in the presence of unwanted dispersion and high beam-energy spread. The effects of a large energy spread on the emittance measurement has been studied for the CLIC decelerator in [72]. Here it is important to point out that by taking into account only linear energy effects, one should re-write Eq. 3.17 as:

$$\sigma_s^2 = \beta_s \epsilon + D_{x,s}^2 \sigma_p^2 = \begin{pmatrix} A^2 & -2AB & B^2 \end{pmatrix} \begin{pmatrix} \beta_0 \epsilon + \sigma_p^2 D_{x,0}^2 \\ \alpha_0 \epsilon - \sigma_p^2 D_{x,0} D_{p_x,0} \\ \gamma_0 \epsilon + \sigma_p^2 D_{p_x,0}^2 \end{pmatrix} \quad (3.19)$$

where $D_{x,s}^2 \sigma_p^2$ is the dispersion contribution to the beam variance. The dispersion at the screen, $D_{x,s}$, is the propagation of the incoming dispersion, $D_{x,0}$, and its derivative with respect to s , $D_{p_x,0}$, that propagate under the effect of the same coefficients A and B . σ_p is the r.m.s. energy spread that here is assumed to be normally distributed. Note that from Eq. 3.19 there is no way with a simple quadrupole scan to disentangle the additional energy effect from the ‘‘betatronic’’ one. In practice one could and should always verify that no residual dispersion is reaching the screen location, such that the measured variance is only due to the betatronic motion of the particles. A good practice would be to vary the beam energy for every setting of the quadrupoles during the scan, and to verify that no orbit variations are visible around the screen area. More complex techniques, not implemented at CTF3, would imply that one be able to modify in a controlled way the dispersion at the screen location, as in [73].

In the absence of dedicated measurements, one can still try to estimate the worst dispersion contribution to a real quadscan measurement. Figure 3.5 shows the result from a quadscan after the DBRC at CTF3. Typically the measurement software performs only a fit of the initial Twiss parameters, assuming no initial dispersion. The opposite strategy is to assume zero beam emittance in Eq. 3.19, and to fit the data as if it would be generated by some incoming dispersion ($D_{x,0}$, $D_{p_x,0}$). In this case a Gaussian energy spread of the beam is assumed, with $\sigma_{\Delta p/p_0} = 0.5\%$. This gives the green fit. Finally one can make a global non-linear fit considering both effects, i.e. by fitting all the unknown quantities of Eq. 3.19 using the previous results as initial conditions for the fit. The new result, not surprisingly, gives the same representation as the first one, but it also gives one of the *possible* guesses for both Twiss and dispersion parameters. The numerical results of this exercise are reported in Table 3.1: The emittance reduction from the fit assuming only the betatron effect and the non-linear fit that assumes both betatron and dispersive effects is remarkable. The initial dispersion parameters, as much as they sound high, could be realistic considering the location at which the quadscan was performed: the screen CC.MTV0970 is installed in the

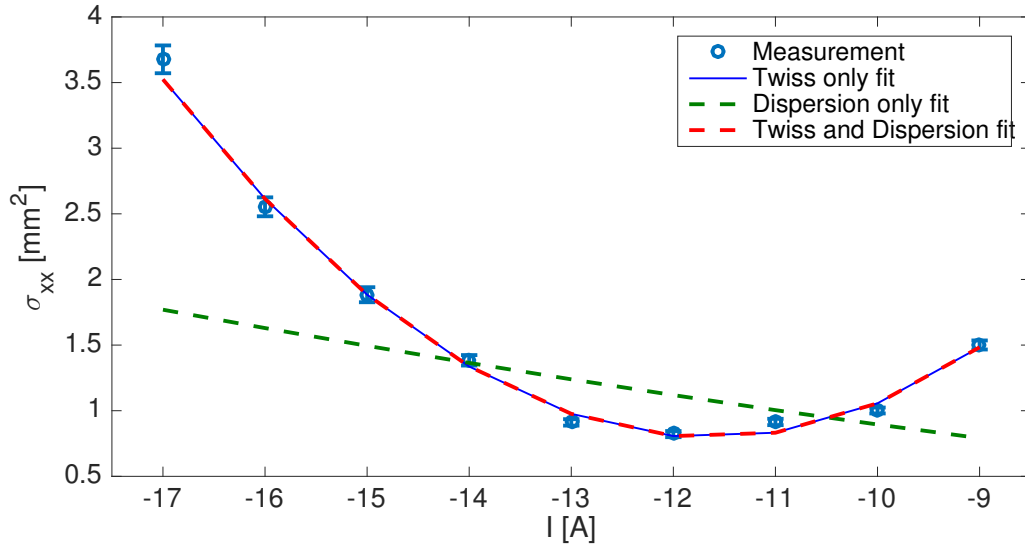


Figure 3.5: Horizontal beam variance measured at screen CC.MTV0970 as a function of a single quadrupole (CC.QDL0920) current. The blue points are the measured values. The error bar is the error on the Gaussian fit of the beam profile at the screen. The blue line is the fit of the data points considering only the Twiss effects. The dashed-green line is the fit of the data points considering only dispersive effects, i.e. imposing zero beam emittance and Gaussian energy spread. The dashed-red line is the fit of the data points considering both dispersive and Twiss effects.

	β_x [m]	α_x	ϵ_{Nx} [μm]	D_x [m]	D_{px} [rad]
Twiss only	4.1 ± 0.3	-0.7 ± 0.1	419 ± 10	–	–
Dispersion only	–	–	–	0.19 ± 0.06	-0.11 ± 0.02
Twiss and Dispersion	8.8 ± 0.6	-1.9 ± 0.2	182 ± 12	0.15 ± 0.08	-0.08 ± 0.01

Table 3.1: Initial Twiss and dispersion parameters obtained from different fit method applied to the quadscan data presented in Figure 3.5.

CLEX area, just after the long TL2 chicane (see Figure 1.4). The order of magnitude of the horizontal dispersion inside the chicane is about 0.5 m. One could think that the TL2 line was badly set up off-energy at the time of the measurement, such that some dispersion was leaking out of the chicane and was reaching to the screen location. However, it has to be stressed that the result obtained is just a possible scenario over infinite, equivalent, ones. Moreover such a high dispersion would have been quickly identified by the operator with the impossibility to transport the beam afterwards. Still the important message here is to underline that one should always take with care the *absolute* values of the Twiss parameters obtained from a quadscan measurement, especially when they are performed in the vicinity of high dispersion regions. On the other hand, the values obtained, especially the emittance, can always be considered as representative of the *local* beam quality, and they are useful indicators for tuning the machine.

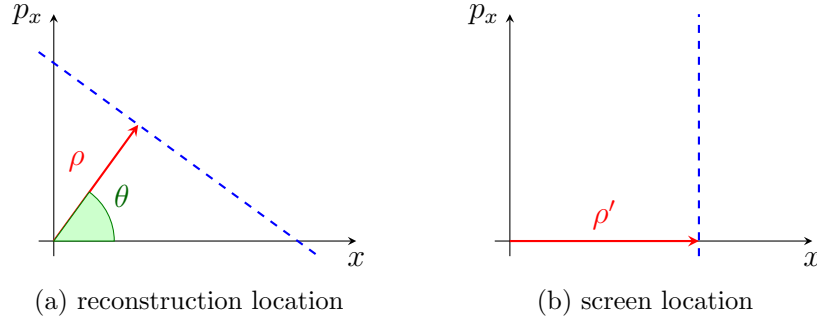


Figure 3.6: Correspondence between a phase-space profile integral line (dashed line) at the reconstruction location (a) and at the screen location (b). The red arrows identify the distance of the integral line from the origin of the axes at the two locations.

3.4.1 Phase-space distribution: Tomography

By construction a quadscan uses the beam size, usually measured as the σ of a Gaussian fit to the measured profile, to determine the Twiss parameters. Experimentally the particle distribution in phase space can be far from bi-Gaussian and one might be interested in a more detailed picture of the phase-space distribution itself, with all its features. This could be achieved by means of transverse phase-space tomography.

In the literature early experimental verification of the use of tomographic techniques to measure the transverse phase-space distribution have been studied and presented in [74, 75]. At CTF3 a tool to perform transverse tomography has been implemented [76, 77]. The current implementation makes use of the Inverse Radon transform [78, 79] offered within the *Image Processing Toolbox* of MATLAB [80, 81]. The idea is to use the same beam profiles acquired during a quadrupole scan to reconstruct, at least qualitatively, the shape of the beam phase-space distribution. In general the Inverse Radon transform is the reconstruction of a two variable function (here the beam phase-space distribution) from a series of *line-integrals* of that function (e.g. beam profiles) taken on straight lines at different angles. The operation of performing a quadrupole scan is equivalent, with the proper transformations, to rotating the phase space and measuring the projection of the beam particle distribution on the axis x . Consider the transformation of the beam-phase space between two beamline locations as represented in Figure 3.6. In linear-optics approximation, as of Eq. 2.2, the parallelism between lines is preserved along the beamline. One can assume that the points represented by the dashed line in the initial phase space in Figure 3.6(a) are transported by the lattice into the vertical line in the final phase space in Figure 3.6(b). While taking a transverse beam profile measurement at the screen location, one is actually computing the line integral of the beam phase-space distribution along the vertical dashed line in Figure 3.6(b). This integral by the rigidity of the transformation has to be the same as the one computed on the correspondent dashed line at the reconstruction location, Figure 3.6(a). By applying simple trigonometric relations, one finds that:

$$\tan(\theta) = \frac{B}{A} \quad (3.20)$$

$$\rho' = \rho\sqrt{A^2 + B^2} \quad (3.21)$$

where A, B are the same coefficients of the transfer matrix from the measurement location up to the screen location as in Eq. 3.17. Thanks to the profile measured at the screen location during a quadrupole scan and at the relations of Eq. 3.20⁶ and Eq. 3.21 one has then all the ingredients to apply the Inverse Radon transform offered by MATLAB and so obtain a 2D representation of the initial phase space.

In order to get a reasonable representation of the phase space one needs many beam profiles taken over a wide range of rotation angles. This unfortunately is most of the time impractical, and not all quadrupole scan data is suitable for this kind of reconstruction. However sometimes the range of the rotation is big enough to allow a qualitative reconstruction, as in the example presented in Figure 3.7. Figure 3.7(a) shows the key ingredients of the reconstruction process. The profiles measured at the screen (top-left plot) are associated to a phase-space rotation (top-right plot) using Eq. 3.20. The profiles are then stretched using the relations of Eq. 3.21 (bottom-left plot) and interpolated over a finer range of angles (bottom-right plot). The final tomography reconstruction using the Inverse Radon transform function [80] is shown in the contour plot in Figure 3.7(b). This has to be compared with the equivalent phase-space reconstruction one obtains using the ordinary quadscan technique on the same data. The colour code represents the height of the beam phase-space density distribution, after being normalised by imposing one as maximum *height* for both tomography and quadscan techniques⁷.

Figure 3.7(b) shows that the tomography reveals a long tail. Tails are also clearly visible in the profiles in the top-left image of Figure 3.7(a), but these are obviously neglected by the quadscan procedure, which is based on Gaussian fit of the profiles. One can identify the core of the beam with the middle contour, which represents the 2D Full Width Half Maximum (FWHM) of the two density distributions (height equal to 0.5 with respect to the peak of 1). It is interesting to see, as one would naively expect, that the simpler and more robust quadscan translates the presence of the tail into a wider FWHM than for the tomography technique.

The experience so far at CTF3 is that the tomography technique can be a powerful tool for qualitative measurement of the beam quality. On the other hand a quantitative measurement using tomography techniques seems more challenging, and further development is needed to correctly interpret the results. Still, it seems to be a complementary tool to the simpler quadrupole scan, and it can help to spot major issues relative to the beam quality, especially in the Drive Beam Recombination Complex.

⁶Care has to be taken while computing the angle θ over the full range from $[0, 2\pi]$, but this can easily be addressed by taking into account the sign of the coefficients A, B .

⁷The correct procedure would probably be to normalise by the *volume* of the distribution. Unfortunately the tomography reconstruction generates long, noisy low tails that heavily affect the total volume, making such normalisation very fragile.

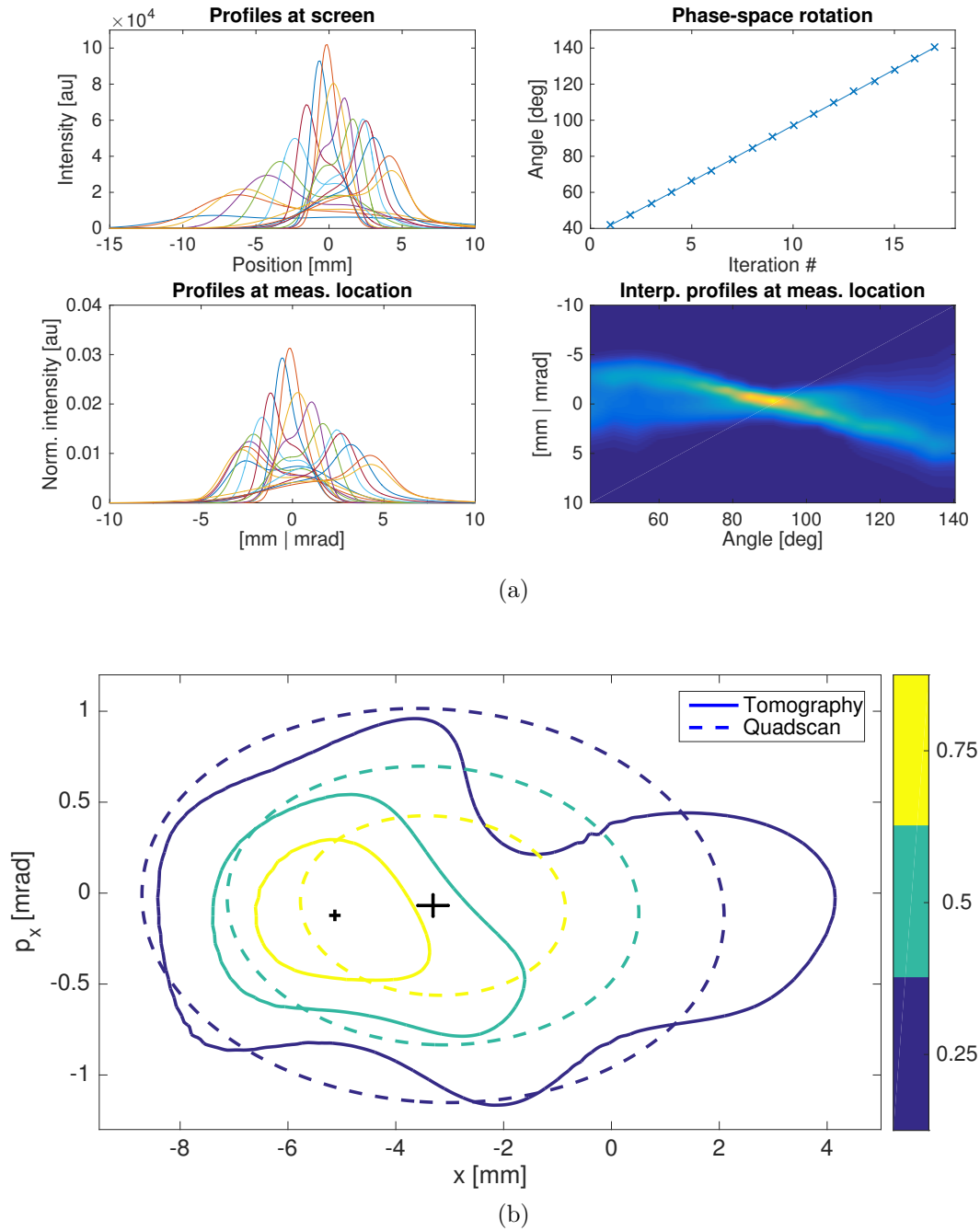


Figure 3.7: Typical tomography reconstruction of a (bad) factor-4 recombined beam at screen CC.MTV0970 at CTF3. (a) the horizontal beam profiles measured at the screen (top-left plot). The profiles are associated to a different phase-space rotation (top-right plot). The same profiles are normalised and scaled according to Eq. 3.21 (bottom-left plot). The obtained profiles are interpolated over a finer range of angles (bottom-right plot). (b) a contour plot of the horizontal phase-space reconstruction by means of the Inverse Radon transform of the interpolated profiles, compared with the equivalent phase-space reconstruction from a quadrupole scan using the same data. The colour code is the density distribution, which has been normalised to have peak (identified by the black cross) equal to 1 in both cases.

Chapter 4

DBRC Optics Verification and Optimisation

In Section 1.3 a general overview of the CLIC design and its Drive Beam Recombination Complex (DBRC) was presented. In the DBRC the different sub-trains of the incoming long train follow different paths of different lengths. All sub-trains finally get recombined in a shorter train with higher bunching frequency and so higher pulse current and power. The goal is to increase the instantaneous power that can be used to accelerate the Main colliding beam, but this is possible only if the longitudinal and transverse quality of the *single bunches* is preserved, as well as the regularity of the longitudinal structure and the projected beam size of the final *train*. This is a challenging task by itself, which becomes even harder considering the order of magnitude of the beam parameters and the expected performance reported in Table 1.4.

Different methods for optimising the different sections of the CLIC DBRC are available in the literature and are summarised in the CLIC Design Report [3]. For CTF3, several optimisations were performed during the design and commissioning of the facility [5, 42, 82, 83]. In this chapter some of the main effects that affect the quality of the beam in the DBRC at CTF3 are identified and quantified. The results obtained suggest possible improvements to the CLIC DBRC design. In this thesis the focus is on the transverse plane. For the longitudinal plane, one can refer to [84, 85] for studies and measurements performed at CTF3. The *projected emittance* of the final train after the different stages of the recombination is used here as a figure of merit of the quality of the DBRC design. One of the objectives of CTF3 is to obtain a factor-8 recombination with $< 150 \mu\text{m}$ projected normalised emittance in both transverse phase spaces.

The present work is one of the first studies that attempts to simulate the full recombination process at CTF3 without the necessity to track single particles. The proposed method allows one to disentangle the contribution of dispersion, chromatic and orbit effects. The simulations presented in this chapter reveal that one of the effects that can spoil the transverse beam quality is the non-linear dispersion. Hints of such effects in the CLIC DBRC design were found already in [86].

At the present stage of the study, only the *ideal*, perfectly aligned, machine is simulated,

considering only linear magnetic elements. In the initial design of CTF3, non-linear corrections with sextupoles were planned [5], but in practice rarely used due to operational difficulties, mainly caused by alignment imperfections. The aim of this study is to evaluate the best performance of the DBRC at CTF3 that one could achieve with an ideal, perfectly aligned machine, but with only linear elements. The next step would be to simulate the effects of imperfections, but this has not been addressed yet.

4.1 Simulations with MAD-X

A standard method to study emittance growth effects in the DBRC would be to simulate the recombination process by tracking all the different bunches up to the point where they merge in the final train, and then to fit the Twiss parameters of the final particle distribution. Unfortunately, most of the particle tracking software that has been designed over the past years is mainly meant to simulate storage rings or simple transfer lines. In these cases all the particles composing the beam follow the same path, eventually some billions of times. In the case of the CLIC DBRC different particles might take different paths, and most of the available software does not allow for this. In order to fill this gap, special software is being developed at CERN [87]. Such software was not available at the start of the work presented in this thesis. For this reason a custom method using MAD-X [6] has been adopted, but *without* performing any particle tracking. The used approach may be simplistic, but it allows one to disentangle what are believed to be the main effects.

The main idea behind the procedure used in this thesis is to represent the beam dynamics by using the formalism of Eq. 2.51. The procedure is then based on the following assumptions:

- The nominal transverse dynamics for a monochromatic beam is mainly of the first order due to the small dimension of the beam (i.e. less than a few mm), and the relatively short length of the lattice (up to a few hundred metres).
- The mean orbit of a monochromatic but off-energy beam is well described by the second-order orbit transport of MAD-X, thanks to the generally small orbit deviation (e.g. less than a few mm).
- By specifying an initial DELTAP in a MAD-X [43] TWISS function call, all the magnetic elements are correctly rescaled to the required energy. This means that the transport map computed for each element is *exact* in terms of the beam energy. The eventually non-zero orbit that is generated is then transported “correctly” up to the second order as in the previous assumption.

The hypothesis behind all these assumptions is that the main non-linear effect that is disturbing the beam recombination is the energy dependence of the DBRC optics. The justification for this assumption comes mainly from the fact that the Drive Beam has a relatively high energy spread ($\sigma_{\Delta p/p_0} \approx 0.6\%$), and, due to the nature of CTF3, the long-term energy varia-

tion and/or energy measurement errors can be up to 0.5%. This means that the total energy acceptance of the machine needs to be $> 1\%$.

The procedure used in the simulations can be summarised as:

1. MAD-X is used to compute independently the *transfer matrices* and *orbits* by means of TWISS function calls for a set of DELTAP values, along each possible path in the DBRC.
2. Given the covariance matrix ($\Sigma_{0,i}$) representing the beam distribution in phase space at the beginning of the line, the *transported* covariance matrix ($\Sigma_{S,i}$) is computed (Eq. 2.7) for each monochromatic beam, and for each possible path, up to any interesting location of the lattice.
3. All the covariance matrices and orbits are combined in the final covariance matrix ($\Sigma_{S,tot}$) describing the projected phase-space distribution of the beam at the interesting locations¹.
4. The statistical emittances and Twiss parameters are extracted from the total covariance matrix (Eq. 2.15).

This technique, apart from the linear approximation to the pure mono-energetic behaviour, is equivalent to performing particle tracking and then computing the covariance matrix of the tracked particles, from which one can extract the Twiss parameters. The main advantage of this method is that the simulation has to be performed a priori only once: once the transfer matrices and orbits are known, one can choose any initial phase-space and energy distribution, and immediately compute the final covariance matrix of the (combined) beam without tracking any single particle. Moreover one can simply “turn off” some effect to study the impact of the others, e.g. one can neglect chromaticity by considering all the covariance matrices being transported as one with nominal energy, and so consider only the effects of orbit and dispersion.

In all simulations presented here the beam at the entrance of the DBRC is assumed to be composed of perfectly Gaussian bunches in both transverse and longitudinal planes, without any coupling. The beam is then split into eight equal sub-train of bunches, one for each possible path that is undertaken by the different parts of the initial beam to finally obtain the design factor-8 recombination. For each of the 8 sub-train a representative bunch is considered. When considering energy effects, each bunch is further split into n mono-energetic slices. Each slice differs from the others only in energy and population, which vary according to the assumed Gaussian energy spread of the beam. All the slices are assumed to be equally described by the same initial Twiss parameters at the entrance of the DBRC. The full recombined beam is then the overlap of $8 \times n$ bunches/slices, each of which is transported to the end of the DBRC following a different path, which is modelled by the respective transport matrix.

¹The covariance matrix that results from the combination of two or more covariance matrices is well defined and is derived in appendix D.

As a cross verification of the results presented, all the simulations have been performed using PTC_TWISS [46, 47]. Moreover, conventional tracking by means of PTC_TRACK has been performed for some key cases. PTC has many options that might affect the final results; the settings that have been chosen are:

```

1 PTC_CREATE_LAYOUT, MODEL=1, METHOD=4, NST=10, EXACT=true, CLOSED_LAYOUT=false;
2 PTC_SETSWITCH, NOCAVITY=true, FRINGE=true, EXACT_MIS=false, TIME=true, ...
   TOTALPATH=false;
3 PTC_TWISS, DELTAP_DEPENDENCY=true, ICASE=56, NO=1, SLICE_MAGNETS=false, ...
   BETX = ..., DELTAP = ...;
4 [...]
5 PTC_START, X=...;
6 PTC_TRACK, ICASE = 56, ONETABLE;
7 [...]

```

4.1.1 Note on the definition of emittance

The final goal is to quantify and eventually optimise the projected transverse emittance of the fully recombined beam after the DBRC. With the simulation procedure presented in the previous section, as well as with normal tracking, the definition of emittance that is conventionally used is the square root of the determinant of the total covariance matrix, Eq. 2.9, which is defined as the *statistical emittance*. This value is actually difficult to interpret, especially if one considers only and independently the 2×2 blocks of the total covariance matrix relative to the two transverse phase spaces. In the case of a mono-chromatic beam one could say that such emittance is indeed the conserved quantity in a *linear* transfer line (see Section 2.1), but in general it is not true that at a given location 68.3% of the beam is enclosed, in real-space, within $\pm\sqrt{\epsilon_\Sigma\beta_s}$, where ϵ_Σ is the computed total statistical emittance and β_s the *nominal* Twiss parameters at the given position s . There are two reasons: first because the final beam could be far from being Gaussian, and second, the beam is not necessarily oriented according to the desired nominal Twiss parameters. Moreover in the case of a non mono-energetic beam, even the conservation of such a quantity might be in doubt. In this case one should at least consider the full 6D phase space, and assume pure linearity of the energy effects. De facto, the value of ϵ_Σ can always be compared with the ideal initial emittance ϵ_0 , and one can perform an optics optimisation using the ratio $(\epsilon_\Sigma - \epsilon_0)/\epsilon_0$ as a *local* figure of merit.

If the total emittance ϵ_Σ is the natural and most commonly used choice, one could still be interested in obtaining some idea of the final beam size if such a beam would be injected into a “nominal” transfer line. For this purpose a different definition of emittance is proposed. $\bar{\epsilon}$ is defined as the minimum emittance associated with an ellipse oriented as in the given nominal optics that contains all, or *at least* a certain percentage, of the simulated particles. Since the simulations presented in this thesis assume that all the initial bunches and slices are Gaussian, and so are well represented in phase space by ellipses, then $\pi\bar{\epsilon}$ represents the area of the ellipse, oriented according to the nominal Twiss parameters, that includes all the ellipses of all the simulated and merged bunches and/or slices. Figure 4.1 helps to clarify the definition of $\bar{\epsilon}$ used in this chapter. A and B represent the distributions of a generic

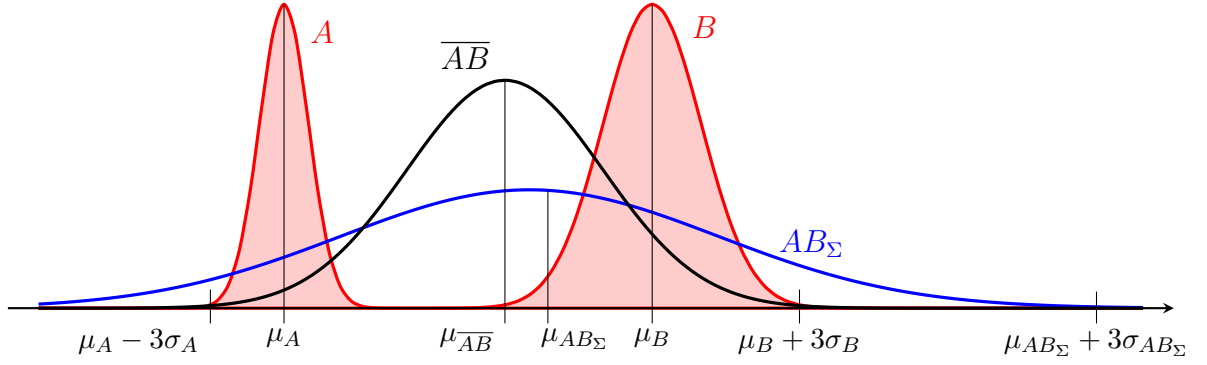


Figure 4.1: A and B represent the distributions of a generic coordinate of two hypothetical Gaussian bunches that are combined together. The Gaussian labeled by AB_Σ is built by using the statistical definition of emittance of the combined beam, while \overline{AB} is built by using the $\bar{\epsilon}$ definition.

coordinate of two Gaussian beams that are recombined into a single beam. The standard deviations of the two Gaussians are respectively σ_A and σ_B and are directly proportional to the square root of the respective emittances. Clearly the distribution for the same coordinate of the combined beam is the sum of the two distributions, i.e. the red area $A + B$, which is far from being Gaussian. However, if one would compute the statistical emittance of the combined beam, and build the Gaussian relative to that emittance, then one would draw the distribution labeled by AB_Σ . Clearly AB_Σ has lost any useful connection with the size of the real distribution of the combined beam: the long tails are heavily overestimating the range of the considered coordinate. The only meaningful quantity in AB_Σ is the mean coordinate μ_{AB_Σ} , which indeed represent a physical quantity for the combined beam. For the purpose of this chapter, it is in some case more important to identify the *size* of the combined beam, which is defined as the coordinate range which contains at least 99.7% of the final particles, i.e. equivalent to $\pm 3\sigma$ of a Gaussian distribution. In Figure 4.1 this would be the coordinate range from $\mu_A - 3\sigma_A$ and $\mu_B + 3\sigma_B$. The $\bar{\epsilon}$ definition of emittance used in this work is then the one that identifies the distribution labeled \overline{AB} in Figure 4.1, i.e. a Gaussian such that $\mu_{\overline{AB}} + 3\sigma_{\overline{AB}} = \mu_B + 3\sigma_B$ and $\mu_{\overline{AB}} - 3\sigma_{\overline{AB}} = \mu_A - 3\sigma_A$. Note that in this case only the standard deviation $\sigma_{\overline{AB}}$ has a physical meaning, while the mean $\mu_{\overline{AB}}$ has not.

By using the Twiss functions the beam size is identified by $\sigma = \sqrt{\beta\epsilon}$. With the given definition of $\bar{\epsilon}$, it is *not* necessarily true that 68.3% of all the particles are included within $\pm\sqrt{\bar{\epsilon}\beta_s}$, where β_s is the value of the Twiss β -function at the location s . However it is true that 99.7% of particles of the final beam are enclosed within $\pm 3\sqrt{\bar{\epsilon}\beta_s}$. Note that for a single Gaussian beam both emittances are identical: $\epsilon_\Sigma = \bar{\epsilon}$.

Coming back to the phase space, where the single bunch or slice is represented by an ellipse, in order to find the ellipse representing $\bar{\epsilon}$, it will be convenient to think of the problem in normalised phase space. This will translate the problem from finding an ellipse, into finding a circle, which is easier. This could be the way to proceed if one would like to apply the same definition for tracked particles: numerically, the problem of finding the smallest circle which contains all the given points is in fact well known [88].

In the following sections of this chapter both definitions of emittance will be used to

study the effects of mis-steering, optics mis-matches and energy spread in the DBRC of CTF3. Note that both quantities ϵ_{Σ} and $\bar{\epsilon}$ are not easily measurable in practice, but they are useful definitions for estimating the final performance of the DBRC.

4.2 Drive Beam Recombination at CTF3

In the Drive Beam Recombination Complex (DBRC) at CTF3 (Section 1.3.2) the initial 1.2 μs -long beam is divided into 8 sub-trains of bunches that follow different paths before being recombined into the final 140 ns-long beam. Here we study the optics currently in use at CTF3 for the bunches, or sub-train, that take the longest path, i.e. one turn in the Delay Loop (DL), one passage in the Transfer Line 1 (TL1) and $3^{1/2}$ turns in the Combiner Ring (CR). Even though the DL and CR are indeed closed rings, they are treated as unfolded transfer lines, e.g. two turns in the CR are treated as a single line twice the length of the CR and so on. Figure 4.2 shows the nominal optics for the longest path, which is taken by the train of bunches arriving first in the DBRC. The later trains follow only parts of this path. For example the second train skips the DL, while the last of the eight sub-trains skips the DL and performs only half a turn in the CR. Ideally all sub-trains are supposed to arrive at the end of the DBRC equally shaped, with their bunches interleaved to obtain a regular 12 GHz beam. Figure 4.2 assumes that all the lines of the DBRC are perfectly modelled by the currently available MAD-X model. It is also assumed that the incoming beam arrive in the DBRC perfectly matched with the ideal Twiss parameters. The key points of the DBRC optics that need to be fulfilled are the following:

- The transverse and longitudinal optics of the DL have to be closed, such that the delayed and bypassing sub-trains recombine without any transverse mismatch or bunch lengthening.
- Similarly, the CR has to be closed in terms of transverse and longitudinal optics, such that the bunch shape is preserved independently of the number of turns in the ring.
- The optics of the TL1 between the DL and CR has mainly to ensure the transport from the closed solution of the DL to the closed solution of the CR. One could be less strict here for the longitudinal plane. Since TL1 is a common line for all the bunches taking part in the recombination, any linear distortion can be re-compensated in the later Transfer Line 2 (TL2) that transports the beam to the Experimental Area (CLEX). The latest TL2 and CLEX lines are not modelled here, since they are beyond the scope of this thesis.

One can observe in Figure 4.2 that from the third turn in the CR the dispersion function is distorted. This is due to the non-closed dispersion of the orbit bump generated by the RF deflectors that are installed to allow the injection of the different sub-trains. With the current optics and layout of the CTF3 CR this is assumed to be unavoidable. For the CLIC design possible solutions have been studied and are described in [3, 86].

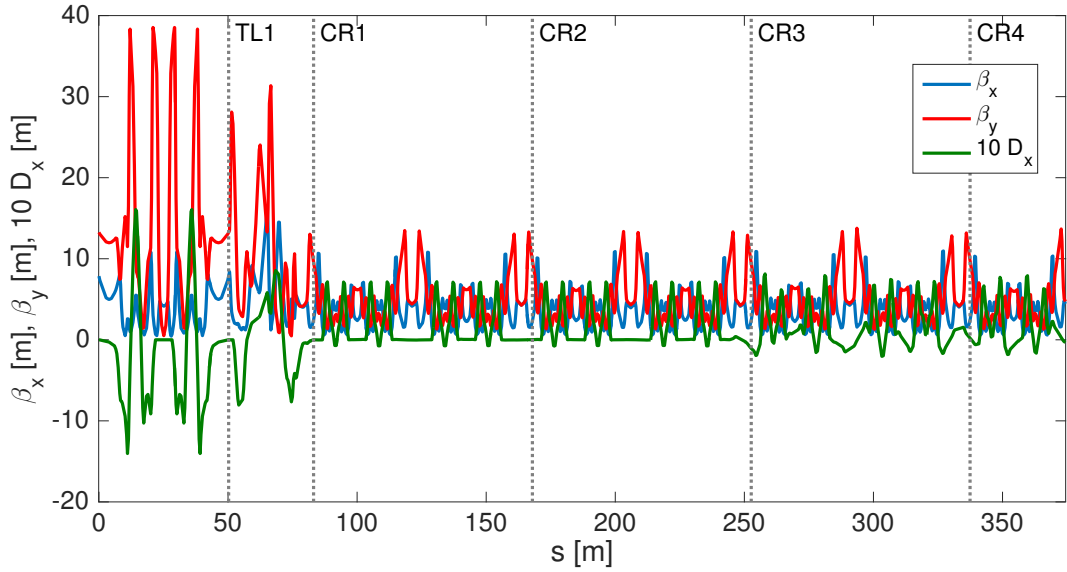


Figure 4.2: Nominal β_x (blue), β_y (red) and horizontal dispersion (green) functions seen by the first arriving train of bunches in the CTF3 DBRC vs. the longitudinal coordinate along the unfolded DBRC lattice. The modelled lattice starts with the DL, followed by the transfer line TL1 and the $3^{1/2}$ turns in the CR (CR1, CR2, CR3, CR4). The lattice ends just before the extraction from the CR.

One can imagine that there could be orbit and transverse optics mismatches that might spoil the final beam quality. The simplest way to show this is to simulate an incoming beam with an offset, either in orbit or transverse optics, with respect to the ideal solution. Figure 4.3 represents the horizontal phase space of an ideal monochromatic beam that has been recombined in the DBRC, but that starts from an orbit offset (1 [mm], 0.5 [mrad]), Figure 4.3(a), or an optics mismatch ($\Delta\beta = -50\%$, $\Delta\alpha = 100\%$), Figure 4.3(b). The simulated transverse beam parameters are compatible with what is typically measured at the entrance of the DBRC at CTF3 and summarised in the following table²:

Beam momentum	140 MeV/c
Normalised horizontal emittance ϵ_{Nx}	60 μm
Normalised vertical emittance ϵ_{Ny}	100 μm

Assuming an incoming bi-Gaussian, uncoupled beam, each solid-line ellipse in Figure 4.3 encloses 99.7% of the particles of the represented beam-let. One can observe that in both cases the eight ellipses separate with respect to each other, leading to emittance growth. The red-dashed ellipses represent the ellipse which area is proportional to nine times the square root of the determinant of the total covariance matrix, i.e. $9\pi\epsilon_\Sigma$, and its orientation is defined by the elements of the total covariance matrix. The black-dashed ellipses are defined by an area of $9\pi\bar{\epsilon}$, and are oriented as the nominal beam (dashed blue contour). The definitions of ϵ_Σ and $\bar{\epsilon}$ are defined in the previous Section 4.1.1. One can observe that the ϵ_Σ

²For these initial simulations an ideal, monochromatic beam is assumed.

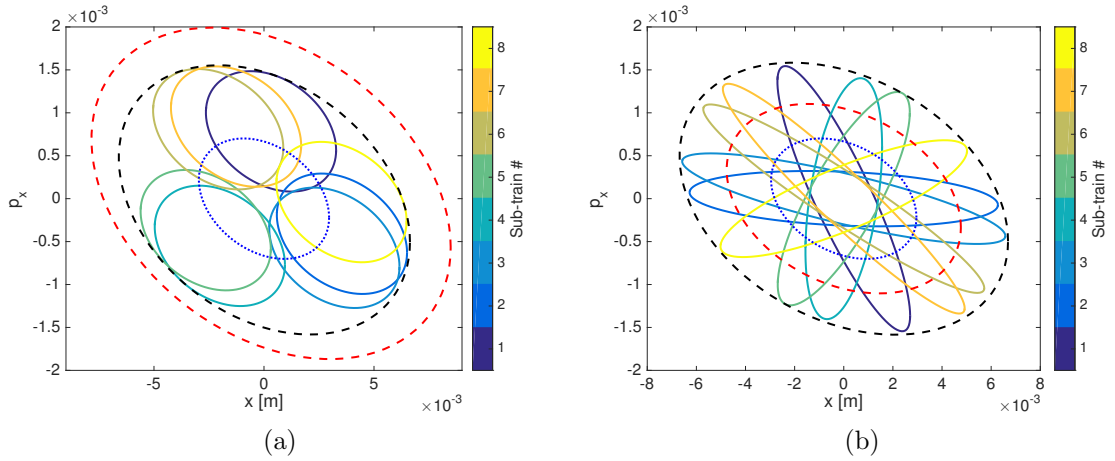


Figure 4.3: Horizontal phase space of a factor-8 combined beam at the end of the DBRC for an incoming beam with an orbit error (a) or transverse optics mismatch (b). Each solid-coloured ellipse represent one of the sub-trains taking part into the recombination. The blue-dashed ellipse represents the unperturbed ideal beam. The black and red-dashed ellipses represent the combined beam respectively following the definition $\bar{\epsilon}$ and ϵ_{Σ} of the combined emittance.

definition might be over-estimating the emittance growth, while under-estimating it in the other. The definition $\bar{\epsilon}$ seems instead to better represent the final beam envelope in both situations.

The aim of the following Section 4.2.1 is to identify and give an order of magnitude of the different effects that might lead to emittance growth during the recombination. From the simulations of the full recombination process, as in Figure 4.3, it is difficult to judge which are the tolerances that one should respect. The method proposed hereafter is instead to first analyse the main effects when combining two beams. Afterwards the developed methodology is applied to the factor-2 recombination that is performed in the DL and the factor-4 in the CR. The obtained rules can be used as a guideline while operating the machine to guess in advance the expected performance of the recombination, given the available signals.

4.2.1 Main emittance growth contributions

While recombining two beams of equal intensity one can distinguish three main effects that could lead to emittance growth:

- Orbit offset.
- Transverse optics mismatch.
- Mismatch due to dispersion, if the two beams are not mono-energetic.

In this section these effects are analysed independently in order to identify the leading orders. The beams are assumed to have the same initial properties, and, independently of the path

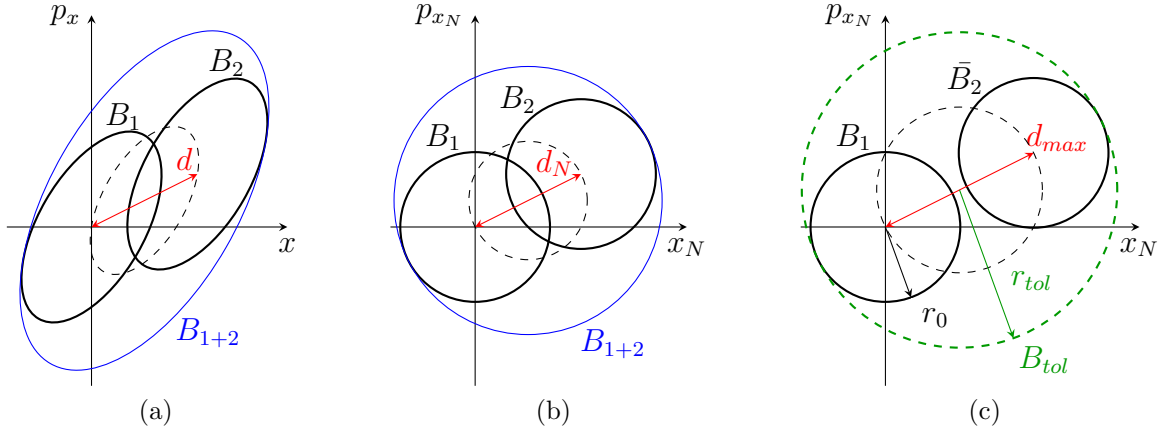


Figure 4.4: (a) horizontal phase space of a factor-2 recombined beam with orbit mismatch between the two beams. The same recombination is represented in normalised phase space (b). B_1 and B_2 are the two initial beams. The blue ellipse B_{1+2} represents the combined beam in terms of the $\bar{\epsilon}$ emittance definition. The dashed-black ellipse is oriented as the beam ellipses and lies on the beam centres. (c) is equivalent to (b), but the orbit mismatch is maximised with respect to the tolerated combined beam envelope (B_{tol}).

taken during the recombination, not to be affected by major single-bunch emittance growth. Effects due to coherent synchrotron radiation (CSR) and transverse non-linearities are not covered in this work (see Appendix B).

All the simulations presented in this thesis assume linear and uncoupled optics. Here only the horizontal plane is considered, but the same description can be applied to the vertical plane. The beams that take part in the recombination process are assumed to be bi-Gaussian distributed in the transverse phase space and monochromatic.

Orbit mismatch

The definition of emittance $\bar{\epsilon}$ introduced in Section 4.1.1 is now considered. Figure 4.4(a) shows a generic representation of what could happen in real phase space if two beams are combined with an orbit mismatch. In order to find the ellipse, oriented according to the nominal optics, that encloses both beams it is convenient to translate the problem in normalised phase space, Figure 4.4(b). In Figure 4.4 each solid-black ellipse, or circle, is assumed to contain 99.7% of the represented Gaussian beam. In normalised phase space the radius of the circle representing a beam must then be equal to three times the square root of the beam r.m.s. emittance. If one has a predefined budget for the emittance growth during the recombination, then it is possible to define a hypothetical tolerated envelope (B_{tol}) within which both beams have to be included, see Figure 4.4(c). The question is then to find the maximum distance (d_{max}) that one can tolerate not to exit from the circle B_{tol} . It is straightforward to see that $d_{max} = 2(r_{tol} - r_0)$. In a real machine it is difficult to perform a direct measurement of the distance d in phase space. However one can imagine that in the later transfer line the two beams will rotate in phase space along the dashed-black circle or ellipse presented in Figure 4.4. The instantaneous projection on the x axis of the distance vector d will then be the orbit separation between the two beams. One can see d_{max} as the diameter

of a “virtual” beam, with its own “virtual emittance” (ϵ_V), that propagates in the transfer line defining its “virtual beam envelope” $\sqrt{\epsilon_V \beta(s)}$, where $\beta(s)$ is the nominal beta function of the transfer line. In Figure 4.4 such an envelope defines a corridor within which the two beam orbits have to be confined to preserve a given tolerated emittance growth. Vice-versa, from the two orbits one can fit the virtual emittance and so measure the expected $\bar{\epsilon}$ growth. Formally, ϵ_V is computed as:

$$\frac{d_{max}}{2} = \sqrt{\epsilon_V} = 3(\sqrt{\overline{\epsilon_{tol}}} - \sqrt{\epsilon_0}) \quad (4.1)$$

$$= 3\sqrt{\epsilon_0} \left[\left(1 + \frac{\Delta \overline{\epsilon_{tol}}}{\epsilon_0} \right)^{\frac{1}{2}} - 1 \right] \quad (4.2)$$

The maximum *orbit* deviation that one tolerates at one location is then:

$$\Delta x_{max} = 2\sqrt{\epsilon_V \beta(s)} = 6\sqrt{\epsilon_0 \beta(s)} \left[\left(1 + \frac{\Delta \overline{\epsilon_{tol}}}{\epsilon_0} \right)^{\frac{1}{2}} - 1 \right] \quad (4.3)$$

where $\beta(s)$ is the nominal Twiss parameter at that location. Clearly it is not enough to fulfil the orbit restriction given by Eq. 4.3 at one single location, but it has to be fulfilled at any location in the transfer line where the two beams travel together, and in particular at the BPMs installed in that line³. One might note that an orbit-mismatch implies also an offset in the outgoing average beam orbit. However this can always be corrected in the following transfer line with the use of steerers, since this is a rigid transformation of the overall beam.

The procedure expressed so far makes the assumption that one does not adapt the transverse optics of the common transfer line to the orbit mismatch. One could in fact rematch the optics so as to enclose the beams B_1 and B_2 of Figure 4.4(a) in a smaller ellipse than B_{1+2} , but differently oriented in phase space. Here this case is not considered. One can in fact imagine a scenario where the orbits drift during machine operations, which would imply the need for a constant rematching of the optics. A more convenient solution is instead to design an orbit feedback that keeps the orbits within the given tolerances.

A different way to see the problem is by using the statistical definition of emittance (ϵ_Σ). In this case the two starting beams, always assumed to be bi-Gaussian distributed, are represented by their covariance matrices as defined in Eq. 2.15:

$$\Sigma_{B_1} = \begin{pmatrix} \epsilon_1 \beta_1 & -\epsilon_1 \alpha_1 \\ -\epsilon_1 \alpha_1 & \epsilon_1 \gamma_1 \end{pmatrix} \quad \Sigma_{B_2} = \begin{pmatrix} \epsilon_2 \beta_2 & -\epsilon_2 \alpha_2 \\ -\epsilon_2 \alpha_2 & \epsilon_2 \gamma_2 \end{pmatrix} \quad (4.4)$$

and their mean location in phase space:

$$\langle B_1 \rangle = \begin{pmatrix} \langle x_1 \rangle \\ \langle p_{x_1} \rangle \end{pmatrix} \quad \langle B_2 \rangle = \begin{pmatrix} \langle x_2 \rangle \\ \langle p_{x_2} \rangle \end{pmatrix} \quad (4.5)$$

where x and p_x are the two coordinates in phase space, and $\langle \cdot \rangle$ denominates the specified mean coordinate. The assumption here is that the two covariance matrices are identical, i.e.

³Normally the BPMs in a transfer line are placed such that they can distinguish all possible orbits, i.e. the phase-advance between the BPMs covers the $[0, 2\pi]$ space.

$\Sigma_{B_1} = \Sigma_{B_2}$, but not centred on the same mean. By following the principle of combination of two covariance matrices described in Appendix D, one can construct a generic element, $\sigma_{\Sigma_x p_x}$, of the covariance matrix representing the ensemble of the two beams:

$$\begin{aligned} \sigma_{\Sigma_x p_x} = \sigma_{x p} + \frac{n_1 \langle x_1 \rangle \langle p_{x_1} \rangle + n_2 \langle x_2 \rangle \langle p_{x_2} \rangle}{n_1 + n_2} + \\ - \frac{n_1^2 \langle x_1 \rangle \langle p_{x_1} \rangle + n_2^2 \langle x_2 \rangle \langle p_{x_2} \rangle + n_1 n_2 (\langle x_1 \rangle \langle p_{x_2} \rangle + \langle x_2 \rangle \langle p_{x_1} \rangle)}{(n_1 + n_2)^2} \end{aligned} \quad (4.6)$$

where n_1, n_2 are the number of particles per beam. Each beam is assumed to have the same intensity, i.e. $n_1 = n_2$, so Eq. 4.6 can be re-written as a function of the relative distance of the two beams (Δx and Δp_x):

$$\begin{aligned} \sigma_{\Sigma_x p_x} = \sigma_{x p_x} + \frac{1}{2} [\langle x_1 \rangle \langle p_{x_1} \rangle + (\langle x_1 \rangle + \Delta x)(\langle p_{x_1} \rangle + \Delta p_x)] + \\ - \frac{1}{4} [\langle x_1 \rangle \langle p_{x_1} \rangle + (\langle x_1 \rangle + \Delta x)(\langle p_{x_1} \rangle + \Delta p_x) + \langle x_1 \rangle (\langle p_{x_1} \rangle + \Delta p_x) + (\langle x_1 \rangle + \Delta x) \langle p_{x_1} \rangle] \end{aligned} \quad (4.7)$$

$$= \sigma_{x p_x} + \frac{1}{4} \Delta x \Delta p_x \quad (4.8)$$

and so the other elements of the covariance matrix are:

$$\sigma_{\Sigma x x} = \sigma_{x x} + \frac{1}{4} \Delta x^2 \quad (4.9)$$

$$\sigma_{\Sigma p_x p_x} = \sigma_{p_x p_x} + \frac{1}{4} \Delta p_x^2. \quad (4.10)$$

One can easily compute the statistical emittance of the combined beam as the square root of the determinant of the total covariance matrix:

$$\epsilon_{\Sigma tot}^2 = \epsilon_0^2 + \frac{1}{4} (\sigma_{x x} \Delta p_x^2 + \sigma_{p_x p_x} \Delta x^2 - 2\sigma_{x p_x} \Delta x \Delta p_x) \quad (4.11)$$

$$= \epsilon_0^2 + \frac{\epsilon_0}{4} (\beta \Delta p_x^2 + \gamma \Delta x^2 + 2\alpha \Delta x \Delta p_x) \quad (4.12)$$

where α, β, γ are the Twiss parameters of the two single beams, which by hypothesis are matched to the designed optics. Equation 4.12 can also be expressed in terms of a fixed tolerated emittance growth, similar to Eq. 4.2:

$$\epsilon_0 \left[\left(1 + \frac{\Delta \epsilon_{\Sigma tol}}{\epsilon_0} \right)^2 - 1 \right] = \beta \left(\frac{\Delta p_x}{2} \right)^2 + \gamma \left(\frac{\Delta x}{2} \right)^2 + 2\alpha \frac{\Delta x \Delta p_x}{4}. \quad (4.13)$$

Equation 4.13 represents an ellipse matched with the nominal beam optics, and with an equivalent emittance defined by the left-end side of the equation. The newly defined emittance has the same role of ϵ_V in Eq. 4.3, and can be used to guess the maximum orbit separation allowed to fulfil certain tolerated statistical emittance growth.

Figure 4.5 shows the comparison between the normalised orbit tolerance at one location using the two different definitions of emittance used in this work. It should be noted that the statistical emittance, ϵ_{Σ} , allows a bigger orbit mismatch than the $\bar{\epsilon}$ definition for a given tolerated emittance growth. This is naively expected due to the fact that the statistical emittance ϵ_{Σ} drops the knowledge of the nominal Twiss parameters, which instead is preserved in the more “geometrical” definition of $\bar{\epsilon}$.

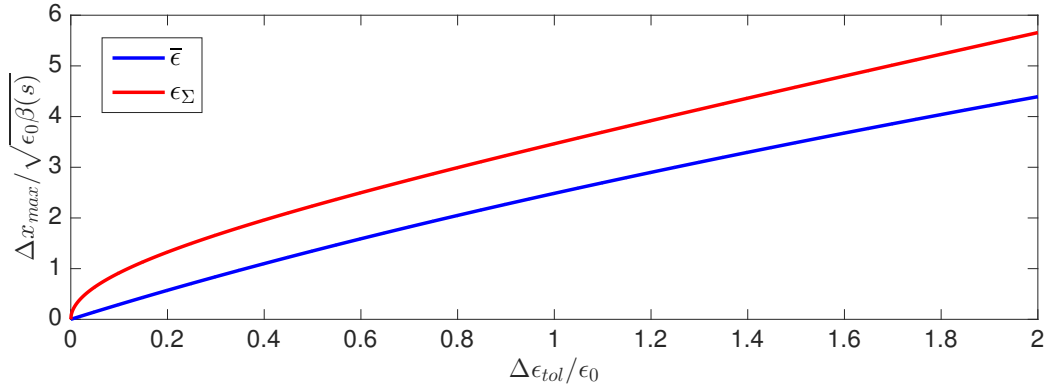


Figure 4.5: Normalised orbit separation ($\Delta x_{max}/\sqrt{\epsilon_0\beta(s)}$) that one can tolerate at one location (s) vs. required emittance growth tolerance ($\Delta\epsilon_{tol}/\epsilon_0$). The emittance definitions are ϵ_Σ (red) and $\bar{\epsilon}$ (blue).

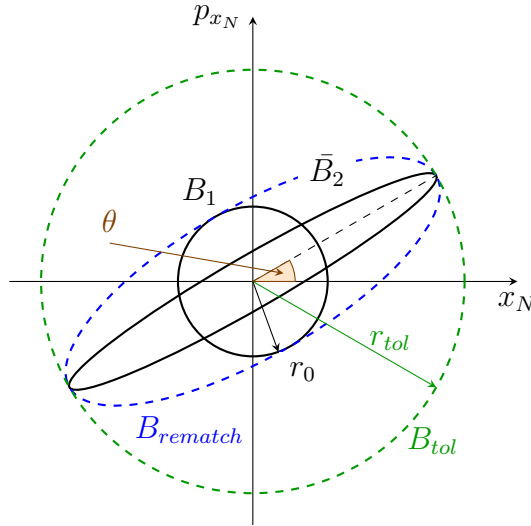


Figure 4.6: Representation in normalised phase space of two beams (B_1 and B_2). Dashed-blue ($B_{rematch}$) and dashed-green (B_{tol}) are respectively the smallest ellipse and circle that contain both beams.

Transverse optics mismatch

For the transverse mismatch while combining two beams one can follow similar procedures as for the orbit mismatch. In this case the two beams are supposed to be centred on the same orbit, but to have different Twiss parameters or, in general, different covariance matrices.

In order to compute the final $\bar{\epsilon}$ one can still represent the problem in normalised phase space with respect to the nominal optics. Figure 4.6 shows a typical scenario. The circle B_1 represent the first beam that is assumed to be matched to the nominal optics. In normalised phase space B_1 is represented as a circle of area $9\epsilon_0\pi$, i.e. such that it contains 99.7% of the represented Gaussian beam. Assuming that one can tolerate a maximum emittance $\bar{\epsilon}_{tol}$, one can combine B_1 with a generic B_2 represented by any ellipse which fits within the tolerated dashed-green circle (B_{tol}) in Figure 4.6. The ellipse \bar{B}_2 represents a possible worst case,

equivalent to any other rotation by θ . The general equation for such an ellipse is:

$$\frac{b^2 \cos^2(\theta) + a^2 \sin^2(\theta)}{a^2 b^2} x^2 + \frac{b^2 \sin^2(\theta) + a^2 \cos^2(\theta)}{a^2 b^2} y^2 + 2xy(a^2 - b^2) \frac{\sin(\theta) \cos(\theta)}{a^2 b^2} = 1 \quad (4.14)$$

where a and b are, respectively, the length of the major and minor semi-axis. Since the ideal case is assumed where the two beams have the same emittance, i.e. the same area in phase space, one finds that a and b must be:

$$a = r_{tol} = 3\sqrt{\overline{\epsilon_{tol}}} \quad (4.15)$$

$$b = 3\frac{\epsilon_0}{\sqrt{\overline{\epsilon_{tol}}}} \quad (4.16)$$

By analogy with Eq. 2.12, any ellipse equivalent to \bar{B}_2 turns out to be identified in normalised phase space by the following Twiss parameters:

$$\bar{B}_2 := \begin{cases} \gamma_N = \frac{\epsilon_0}{\overline{\epsilon_{tol}}} \cos^2(\theta) + \frac{\overline{\epsilon_{tol}}}{\epsilon_0} \sin^2(\theta) \\ \beta_N = \frac{\epsilon_0}{\overline{\epsilon_{tol}}} \sin^2(\theta) + \frac{\overline{\epsilon_{tol}}}{\epsilon_0} \cos^2(\theta) \\ \alpha_N = \frac{\overline{\epsilon_{tol}}^2 - \epsilon_0^2}{\overline{\epsilon_{tol}}\epsilon_0} \sin(\theta) \cos(\theta) \end{cases} \quad (4.17)$$

In real phase space (see transformation introduced in Eq. 2.27 and Eq. 2.28) with respect to the nominal optics parameters (β^* , α^*) one finds:

$$\beta_{tol} = \beta^* \left(\frac{\epsilon_0}{\overline{\epsilon_{tol}}} \sin^2(\theta) + \frac{\overline{\epsilon_{tol}}}{\epsilon_0} \cos^2(\theta) \right) \quad (4.18)$$

$$\alpha_{tol} = \alpha^* \left(\frac{\epsilon_0}{\overline{\epsilon_{tol}}} \sin^2(\theta) + \frac{\overline{\epsilon_{tol}}}{\epsilon_0} \cos^2(\theta) \right) + \frac{\overline{\epsilon_{tol}}^2 - \epsilon_0^2}{\overline{\epsilon_{tol}}\epsilon_0} \sin(\theta) \cos(\theta) \quad (4.19)$$

or in terms of the relative emittance growth:

$$\beta_{tol} = \frac{\beta^*}{1 + \overline{\Delta\epsilon}/\epsilon_0} \left[\sin^2(\theta) + (1 + \overline{\Delta\epsilon}/\epsilon_0)^2 \cos^2(\theta) \right] \quad (4.20)$$

$$\alpha_{tol} = \frac{\alpha^*}{1 + \overline{\Delta\epsilon}/\epsilon_0} \left[\sin^2(\theta) + (1 + \overline{\Delta\epsilon}/\epsilon_0)^2 \cos^2(\theta) \right] + \frac{(1 + \overline{\Delta\epsilon}/\epsilon_0)^2 - 1}{1 + \overline{\Delta\epsilon}/\epsilon_0} \sin(\theta) \cos(\theta) \quad (4.21)$$

In the case of optics mismatch one can imagine rematching the following transfer line to the new beam, i.e. enclosing the beam in the dashed-blue ellipse $B_{rematch}$ in Figure 4.6. The final emittance would then be the area $B_{rematch} = \pi\sqrt{\overline{\epsilon_{tol}}\epsilon_0}$, which is much smaller than the area of $B_{tol} = \pi\overline{\epsilon_{tol}}$. The previous computations remain valid, but one has to replace in Eq. 4.19 and 4.18 $\overline{\epsilon_{tol}}$ by $\overline{\epsilon_{tol}}^2/\epsilon_0$, i.e. allow a bigger emittance growth in the recombination, which is recovered by the rematching of the line. Equations 4.18 and 4.19 become:

$$\beta_{tol_{rem}} = \frac{\beta^*}{(1 + \overline{\Delta\epsilon}/\epsilon_0)^2} \left[\sin^2(\theta) + (1 + \overline{\Delta\epsilon}/\epsilon_0)^4 \cos^2(\theta) \right] \quad (4.22)$$

$$\alpha_{tol_{rem}} = \frac{\alpha^*}{(1 + \overline{\Delta\epsilon}/\epsilon_0)^2} \left[\sin^2(\theta) + (1 + \overline{\Delta\epsilon}/\epsilon_0)^4 \cos^2(\theta) \right] + \frac{(1 + \overline{\Delta\epsilon}/\epsilon_0)^4 - 1}{(1 + \overline{\Delta\epsilon}/\epsilon_0)^2} \sin(\theta) \cos(\theta). \quad (4.23)$$

One can treat the same problem by using the statistical definition of emittance. Similar to the orbit mismatch case, by following the definition of covariance in Appendix D, one finds that the overall covariance matrix is just the mean of the Σ_{B_1} and Σ_{B_2} , leading to the total statistical emittance:

$$\epsilon_{\Sigma_{tot}}^2 = \det(\Sigma_{B_1+B_2}) \quad (4.24)$$

$$= \frac{1}{4} \left[\epsilon_1^2 + \epsilon_2^2 + \epsilon_1 \epsilon_2 \left(\frac{\beta_1}{\beta_2} (1 + \alpha_2^2) + \frac{\beta_2}{\beta_1} (1 + \alpha_1^2) - 2\alpha_1 \alpha_2 \right) \right] \quad (4.25)$$

Equation 4.25 considers the general case where the two beams could have a different emittance and generic Twiss parameters. If it is assumed that the emittance is the same for the two beams, and that the first beam is matched to the nominal optics (β^*, α^*) , then Eq. 4.25 becomes:

$$\frac{\Delta \epsilon_{\Sigma}}{\epsilon_0} = -1 + \frac{1}{2} \sqrt{2 + \frac{\beta^*}{\beta_2} (1 + \alpha_2^2) + \frac{\beta_2}{\beta^*} (1 + (\alpha^*)^2) - 2\alpha^* \alpha_2} \quad (4.26)$$

In addition to the orbit mismatch case, one has to be careful in interpreting the emittance growth derived by Eq. 4.26. The total statistical emittance of the combined beam (ϵ_{Σ}) has lost, a priori, any strict relation to the nominal optics of the subsequent transfer line, leading to a non well defined concept of beam size.

A special case can be identified when the nominal Twiss α^* parameter is zero. In this case the absolute value of the tolerated α_{tol} depends only on the allowed emittance growth, as well as the ratio β_{tol}/β^* . Figure 4.7 shows the tolerances one should fulfil for this particular case, using the two definitions of emittance used in this chapter. Note that the statistical

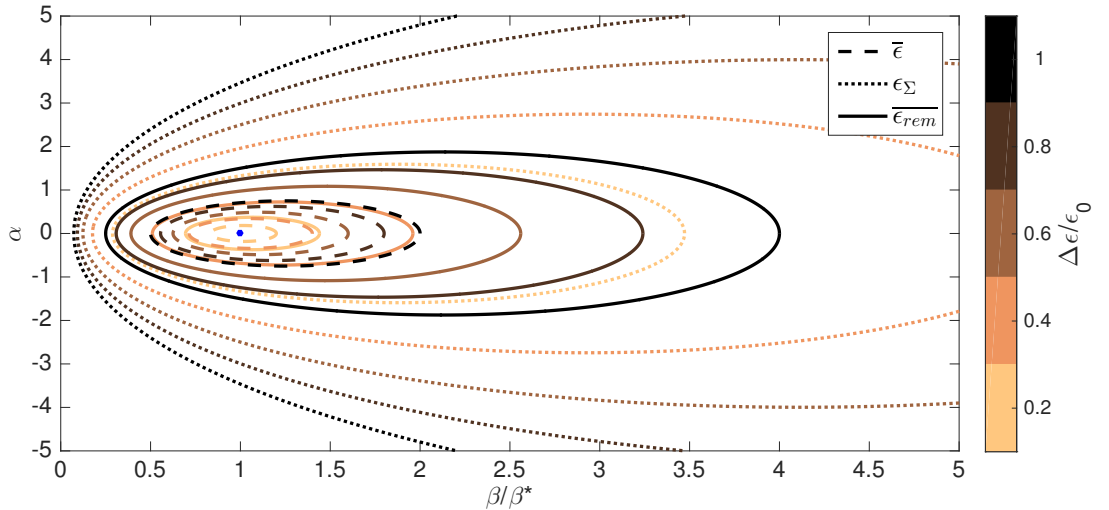


Figure 4.7: Contour plot of the emittance growth while combining two beams as a function of their Twiss parameters. One beam is assumed to have Twiss parameters $\alpha^* = 0$ and $\beta^* > 0$. Dashed, dotted and continuous contours use respectively the emittance definitions $\bar{\epsilon}$, ϵ_{Σ} and $\bar{\epsilon}$ with optics rematching $\overline{\epsilon_{rem}}$.

emittance definition is the less restrictive, while using the $\bar{\epsilon}$ definition one is much more sensitive to mismatches. This is naively understandable by looking at Figure 4.6. It is

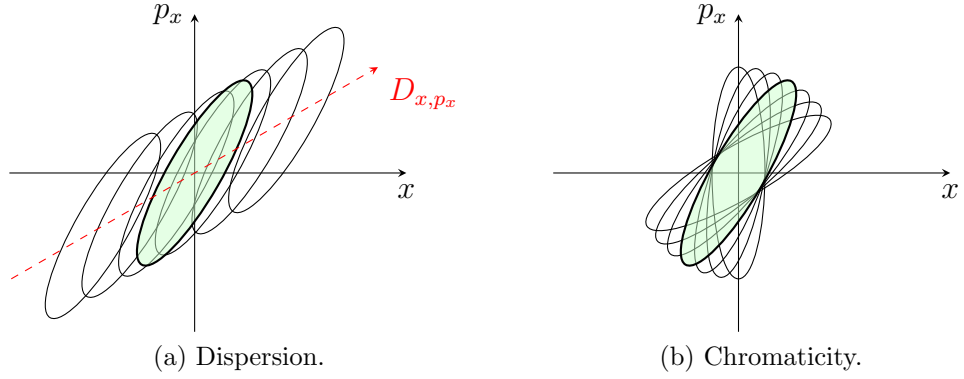


Figure 4.8: Representation of the bunch broadening in the horizontal phase space (x - p_x) due to energy effects. Each ellipse is representative of a sub-set of particles with the same energy, with the light-green filled ellipse representing the on-energy particles. D_{x,p_x} represents the horizontal linear dispersion vector.

clear that the green B_{tol} circle is mainly empty, while the blue $B_{rematch}$ better describes the combined beam, but it still covers big empty areas of the phase space. The statistical emittance definition on the contrary is closer to the effective area spanned by the beam, which slowly grows: the bigger the β mismatch is, the thinner is the ellipse \overline{B}_2 .

Linear dispersion mismatch

So far, the effects considered were assuming ideal monochromatic beams. In reality the CLIC and the CTF3 Drive Beam are far from being monochromatic. In general the energy dependence might be strongly non-linear, as will be shown later. Here only the *linear dispersion* case is exploited, in order to have a first-order approximation of what one should expect.

By the assumptions already presented in Section 4.1, at the entrance of the DBRC the beam is perfectly bi-Gaussian in all horizontal, vertical and longitudinal phase spaces, and is matched with the ideal initial conditions of the DBRC optics. Since the DBRC is a complex ensemble of rings, one should expect non-zero dispersion at some location. A non-monochromatic beam in the presence of *linear* dispersion would spread itself in phase space as depicted in Figure 4.8a. A similar effect is the chromatic one, depicted in Figure 4.8b. The chromatic effect is neglected here, and only the dispersive effect is treated.

While discussing emittance growth due to energy dependence it might not make too much sense to search for an ellipse that contains all the ellipses of Figure 4.8. The different slices/ellipses “contain” a different number of particles, which decreases with distance from the central/nominal one. Moreover the whole idea of the previously defined emittance $\bar{\epsilon}$ is to measure the actual beam envelope in a later transfer line, but the energy effects, e.g. dispersion, will vary from point to point in the DBRC. Therefore only the statistical definition of emittance ϵ_Σ (i.e. the determinant of the covariance matrix) is used here as a figure of merit of the emittance growth.

By analogy with Eq. 4.6 one can compute the overall covariance matrix of a beam that is

broadened in phase space due to linear dispersion. By construction, and by the hypothesis of Gaussian energy spread, centred on zero, one obtains:

$$\langle x_i \rangle = D_x \frac{\Delta p_i}{p_0} \quad (4.27)$$

$$\langle p_{x_i} \rangle = D_{p_x} \frac{\Delta p_i}{p_0} \quad (4.28)$$

$$n_i = \frac{1}{\sqrt{2\pi}\sigma_{\Delta p/p_0}} \exp\left(-\frac{1}{2}\left(\frac{\Delta p_i/p_0}{\sigma_{\Delta p/p_0}}\right)^2\right) \quad (4.29)$$

where $\langle x_i \rangle$ and $\langle p_{x_i} \rangle$ are the mean coordinate of the i -th beam-let that contains n_i particles all with the same energy deviation $\Delta p_i/p_0$ from the nominal momentum p_0 . D_x and D_{p_x} are the linear coefficients of the horizontal dispersion. By symmetry the average beam position is zero in both coordinates. This leads to:

$$\sigma_{\Sigma x p_x} = \sigma_{x p_x} + \int_{-\infty}^{\infty} d\frac{\Delta p}{p_0} D_x D_{p_x} \left(\frac{\Delta p}{p_0}\right)^2 \frac{1}{\sigma_{\Delta p/p_0} \sqrt{2\pi}} \exp\left(-\frac{1}{2}\left(\frac{\Delta p/p_0}{\sigma_{\Delta p/p_0}}\right)^2\right) \quad (4.30)$$

$$= \sigma_{x p_x} + D_x D_{p_x} \sigma_{\Delta p/p_0}^2. \quad (4.31)$$

One can use Eq. 4.31 to reconstruct the covariance matrix of the full distribution, and so compute the total statistical emittance as:

$$\epsilon_{\Sigma tot}^2 = \epsilon_0^2 + \sigma_{\Delta p/p_0}^2 (D_x^2 \sigma_{p_x p_x} + D_{p_x}^2 \sigma_{x x} - 2D_x D_{p_x} \sigma_{x p_x}) \quad (4.32)$$

$$= \epsilon_0^2 + \sigma_{\Delta p/p_0}^2 \epsilon_0 (D_x^2 \gamma + D_{p_x}^2 \beta + 2D_x D_{p_x} \alpha) \quad (4.33)$$

where $\sigma_{\Delta p/p_0}$ is the standard deviation of the beam-energy spread, and $\sigma_{x p_x}$, $\sigma_{x x}$, $\sigma_{p_x p_x}$ are the transverse covariances of each slice, that are assumed to be all equal. One has to be careful here: the quantity calculated in Eq. 4.33 is far from being conserved subsequently. The dispersion function varies along the lattice, so from Eq. 4.33 one should expect to see the emittance increase and decrease along the lattice. This does not contradict the law of emittance preservation (see Section 2.1): what is preserved is the determinant of the full covariance matrix, which includes the coordinates $(t, \Delta p/p_0)$. Indeed the emittance broadening due to linear dispersion is not a problem by itself, but it becomes so when one combines two beams with different dispersions: further down the beamline it will be impossible to cure the dispersions of both beams at the same time, so the overall emittance of the beam will always be bigger than the initial one.

The simplest case is when one of the two beams has no dispersion, while the other one does. Assuming that this is the only mis-match between the two, the generic covariance matrix element of the combined beam is expressed as:

$$\sigma_{\Sigma x p_x} = \frac{1}{2} (2\sigma_{x p_x} + D_x D_{p_x} \sigma_{\Delta p/p_0}^2) \quad (4.34)$$

leading to a final projected emittance of:

$$\epsilon_{\Sigma tot}^2 = \epsilon_0^2 + \frac{1}{2} \sigma_{\Delta p/p_0}^2 (\sigma_{x x} D_{p_x}^2 + \sigma_{p_x p_x} D_x^2 - 2\sigma_{x p_x} D_x D_{p_x}) \quad (4.35)$$

$$= \epsilon_0^2 + \frac{1}{2} \sigma_{\Delta p/p_0}^2 \epsilon_0 (D_x^2 \gamma + D_{p_x}^2 \beta + 2D_x D_{p_x} \alpha). \quad (4.36)$$

The result obtained in Eq. 4.36 is naively expected: the resulting pseudo-emittance⁴growth is half the broadening experienced by a single beam in a dispersive region, Eq. 4.33.

If both beams suffer from dispersion, and those are mismatched with respect to each other, then the resulting pseudo-emittance clearly depends on both dispersions:

$$\begin{aligned} \epsilon_{\Sigma tot}^2 &= \epsilon_0^2 + \frac{1}{2}\sigma_{\Delta p/p_0}^2 \left[\sigma_{xx}(D_{p_{x1}}^2 + D_{p_{x2}}^2) + \sigma_{p_x p_x}(D_{x1}^2 + D_{x2}^2) - 2\sigma_{x p_x}(D_{x1}D_{p_{x1}} + D_{x2}D_{p_{x2}}) \right] + \\ &\quad + \frac{1}{4}\sigma_{\Delta p/p_0}^4 (D_{x1}D_{p_{x2}} - D_{x2}D_{p_{x1}})^2 \end{aligned} \quad (4.37)$$

$$\begin{aligned} &= \epsilon_0^2 + \frac{1}{2}\sigma_{\Delta p/p_0}^2 \epsilon_0 \left[\gamma(D_{p_{x1}}^2 + D_{p_{x2}}^2) + \beta(D_{x1}^2 + D_{x2}^2) + 2\alpha(D_{x1}D_{p_{x1}} + D_{x2}D_{p_{x2}}) \right] + \\ &\quad + \frac{1}{4}\sigma_{\Delta p/p_0}^4 (D_{x1}D_{p_{x2}} - D_{x2}D_{p_{x1}})^2 \end{aligned} \quad (4.38)$$

Both Eq. 4.34 and Eq. 4.38 clarify the final statistical emittance behaviour as a function of the different components, but are actually not too useful to find a generic behaviour. It is important to stress once again that the identified pseudo-emittance is a not conserved quantity, so its utility might be limited. What could be interesting is to provide a value related to the horizontal beam variance, by writing explicitly the dependence of $\sigma_{\Sigma xx}$:

$$\sigma_{\Sigma xx} = \sigma_{xx} + \frac{1}{2}(D_{x1}^2 + D_{x2}^2)\sigma_{\Delta p/p_0}^2. \quad (4.39)$$

As for Eq. 4.34, one could have naively expected the result obtained in Eq. 4.39.

It is not interesting to develop further the study in this direction, especially if one is expecting the energy effects to be highly non-linear in the actual machine. The same applies to the chromatic aberrations of the transverse phase space. Later in this chapter the energy dependence is treated instead with numerical simulations of the actual DBRC optics.

4.2.2 Monochromatic effects after the Delay Loop

In the CTF3 DBRC the first step is to perform the factor-2 recombination. The first arriving bunches are delayed in the Delay Loop, while the second ones bypass it. The process is then repeated a further three times to prepare the four trains of bunches that will be recombined in the CR. In Section 4.2.1 the mono-chromatic effects that may lead to emittance growth have been identified to be the orbit and transverse optics mismatch of the two beams in the following transfer line.

The first effect is due to the non-closure of the two orbits between delayed and bypassing bunches. The natural place at which it is possible to verify the orbit closure is in the following transfer line (TL1). By applying Eq. 4.3 at the location where BPMs are installed in TL1, one obtains the plots in Figure 4.9(a) and 4.9(b), for the horizontal and vertical planes respectively. For each tolerated emittance growth, a coloured corridor is identified in Figure 4.9. In order to fulfil a desired emittance growth tolerance, defined in terms of $\bar{\epsilon}$ (Section 4.1.1), the orbits of delayed and bypassing bunches have to be confined within the desired corridor at *all* the BPM positions. By using the statistical definition of emittance,

⁴The added prefix *pseudo* refers to the non-preservation of this quantity along a transfer line.

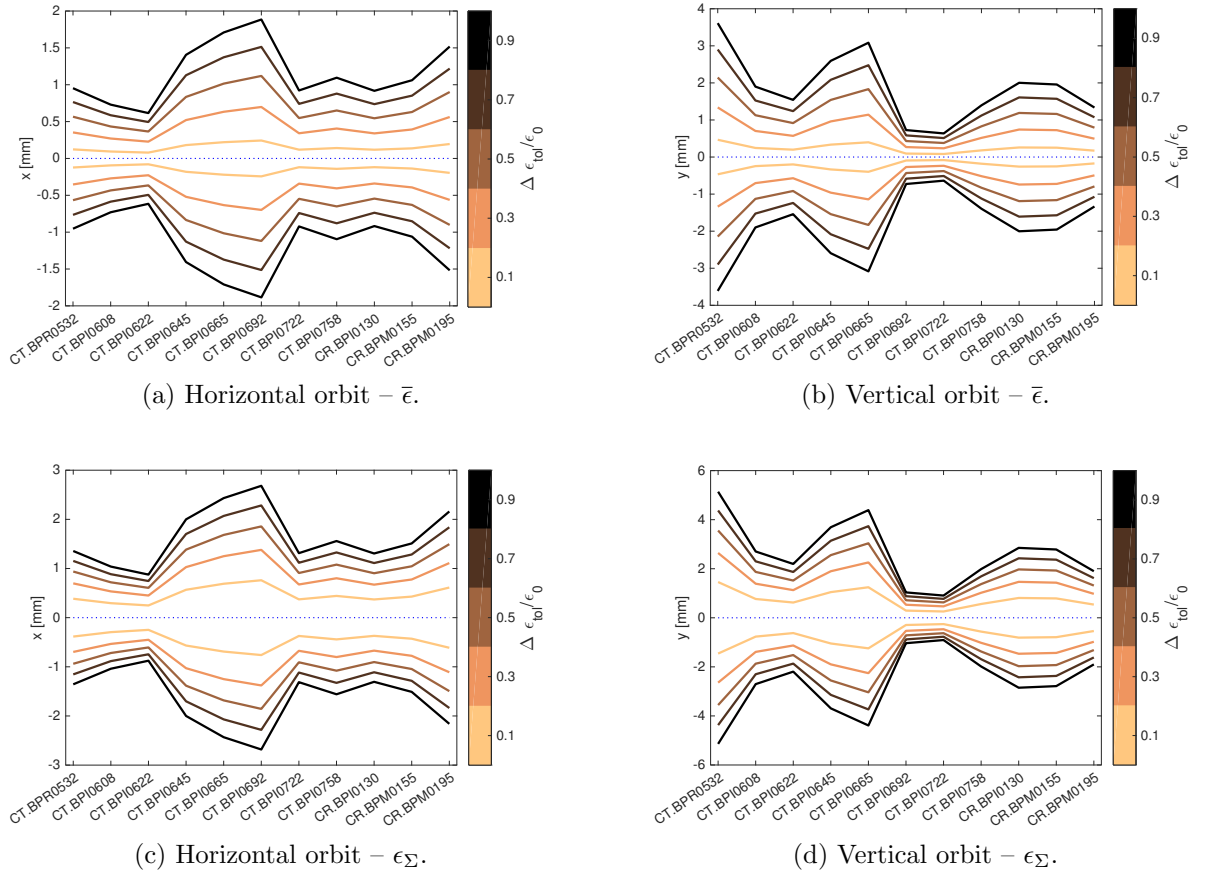


Figure 4.9: Orbit tolerances in TL1 for different tolerated emittance growth ($\Delta\epsilon_{tol}/\epsilon_0$). On the horizontal axis are the BPMs installed in this region at CTF3. The used definition of emittance is $\bar{\epsilon}$ in (a) and (b), ϵ_{Σ} in (c) and (d). (a) and (c) are for the horizontal direction, while (b) and (d) are for the vertical one.

ϵ_Σ , and so considering Eq. 4.13, one can obtain slightly relaxed tolerances, that are reported in the same manner in Figure 4.9c and 4.9d.

It should be noted that in all cases the two orbits do not necessarily need to be centred on zero. The zero orbit in Figure 4.9 is meant to be considered as the mean orbit of the two train of bunches. Both definitions of emittance indicate that a few hundred micron orbit difference between the two trains may lead to considerable emittance growth.

At CTF3 the transverse Twiss parameters are measured by means of quadrupole scans in a few locations. The quadrupole scan technique has been described in Section 3.4. After the DL the closest locations where it is possible to perform such measurement are in the so called CTS line, right after the DL, and in the CRM line, right after the injection into the CR (see the CTF3 layout in Figure 1.4). At both locations one can measure the transverse mismatch between delayed and bypassing bunches with two dedicated beam set-ups: one in which the whole beam bypasses the DL and one in which the beam is delayed in the DL. One might rematch the incoming beamline in order to match the bypassing beam with nominal Twiss parameters expected at the measurement location, but the delayed beam might still be distorted due to errors in the DL optics. Figure 4.10 shows the delayed beam tolerances on the Twiss parameters which one has to respect in order to obtain a combined beam which is within the desired emittance growth tolerance. Figures 4.10(a), 4.10(b) are the tolerances with respect to $\bar{\epsilon}$ definition, i.e. they are generated by using Eqs. 4.20 and 4.21. The tolerances are relaxed in Figures 4.10(c), 4.10(d), by using the same $\bar{\epsilon}$ definition, but assuming a re-matched optics for the combined beam, i.e. they are computed using Eq. 4.22 and 4.23. By using the statistical definition of emittance, ϵ_Σ , and so by using Eq. 4.26, one can obtain even more relaxed tolerances as in Figure 4.10(e) and 4.10(f). The same plots are generated for the CRM measurement location and they are shown in Figure 4.11.

4.2.3 Monochromatic effects at the Combiner Ring

In the Combiner Ring (CR) the four arriving train of bunches are injected and interleaved with each other. Ideally the injection is supposed to put each train on the closed orbit and matched with the closed optics solution of the ring. At the end of the recombination the four trains have performed a different number of turns in the CR: the first-injected has done 4 turns, while the latest-injected only one.

In the case of an injection orbit error, the four trains spread around in the phase space according to the tune of the CR. Figure 4.12(a) shows in normalised phase space the worst case, i.e. assuming a CR tune of $1/4$. By using the $\bar{\epsilon}$ definition, the total emittance is represented by the circle which contains all the four circles (B_1, B_2, B_3, B_4) representing the 4 trains. Also for the factor 4 case one can compute the “virtual” emittance (ϵ_V) associated with the dashed-black circle passing through the centre of all four circles. Equation 4.2 remains valid, and one can compute the tolerated distance between the orbits of the 4 trains in order to stay within the maximum emittance growth requirements.

In a similar way one can treat the transverse optics injection mismatch. Figure 4.12(b) shows the worst case, i.e. in a hypothetical CR with tune of $1/8$ such that the separation

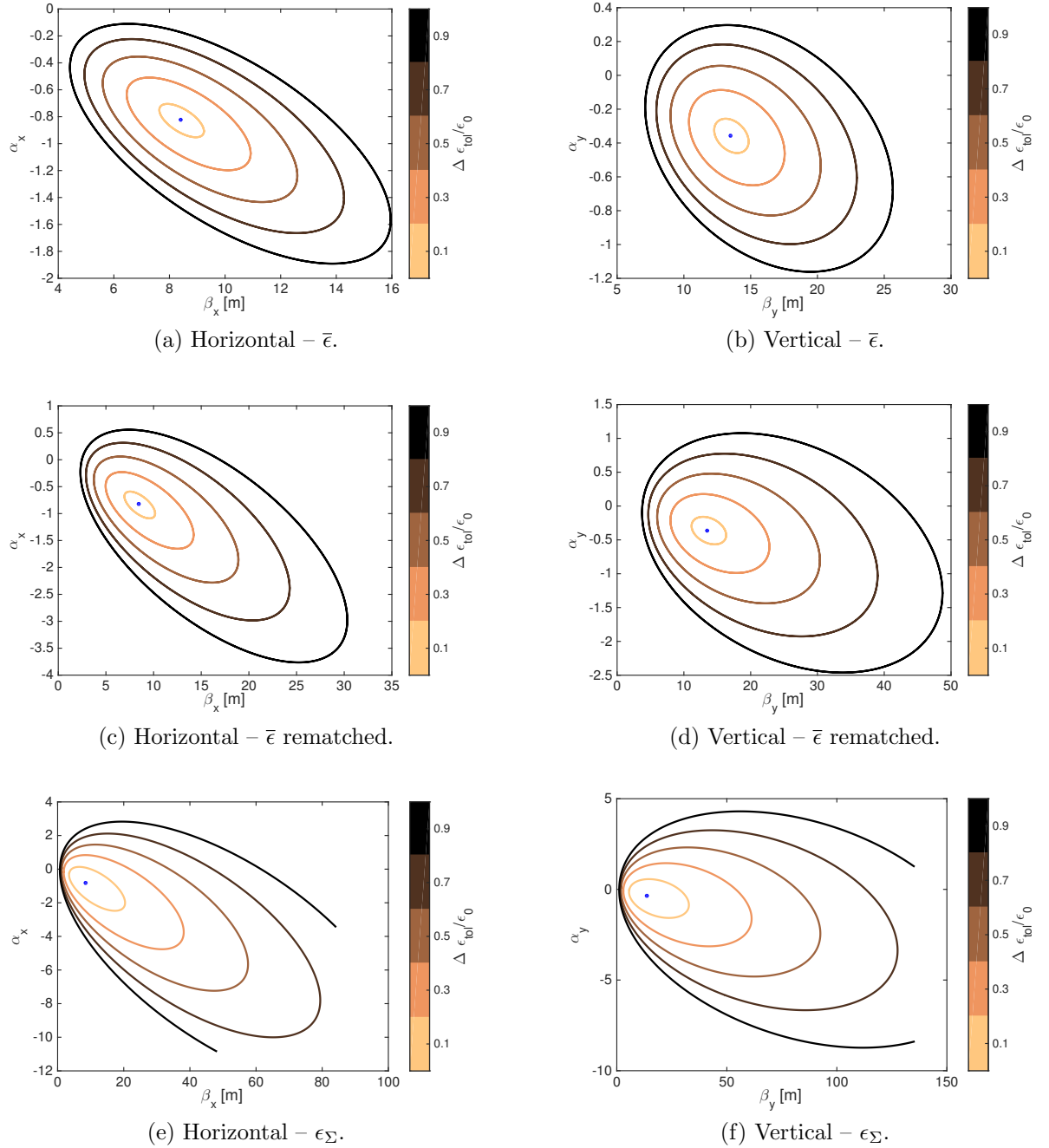


Figure 4.10: Contour plots of the emittance growth ($\Delta \epsilon_{tol}/\epsilon_0$) as a function of the delayed beam Twiss parameters (α and β) measured at the CTS measuring point. (a), (c) and (e) are for the horizontal phase space, while (b), (d) and (f) are for the vertical one. The definitions of emittance in use are $\bar{\epsilon}$ in (a) and (b), $\bar{\epsilon}$ with rematching in (c) and (d), ϵ_{Σ} in (e) and (f).

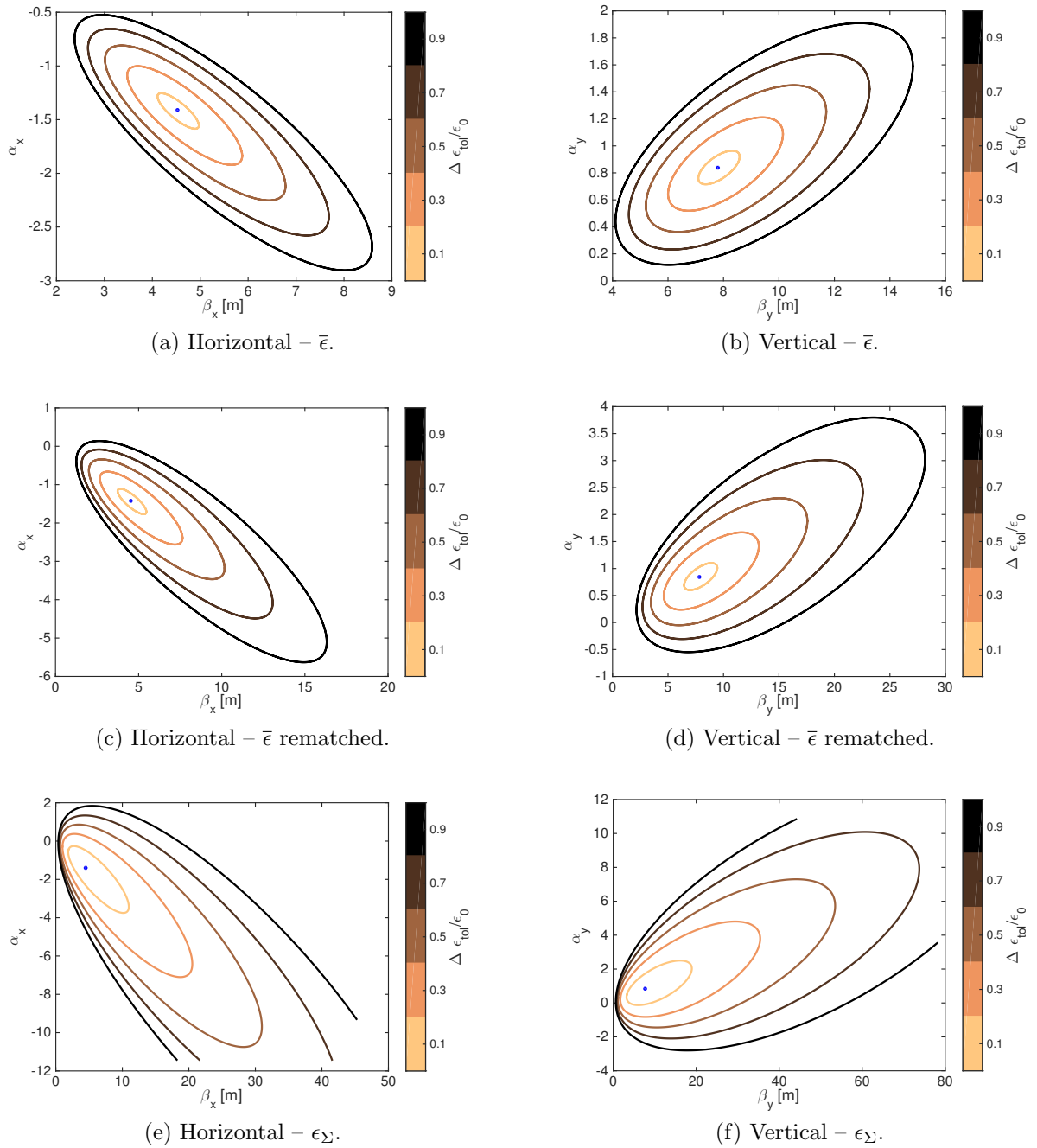


Figure 4.11: As in Figure 4.10, but for the CRM measuring point.

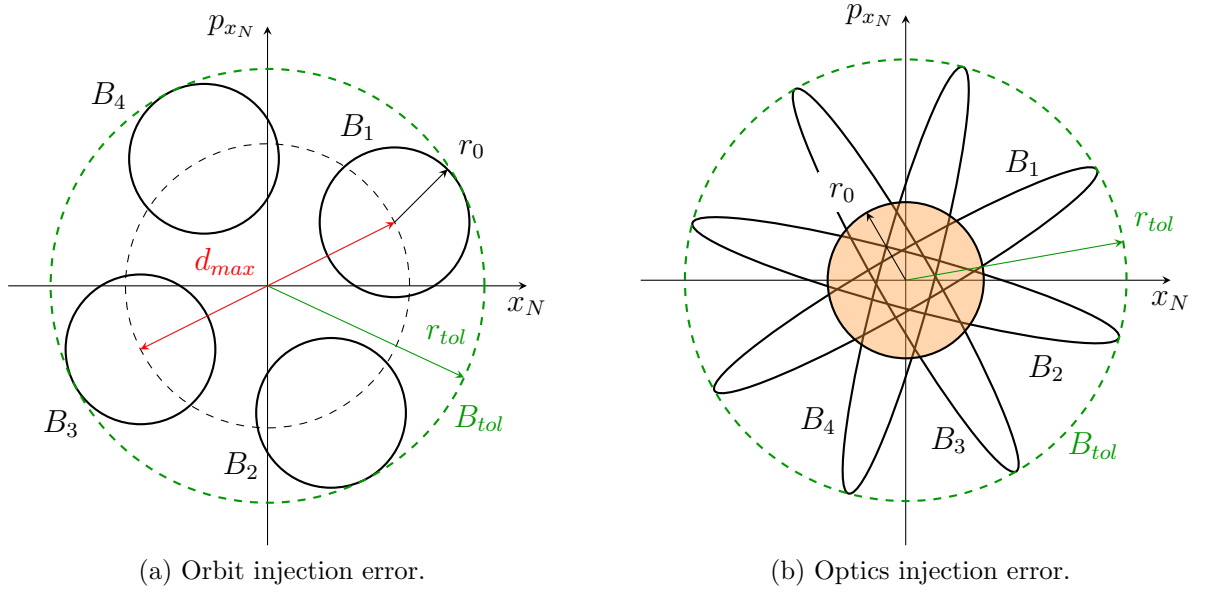


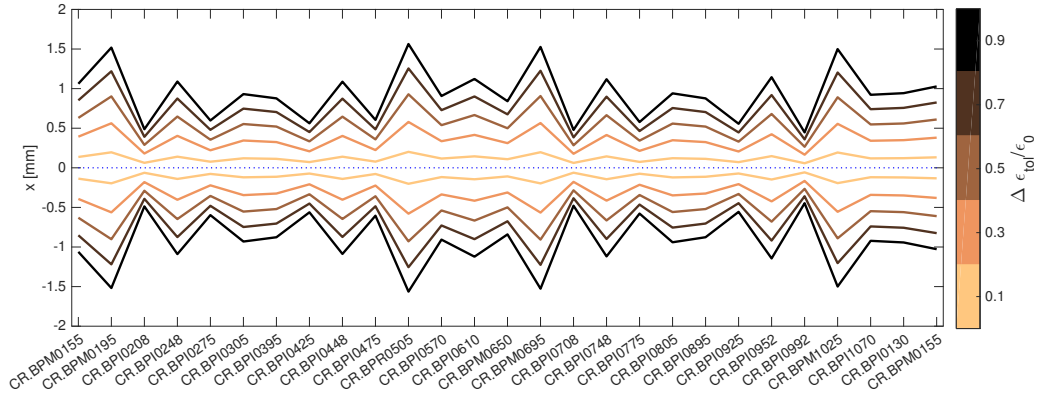
Figure 4.12: Representation in normalised phase space of a factor-4 recombined beam after an injection orbit (a) or optics (b) error. The black circles/ellipses B_1 , B_2 , B_3 , B_4 represent the four trains taking part in the recombination, which have respectively done one to four turns in the CR. The dashed-green circle represents the combined beam envelope according to the $\bar{\epsilon}$ definition of emittance. In (b) the central circle represents the matched scenario.

between the un-matched ellipses is maximum. Equations 4.19 and 4.18 apply also to this case. It is not possible to perform a rematching to better enclose all the ellipses. The alternative would be to actually change the tune of the ring to make the effect more favourable: the closer to an integer, the better. However no further investigation in this direction has been conducted for this thesis.

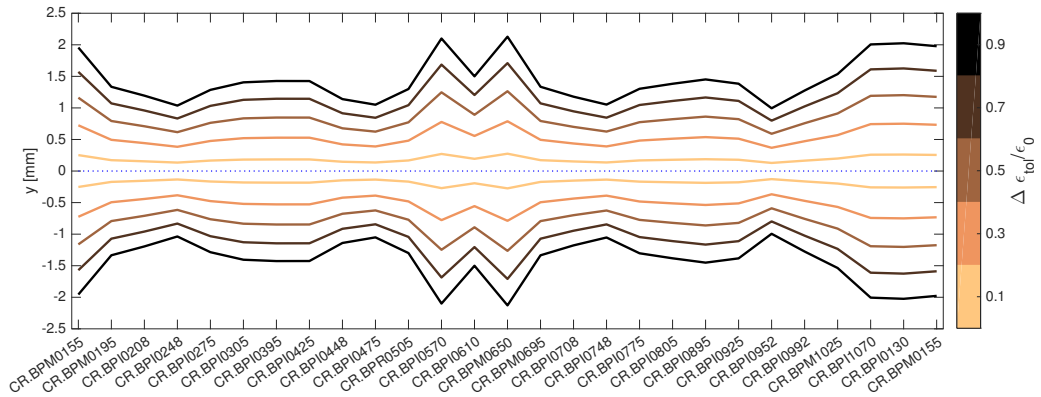
Similar to Figures 4.9(a) and 4.9(b), Figure 4.13 shows the orbit tolerances one has to fulfil at the CR BPMs. Given the tolerated emittance growth ($\Delta\epsilon/\epsilon_0$) in terms of the $\bar{\epsilon}$ definition, the orbit of a beam performing *four* consecutive turns in the ring has to be enclosed, for *all* turns, within the respective corridor. The result is obtained by using Eq. 4.3.

Regarding the transverse optics mismatch case, at CTF3 the first quadrupole scan measurement point after the CR is right at the beginning of the next transfer line (TL2). Depending on the tolerated emittance growth (identified by a different colour) the plots in Figure 4.14 define the domains of the Twiss parameters that a not-recombined beam has to respect irrespectively of the number of turns performed by the beam in the CR. These domains have been generated from Eqs. 4.20 and 4.21, by considering the nominal Twiss parameters that one should expect at this measurement point in TL2.

For the statistical definition of emittance (ϵ_Σ) the description would be more complex due to the larger number of trains. The final result will also heavily depend on the specific optics of the ring. For this reason no detailed calculations are conducted for this case. For the factor-2 recombination the $\bar{\epsilon}$ definition of emittance gives the tighter tolerances (e.g. Figure 4.10), so one could expect the same behaviour also for the factor 4 case.

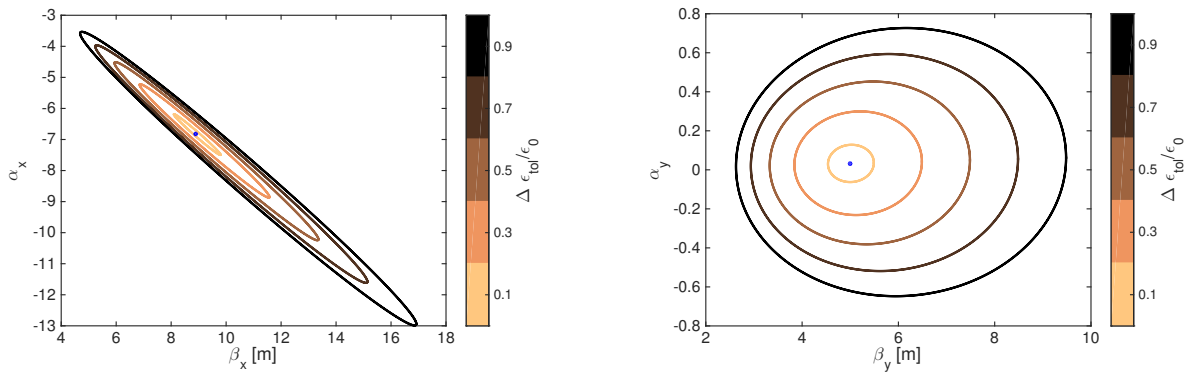


(a) Horizontal orbit.



(b) Vertical orbit.

Figure 4.13: Horizontal (a) and vertical (b) orbit tolerances in the CR for different tolerated geometric emittance growth according to the $\bar{\epsilon}$ definition. On the horizontal axis are the BPMs installed in the CR at CTF3 starting from the injection.



(a) Horizontal - CC.

(b) Vertical - CC.

Figure 4.14: Contour plots of the emittance growth ($\Delta\epsilon_{tol}/\epsilon_0$) as a function of the Twiss parameters (α and β) measured at the first quadrupole scan measurement point in TL2 after any number of turns in the CR. The nominal Twiss parameters expected for a matched beam are defined by the blue dot (i.e. no emittance growth). (a) and (b) are respectively for the horizontal and vertical phase spaces. Tolerances are given with respect to the $\bar{\epsilon}$ emittance definition.

4.3 Energy spread effects

The effects presented so far assume monochromatic beams. The Drive Beam is actually far from being monochromatic, with an energy spread (see Table 1.4) that is typically a factor 10 bigger than any modern storage ring (e.g. in the LHC $\sigma_{\Delta p/p_0} \approx 10^{-4}$ [1]). In Section 4.2.1 the effect of linear dispersion was mentioned, but the complexity and non-linearity of the effect requires detailed numerical simulations of the real lattice to be meaningful. In this chapter the energy effects are simulated by means of MAD-X simulations for the DBRC of CTF3. The goal is to estimate the best recombination performance one should expect in the ideal situation where only single-bunch energy effects are present, i.e. with no orbit or transverse mismatch errors. This should allow one to set a limit on the best recombination performance achievable in the current design of CTF3.

The simulations presented in this chapter have been performed according to the procedure described in Section 4.1. The lattice of the DBRC is assumed to be ideal, with no misalignments or imperfections of the magnetic elements. The initial beam parameter which have been considered are reported in Table 4.1. For simplicity each incoming bunch is assumed to be identical, and perfectly Gaussian in all the 6D phase space. The chosen values for the energy spread and normalised emittances are the typical values observed at CTF3 at the end of the Drive Beam linac. The initial Twiss parameters are chosen to be perfectly matched with the DL and CR closure. For the longest path undertaken by a monochromatic beam the Twiss functions have been reported in Figure 4.2. The simulation strategy adopted foresees to split the non-monochromatic beam into several monochromatic slices which are simulated independently. The granularity of such an energy sampling is also reported in Table 4.1.

Parameter:	Value:
Beam Energy	140 MeV
Energy spread single bunch r.m.s. σ_p	0.6%
Max energy deviation	from -2 to +2%
Energy granularity	0.01% (0.001% DL optimisation)
Twiss β_{x0}	7.854 m
Twiss α_{x0}	0.756
Twiss β_{y0}	13.259 m
Twiss α_{y0}	0.327
Hor. Emittance (Normalised) ϵ_{x0}	60 μm
Vert. Emittance (Normalised) ϵ_{y0}	100 μm
Bunch length r.m.s. σ_{T_0}	1 mm

Table 4.1: Assumed beam parameters at the entrance of the DBRC at CTF3 used for MAD-X and PTC simulations.

At CTF3 the recombination is performed first in the DL (factor 2), then in the CR (factor 4). The train of bunches that arrives first in the DBRC takes the longest path

(i.e. one turn in the DL, $3^{1/2}$ turns in the CR). The last train takes the shortest path (i.e. $1/2$ turn in CR), such that all the 8 trains of bunches arrive at the end of the DBRC at the same time, i.e. are combined. For each of the 8 incoming trains only one bunch is considered to be representative of the full train. The simulated CTF3 DBRC starts from the entrance of the DL injection small bending (called CT.BHD0490) and ends at the entrance of the extraction septum of the CR (called CC.SHD0110). Figure 4.15 shows the outcome of the first full recombination simulation of the CTF3 DBRC. The area of each ellipse in Figure 4.15 is equal to $9\epsilon_0\pi$, i.e. such that it contains most of the mono-chromatic bunch slice that it represents. By hypothesis the size of each ellipse is preserved along the whole lattice, independent of the path taken. In the y - p_y phase space (Figure 4.15(b)) only chromatic effects are visible, i.e. the ellipses representing off-energy particles are deformed with respect to the on-energy one. No dispersion effects are visible because of the ideal design simulated: if no vertical bending magnets are present in a lattice, then no dispersion can be generated, at any order. In reality parasite dispersion is always generated by misalignments and a non-zero incoming orbit. In this work such effects are not considered. In the x - p_x phase space, (Figure 4.15(a)) the scenario is very different. The energy tails separate from the core in a highly non-linear way. Distortions of the ellipses due to chromaticity are also visible, but this is a less pronounced effect.

Each ellipse in Figure 4.15 is associated with a covariance matrix, and all the covariance matrices can be merged, so as to form the total covariance matrix representing the combined beam. From the total covariance it is then possible to extract the statistical emittance of the combined beam⁵. The emittance increase with respect to the initial one (Table 4.1) turns out to be $\Delta\epsilon_x \approx 233\%$; $\Delta\epsilon_y \approx 2\%$. The same result can be obtained by populating the ellipses with particles according to the beam-energy distribution. In all the simulations presented in this work the typical amount of particles generated per bunch is about 30000, which leads to very few particles in the off-energy tails, and most of the particles being generated in the energy core (Figure 4.15). The histograms reported on the axis of each plot in Figure 4.15 help in analysing the result obtained. Clearly, in the horizontal phase space the beam is far from being Gaussian. This explains why the statistical emittance is over-estimating the beam size (see the dashed-black profiles in Figure 4.15(a)), which is better represented by the particles histogram (red profiles). In the vertical phase space all profiles are superimposed: the chromatic effects does not seem to have a significant impact on the total emittance growth.

A numerical estimation of the increased size of the beam can be extracted from the Full Width Half Maximum (FWHM) of the beam profiles. Table 4.2 reports the FWHM of the profiles presented in Figure 4.15.

Even though in Figure 4.15(a) the tails of the distributions are qualitatively small with respect to the core of the beam, if one considers the case where the beam-energy distribution is not centred on the nominal energy, or a case where the energy distribution is not skewed, then the tails might become extremely important, and one would need to be able to transport them later in the machine. Figure 4.16 shows an example in which the mean energy of the

⁵In this section the definition of emittance used to characterise the combined beam will always be the statistical one (ϵ_Σ), unless otherwise specified.

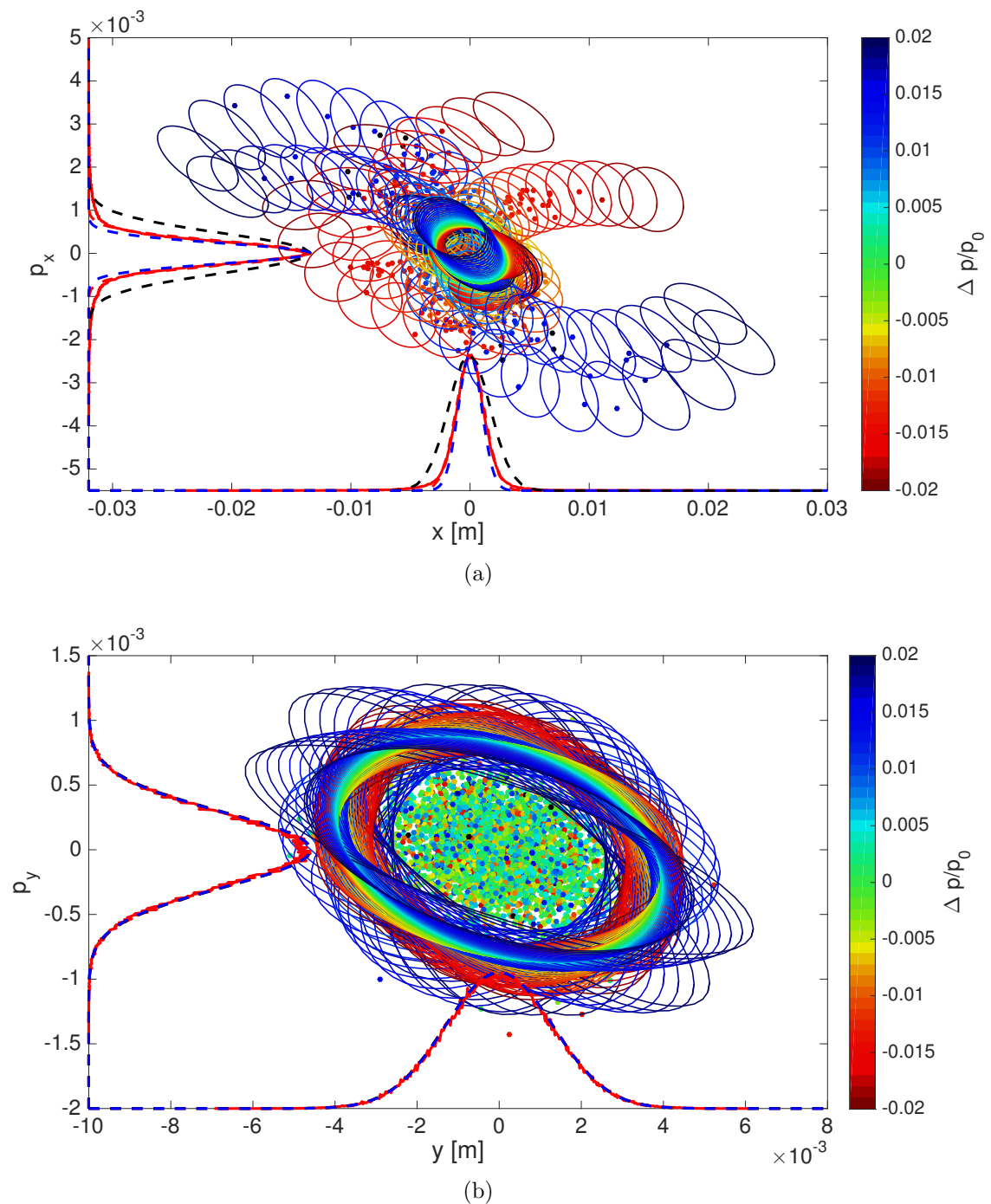


Figure 4.15: Final representation of the x - p_x (a) and y - p_y (b) phase spaces for a factor-8 combined beam at CTF3. Each coloured ellipse represents a monochromatic slice of the full beam, and it is populated by a number of particles according to the Gaussian energy spread of the bunch. The colour scale is given in terms of energy variation with respect to the on-energy particle ($\Delta p/p_0$). The histograms on the axis are meant to guide the analysis: dashed-blue are the ideal Gaussian profiles of a monochromatic recombination; solid-red are the histograms of the generated particles, which are fitted by a dashed-red Gaussian; dashed-black are Gaussian profiles of a hypothetical recombined beam whose emittance is equal to the total statistical emittance (ϵ_Σ). Histograms might be overlapping. Simulations have been performed by means of calls of the MAD-X TWISS function.

	Nominal	from Gaussian fit	from ϵ_Σ
x [mm]	2.31	2.75	4.16
p_x [10^{-3}]	0.55	0.65	1.08
y [mm]	3.09	3.10	3.09
p_y [10^{-3}]	0.68	0.69	0.68

Table 4.2: Comparison of the nominal FWHM of the combined beam profiles; the Gaussian fit of the generated particles and a hypothetical Gaussian associated with the computed statistical emittance.

	Bunch #							
	1	2	3	4	5	6	7	8
$\Delta\epsilon_x$ [%]	440	23	486	50	279	2	336	8
$\Delta\epsilon_y$ [%]	2	1	2	< 1	2	1	1	< 1

Table 4.3: Statistical emittance growth for each bunch representative of a different path in the DBRC of CTF3 during the factor-8 recombination. The values are computed by merging the covariance matrices associated with the ellipses in Figure 4.17, which have been obtained by means of MAD-X simulations.

beam is shifted by 0.5%, which is the order of magnitude of a typical error while setting up the machine or due to beam energy drifts. In this case the statistical emittance growth is 542% in the horizontal plane, while it stays confined to about 3% in the vertical plane. The FWHM of the particles histogram generated in Figure 4.16 is also slightly increased to about 2.85 mm in x and 0.70×10^{-3} in p_x , however the biggest effect is visible in the tails which increase their weight in the continuous-red profile of Figure 4.16.

In general, it might not be too important to be able to transport the tails down to the decelerator. The tails could even be cleaned on purpose by means of a system of collimators. However this might compromise the total charge stability delivered by the DBRC to the following experimental area, and hence the efficiency of the power production.

In order to better understand the source of the tails clearly visible in Figure 4.15(a), it is convenient to show independently the phase space of the 8 representative bunches that take part in the factor-8 recombination. Figure 4.17 shows the final phase-space distribution of each bunch. In this case the ellipses are not populated with particles for ease of viewing. From Figure 4.17 it is clear that the bunches that get delayed in the DL (odd bunches) perform worse than the bunches bypassing the DL (even bunches). Table 4.3 shows the statistical emittance growth for the 8 bunches at the end of the recombination.

One should also consider the evolution of the emittance along the path followed by the bunch in the DBRC. Clearly one would expect higher transverse emittance at the locations where the nominal dispersion is non-zero. According to the nominal design of the DBRC (Figure 4.2) the linear dispersion is higher in the DL, in particular at the location of the quadrupole magnet CD.QDF0460. There the dispersion is by design about $D_x = 1.61$ m

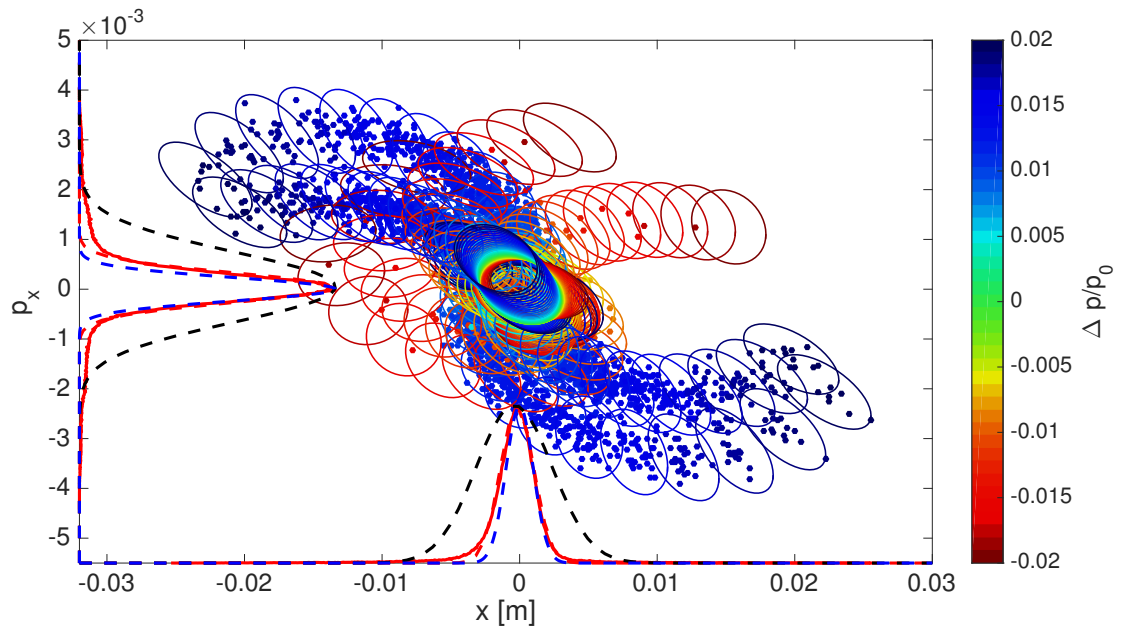


Figure 4.16: Final representation of the x - p_x phase space for a factor 8 combined beam at CTF3. In this case the mean energy of the beam is shifted by +0.5% with respect to the nominal. Each coloured ellipse represents a monochromatic slice of the full beam, and it is populated by a number of particles according to the Gaussian energy spread of the bunch. The colour scale is given in terms of energy variation with respect to the on-energy particle ($\Delta p/p_0$). The histograms on the axis are meant to guide the analysis: dashed-blue are the ideal Gaussian profiles of a monochromatic recombination; solid-red are the histograms of the generated particles, which are fitted by a dashed-red Gaussian; dashed-black are Gaussian profiles of a hypothetical recombined beam whose emittance is equal to the total statistical emittance (ϵ_Σ). Histograms might be overlapping. Simulations have been performed by means of calls of the MAD-X TWISS function.

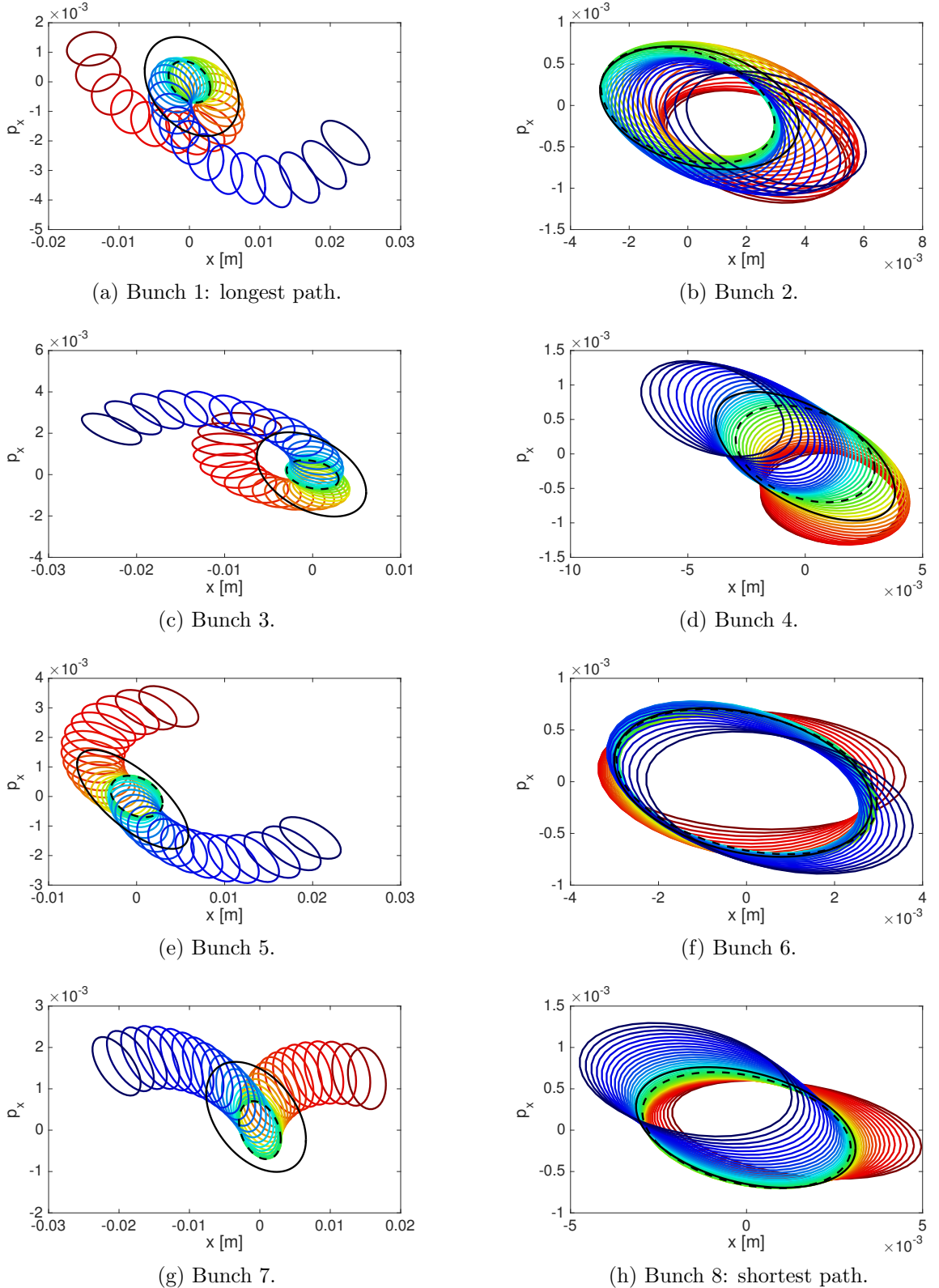


Figure 4.17: Final x - p_x phase space of 8 bunches, each representative of a different path in the DBRC at CTF3 for a factor-8 recombination. Each ellipse represents a mono-chromatic slice of the bunch. The colour code represents the energy offset with respect to the nominal energy (i.e. $\Delta p/p_0$): the scale is from -2% (red) up to +2% (blue) with granularity of 0.1%. The area of each ellipse is constant for all the plots, and it is equal to $9\epsilon_0\pi$, i.e. it contains 99.7% of the particles that is meant to represent. The dashed-black ellipse represents the ideal monochromatic and on energy bunch, which is identical for all the plots. The solid-black ellipse represents a hypothetical Gaussian beam whose emittance is equal to the statistical emittance of the weighted sum of all the slices.

and $D'_x = -0.56$. Figure 4.18 shows the horizontal phase space at that location by means of the different ellipses representing different mono-chromatic slices of a hypothetical bunch. In Figure 4.18(a) it is evident that the total emittance of the beam, represented by the solid-

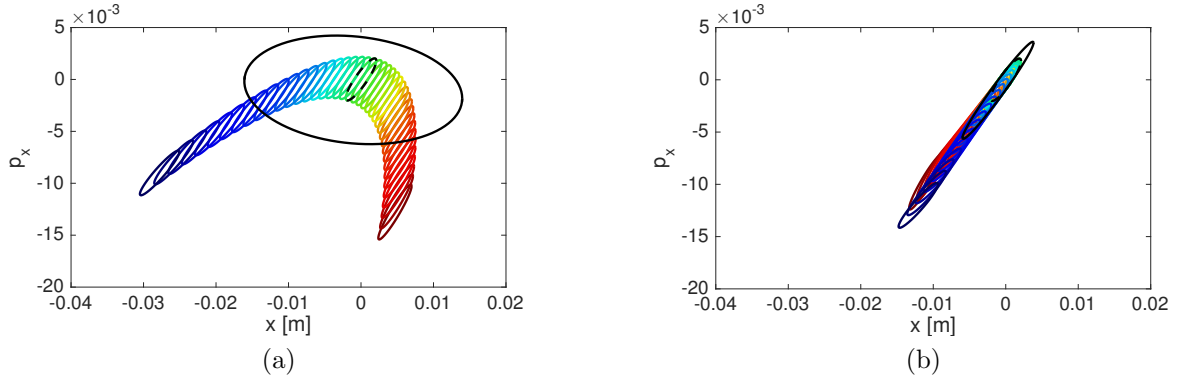
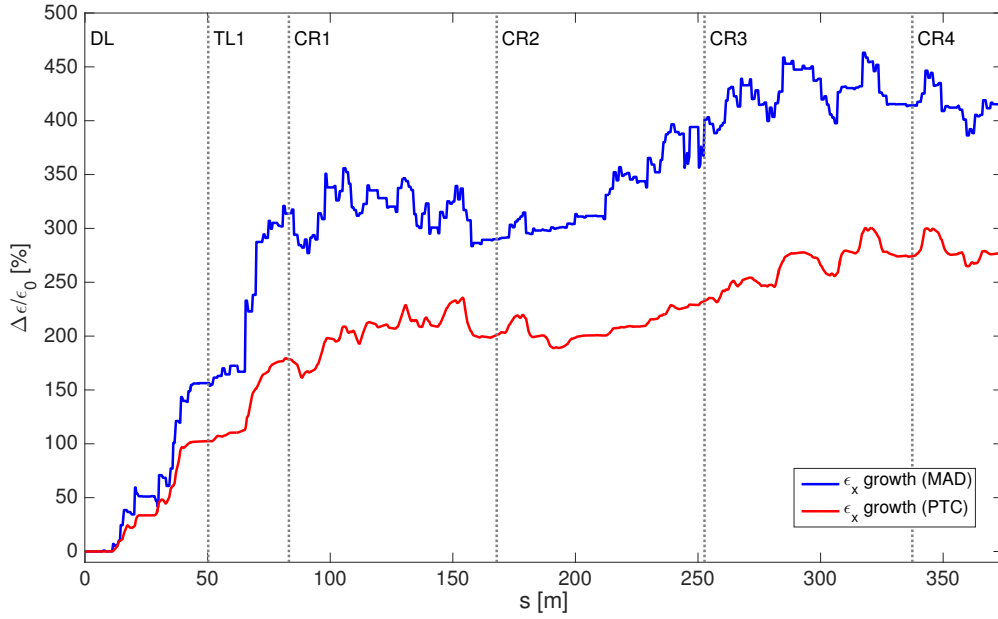


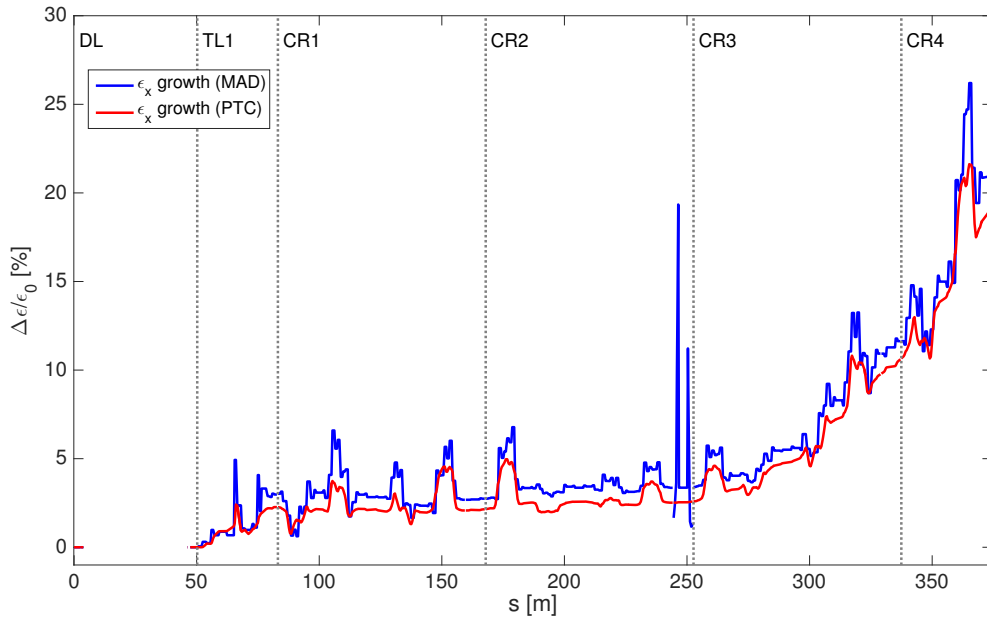
Figure 4.18: Representation of the x - p_x phase space at the entrance of quadrupole CD.QDF0460. Each ellipse represents a mono-chromatic slice of a bunch, whose momentum goes from -2% (red) up to $+2\%$ (blue). The dashed-black ellipse represents the ideal mono-chromatic and on-energy slice, which is identical for all the plots. The solid-black ellipse represents a hypothetical Gaussian beam whose emittance is equal to the statistical emittance of the weighted sum of all the slices. In (a) all chromatic, linear and non-linear dispersion effects are visible. In (b) the linear dispersion effect is suppressed.

black ellipse, is due to the separation in phase space of the coloured ellipses representing the different energy slices. In this case the emittance growth one would measure with respect to the mono-chromatic beam is about 3840%. The visible sources of emittance are identified as: linear dispersion, non-linear dispersion and chromaticity. The method used for the simulations allows one to separate the three source: for example it is enough to shape all the ellipses as the nominal one (dashed-black ellipse) in order to “switch off” any chromatic effect. Figure 4.18(b) shows the phase space of the same beam, but removing the design linear dispersion component. If one would consider this case then the emittance growth is only about 140%, and this is only due to the non-linear dispersion and chromatic aberration of the ellipse orientations, i.e. of the Twiss parameters.

For the study presented in this chapter the most meaningful quantity is the emittance growth due to the chromaticity and the non-linear component of the dispersion. Figure 4.19 shows the horizontal emittance growth along the two longest paths of the CTF3 DBRC, i.e. the paths followed by the two bunches representative of the first and second sub-trains which take part in the recombination. The emittance growth is reported both by using the conventional MAD-X code and by using the more advanced PTC_TWISS code. There is a noticeable difference between the two codes, which could be explained by a better treatment of non-linearities in PTC. However no evident explanation has been found at the time of writing. Both simulation codes agree qualitatively showing that the horizontal emittance growth is clearly generated mainly in the DL, Figure 4.19(a). For the bunches that bypass the DL, represented by Figure 4.19(a), a considerable emittance growth arises at the beginning of the third turn. The spikes visible around $s = 250$ m are due to the orbit bump generated by the RF deflector of the CR. Still there is a factor 10 difference between



(a) Bunch 1: longest path



(b) Bunch 2: longest path without DL

Figure 4.19: Horizontal emittance growth along the unfolded DBRC. Figure (a) represent the bunch that follows the longest path, i.e. one turn in DL, single passage in TL1, 3.5 turns in CR. Figure (b) represent the second bunch that bypasses the DL and later follows the same path as the first bunch. The quoted emittance growth is the statistical emittance of a single bunch which has been split into many slices of different energies. The *linear* dispersion component has been suppressed in the calculation of the combined covariance matrix. The simulations have been performed by means of MAD-X TWISS (blue lines), and PTC_TWISS (red lines).

the final emittance growth of the first bunch and the second, suggesting that the DL optics should be examined in more detail.

In a similar way Figure 4.20 represents the vertical emittance growth along the two longest paths. In this case no linear and non-linear dispersion is present by design, so the only visible effect is due to chromatic aberration of the ellipse orientations. Two main features are visible in Figure 4.20(a): the MAD-X simulation shows an emittance increase in the DL, which is then amplified by a sharp jump in TL1. For the bypassing beam, Figure 4.20(b), the jump in TL1 is confirmed, but the PTC_TWISS code shows in general a much weaker effect. Still, for both codes and beams, the emittance growth is much less pronounced than in the horizontal plane.

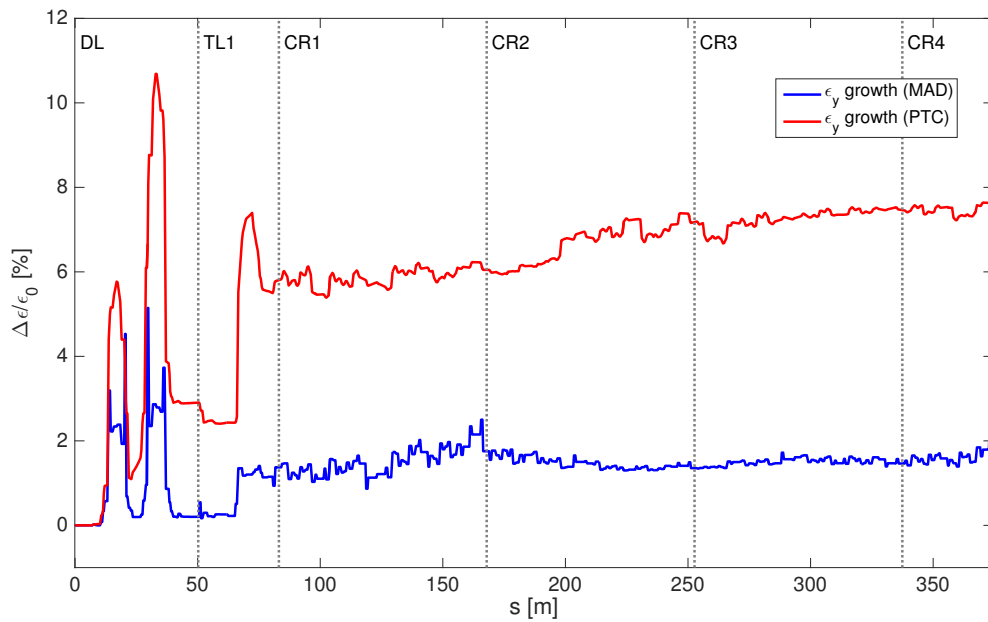
From Figure 4.19 one might think that the high non-linear dispersion might give an effect on the mean beam position along the path. This is shown in Figure 4.21. The dashed lines correspond to an envelope that contains all the particles within $\pm 3\sigma$ of each mono-energetic bunch slice, whose energy is as well within $\pm 3\sigma$ from the nominal energy. This envelope is comparable with the envelope defined by the $\bar{\epsilon}$ definition of emittance⁶ (Section 4.1.1). Given the assumptions of the simulation procedure one can state that *at least* 99.7% of the bunch particles are within the boundaries shown in Figure 4.21. The difference in beam envelope between the first and second bunch is clearly evident. However what is most dangerous is the mean orbit identified by the first bunch (Figure 4.21(a)). In the TL1 transfer line the first bunch exhibits an orbit of a few mm, which is not visible in the bypassing beam (Figure 4.21(b)). From Figure 4.9 one would need to match the orbits of the delayed and bypassing beams within ≈ 1 mm in order not to increase noticeably the emittance of the combined beam. On the other hand, Figure 4.21 shows that the orbit of the two ideal beams might differ by more than that just by considering the offset induced by the non-linear dispersion.

It might be interesting to see what is happening at one of the locations where the average beam position is heavily affected. Eg. at $s \approx 68$ m, the location of BPM CT.BPI0692, the average x-position of the bunch is simulated to be of about 2.5 mm. The horizontal phase space at this location is shown in Figure 4.22. The long asymmetric tails visible in the solid-red histograms of the generated particles justify the offset in mean bunch position at this location. The same information is also visible in Figure 4.21a: in the approximate region $60 < s < 75$ m, where this BPM is installed, the boundaries of the bunch are extremely asymmetric toward negative values as is the phase space presented in Figure 4.22.

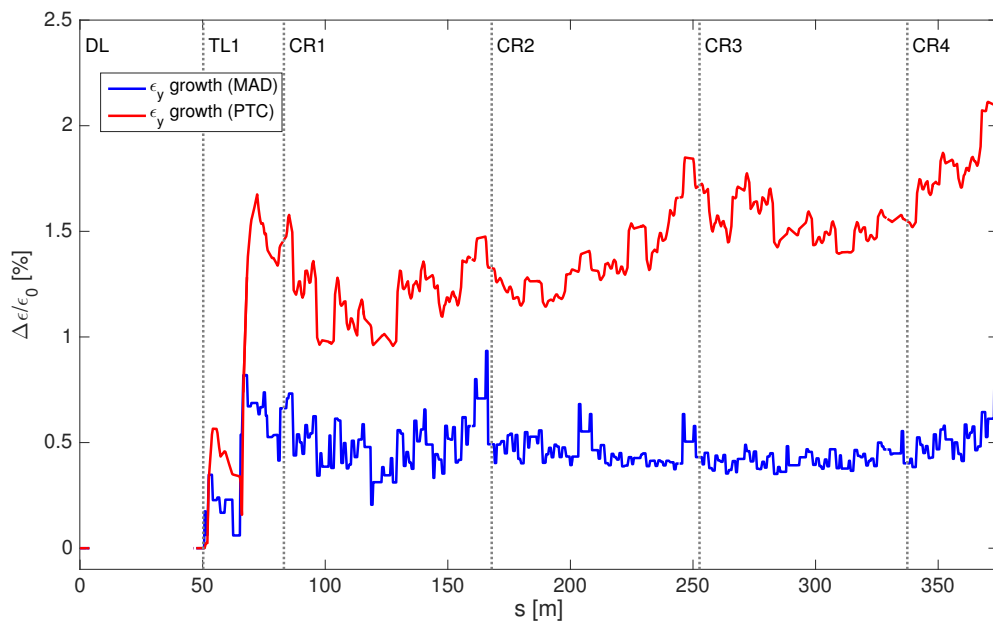
For the vertical plane the mean orbit is expected to be zero since by construction all the energetic slices in which each bunch is divided are all centred on zero and symmetric. However it is interesting to compare the vertical beam envelope along the DBRC between the two longest paths, i.e. for the usual first two bunches representing the Drive Beam recombination. Figure 4.23 shows that the chromatic effects, mainly developed in the DL, lead to a sensible increase of the vertical beam size. This could be a potential issue for obtaining a loss-less transport of the delayed bunches.

Even though it is not of main concern for this thesis, it is interesting to look at the final

⁶With respect to the $\bar{\epsilon}$ here there is no constraint on the actual nominal Twiss function at each location.

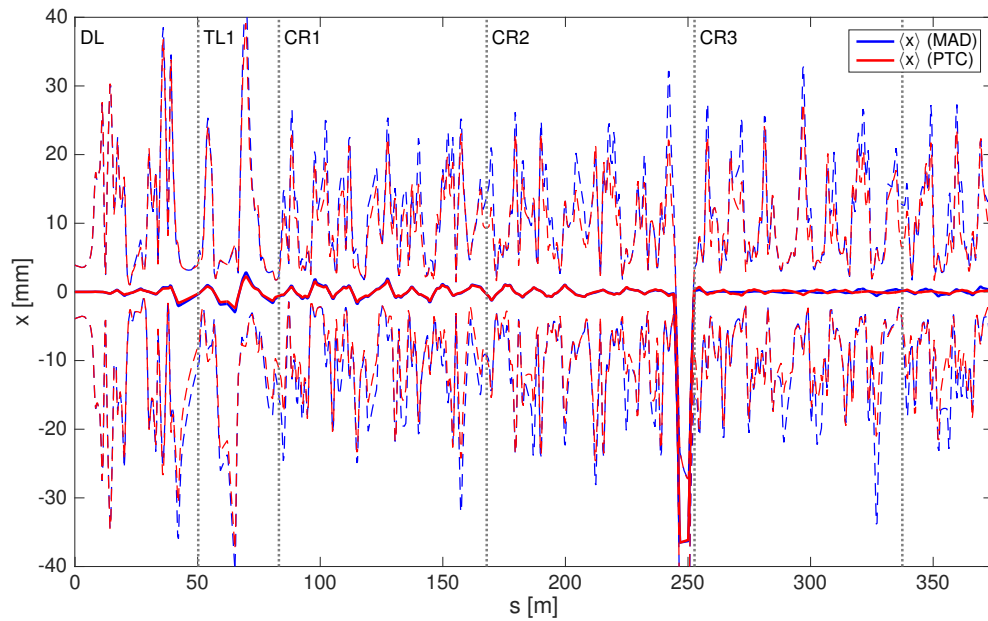


(a) Bunch 1: longest path

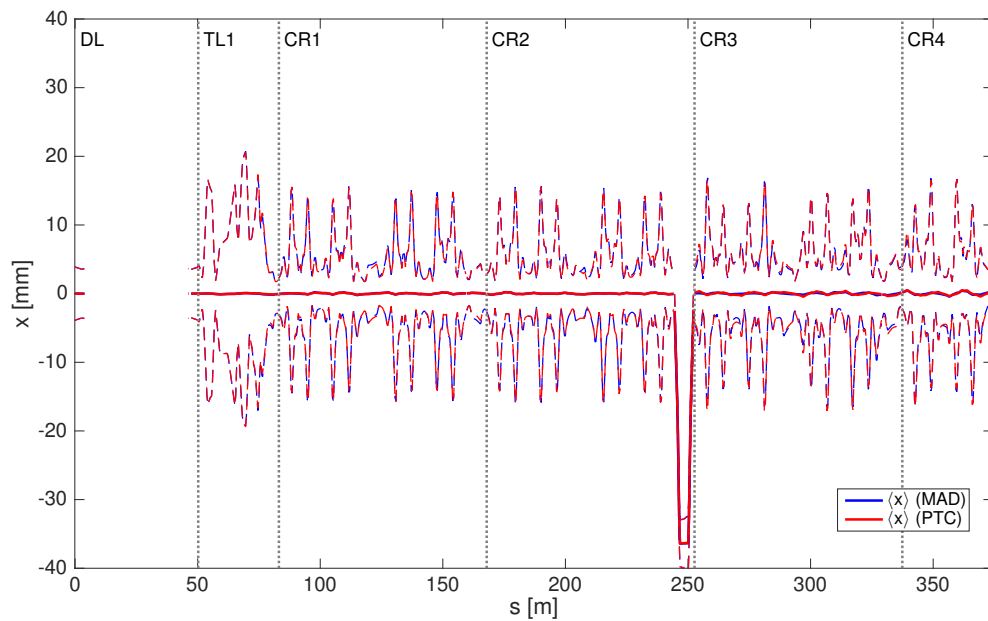


(b) Bunch 2: longest path without DL

Figure 4.20: As Figure 4.19, vertical emittance growth along the unfolded DBRC for the first two longest path, i.e. with (a) or without (b) the single passage in the DL. With respect to Figure 4.19, here the only source of emittance growth is assumed to be the chromaticity.



(a) Bunch 1: longest path



(b) Bunch 2: longest path without DL

Figure 4.21: Mean horizontal orbit and 3σ boundaries of a bunch traveling along the two longest paths in the DBRC at CTF3. The solid lines show the mean bunch position taking into account the non-linear dispersion effect, and assuming the beam parameters of Table 4.1. The dashed lines show the extreme boundaries which contains the $\pm 3\sigma$ core of the bunch both in energy and betatron transverse size, i.e. representing 99.7% of the bunch particles. The boundaries are computed taking into account both linear and non-linear energy effects. Simulations performed with MAD-X TWISS (blue) and PTC_TWISS (red).

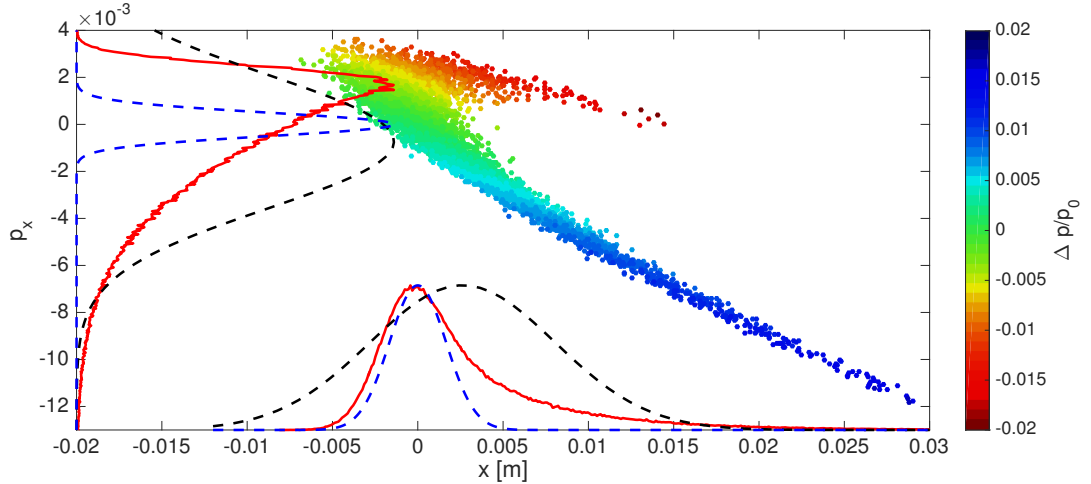


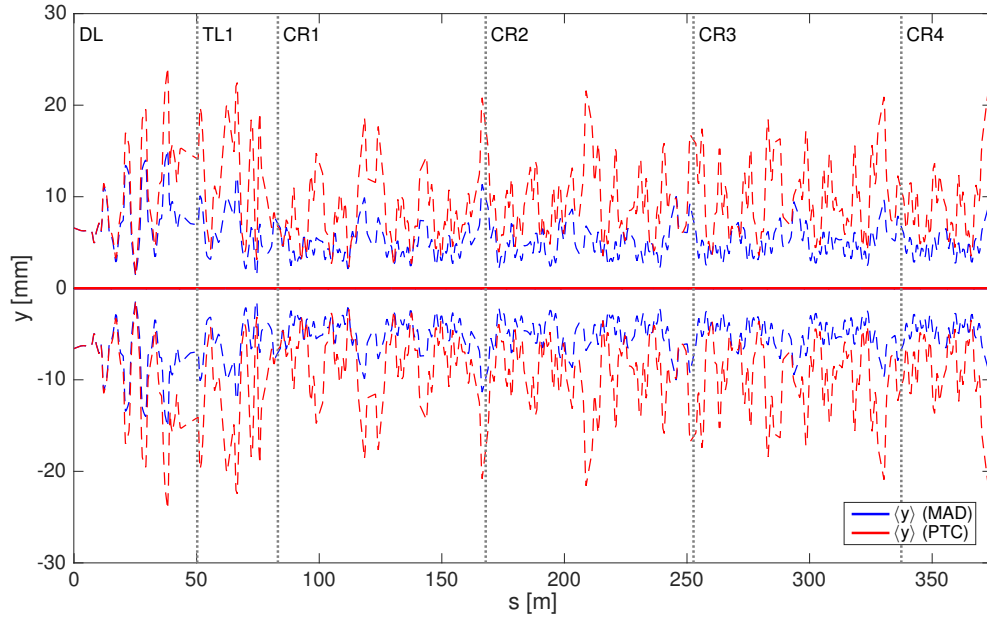
Figure 4.22: x - p_x phase space of a bunch that was delayed in DL and transported up to the CT.BPI0692 BPM location ($s \approx 68$ m). Each point represents a particle whose momentum deviation with respect to the nominal is identified by its colour. The profiles reported on the axis are: the nominal, monochromatic, Gaussian beam (dashed-blue), which are clearly centred on 0; the 500000 generated particles (solid-red); the hypothetical Gaussian beam whose emittance is defined by the statistical emittance ϵ_Σ of all the energy slices (dashed-black).

longitudinal distribution of the recombined beam, which is reported in Figure 4.24. Note that the non linear effects seem to affect considerably the final beam form factor, which might affect the RF power production in the later experimental area. The simulation with PTC_TWISS (Figure 4.24(b)) shows a much weaker effect than the one performed with the conventional MAD-X TWISS function (Figure 4.24(a)). The discrepancy between the two codes is not yet fully understood. Following a discussion with the MAD-X developers [67], it seems that the pure MAD-X TWISS function might be less accurate on the longitudinal plane with respect to the PTC_TWISS function. However a further investigation is needed. Also for this reason the simulations in this chapter have been performed with both codes, and, where necessary, both results are quoted. The bunch lengthening is reported for the different bunches and different codes in Table 4.4.

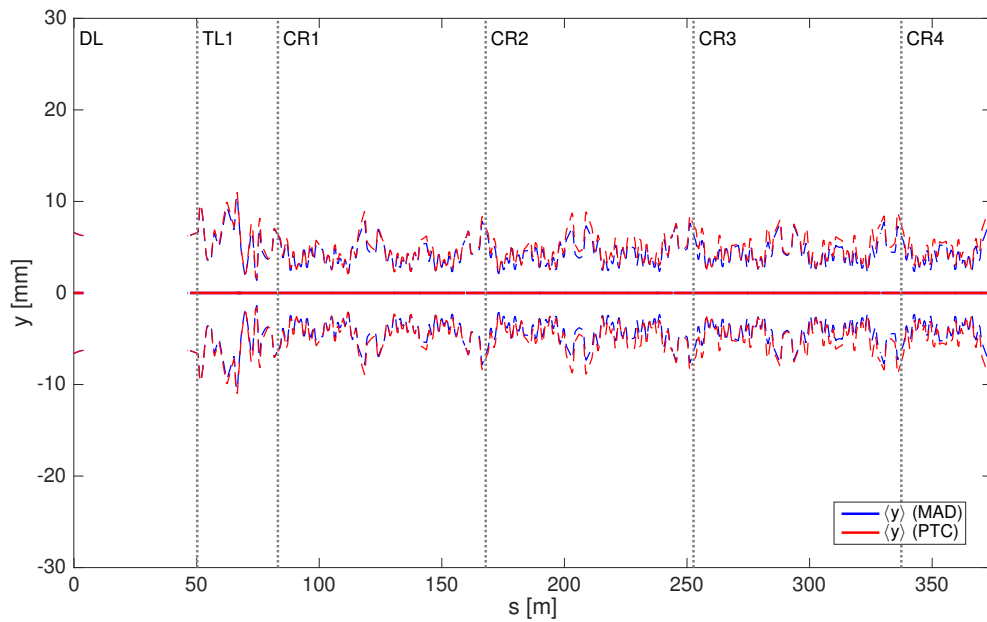
	Bunch #							
	1	2	3	4	5	6	7	8
$\Delta\sigma_t$ [%] (MAD)	995	368	808	252	635	142	455	43
$\Delta\sigma_t$ [%] (PTC)	220	81	175	50	132	23	91	6

Table 4.4: Bunch lengthening ($\sigma_t = \sqrt{\sigma_{tt}}$) at the end of the DBRC for the different beam paths undertaken during the recombination. The reported values are the square root of variances of the t coordinate in phase space with respect to the ideal initial bunch length. The values have been computed by means of MAD-X TWISS and PTC_TWISS simulations.

Another figure of merit of the longitudinal lengthening of a bunch is the mean t coordinate as it evolves along the DBRC for the two longest paths. This is presented in Figure 4.25.

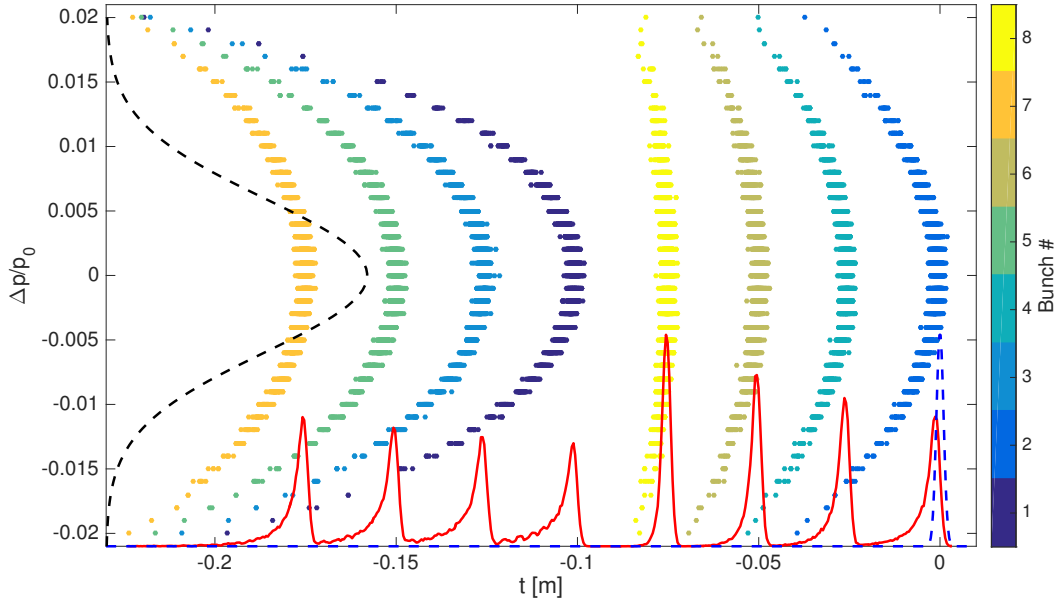


(a) Bunch 1: longest path

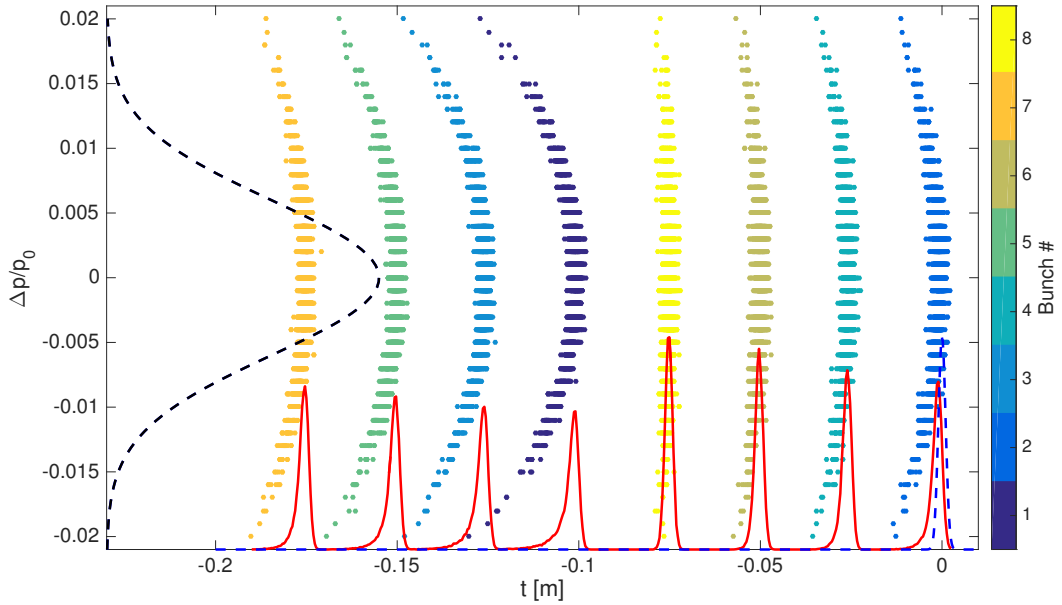


(b) Bunch 2: longest path without DL

Figure 4.23: As Figure 4.21, mean vertical orbit and 3σ boundaries of a bunch traveling along the two longest paths in the DBRC at CTF3.



(a) MAD-X



(b) PTC_TWISS

Figure 4.24: Representation of T-PT phase space at end of DBRC at CTF3 for an ideal 12 GHz recombined beam. Each point represents a single particle, which has been generated according to the relative covariance matrix transported up to the end of the DBRC. The colour code represents the different bunches taking part in the recombination, being the first one to the left the bunch that has performed the longest path in the DBRC. The simulations have been performed by means of the MAD-X TWISS function in Figure (a), while PTC_TWISS was used in Figure (b). The discrete sampling in energy reveals the energy resolution used for the simulations performed in this section (Table 4.1). The dashed-black profile on the vertical axis is the assumed energy distribution of the beam.

The dashed lines correspond to the boundaries of the one sigma core of the bunch, i.e. the minimum length that includes at least one sigma in t of each mono-chromatic slice within one sigma in $\Delta p/p_0$.

The study on the DBRC of CTF3 presented so far can be summarised in the following points:

- For the nominal and ideal set-up, without non-linear corrections (sextupoles), the non-linear dispersion and chromatic effects lead to long tails mainly in the x - p_x and t - $\Delta p/p_0$ phase spaces. If one can afford to cut the tails (e.g. by means of collimators), then this might not be a problem, but one should analyse the beam current stability degradation that this would imply.
- If the beam injected into the DBRC is on average off-energy, then the tails might become highly populated and extremely important. This means that energy drifts could quickly degrade the performance of the DBRC.
- One of the main sources of non-linearities is the DL optics. This should be the first part of the CTF3 DBRC that might be worth further investigation and optimisation.
- For the longitudinal phase space, the strong non-linearities might affect the form factor of the final combined beam, which could induce an efficiency degradation in the later decelerator. However strong discrepancies are noticed between the different codes used. A detailed investigation is necessary to understand which code is more accurate and realistic.

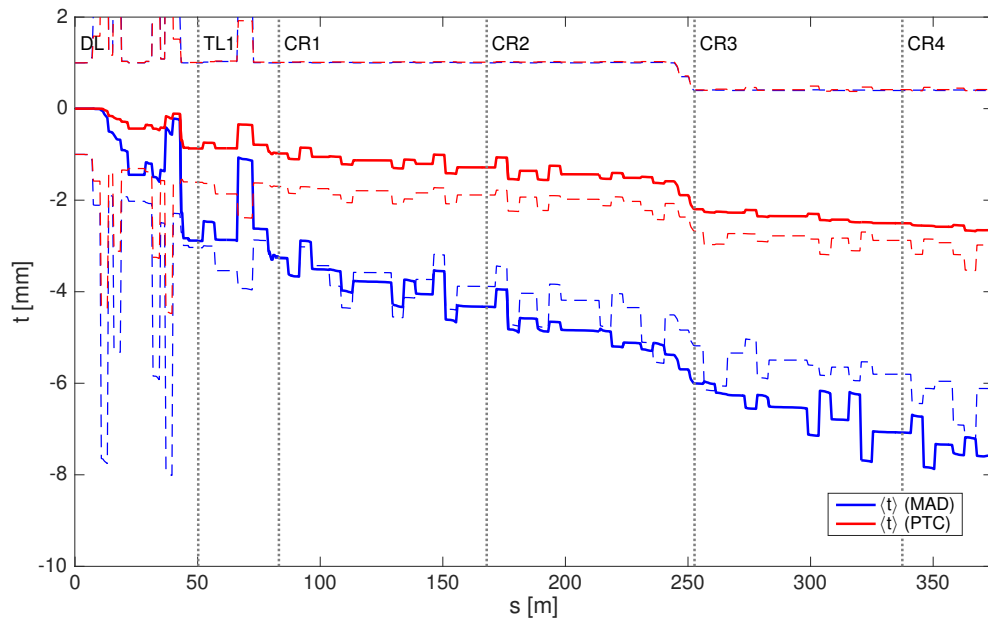
In the following section the DL optics is analysed in more detail, and a possible alternative mitigation of the non-linearities is proposed.

4.4 Possible cure of non-linear dispersion in DL

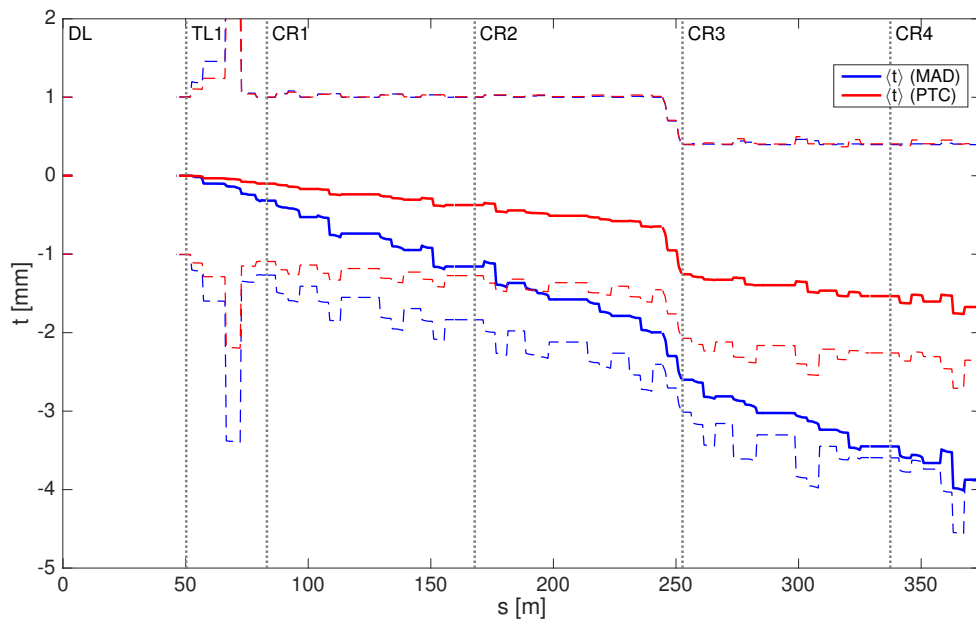
Two possible solutions that mitigate the emittance growth in the DL are presented here. The following simulations are obtained by using the same strategy as in the previous section and described in Section 4.1. Also the initial beam parameters are supposed to be the same, i.e. as in Table 4.1. Here on the other hand a higher beam-energy resolution is used: the simulations have been performed with a granularity of 0.01% instead of 0.1% in beam-momentum deviation. Moreover some of the simulations have been cross-checked by means of particle tracking with PTC_TRACK.

Figure 4.26 shows the nominal optics of the DL. The DL line is considered starting from the entrance of the injection bending magnet CT.BHD0490, which is placed just before the injection, up to the end of the dipole CT.BHD0510 after the extraction. At this last location BPM CT.BPM0515 is also installed⁷. An RF deflector is used to inject and to extract the bunches from the DL. The bunches that bypass the DL during the Drive Beam

⁷This location will be used as the reference point for most of the plots in this section.



(a) Bunch 1: longest path



(b) Bunch 2: longest path without DL

Figure 4.25: Average longitudinal displacement of the bunch vs. s for the two longest paths in the DBRC, with respect to the ideal particle. The dashed boundaries represents the $\pm 1\sigma$ core of the bunch, with respect both to energy and to the monochromatic Gaussian bunch length.

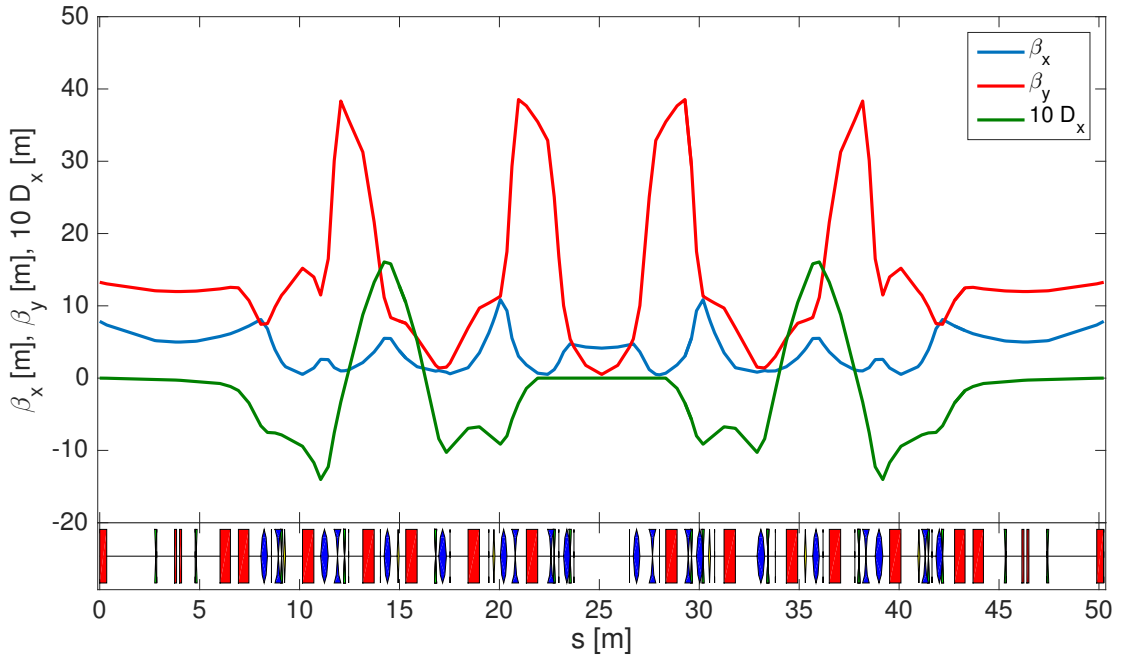


Figure 4.26: Nominal optics of the DL. On the x axis is the longitudinal coordinate along one turn in the DL. The blue and red curves are respectively the horizontal and the vertical Twiss β functions. The dispersion function in green is scaled by a factor 10. At the bottom of the plot is a schematic of the lattice elements: the red squares represent the bending magnets, while the quadrupoles are shown in blue.

recombination pass the RF deflector only once. The bunches that are instead delayed in the DL, i.e. following the optics of Figure 4.26, pass the RF deflector twice: once at injection ($s = 4$ m) and once at extraction ($s = 46$ m)⁸. In the ideal set-up the DL optics must be closed at the centre of the RF deflectors, i.e. here the beta functions need to be equal and with the same derivative. The quadrupoles installed in the DL are powered in series between the two halves of the ring. This means that the only possible closed solution of the ring must be symmetric, as it is in Figure 4.26. In the middle of the DL (i.e. around $s = 25$ m) the long empty section is in reality filled with a wiggler magnet. This is meant to be used to adjust the length of the DL at the picosecond level so as to ensure a correct recombination in the longitudinal direction between the delayed and bypassing bunches. For the nominal optics the wiggler magnet is supposed to be transparent. In practice possible distortions of the transverse optics can arise when the wiggler is in use. However the quadrupoles at the sides of the wiggler can be tuned to cancel these distortions.

The linear-dispersion function in Figure 4.26 is obviously non-zero inside the DL, but the optics is tuned so that no dispersion leaks outside the ring. However Figure 4.27 shows that the non-linear dispersion is significantly different from zero.

A more global picture of the energy effects is visible in Figure 4.28, which has been generated using the same technique and conventions used in Figure 4.17⁹. Figure 4.28 shows

⁸Recall that the DL is supposed to delay 140 ns-long sub-trains of bunches, which at the speed of light gives about 42 m.

⁹The same kind of phase-space representations will be shown in the following sections.

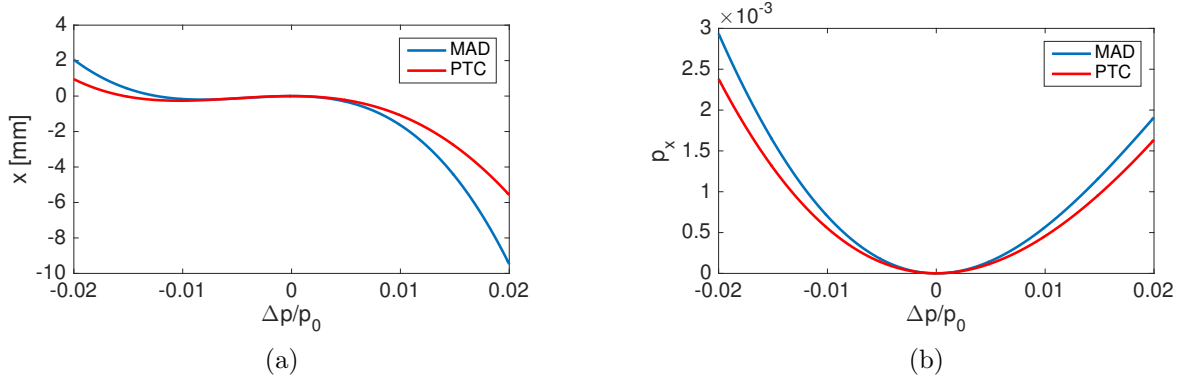


Figure 4.27: Transverse x position (a) and normalised transverse momentum p_x (b) as a function of the momentum deviation of a particle at BPM CT.BPM0515 after a single passage in the DL with nominal optics. The blue and red traces are obtained by means of MAD-X TWISS and PTC_TWISS simulations respectively.

the phase-space ellipses of many monochromatic slices of the beam after a single passage in the DL with the optics presented in Figure 4.26. As already seen in the previous section for the fully recombined beam, the chromatic aberration of the ellipses seems to be more pronounced in the vertical plane (b), while the separation of the different ellipses representing different energies is the dominant effect in the horizontal plane (a), and it corresponds to the non-linear dispersion of Figure 4.27. Using the same assumption on the initial beam

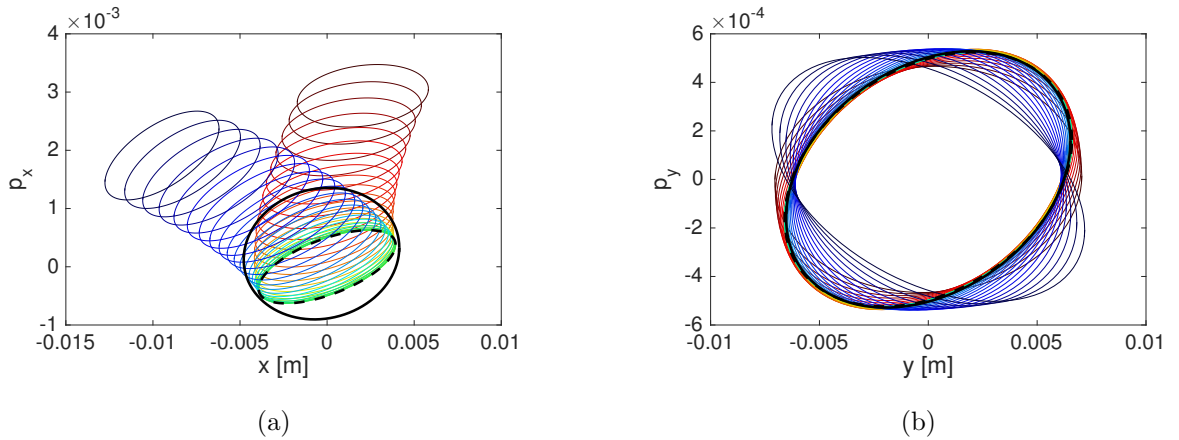


Figure 4.28: Horizontal (a) and vertical (b) phase spaces at BPM CT.BPM0515 of a beam passing once into the DL of CTF3 with nominal optics. Each coloured ellipse represents a mono-chromatic slice of an ideal Gaussian beam. The colour code is from -2% (red) up to +2% (blue) in momentum deviation ($\Delta p/p_0$) with granularity of 0.1%. The area of each ellipse is $9\epsilon_0$, where ϵ_0 is the assumed initial emittance of the beam (Table 4.1), which is different for the two planes. The dashed-black ellipse represents the ideal monochromatic on-energy slice. The solid-black ellipse represents a hypothetical Gaussian beam whose emittance is equal to the statistical emittance of the weighted sum of all the slices. Simulations have been performed by means of MAD-X TWISS.

parameters as in the previous section (summarised in Table 4.1), the statistical emittance growth is 155% (horizontal) and 1% (vertical). If this emittance is associated with a Gaussian beam, then one would obtain in the transverse phase spaces the solid-black ellipses shown

in Figure 4.28.

Figure 4.29 is a detailed view of the first part of Figures 4.19(a) and 4.20(a). The focusing quadrupole installed at $s \approx 11$ m is used to invert the dispersion that at this location is about -1.5 m (see Figure 4.26). The inversion of the dispersion requires a strong quadrupole strength, so the combination of high dispersion and strong quadrupole develops non-linear dispersion which is not compensated afterwards. The result is the increase of the non-linear dispersion and so the horizontal emittance growth, which is visible in Figure 4.29 along the DL. In the vertical plane the emittance growth is marginal.

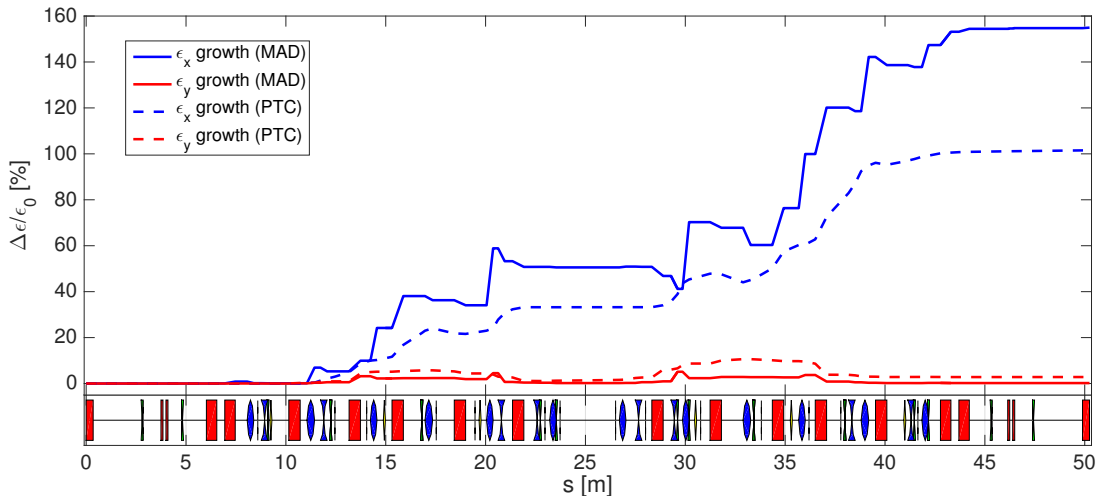


Figure 4.29: Statistical emittance growth along the DL with nominal optics. In blue is the horizontal emittance, in red the vertical. The linear dispersion component has been subtracted in the horizontal plane while it is naturally not present in the vertical one. Solid and dashed lines have been produced respectively by means of MAD-X TWISS and PTC TWISS simulations. At the bottom of the plot is a schematic of the lattice elements: the red squares represent the bending magnets, while the quadrupoles are shown in blue.

4.4.1 Design solution using sextupoles

Non-linear correction by means of sextupoles was already studied and integrated in the DL optics in [5] with the intention to mainly correct the longitudinal energy-effects. From an operational point of view the use of sextupoles at CTF3 turned out to be challenging. It is clear that the use of non-linear magnetic element in a transfer line is possible only when the linear effects are perfectly under control. However due to the misalignment of the elements, aperture limitations, and the strong optics of the DL, the operators of CTF3 experienced difficulties in measuring any positive benefit of powering the sextupoles.

A possible non-linear dispersion correction with sextupoles was studied [67]. In the DL 6 sextupoles are installed, but powered in pairs. This identifies 3 families. Figure 4.30 shows the outcome of the correction obtained by means of MAD-X MATCH [43]. The conditions for the matching were to obtain no second-order dispersion (DDX and DDPX) at the exit from the DL. Table 4.5 shows the currents that one would need to apply to each sextupole family

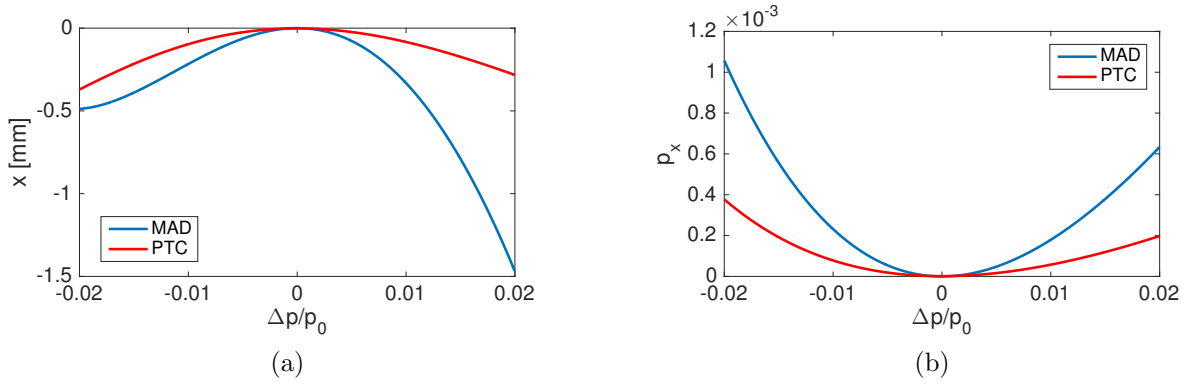


Figure 4.30: Transverse x position (a) and normalised transverse momentum p_x (b) as a function of the momentum deviation of a particle at BPM CT.BPM0515 after a single passage in the DL with nominal optics and sextupoles to correct the final non-linear dispersion. The blue and red traces are obtained respectively by means of MAD-X TWISS and PTC_TWISS simulations.

to obtain the simulated correction assuming a beam energy of 140 MeV. The dispersion

Sextupole Family	Current [A]
CD.XLA0145	-26.86
CD.XVA0215	15.82
CD.XHA0245	66.72

Table 4.5: Sextupoles currents needed for a non-linear dispersion correction in the DL for a beam energy of 140 MeV.

behaviour obtained in Figure 4.30 has to be compared with the case without sextupoles in Figure 4.27. The improvement on the total excursion of the non-linear dispersion is clearly visible.

An attempt to implement this correction in the actual machine was performed [67]. Only two machine set-ups with sextupoles were possible without significant beam losses:

1. First family of sextupoles set to -23 A. Second and third families not powered.
2. First family of sextupoles set to -23 A. Second family set to +9 A. Third family not powered.

The energy of the beam at the time of the test was of 119 MeV. The third sextupole family caused immediate beam loss when powered, hence it was not used. With this partial implementation of the correction a non-conclusive result was obtained by measuring the Twiss parameters of the beam by means of quadrupole scans in the following CRM line (see Figure 1.4). The values obtained are reported in Table 4.6. The reduction of the measured emittance is consistent with the trend one would expect. However the difficulties encountered in the beam transmission and the impossibility to reach the full correction do not allow one

	Set-up:		
	No sext.	1 st sext. on only	1 st and 2 nd sext. on only
ϵ_x [μm]	363.6 ± 18.5	295.3 ± 28.2	232.7 ± 14.3
β_x [m]	4.8 ± 0.6	5.6 ± 1.2	5.8 ± 0.7
α_x	-2.1 ± 0.3	-2.6 ± 0.6	-2.8 ± 0.4

Table 4.6: Twiss parameters measured in CRM line of a beam delayed in DL with different sextupole corrections.

to draw any conclusion on the non-linear dispersion correction. The only conclusion possible is that it was indeed very difficult to make use of any sextupole correction.

A more careful analysis of the complete sextupole correction is shown in Figure 4.31. Once again the phase space at BPM CT.BPM0515 after one passage in the DL is shown. This time the sextupoles in the DL are powered according to Table 4.5. Figure 4.31(b) shows

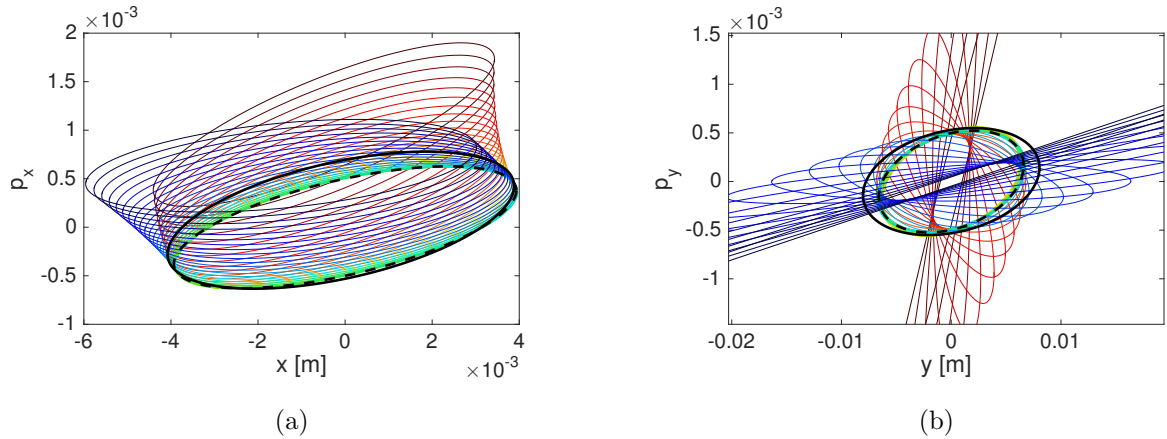


Figure 4.31: Horizontal (a) and vertical (b) phase spaces at BPM CT.BPM0515 of a beam passing once into the DL of CTF3 with nominal optics and sextupoles powered as in Table 4.5. Each coloured ellipse represents a mono-chromatic slice of an ideal Gaussian beam. The colour code is from -2% (red) up to +2% (blue) in momentum deviation ($\Delta p/p_0$) with granularity of 0.1%. The area of each ellipse is $9\epsilon_0$, where ϵ_0 is the assumed initial emittance of the beam (Table 4.1), which is different for the two planes. The dashed-black ellipse represents the ideal monochromatic and on-energy beam. The solid-black ellipse represents a hypothetical Gaussian beam whose emittance is equal to the statistical emittance of the weighted sum of all the slices. Simulations performed by means of MAD-X TWISS.

that the chromatic aberrations of the vertical phase space are much worse than in the case without sextupoles. The statistical emittance growth in the vertical plane is about 30%. A priori this would not be an issue, but the long off-energy tails make this solution impractical. Indeed the sextupole correction found did not have any constraint on the chromaticity of transverse phase spaces. This could be a possible explanation for why it was not possible to reach the full correction, but only a poorly-defined intermediate state.

4.4.2 Optimisation using linear elements

A more practical solution could be to optimise the linear optics, i.e. change the quadrupole currents to find a new solution more forgiving in terms of energy related non-linearities. In order to find such a solution a special MAD-X MATCH [43] was performed. For each iteration of the MAD-X matching procedure the beamline was simulated with 3 independent TWISS calls: one for a beam momentum of -0.5% with respect to the nominal, one for the nominal beam momentum and one for a beam momentum of $+0.5\%$. The condition for the matching was to obtain zero as the final X and PX MAD-X coordinates for all three beam momenta. This procedure is similar to require 0 second-order dispersion (MAD-X variables DDX and $DDPX$) as it was done for finding the sextupole correction. However the method used here is not bounded to second order, and it allows one to control the momentum range for which the correction is needed (in this case 0.5% , which is comparable with the expected beam energy-spread). Moreover one could specify to obtain the same final Twiss parameters for the three momenta, which would be equivalent to reduce the chromatic aberrations. The overall procedure has connections with the more theoretical formalism used in [89, 90, 91] where achromatic drift-quadrupole beam lines are studied in analytical form. The DL optics needs to be isochronous in order to preserve the bunch length. This condition was also preserved during the optimisation.

The outcome of the optimisation is the optics shown in Figure 4.32. This optics gives the final dispersion presented in Figure 4.33. Note that in the middle of the DL ($s \approx 25$ m) the

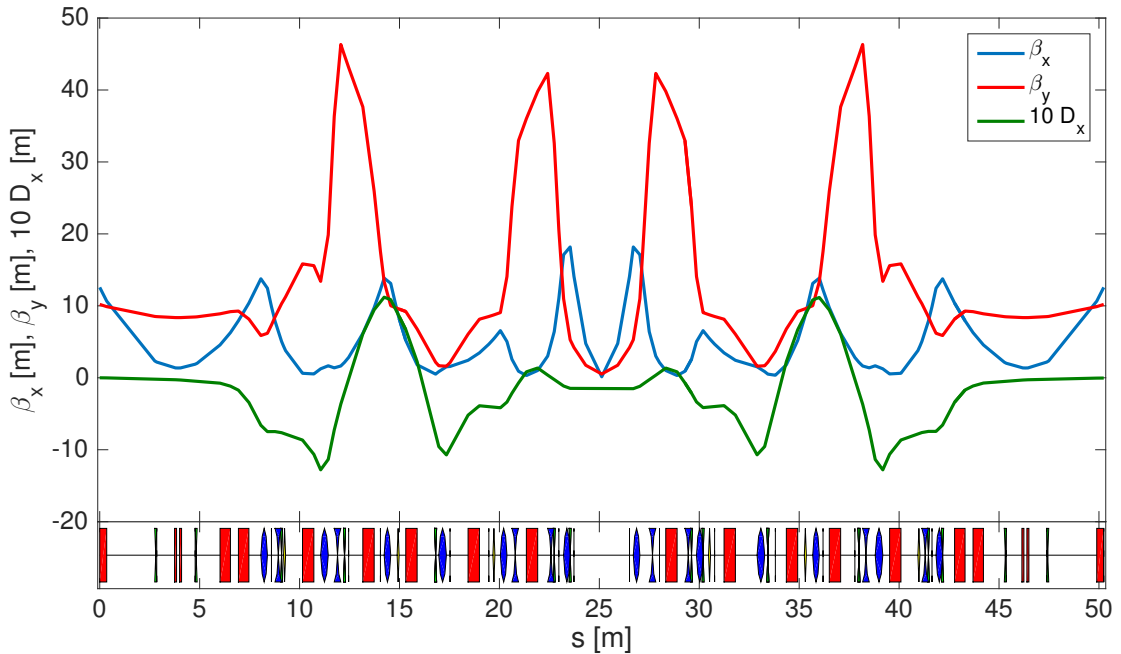


Figure 4.32: Horizontal (blue) and vertical (red) beta functions along the DL of the newly proposed optics. In green is the horizontal dispersion function scaled by a factor 10. Optics computed by means of MAD-X TWISS. At the bottom of the plot is a schematic of the lattice elements: the red squares represent the bending magnets, while the quadrupoles are shown in blue.

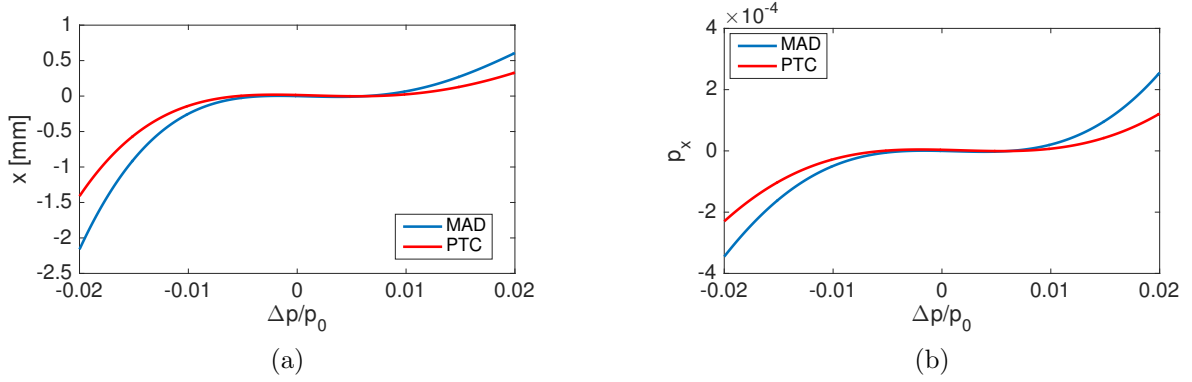


Figure 4.33: Transverse x position (a) and normalised transverse momentum p_x (b) as a function of the momentum deviation of a particle at BPM CT.BPM0515 after a single passage in the DL with the newly proposed optics. The blue and red traces are obtained respectively by means of MAD-X TWISS and PTC_TWISS simulations.

dispersion function is now non zero with respect to the initial optics of Figure 4.26. Moreover the closed optics solution of the ring is different and so it requires different initial Twiss parameters for the incoming beam. A priori both features should not be limiting factors for the new optics: the initial Twiss parameters can be adjusted by properly matching the optics before and after the DL, while there is no a priori limitation in having non zero dispersion in the centre of the DL. However the zero dispersion in the middle of the lattice would be beneficial when the wiggler installed in this area is powered. In that case the possible transverse optics dispersions introduced by the wiggler could be compensated by changing the strength of the quadrupoles in that section. However if the dispersion is non zero in the quadrupoles, as in Figure 4.32, these are constrained to match the dispersion pattern, and cannot be modified anymore. For this reason a further optimisation has been performed assuming to have the wiggler powered at the typical value of 55 A^{10} . In this case a further constraint was imposed to obtain the same initial Twiss parameters as the nominal optics in order to facilitate the implementation of the optics in the machine. Figure 4.34 shows the outcome of the new optimisation. Note that in this case in the middle of the lattice the wiggler magnet is modelled as a series of bending magnets. In this case the initial conditions for the periodic lattice are identical to the nominal case in Figure 4.26.

The final single particle position as a function of its momentum deviation for this new optics is shown in Figure 4.35. Note that the excursion of the non-linear dispersion over the proposed range is considerably reduced with respect to the nominal case (Figure 4.27), and it is comparable with the sextupole correction case (Figure 4.30).

The final phase space of the beam is shown in Figure 4.36 using the usual ellipses representation. Here the statistical emittance growth is computed to be about 2% in the horizontal plane and $< 1\%$ in the vertical one. One can clearly appreciate an improvement in the chromatic aberrations of the final vertical phase space in Figure 4.36(b) with respect to the correction with sextupoles shown in Figure 4.31(b).

¹⁰This is the typical strength used at CTF3 to optimise the longitudinal recombination of delayed and bypassing beams.

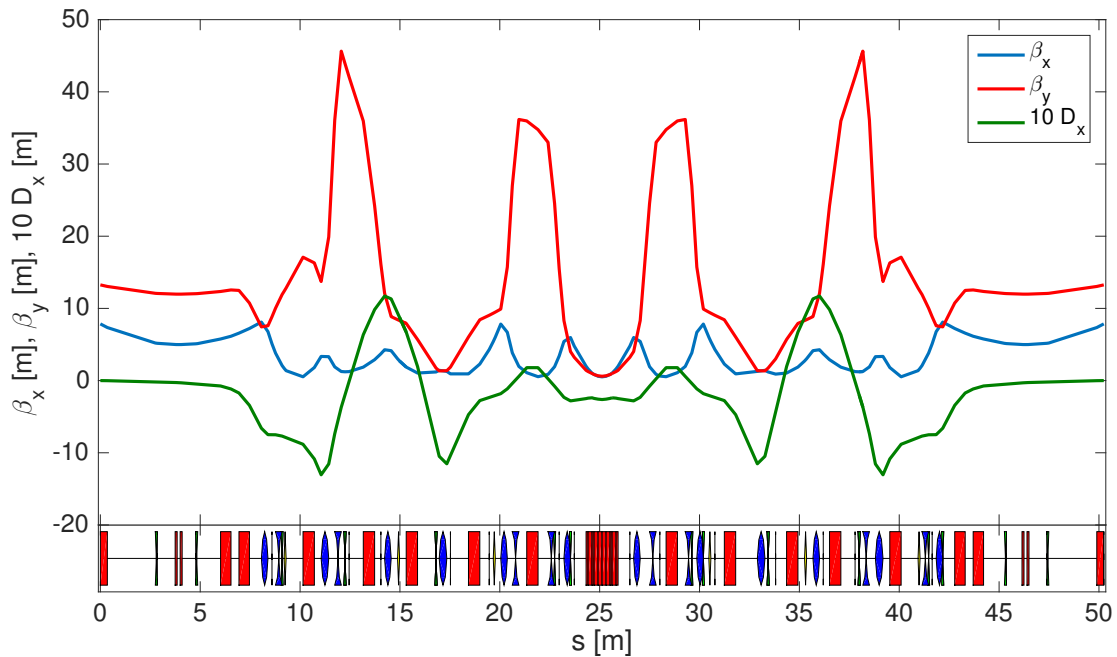


Figure 4.34: Horizontal (blue) and vertical (red) beta functions of a proposed new optics for the DL with wiggler power at 55 A. In green is the horizontal dispersion function scaled by a factor 10. Optics computed by means of MAD-X TWISS. At the bottom of the plot is a schematic of the lattice elements: the red squares represent the bending magnets, while the quadrupoles are shown in blue.

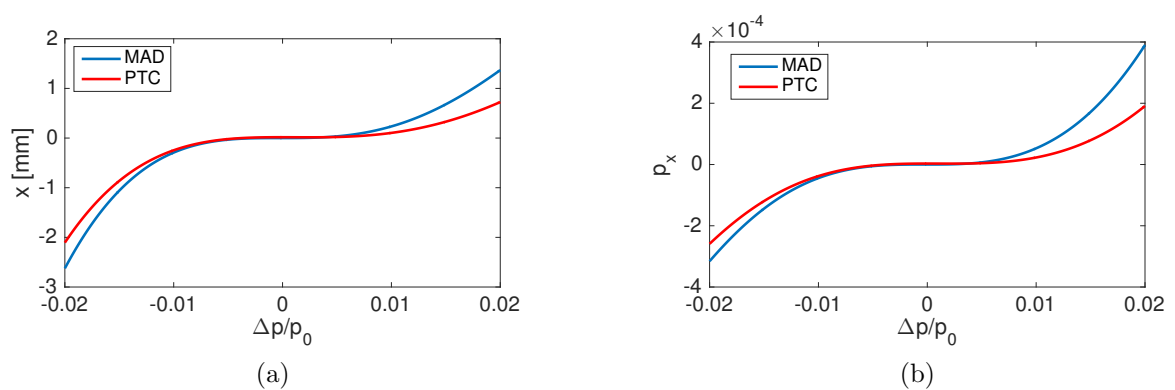


Figure 4.35: Transverse x position (a) and normalised transverse momentum p_x (b) as a function of the momentum deviation of a particle at BPM CT.BPM0515 after a single passage in the DL with the newly proposed optics with DL wiggler powered at 55 A. The blue and red traces are obtained by means of MAD-X TWISS and PTC_TWISS simulations respectively.

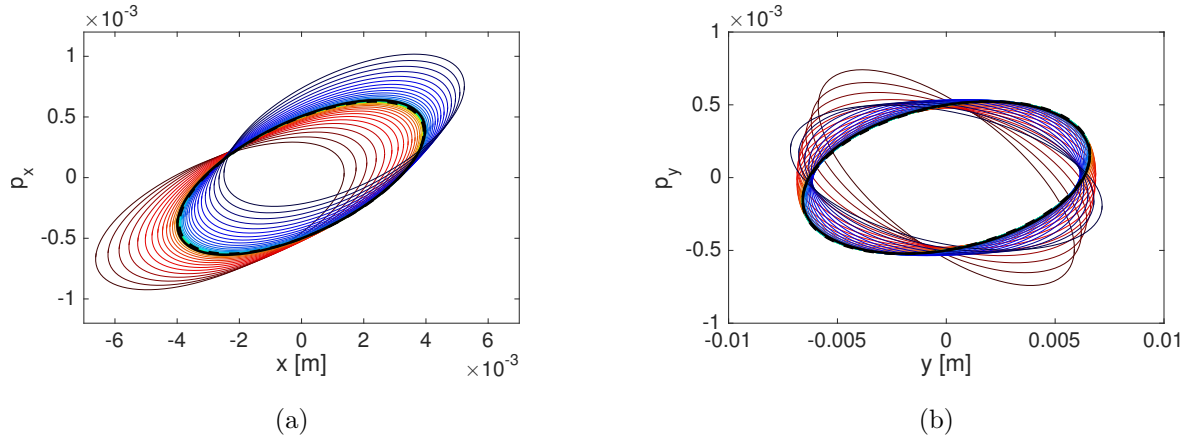


Figure 4.36: Horizontal (a) and vertical (b) phase spaces at BPM CT.BPM0515 of a beam passing once into the DL of CTF3 with newly proposed optics as in Figure 4.34. Each coloured ellipse represents a mono-chromatic slice of an ideal Gaussian beam. The colour code is from -2% (red) up to +2% (blue) in momentum deviation ($\Delta p/p_0$) with granularity of 0.1%. The area of each ellipse is $9\epsilon_0$, where ϵ_0 is the assumed initial emittance of the beam (Table 4.1), which is different for the two planes. Simulations performed by means of MAD-X TWISS.

The statistical emittance growth along the DL with the new optics is visible in Figure 4.37. Compared with the nominal optics case in Figure 4.29, the non-linear dispersion and chromatic effects still grow in the first half of the lattice, but they are then compensated in the second half. Note that the same analysis conducted with PTC_TWISS reveals a significant increase of the vertical emittance, which is not visible for the MAD-X case. This could remain a limitation on the stability of the beam current as in the sextupole correction case. Plot of the phase spaces using the PTC data are shown in Section 4.4.3.

The different quadrupole strengths for the different DL set-ups proposed are shown in Table 4.7. Note that the main difference between the nominal optics and the newly-proposed ones is in the last quadrupole families. These quadrupoles are the ones in the middle of the lattice, i.e. around the wiggler magnet, corresponding to the main difference in the dispersion function with respect to the nominal case.

The use of only linear elements should allow an easier implementation of this correction than the sextupole one: since only linear elements are used the optics does not depend on the orbit of the beam, which is instead the case if sextupoles are powered. The main concern of the new optics is that no quadrupoles are free from dispersion, and so one cannot tune the transverse optics of the DL without affecting dispersion. This could be particularly critical if one needs to change the ring length by changing considerably the strength of the wiggler magnet. For the same reason the new optics requires one to modify the quadrupoles external to the DL in the case of transverse mismatch between the bypassing and delayed bunches. This of course affects both beams and so an effective correction is more difficult to find, while with the nominal optics one could empirically tune the dispersion-free quadrupoles in the middle of the DL lattice without affecting the bypassing beam.

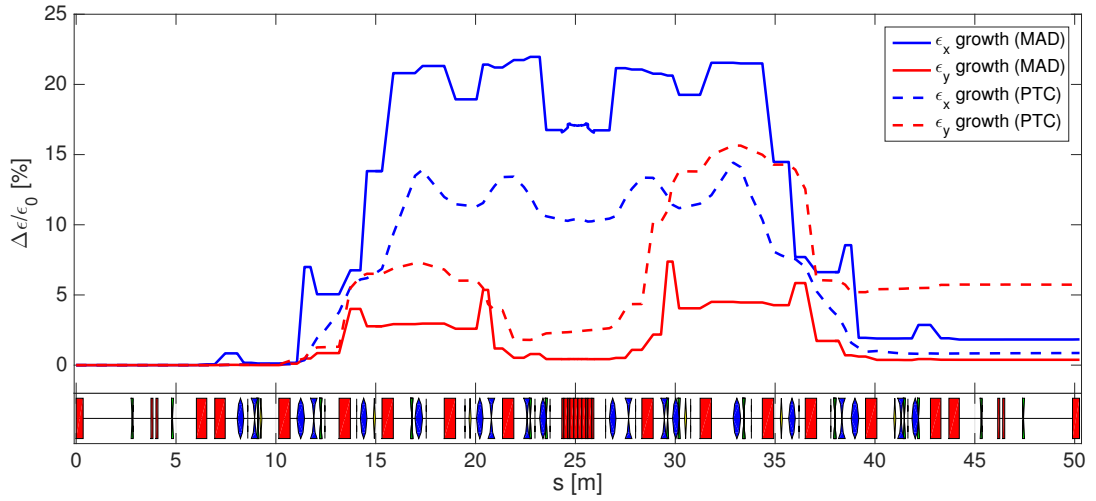


Figure 4.37: Statistical emittance growth along the DL with optimised linear optics. In blue is the horizontal emittance, in red the vertical. The linear dispersion component has been subtracted in the horizontal plane while it is naturally not present in the vertical one. Solid and dashed lines have been produced respectively by means of MAD-X TWISS and PTC TWISS simulations. At the bottom of the plot is a schematic of the lattice elements: the red squares represent the bending magnets, while the quadrupoles are shown in blue.

Quadrupole family	Nominal Optics	New Optics	New Optics with wiggler
CD.QFF0130	63.1	65.7	65.0
CD.QDF0140	15.3	11.8	12.3
CD.QFE0170	64.5	62.3	62.4
CD.QDF0180	78.7	79.1	79.5
CD.QFF0210	69.5	71.2	74.4
CD.QFE0230	62.8	59.6	60.9
CD.QFF0250	113.4	118.0	120.9
CD.QDF0260	76.2	63.3	77.0
CD.QDF0280	56.9	78.3	67.2
CD.QFF0290	85.5	124.5	123.2

Table 4.7: Comparison of the quadrupole currents which are needed to be applied to the DL quadrupole families to obtain the DL optics presented in this section. The currents are given in A for a beam energy of 140 MeV.

4.4.3 Summary on the studied non-linear chromatic effects

In the previous sections two possible corrections of the non-linear dispersion in the DL have been identified. The first requires one to power the sextupoles installed in the DL. The second solution is to slightly modify the optics of the ring in order to compensate the non-linear behaviour but without using sextupoles. Figures 4.38, 4.39 and 4.40 show a summary of the final phase space after one passage in the DL of a beam with initial conditions specified in Table 4.1. The simulations have been performed respectively with MAD-X TWISS, PTC_TWISS and PTC_TRACK, the last one being the conventional method for studying non-linearities. In each figure the final phase space is proposed for the nominal optics, nominal optics with non-linear dispersion correction with sextupoles (see Table 4.5) and new optics with wiggler magnet powered at 55 A (see Table 4.7). The statistical emittance growth that one would expect with the nominal optics and with the two dispersion corrections is summarised in Table 4.8. Note that there is a constant discrepancy between the

Set-up:	Nominal	With sextupole	New optics with wiggler
$\Delta\epsilon_x$ [%] (MAD-X TWISS)	155	24	2
$\Delta\epsilon_x$ [%] (PTC_TWISS)	101	4	< 1
$\Delta\epsilon_x$ [%] (PTC_TRACK)	107 ± 1	16 ± 1	1 ± 1
$\Delta\epsilon_y$ [%] (MAD-X TWISS)	< 1	30	< 1
$\Delta\epsilon_y$ [%] (PTC_TWISS)	3	132	6
$\Delta\epsilon_y$ [%] (PTC_TRACK)	3 ± 1	152 ± 3	7 ± 1

Table 4.8: Statistical emittance growth after one passage in DL for different non-linear dispersion corrections and different simulation methods. The PTC_TRACK value is obtained by tracking 10 Gaussian beams of 30000 particles each and then by computing the mean emittance growth and its standard error.

MAD-X and PTC based simulations. Moreover in the set-up with sextupoles the analysis with the PTC_TWISS method, which as the MAD-X TWISS method is based on the procedure introduced in Section 4.1, does not fully agree with the simulations performed with PTC_TRACK. This is due to the assumption made in Section 4.1 that the phase space of a mono-chromatic beam is not affected by any non-linear effect, while clearly the introduction of sextupoles could lead to distortions also for such a beam. The distortion of the initially Gaussian phase space due to the presence of sextupoles is visible in Figure B.1 in the appendix. In any case from Table 4.8 one can see that the dominant effect seems to be driven by the non-linear energy dependency of the Twiss functions and dispersion, and that the new optics shows a remarkable improvement in terms of emittance preservation at least on the horizontal plane. Only the PTC based simulations show a small deterioration of the emittance preservation in the vertical plane, but this would anyway be acceptable.

For completeness in Table 4.9 is reported the bunch lengthening one could expect in the DL for the three set-ups under analysis. The simulation procedure is identical to the transverse plane described in Section 4.1. Note that no optimisation was performed on this

optics	$\Delta\sigma_t$ [%] (MAD)	$\Delta\sigma_t$ [%] (PTC)
Nominal	71	95
With sextupoles	40	29
New optics with wiggler	45	37

Table 4.9: Bunch lengthening ($\sigma_t = \sqrt{\sigma_{tt}}$) after one passage in the DL for different optics and simulation code.

plane, but the requirement for all solutions not to have any bunch lengthening at first order (i.e. $R_{56} = 0$) was maintained. Table 4.9 shows that both the correction with sextupoles or the new DL optics better preserve the final bunch length. However the results should be analysed also with dedicated tracking which has not yet been performed.

An attempt to apply the sextupole correction to the actual CTF3 machine was performed, but without clear results as presented in Section 4.4.1. For this reason the current strategy at CTF3 is to try to use, and eventually further optimise, new linear optics with non-linear compensation such as the one presented in the previous section for the DL.

Figure 4.41 shows the transverse phase spaces at the end of the DBRC for a factor-8 recombination considering the new DL optics while keeping the same beam parameters specified in Table 4.1. These should be compared with the same picture obtained for the nominal optics in Figure 4.15. A considerable reduction in the horizontal phase space of the spread of the different ellipses representing different energy slices of the initial beam is evident. This can be seen also from the final statistical emittance of the combined beam that is reported in Table 4.10, where the values obtained for the nominal case are also summarised. The evolution of the horizontal and vertical emittances without the linear

	MAD-X nominal	PTC nominal	MAD-X new	PTC new
$\Delta\epsilon_x$ [%]	233	162	27	30
$\Delta\epsilon_y$ [%]	2	5	1	7

Table 4.10: Statistical emittance growth after the factor-8 beam recombination at CTF3 using the nominal and new DL optics and for both MAD-X TWISS and PTC_TWISS simulation procedures.

dispersion component for the bunch undertaking the longest path in DBRC are shown in Figure 4.42. These evolutions have to be compared with the nominal optics case presented in Figures 4.21(a) and 4.23(a). In the horizontal plane the reduction of the statistical emittance is significant for both MAD-X TWISS and PTC_TWISS simulations, however in the vertical plane there might be a slight degradation if one considers the PTC_TWISS simulations to be more accurate than MAD-X.

For the beam current stability it is also important to see the overall envelope of the beam. Figure 4.43 shows it for the longest path in the DBRC considering the new DL optics, and it has to be compared with Figures 4.21(a) and 4.21(a). With the new DL optics the mean horizontal beam position is much closer to zero than with the nominal optics.

This is clearly beneficial for matching the orbits of the bunches delayed in the DL and the ones bypassing the DL. Also the overall beam envelope in the horizontal plane appear more symmetric and consistent with the linear dispersion pattern of the beamline. Moreover no major difference are in the horizontal transverse size between the new bunches delayed in the DL (Figure 4.43(a)) and the bunches bypassing the DL (Figure 4.21(a)), which is a good sign for improving the beam current stability. Unfortunately in the vertical plane the envelope seems to be slightly worse than with the nominal optics. One should consider that the vertical aperture of the beam pipe at CTF3 is about ± 2.5 cm. If the PTC based simulations are correct, than the vertical plane could remain a major issue for transport and beam current stability. This is compatible with the experience operating the machine at CTF3, but no dedicated and systematic measurements are available yet.

The overall discrepancy between the simulations performed by means of MAD-X TWISS and PTC_TWISS is not yet fully understood, and it might require further analysis. Note that the optimisation of the DL optics presented here has been performed with MAD-X. This means that if PTC_TWISS turns out to be more accurate one might want to repeat the optimisation with that.

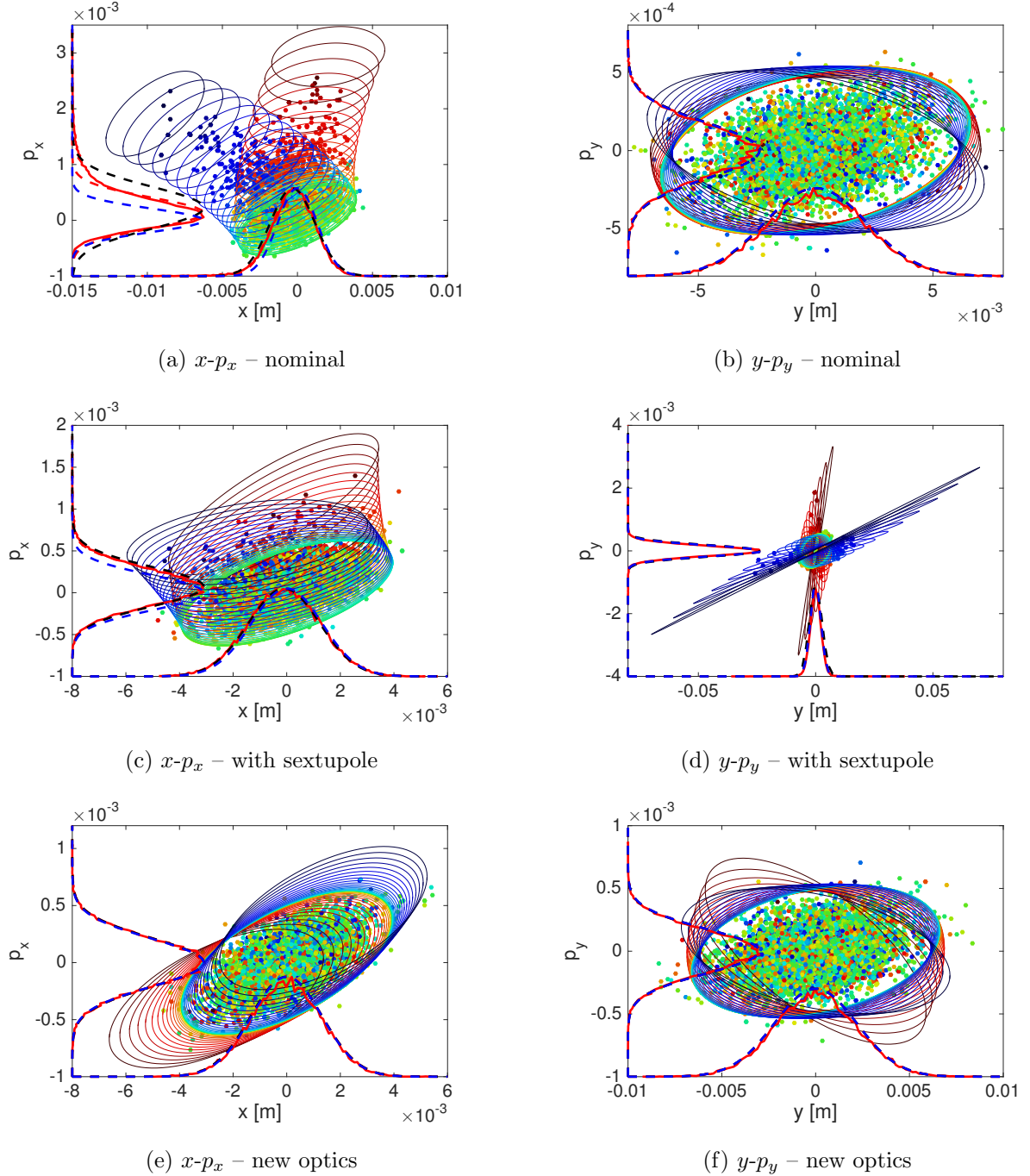


Figure 4.38: Representation of the $x-p_x$ ((a), (c), (e)) and $y-p_y$ ((b), (d), (f)) phase spaces after one passage in the DL for the different optics presented in this chapter. The optics is identified in the sub-caption of each figure. Each coloured ellipse represents a monochromatic slice of the full beam, and it is populated by a number of particles according to the Gaussian energy spread of the bunch. The colour scale is in terms of the momentum variation ($\Delta p/p_0$) with respect to the on-energy particle from -2% (red) up to +2% (blue) with granularity of 0.01%. The histograms on the axis are meant to guide the analysis: dashed-blue are the ideal Gaussian profiles of a monochromatic recombination; solid-red are the histograms of the generated particles, which are fitted by a dashed-red Gaussian; dashed-black are Gaussian profiles of a hypothetical recombined beam whose emittance is equal to the total statistical emittance (ϵ_{Σ}). Histograms might be overlapping. Simulations have been performed by means of calls of the MAD-X TWISS function.

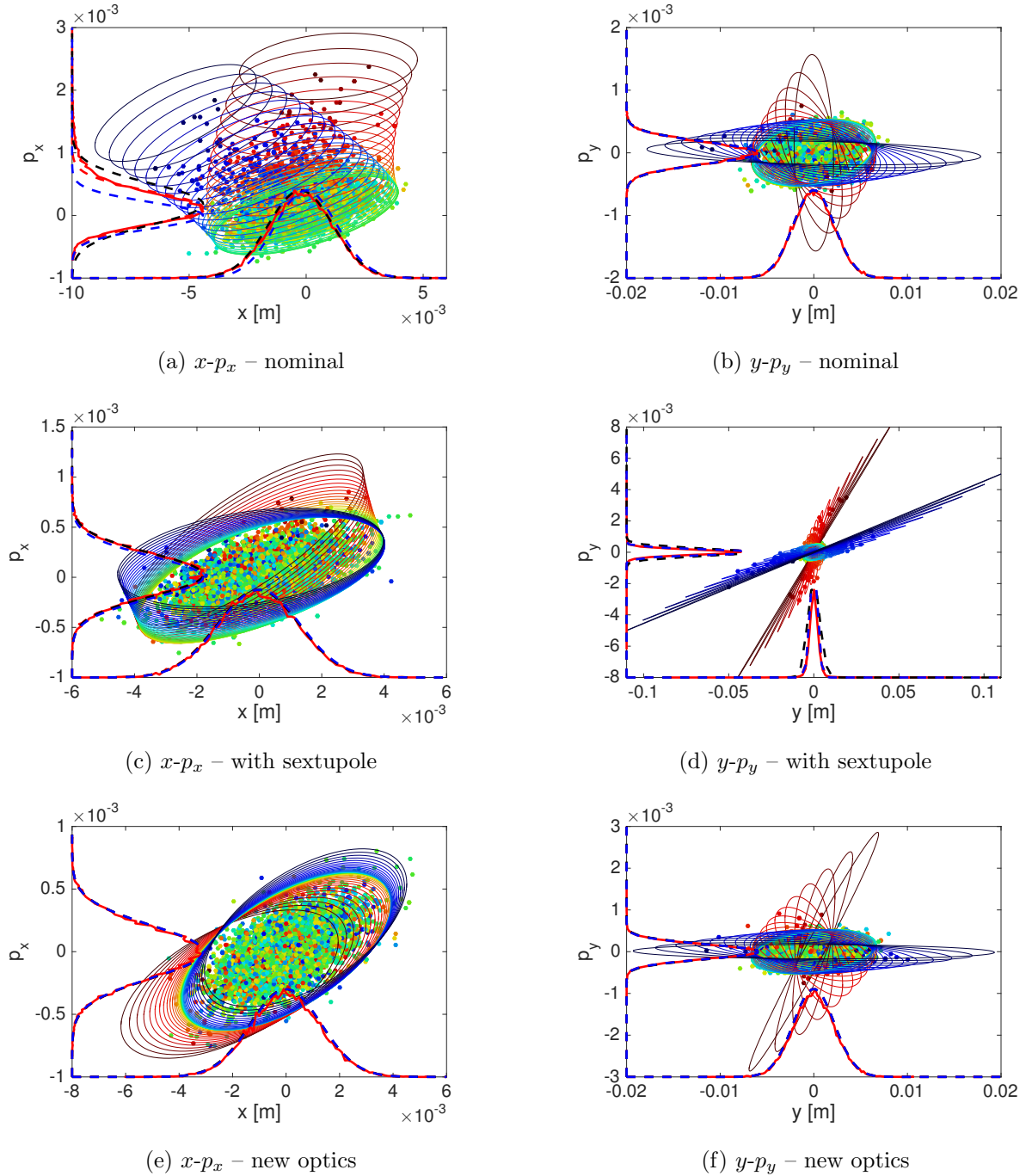


Figure 4.39: Representation of the $x-p_x$ ((a), (c), (e)) and $y-p_y$ ((b), (d), (f)) phase spaces after one passage in the DL for the different optics presented in this chapter. The optics is identified in the sub-caption of each figure. Each coloured ellipse represents a monochromatic slice of the full beam, and it is populated by a number of particles according to the Gaussian energy spread of the bunch. The colour scale is in terms of the momentum variation ($\Delta p/p_0$) with respect to the on-energy particle from -2% (red) up to $+2\%$ (blue) with granularity of 0.01% . The histograms on the axis are meant to guide the analysis: dashed-blue are the ideal Gaussian profiles of a monochromatic recombination; solid-red are the histograms of the generated particles, which are fitted by a dashed-red Gaussian; dashed-black are Gaussian profiles of a hypothetical recombined beam whose emittance is equal to the total statistical emittance (ϵ_{Σ}). Histograms might be overlapping. Simulations have been performed by means of calls of the PTC_TWISS function.

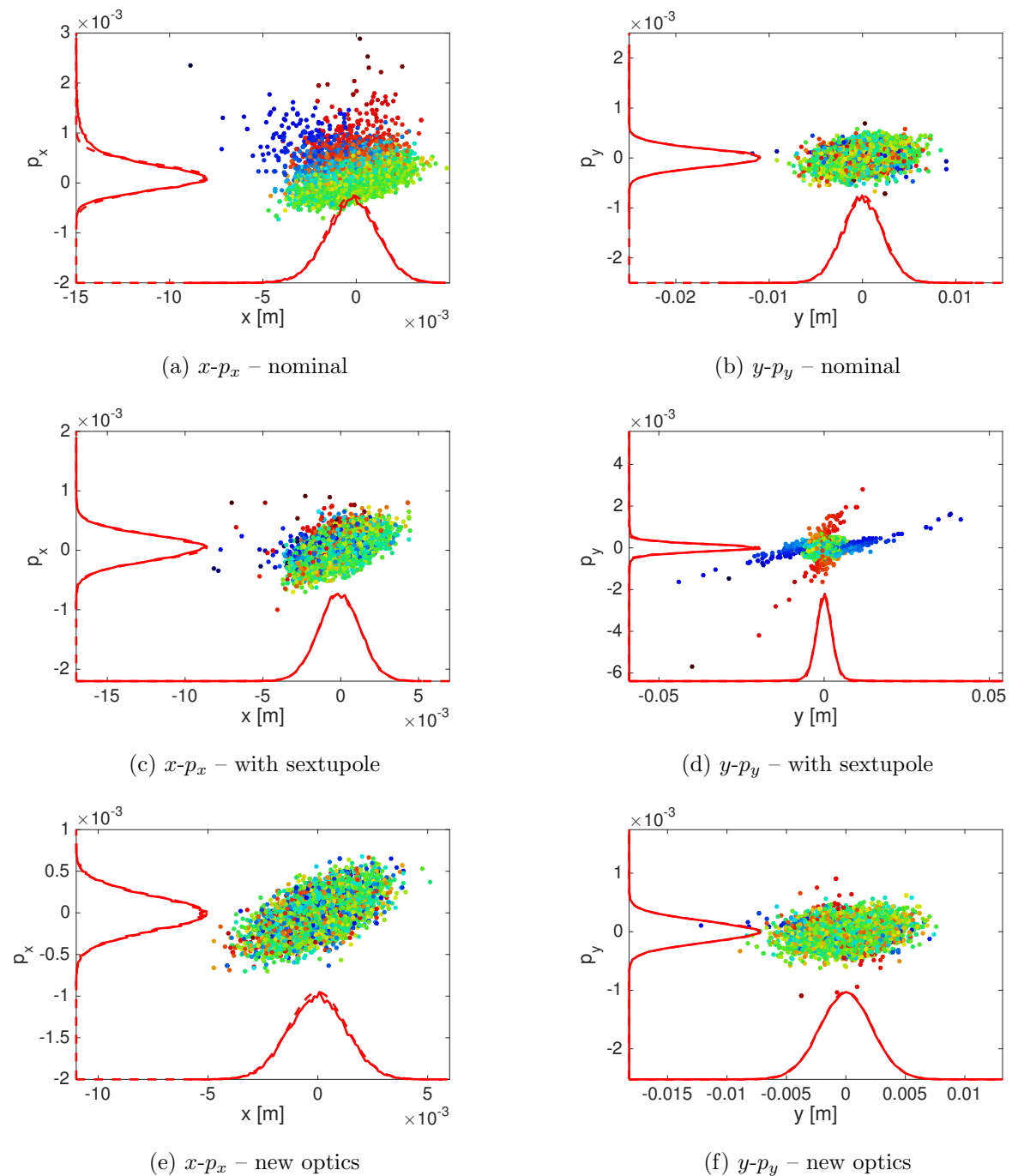


Figure 4.40: Representation of the x - p_x ((a), (c), (e)) and y - p_y ((b), (d), (f)) phase spaces after one passage in the DL for the different optics presented in this chapter. The optics is identified in the sub-caption of each figure. Each coloured ellipse represents a monochromatic slice of the full beam, and it is populated by a number of particles according to the Gaussian energy spread of the bunch. The colour scale is in terms of the momentum variation ($\Delta p/p_0$) with respect to the on-energy particle from -2.5% (red) up to +2.5% (blue). The histograms on the axis are meant to guide the analysis: solid-red are the histograms of the tracked particles, which are fitted by a dashed-red Gaussian; Histograms might be overlapping. Simulations have been performed by means of PTC tracking of 30000 particles assuming Gaussian initial conditions.

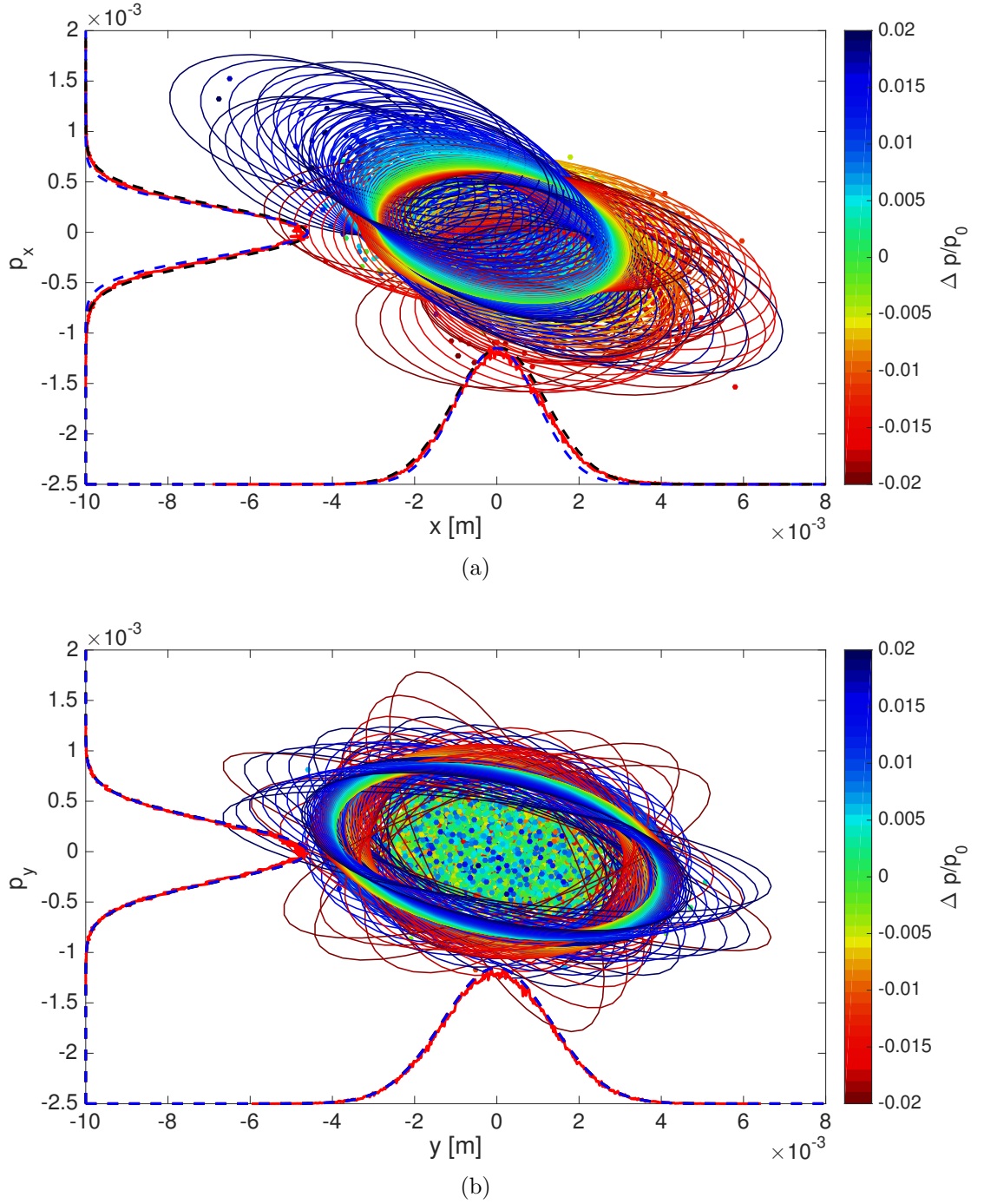
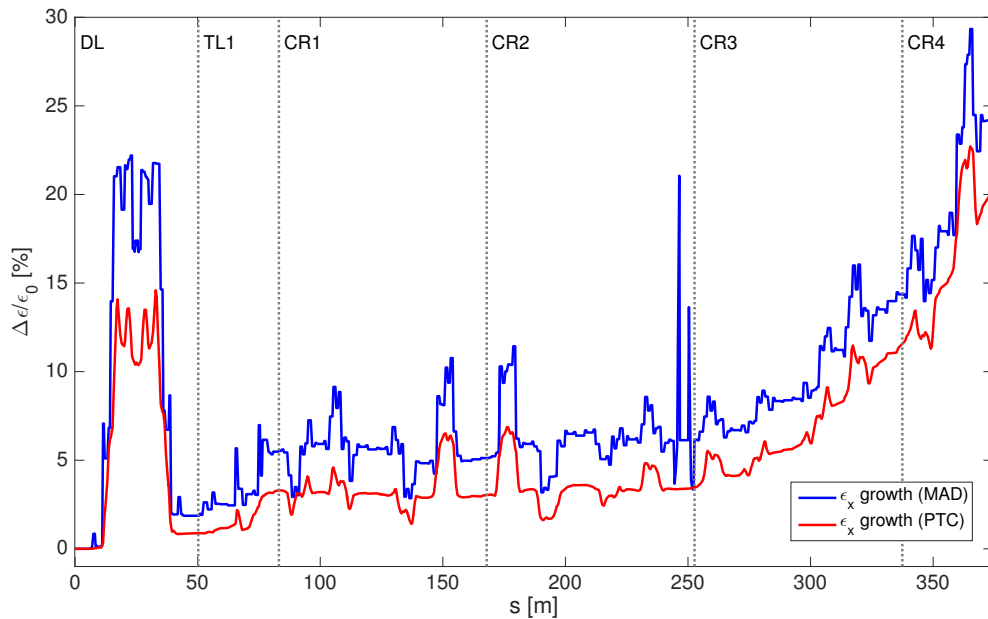
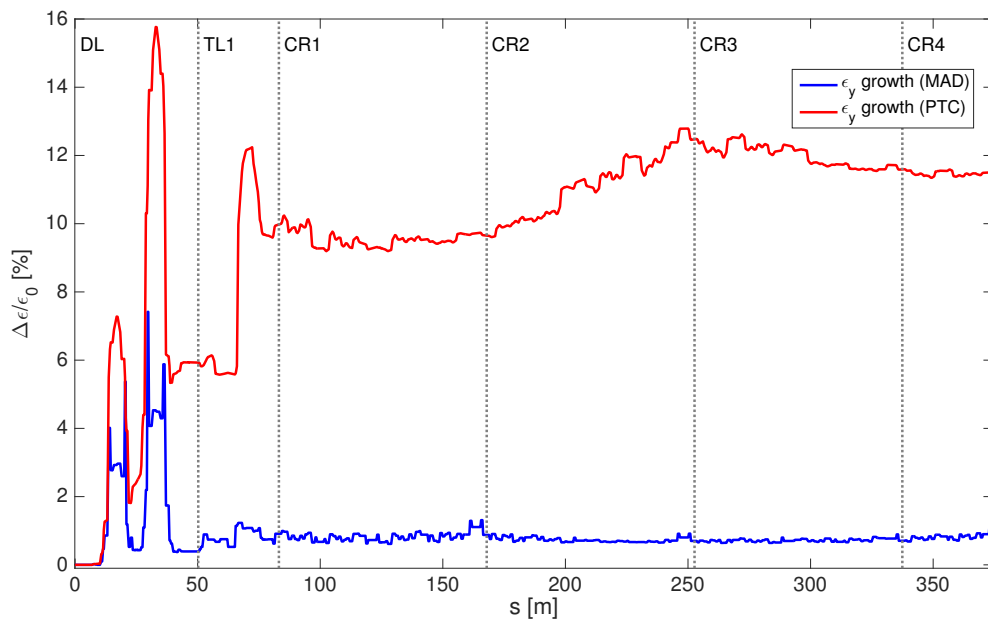


Figure 4.41: Final representation of the $x-p_x$ (a) and $y-p_y$ (b) phase spaces for a factor 8 combined beam at CTF3 with new DL optics. Each coloured ellipse represents a monochromatic slice of the full beam, and it is populated by a number of particles according to the Gaussian energy spread of the bunch. The colour scale is given in terms of energy variation with respect to the on-energy particle ($\Delta p/p_0$). The histograms on the axis are meant to guide the analysis: dashed-blue are the ideal Gaussian profiles of a monochromatic recombination; solid-red are the histograms of the generated particles, which are fitted by a dashed-red Gaussian; dashed-black are Gaussian profiles of a hypothetical recombined beam whose emittance is equal to the total statistical emittance (ϵ_Σ). Histograms might be overlapping. Simulations have been performed by means of calls of the MAD-X TWISS function.

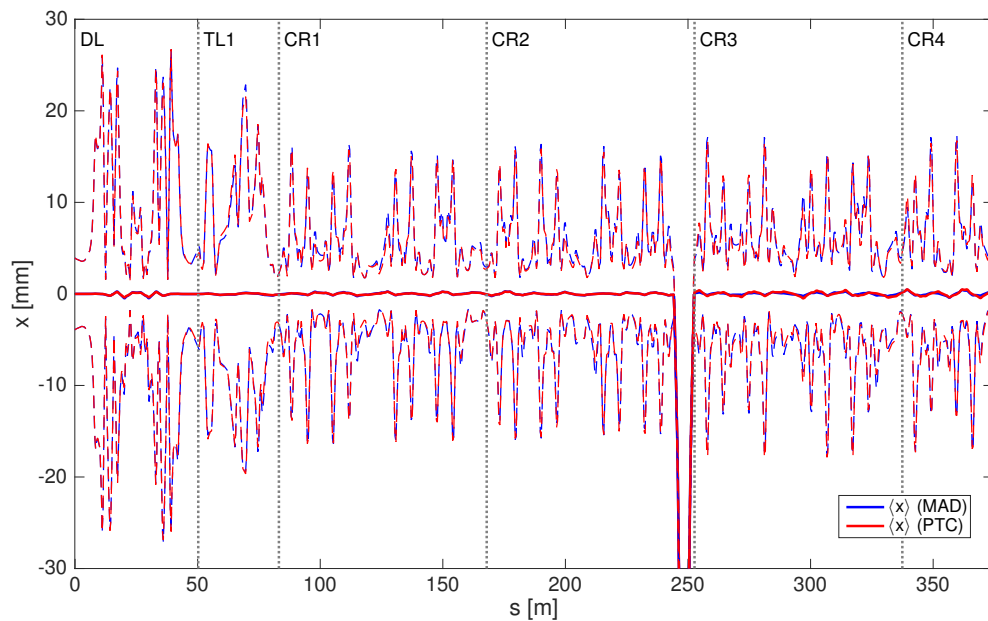


(a)

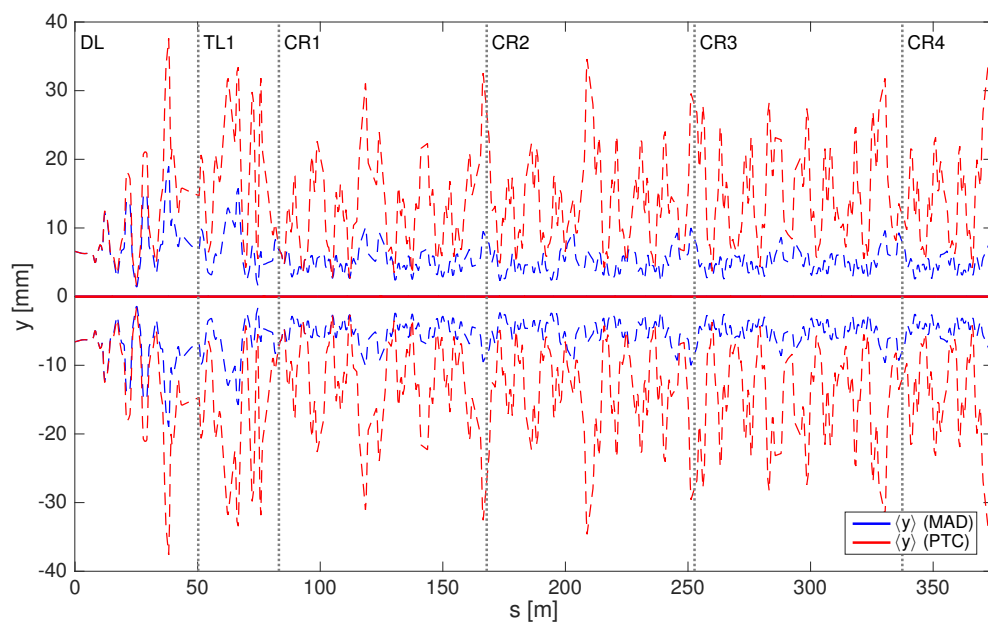


(b)

Figure 4.42: Horizontal (a) and vertical (b) emittance growth along the unfolded DBRC for the bunches undertaking the longest path, i.e. one turn in DL, a single passage in TL1 and $3\frac{1}{2}$ turns in CR. The quoted emittance growth is referred to the statistical emittance of the single bunch which has been split in many slices of different energies. The *linear* dispersion component has been suppressed in the calculation of the combined covariance matrix. The simulations have been performed by means of MAD-X TWISS (blue lines), and PTC_TWISS (red lines).



(a)



(b)

Figure 4.43: Mean horizontal (a) and vertical (b) orbit and 3σ boundaries along the longest path in the DBRC at CTF3 with new DL optics. The solid lines show the mean bunch position taking into account the non-linear dispersion effect, and assuming the beam parameters of Table 4.1. The dashed lines show the extreme boundaries which contains the $\pm 3\sigma$ core of the beam both in energy and betatron transverse size, i.e. representing 99.7% of the bunch particles. The boundaries are computed taking into account both linear and non-linear energy effects.

Chapter 5

Transverse dynamics optimisation at CTF3

The results presented in this chapter have been obtained at the CLIC Test Facility (CTF3) at CERN. A main overview of the facility has been presented in Section 1.3. Before presenting the actual measurements it is important to stress a few details of the relevant technical aspects that one has to keep in mind to interpret the results.

Most of the experience treated here is related to the control of the beam orbit, i.e. the transverse beam position along the beamline under consideration. This applies also when talking about *dispersion*, i.e. the energy dependence of the beam orbit as defined in Section 3.2. BPMs are the most common and useful beam instrumentation devices installed in a beamline to measure the beam orbit. The design of the CLIC Drive Beam BPMs is challenging for many reasons. One of the peculiarities is that during the recombination in the DBRC the same BPM is crossed by beams with different bunching frequency (at CTF3 from 1.5 GHz up to 12 GHz) and average intensity (at CTF3 from 2 A up to 32 A) within a short time (at CTF3 typically 1.2 μ s). CTF3 has been the test bed for different kinds and version of BPMs. During the construction and commissioning of the facility inductive pick-ups [92, 93] and stripline BPMs [94] have been installed. The data acquisition is handled by a custom-made electronics chain [95] that has evolved over time. The development of CLIC BPMs is still ongoing [96, 97] and CTF3 remains an important facility for their experimental verification. Since at CTF3 different kinds of BPM are installed in different areas of the facility, the precision and accuracy of the measurements in different areas might be different. The absolute and relative calibrations and the linear behaviour is also a long-standing problem that is intrinsically difficult to address due to the variety of devices and lack of time and resources. As a baseline one can assume that any kind of BPMs installed at CTF3 has resolution which is better than 100 μ m and a linear response within a couple of centimetres from the axis of the device.

The mechanical alignment of the magnetic elements in the beamline at CTF3 is supposed and assumed to be of the order of 100 μ m r.m.s. This also applies for BPMs. However a recent survey campaign [98] revealed that some elements, and in particular BPMs, might have alignment errors of the order of 1 mm in the transverse plane. This is an important

limitation on the absolute measurement of beam orbit, but it is less problematic for relative measurements such as orbit differences and dispersion measurements.

In some of the presented results the improvement in the beam quality could be verified by transverse-optics measurements by means of quadrupole scans and tomography using the tools described in Section 3.4. Note that these measurements can be directly affected by non-zero dispersion at the screen location as in Eq. 3.19, as well as phase-space distribution tails like the one visible in Figure 3.7(b). On top of the physical effects described in Section 3.4, one should take into account the systematic errors that might be introduced by calibration, alignment and radiation-related effects. Up to the time of writing not all the systematic errors present at the different quadrupole scan location have been clearly identified. This leads to low confidence in the absolute value of such measurements. One should then consider the quadrupole scan measurements as relative comparisons between different set-ups, which eventually show some improvement in the beam quality due to a variety of effects presented in this work.

Finally, the day-to-day stability and the extremely diverse scientific programme of CTF3 does not always allow comparison of measurements and results over different days and sometimes even hours. For this reason here are presented only the results which have been obtained in a relatively short period of time, i.e. where it was possible to identify a clear status of the machine *before* and *after* the optimisation of some beam parameters. Unfortunately this was not always possible due to limitations in time and resources and arising technical issues.

The aim of this chapter is to demonstrate the current understanding and control over different aspects related to orbit and dispersion in the CTF3 Drive Beam. This is one of the key ingredients of the daily optimisations that made the machine operations easier over the past years, and which allowed one to obtain reasonable machine set-up in a short period of time. In the following sections all the measurements and corrections have been performed by using the tools presented in Chapter 3. For all the orbit or dispersion corrections the generic feedback tool presented in Section 3.3 was used. The response matrix between actuators (normally dipole correctors) and the observables (orbit or dispersion) have been measured with the feedback application itself by using its system identification capabilities.

5.1 Device naming conventions

Before presenting the results it is useful to introduce the naming conventions for the elements of the CTF3 beamlines. The overall layout of the facility has been presented in Figure 1.4. Each element has a name which is composed of a two- (rarely three-) letter prefix that indicates the specific beamline to which the device belongs to. It normally follows a three-letter code that specifies the kind of element and a four-digits number that specifies the position of the element within the specified beamline. The third letter of the element type code is actually used to differentiate between different version of the same type (e.g. the BPMs are divided into “BPE”, “BPM”, “BPI” and “BPS”, which all start with the “BP” code.) The number indicating the position has no actual unit, but it represents only the

order in which the elements are installed. The relevant beamline prefixes are the following:

Naming prefix	Beamline
CL	Drive Beam Linac up to Frascati chicane.
CD	Delay Loop (DL).
CT	From Frascati chicane up to Combiner Ring (DL excluded).
CTS	Beam dump at the end of the linac.
CR	Combiner Ring (CR).
CRM	Beam dump right after injection into CR.
CC	From the extraction from CR up to the CLEX area (excluded).

The element types can be summarised as the following:

Naming code	Element type	Note
BH and BV	Bending magnet	The second letter specifies if the magnet bends the beam Horizontally or Vertically.
QF and QD	Quadrupole magnet	The second letter specifies if it is a Focusing or Defocusing quadrupole.
DH and DV	Dipole corrector	The second letter specifies if the corrector kicks the beam Horizontally or Vertically.
BP	BPM	
MTV	Screen	

For the BPMs a final letter might be added at the end of the device name to indicate if the signal to which one refers is the horizontal (H) or vertical (V) beam position, or the beam current (S).

To summarise with an example, the element CL.BPM0402 is a BPM (element type BP) which is installed in the Drive Beam linac (CL) and is before the focusing quadrupole (QF) “CL.QFA0505” which also belongs to the linac (CL).

5.2 Dispersion Free Steering

The first experiment to test the orbit and dispersion feedback tools described in Chapter 3 is the orbit control in the Drive Beam linac. An experiment could be to steer the beam on the “golden” orbit, but this unfortunately might not always be well defined or known. Intuitively the best option would be to steer the beam towards the centre of all available BPMs, but this might be inefficient: due to magnetic element and BPM misalignments one might end up in a configuration where the beam receives many sharp kicks that spoil the beam quality. A more robust approach would be to steer the beam such that the kick received is minimised.

This requires a perfect knowledge of the element misalignments that is not always available. In recent works [99, 100, 101] the trend is instead to use some *differential* measurement to optimise the orbit: one example is to target a desired dispersion. In a linac, where the nominal dispersion is supposed to be zero, a strong steering naturally results in unwanted dispersion that might be harmful for the beam. The hope is that by steering the beam such that the dispersion is canceled at the BPM locations one ends up with an orbit that best preserves the beam quality.

The Dispersion Free Steering (DFS) [102] technique was successfully applied in the CTF3 Drive Beam linac by using the developed tools. The results obtained at the end of November 2015 are presented in Figure 5.1 for the horizontal plane and in Figure 5.2 for the vertical plane. The result presented for the horizontal plane was obtained after two independent correction iterations in two consecutive days. The result presented in Figure 5.1 is then the comparison between the beam before the first iteration and after the second iteration. This is not the case for the vertical correction, Figure 5.2, which was performed in a single correction iteration.

The measurements were performed by varying the beam current by about $\pm 1\%$. Each dispersion pattern is normalised with respect to the nominal horizontal dispersion one expects after the linac in the first dispersive BPM of the TL1 transfer line. Since the reference BPM is actually *after* the beamline of interest, the horizontal correction which was performed (Figure 5.1) might have affected the actual dispersion at the reference BPM. This leads to a systematic error in comparing the dispersion before and after the correction. However the nominal dispersion expected at the reference BPM is about 605 mm, which is about 10 times bigger than the maximum dispersion observed in the linac in the uncorrected case (red line in Figure 5.1(a)). It is then reasonable to estimate the systematic error to be of the order of 10% at most. Even in that case the effect of the correction is non-negligible.

Note that for both planes in the uncorrected set-up a dispersive wave starts at the beginning of the linac and is amplified along the linac. For the vertical plane it is indeed clear that most of the correction is applied by the first correctors, Figure 5.2(b). In the horizontal plane it is interesting to note the strong correction that is normally applied starting around the Frascati chicane (elements with prefix CT in Figure 5.1). At the time of the measurement the chicane was bypassed by switching off its bending magnets. It is believed that the residual magnetic field of the bending magnets is compensated by the correctors CTDHD0160 and CTDHD0308. The target horizontal dispersion in Figure 5.1(a) is actually not zero at the BPMs CTBPI0495 and CTBPI0105¹. This is because these two BPMs are installed around the DL injection where the design foresees an orbit bump and hence non-zero dispersion is expected.

At the end of the linac there is the possibility to perform a quadrupole scan in the CTS dump line (see Figure 1.4). Measurements of the Twiss parameters of the beam were performed before and after the dispersion correction. The measured values are summarised in Table 5.1. Note that the measured emittance is reduced by about 20% in both planes after the DFS in the linac. Due to the remarks on the quadrupole scan measurements given in

¹The name of this BPM does not strictly follow the naming convention of Section 5.1. Its actual location is between CTBPI0495 and CTBPM0515.

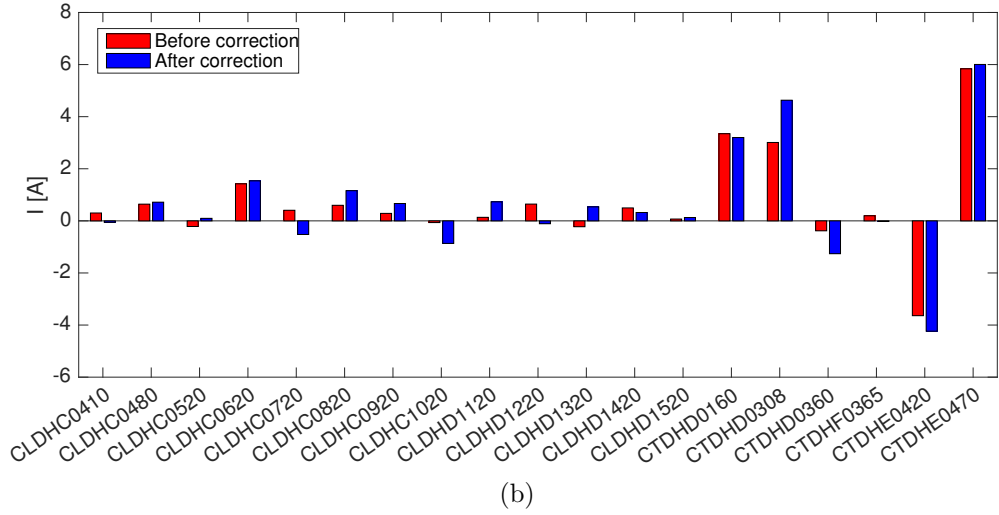
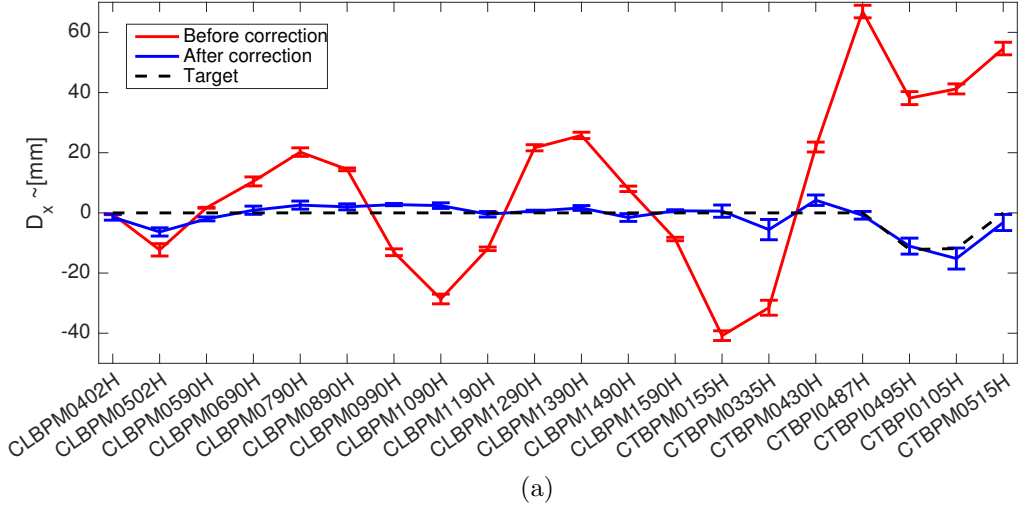
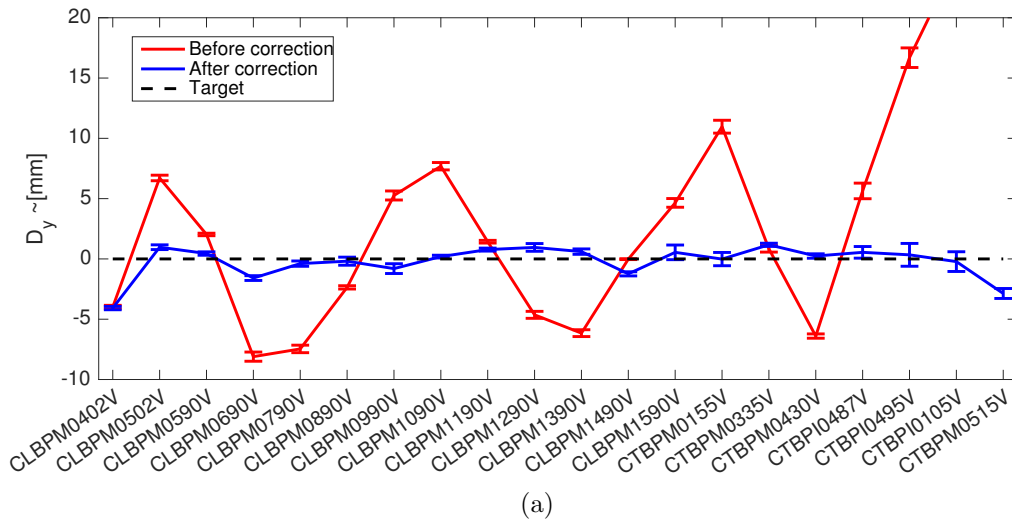


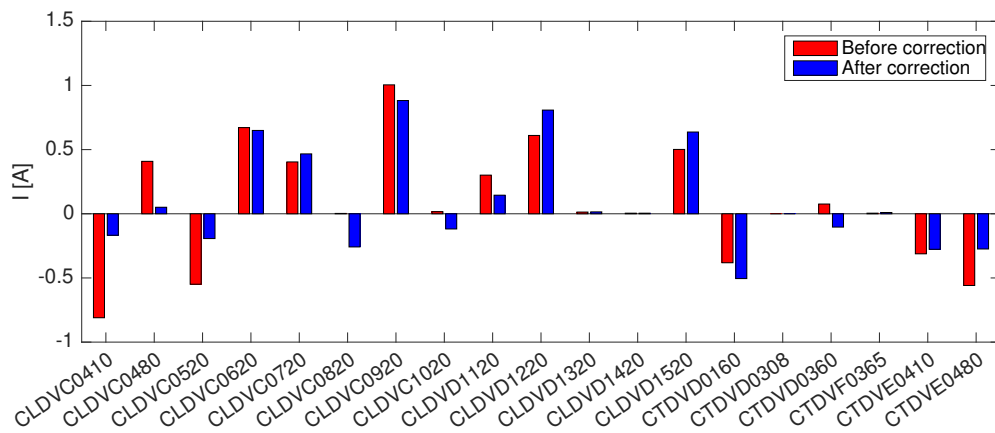
Figure 5.1: Results of a DFS correction in the horizontal plane at the CTF3 Drive Beam linac. Figure (a) shows the horizontal dispersion measured at the different BPMs installed in the beamline. The red and blue lines are respectively the dispersion measured before and after the correction. The error bars represent the statistical error over a few consecutive measurements. The dashed black line is the desired target dispersion. Figure (b) shows the strength of the dipole correctors used for the correction. In red are the strength before the correction, blue are after the correction. The device names follow the naming conventions described in Section 5.1 except for BPM CTBPI0105.

	β_x [m]	α_x	ϵ_{Nx} [μm]	β_y [m]	α_y	ϵ_{Ny} [μm]
Nominal values	8.4	-0.8	-	13.5	-0.4	-
Before correction	9.2 ± 0.4	-0.7 ± 0.1	63 ± 1	11.3 ± 1.2	-0.1 ± 0.1	129 ± 8
After correction	8.7 ± 0.4	-0.5 ± 0.1	52 ± 1	10.3 ± 1.0	-0.1 ± 0.1	102 ± 5

Table 5.1: Transverse Twiss parameters of the beam measured in the CTS dump line before and after DFS in the Drive Beam linac at CTF3. Also shown are the nominal values for the ideal machine.



(a)



(b)

Figure 5.2: Results of a DFS correction in the vertical plane in the Drive Beam linac. (a) the vertical dispersion measured at the different BPMs installed in the beamline. The red and blue lines are respectively the dispersion measured before and after the correction. The error bars represent the statistical error over a few consecutive measurements. The dashed black line is the desired target dispersion. (b) the strength of the dipole correctors used for the correction. In red are the strengths before the correction; blue are after the correction. The device names follow the naming conventions described in Section 5.1 except for BPM CTBPM0105.

Section 3.4, Figure 5.3 shows the beam size measurements used to fit the Twiss parameters quoted in Table 5.1. Note that for both vertical and horizontal planes the overall behaviour

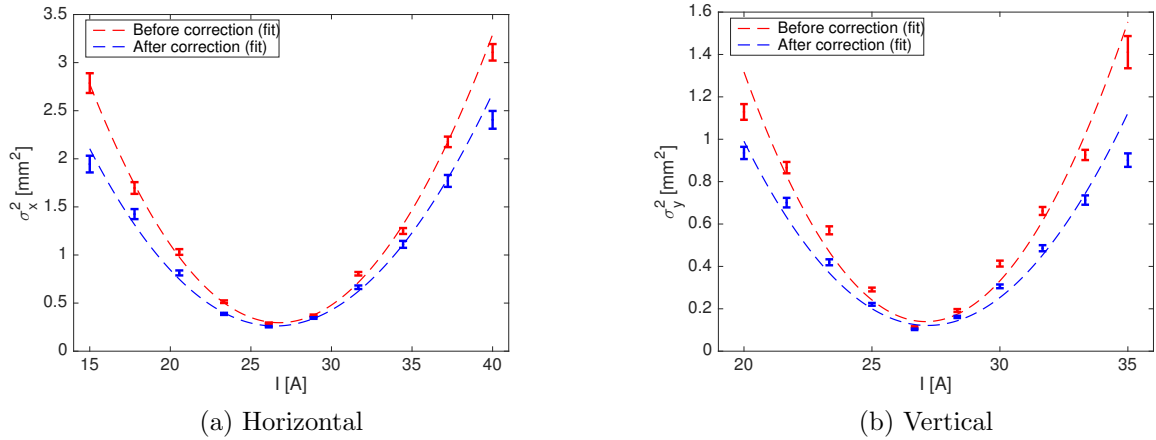


Figure 5.3: The beam variance measured at CT.MTV0550 in the CTS dump line as a function of the quadrupole current used to perform quadrupole scan measurements before (red) and after (blue) DFS correction in the linac. The error bars are the from the Gaussian fit of the beam profiles measured at the screen. (a) and (b) are relative to the horizontal and vertical scans respectively. The dashed lines are the fit of the data according to the Twiss parameters that are reported in Table 5.1.

of the beam size as a function of the quadrupole current is comparable, but an overall beam size reduction is visible after the dispersion correction performed in the upstream linac.

The Drive Beam lies in the horizontal plane up to the end of the DBRC. Only after the CR a vertical dogleg is installed with the purpose of fitting inside the building. Up to this point one should then expect no vertical dispersion. In this plane one can apply the same DFS technique used in the linac. Figure 5.4 shows the results of a vertical dispersion correction in the transfer line TL1 that is used to transport the beam into the CR. Note that the first corrector in use for the correction is the CTDFV0612 which is right before the BPM CTBPI0622. It is then natural that the dispersion measured in the first three BPMs in Figure 5.4(a) does not change before and after the correction. During the correction higher weight was put on the BPMs of the CR (i.e. last three BPMs in Figure 5.4(a)) where indeed it was possible to reach the most effective correction.

The correction presented in Figure 5.4 was beneficial also for the vertical dispersion in the CR. Figure 5.5 shows the dispersion in the CR before and after the DFS in TL1. Note that for the correction only the first three BPMs in the CR were used.

5.3 Commissioning of a new Delay Loop optics

In Section 4.3 it is shown that non-linear dispersion, in association with the high energy spread of the Drive Beam, might have a considerable impact on the performance of the DBRC at CTF3. One of the main contributions has been identified in the strong optics of the Delay Loop (DL) and possible solutions have been described in Section 4.4. The most

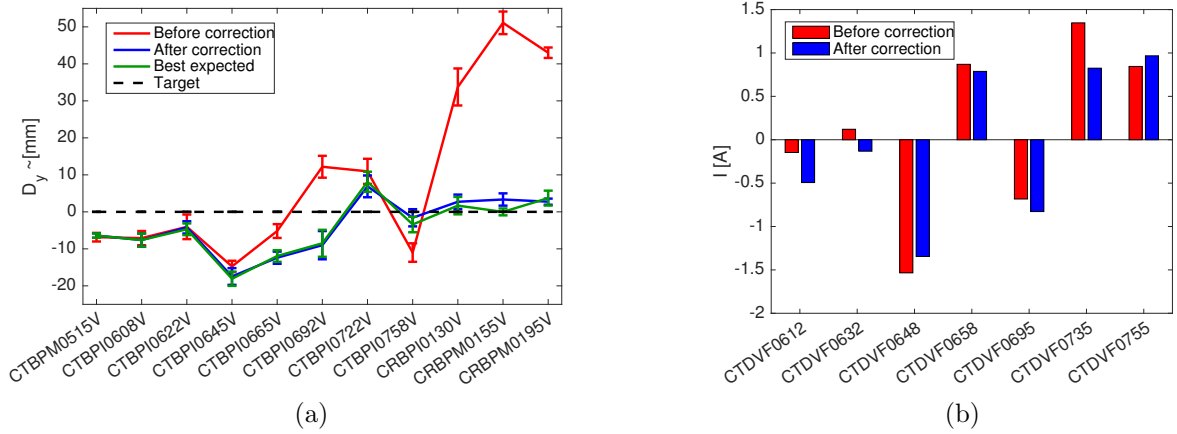


Figure 5.4: Result of a DFS correction in the vertical plane in TL1. (a) the vertical dispersion measured at the different BPMs installed in the beamline. The red and blue lines are respectively the dispersion measured before and after the correction. The error bars represent the statistical error over a few consecutive measurements. The dashed black line is the desired target dispersion. (b) the strength of the dipole correctors used for the correction. In red are the strengths before the correction, blue are after the correction. The device names follow the naming conventions described in Section 5.1.

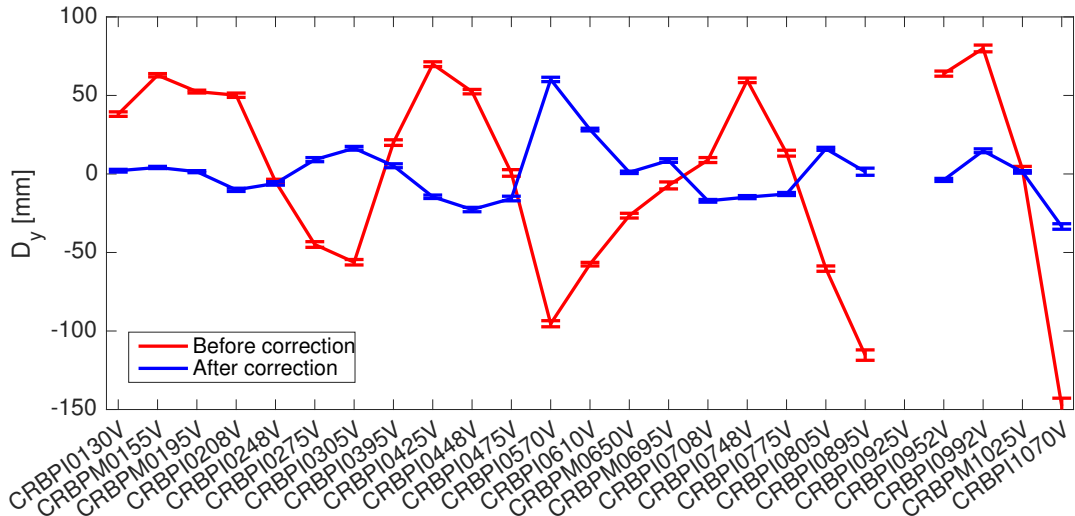


Figure 5.5: Comparison of the vertical dispersion measured in the BPMs installed in CR before (red) and after (blue) a vertical dispersion correction in the preceding transfer line TL1. The device names follow the naming conventions described in Section 5.1. The BPM CRBPI0925 was defective at the time of the measurement.

promising proposal in Section 4.4.2 is to implement a modified linear optics in the DL that, from simulations, seems to develop weaker non-linear dispersion at least in the horizontal plane. In the late 2015 machine run an attempt to commission the new DL optics in the actual machine was performed.

Figure 5.6 shows a comparison measurement of the first- and second-order dispersion patterns in the DL and in the following transfer line TL1 between the nominal optics and new

optics proposed in Section 4.4.2. This measurement was performed with a 3GHz beam magnetically injected and extracted from the DL, i.e. without using the RF deflector normally used for the factor-2 recombination. About 150 consecutive beam-shots were collected with the use of the dispersion monitor application described in Section 3.2. During the acquisition the beam-energy shot-to-shot jitter was enhanced by wiggling the beam current delivered by the thermionic gun at the beginning of the linac. The measurements assume perfectly linear horizontal dispersion at BPM CD.BPI0135, which is the first BPM encountered by the beam where the nominal dispersion is high. For this reason CD.BPI0135 was used as an energy meter assuming the nominal dispersion of -0.743 m. The simulated behaviour also presented in Figure 5.6 is expected from the ideal machine studied in Chapter 4. It must be said that both optics were not implemented in the machine exactly as defined in Table 4.7, but both were partially tweaked to allow a reasonable beam transmission that was not quickly achievable otherwise. Also the optics in the transfer line TL1 was slightly tweaked and this might explain the discrepancy already at first order.

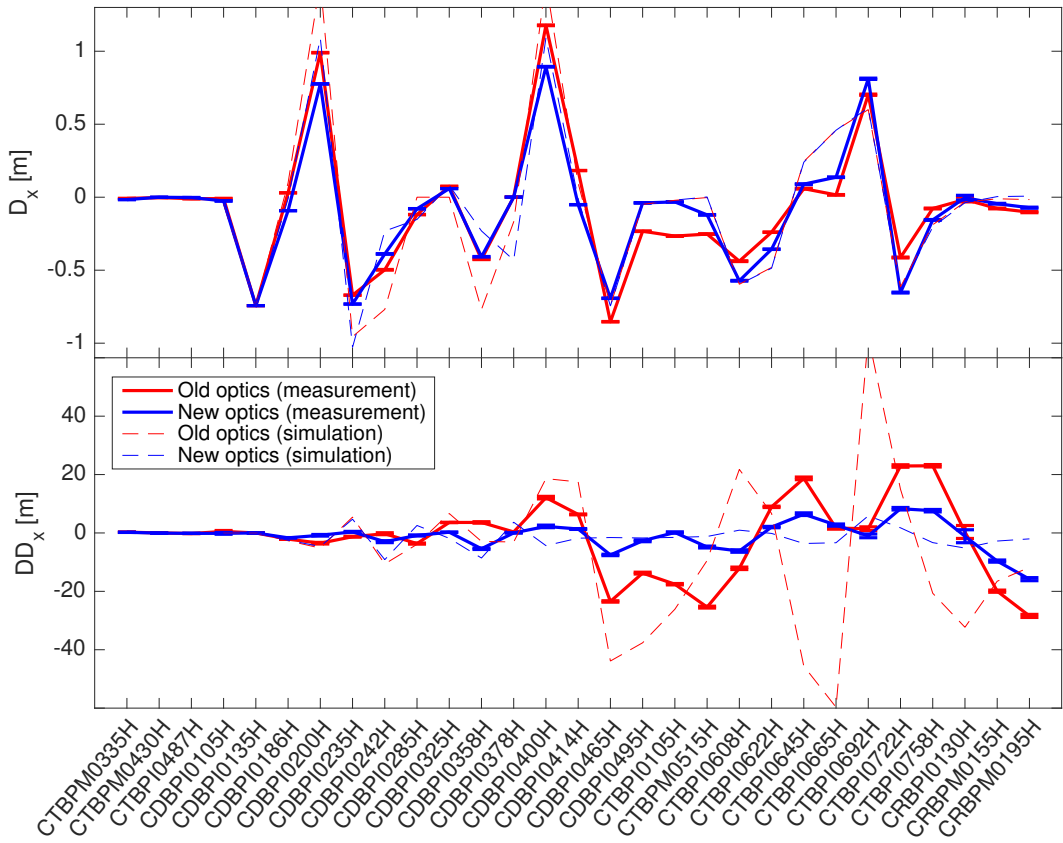


Figure 5.6: Comparison of the measured and simulated first-order (D_x) and second-order (DD_x) horizontal dispersions in DL and following transfer line TL1 between the old (solid-red) and new (solid-blue) optics of DL. The dashed lines are the simulated first- and second-order dispersions for the two ideal optics. On the horizontal axis are the BPMs in order of appearance on the path of the beam.

An analogous measurement was performed for the vertical plane and is presented in Figure 5.7. In the vertical plane one would expect no dispersion at any order from an ideal machine. However element imperfections and misalignments can explain the dispersion

which is visible in Figure 5.7.

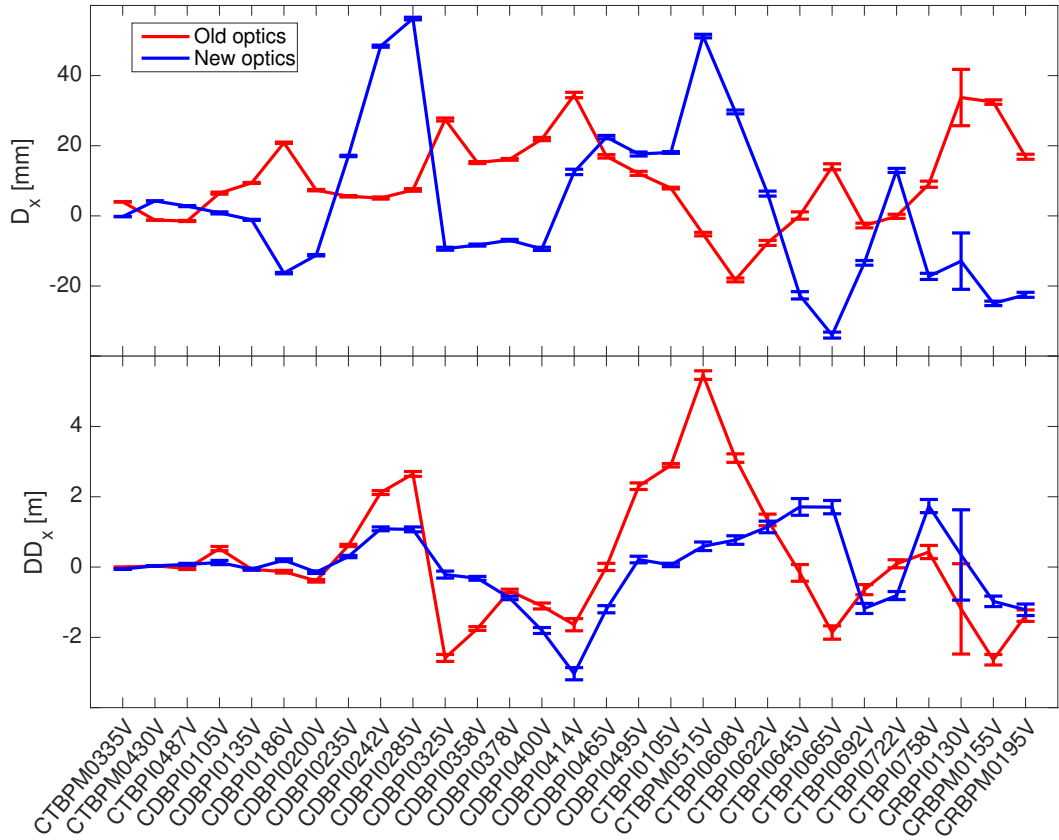


Figure 5.7: Comparison of the measured first-order (D_y) and second-order (DD_y) vertical dispersions at the BPMs installed in DL and following transfer line TL1 between the old (red) and new (blue) optics of DL. On the horizontal axis are the BPMs in order of appearance on the path of the beam.

For completeness, Figure 5.8 shows a selection of the measured orbits used to obtain the fits presented in Figures 5.6 and 5.7 in the form of scatter plots.

Another measurement was performed a few days after the first commissioning of the new optics. This time the optics in use in the DL was exactly as the newly-proposed optics in Table 4.7, but scaled 4% lower than the expected beam energy. This scaling was necessary to obtain the best beam transmission through the DL. Figure 5.9 shows the linear and non-linear dispersion measured for different scaling of the DL quadrupoles with respect to the desired ideal set-up. Note that the non-linear dispersion in TL1 seems to decrease the more one matches the actual energy of the beam by increasing the strength of the quadrupoles. Unfortunately this was degrading the beam transmission through the DL, and no time was available to further investigate the source of the losses.

From all the measurements it can be seen that there is a general reduction of the second order dispersion in TL1 (i.e. second half of the set of BPMs in Figures 5.6 and 5.7) for both planes between the old nominal optics and the new optics proposed in Section 4.4.2. The disagreement between simulations and measurement could be justified by the inexact implementation of the optics in the area, element misalignments, and calibration issues. A

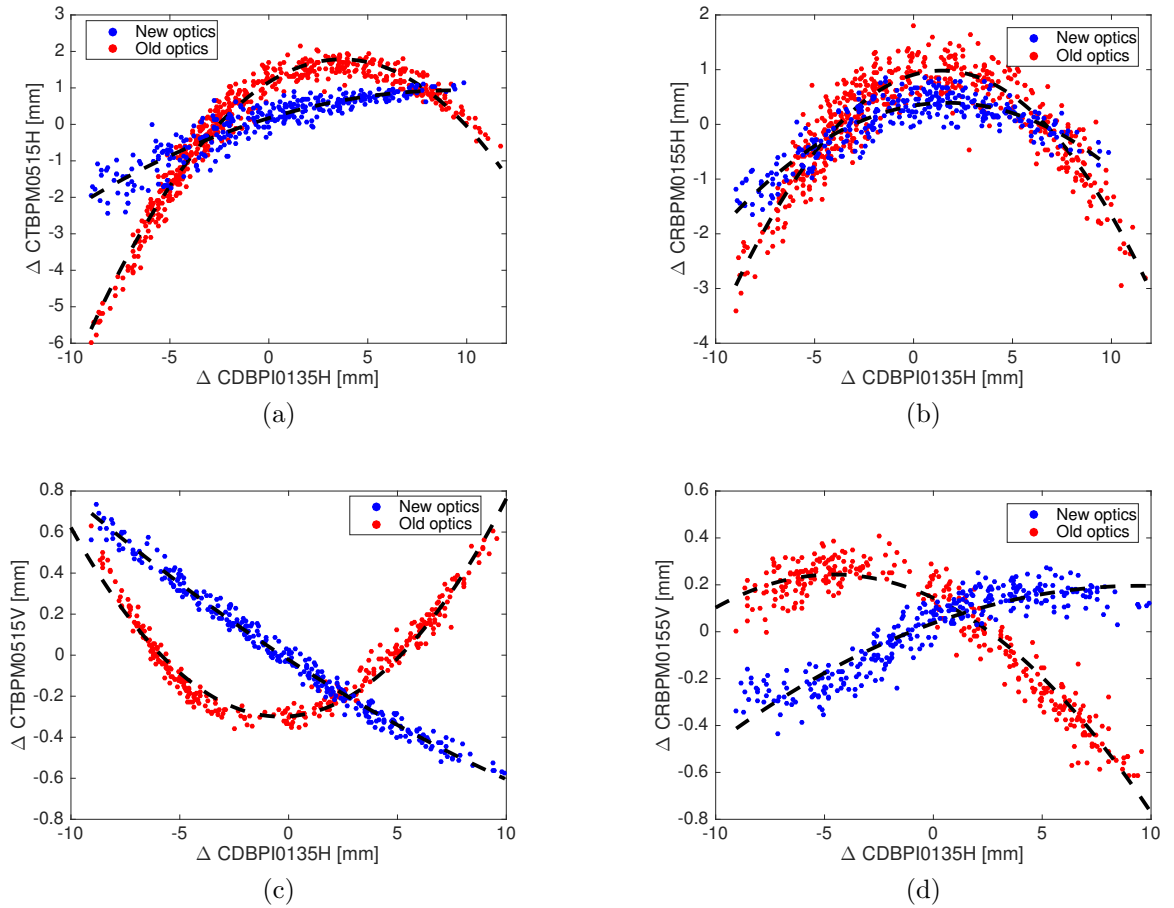


Figure 5.8: On the horizontal axis of each plot is the horizontal beam position measured at the BPM CD.BPI0135. On the vertical axis are the measured horizontal ((a) and (b)) and vertical ((c) and (d)) beam positions measured at the same time at BPM CT.MTV0515 ((a) and (c)) and CR.MTV0155 ((b) and (d)). The average beam positions are subtracted. The red points were measured with the nominal DL optics, the blue points with the new DL optics. The dashed-black curves represents the fits from which first- and second-order dispersions are measured in Figures 5.6 and 5.7.

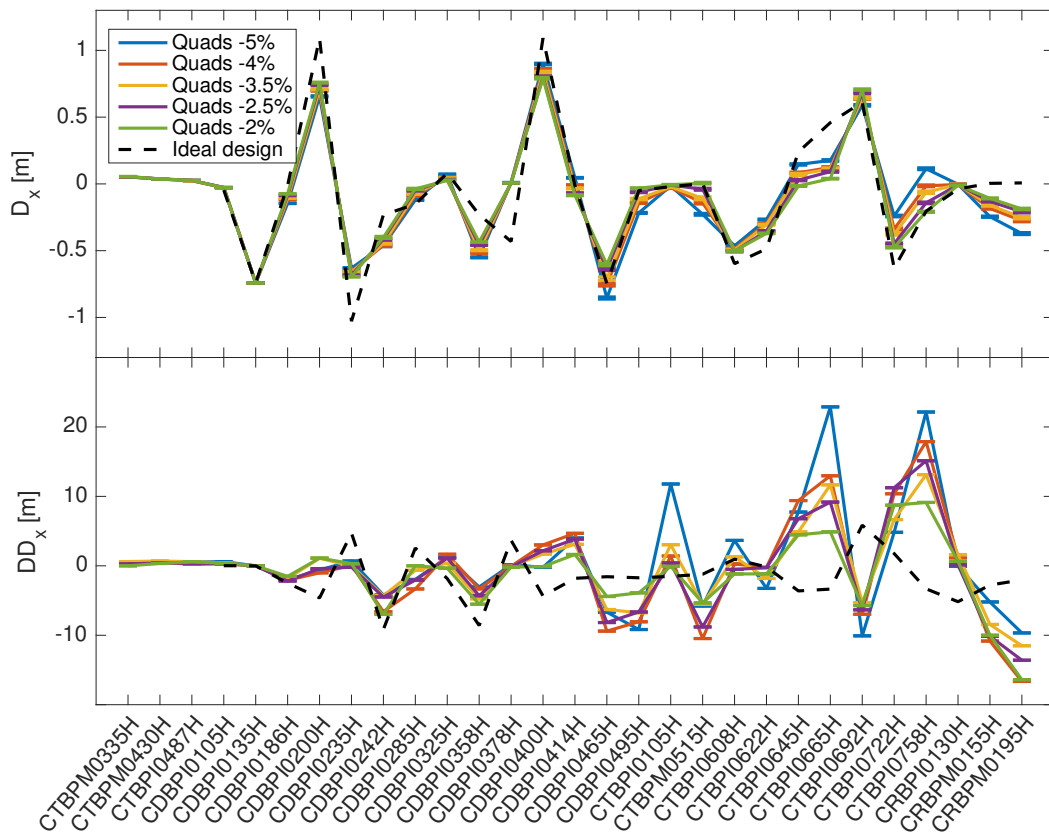


Figure 5.9: First-order (D_x) and second-order (DD_x) horizontal dispersions at the BPMs installed in DL and following transfer line TL1. On the horizontal axis are the BPMs in order of appearance on the path of the beam. The dashed-black line is the nominal dispersion using the new DL optics presented in Section 4.4.2. The continuous lines are measurements in which the DL quadrupoles were scaled with respect to the designed values.

clean measurement of the improvement would require one to first steer the beam on the same orbit and to correct the first-order dispersion for both optics. Unfortunately such a correction is extremely unlikely at CTF3 due to tight acceptance of the DL. By considering only the horizontal plane one should actually expect an improved acceptance with the newly-developed optics. In this sense the PTC simulations presented in Figure 4.43(b) show a possible issue in the vertical plane (see Figures 4.38, 4.39, 4.40), which could be a hint for further studies. A posteriori this could also explain the difficulties in transporting the beam into the DL, but no experimental measurements are available to support this hypothesis yet.

5.4 Matching between delayed and bypassing bunches

In Section 4.2.1 the main effects that affect the transverse quality of the Drive Beam recombination have been described in an ideal sense. Operationally the first task is to ensure a reasonable orbit closure and transverse optics matching between the bunches being delayed in the DL and the bunches bypassing it. In this section a selection of measurements and corrections conducted in this part of the CTF3 DBRC are presented.

5.4.1 Horizontal and vertical orbit matching

The most obvious effect is the orbit mismatch between delayed and bypassing bunches. Unfortunately the BPMs installed at CTF3 cannot resolve the single bunch orbit, and it would be impossible to measure the mismatch while the factor-2 recombination is performed. A first workaround is to perform the measurement of the mismatch by using a single beam shot in which the first half of the bunch train bypasses the DL, while the second half is delayed in the DL and then it follows the first half but delayed by the DL length. Operationally at CTF3 this would require setting up a 280 ns-long train of bunches at 1.5 GHz. The phase of the bunches has to be flipped by 180 degrees (at 1.5 GHz) with respect to the nominal setup. In this way the 1.5 GHz RF deflector installed at the entrance of the DL instead of injecting the first half of the train will inject the second half, and hence instead of combining the two sub-trains of bunches, they will be separated from each other and their orbit difference is easily accessible in the following transfer line TL1. Unfortunately this technique has two main disadvantages:

- In order to perform the measurement and correction a dedicated beam has to be set-up starting from the injector. This means that the measured orbit difference might not be the actual mismatch that is in place during the factor-2 recombination.
- The BPMs installed in the TL1 transfer line are known to misbehave with such a beam, providing inconsistent performances between the measurement of the delayed and bypassing bunches. This issue is not yet fully understood.

In order to avoid these issues a simpler set-up was used for the results presented in this work. The target orbit in TL1 was measured by using the nominal 1.5 GHz beam, but

forcing it to bypass the DL by switching off the RF deflector and replacing its function with two static corrector magnets. This is a standard procedure to bypass the DL independently of the kind of beam that is produced in the linac². Afterwards the beam was magnetically injected and extracted from the DL, and its orbit in TL1 was corrected by acting only on the correctors inside the DL. The magnetic injection makes use of the same correctors used to magnetically bypass the DL, but with opposite kick.

Figure 5.10 shows an example of horizontal (a) and vertical (b) orbit corrections achieved in the latest CTF3 run of 2015. For these corrections the variation of the DL corrector strengths is shown in Figure 5.11. The final orbit matching obtained in Figure 5.10 has to

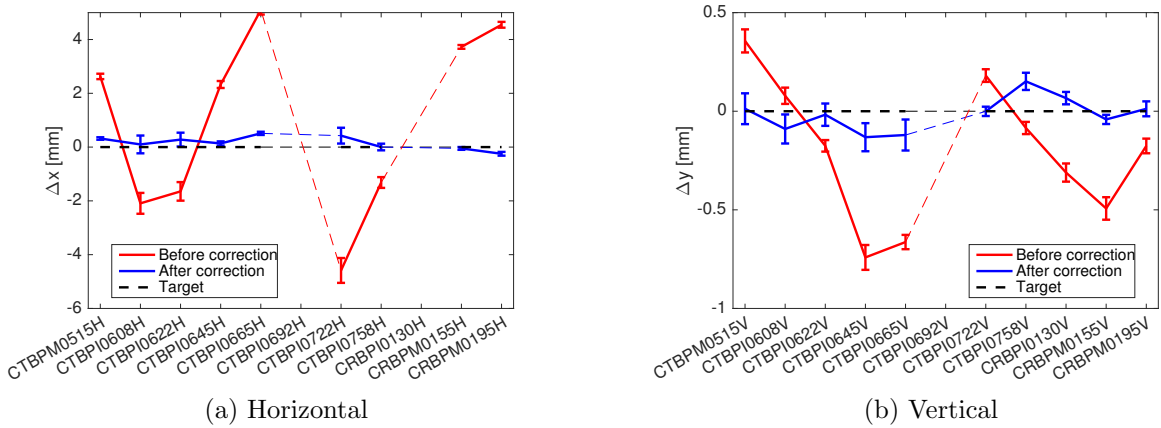


Figure 5.10: Difference between the delayed and bypassing beam orbits in the TL1 BPMs before (red) and after (blue) orbit matching correction. (a) horizontal plane. (b) vertical plane. The error bars are the statistical error on about 20 orbit measurements. The dashed-black lines represent the desired difference that is naturally zero. Note that BPM CTBPM10692 was not operational at the time of the experiment, while the horizontal position in BPM CRBPM10130 was not usable due to hardware limitations. No values are given in these cases and dashed lines connect the points before and after the faulty BPMs.

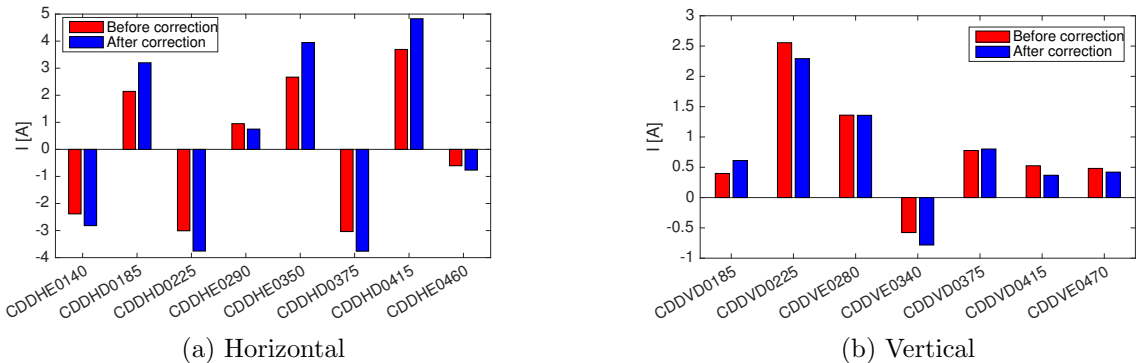


Figure 5.11: DL corrector strengths before (red) and after (blue) the orbit matching in TL1 between the delayed beam and bypassing beam. (a) is for to the horizontal plane, while (b) is for the vertical one.

²Note that the CTF3 drive beam linac can produce train of bunches at 1.5 GHz and 3 GHz.

be compared with the tolerances derived in Section 4.2.2 and presented in Figure 4.9. For both planes, if one trusts the calibrations of the BPMs, after the correction the expected projected emittance growth is below 50% for both definitions of emittance presented in Section 4.1.1. A better correction appears to be challenging with the aperture constraints of the DL. However such an emittance growth can be acceptable.

It is interesting to note in Figure 5.11(a) that the DL correctors are fired in an alternating pattern. The linearFeedback application used for the correction is normally able to remove unnecessary correction by targeting a proper correctors pattern, e.g. all the correctors with null strength. Unfortunately the dynamic aperture of the DBRC at CTF3 and in particular of the DL does not allow much freedom. For this reason most of the corrections presented in this chapter are not targeting a null strength on the correctors, but rather the initial corrector strengths that were empirically found by optimising beam transmission. However Figure 5.11(a) suggests that the bending magnets of the DL could have been wrongly set with respect to the beam energy, and hence the correctors are compensating for this error. A possible improvement of the correction could then be to use not only the correctors, but also the strengths of the bending magnets.

5.4.2 Horizontal and vertical dispersion matching

The dispersion of the bunches that are delayed in DL and the ones that bypass it could be easily verified by using the developed application described in Section 3.2 and by using the same beam setup used for the previous orbit correction. A measurement performed towards the end of the CTF3 run of 2015 is shown in Figure 5.12. The dispersion patterns are normalised assuming the nominal dispersion (-0.605 m) at the first dispersive BPM in TL1, which is CTBPI0608H. The agreement between two beam dispersions in the horizontal plane seems to be reasonable, even if masked by the naturally high design dispersion. In the

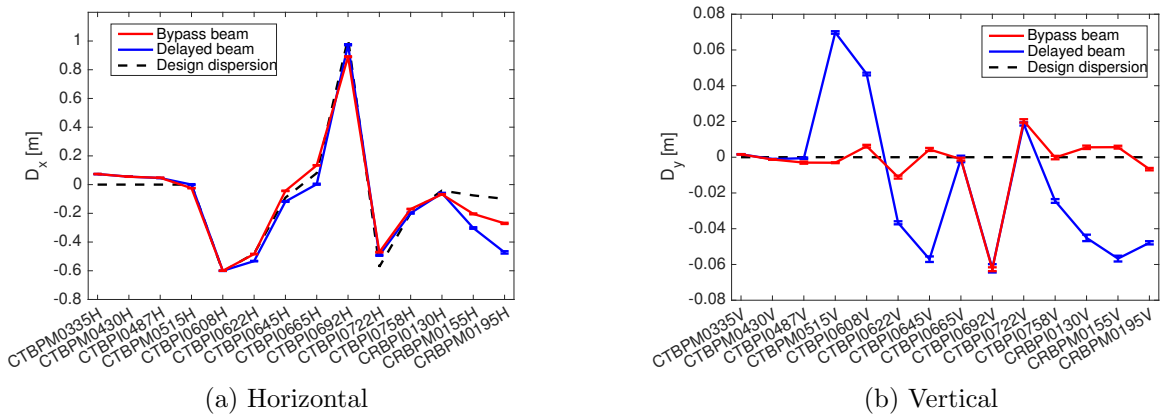


Figure 5.12: Comparison of the measured horizontal (a) and vertical (b) dispersions at the BPMs installed around the DL at CTF3 between the train of bunches that are delayed into the DL (blue) and the ones that bypass it (red). The dashed-black curve is the ideal dispersion one should expect for both trains of bunches. The BPMs up to CTBPM0487 are before the DL, while the others are after the DL.

vertical plane the agreement appears to be worse, but the scale is naturally much smaller. The behaviour of the BPM CTBPI0692 in the vertical plane is anomalous. Note that the measurement was performed a few days *before* the orbit matching presented in the previous section (Figure 5.10). It is reasonable to assume that the correction did not change the dispersion of the bypassing beam, while the different orbit of the delayed beam might have drastically changed its dispersion pattern.

For completeness it is interesting to see the data used to perform the measurements presented in Figure 5.12. Figure 5.13 shows some scatter plots for a few BPMs where the measured discrepancies between delayed and bypassing beams were more pronounced. Note

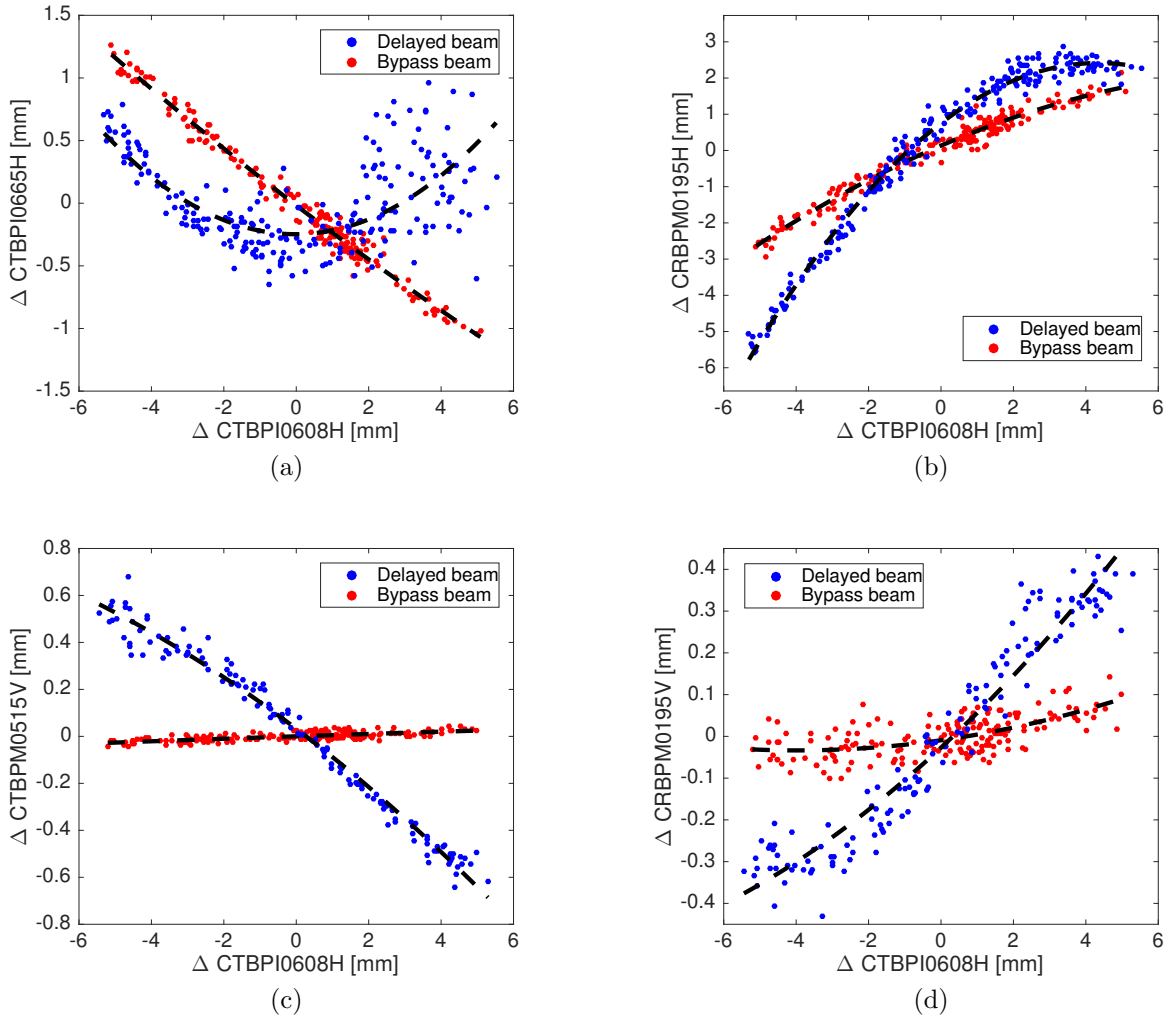


Figure 5.13: Scatter plots of the beam orbit measured at several BPMs in TL1 as a function of the horizontal orbit measured at BPM CTBPI0608. On the vertical axis are the horizontal beam position in CTBPI0665 (a) and in CRBPM0195 (b), the vertical beam position in CTBPM0515 (c) and in CRBPM0195 (d). The red points were measured with a beam bypassing the DL, while the blue points with a beam delayed in the DL. The average beam positions is subtracted independently from each dataset. The dashed-black curves represents the second order fit to the data.

that the noisy data shown in Figure 5.13(a) are an indication of beam losses during the measurement. In general in the horizontal plane the discrepancies seem to be dominated by

non-linear dispersion, while in the vertical plane the effect is clearly dominated by differences in the first-order dispersion of the two beams. From experience at CTF3 it seems hard to achieve better results in the horizontal plane, but one could think of performing an orbit *and* dispersion matching between the two beams in the vertical one. This could be a possible path to further improve the recombination quality at CTF3.

5.4.3 Transverse optics matching

The other verification that is needed in order to ensure a good recombination between the bypassing and delayed beams is the transverse optics matching of the two beams. Figure 5.14 shows the quadrupole scan data obtained before and after a recent attempt to match the horizontal transverse optics of the delayed and bypassing beams. The beam used was a nominal 1.5 GHz beam magnetically injected, or not, into the DL. The optics in use in the DL was the new one proposed in Section 4.4.2. The rematching procedure used was to

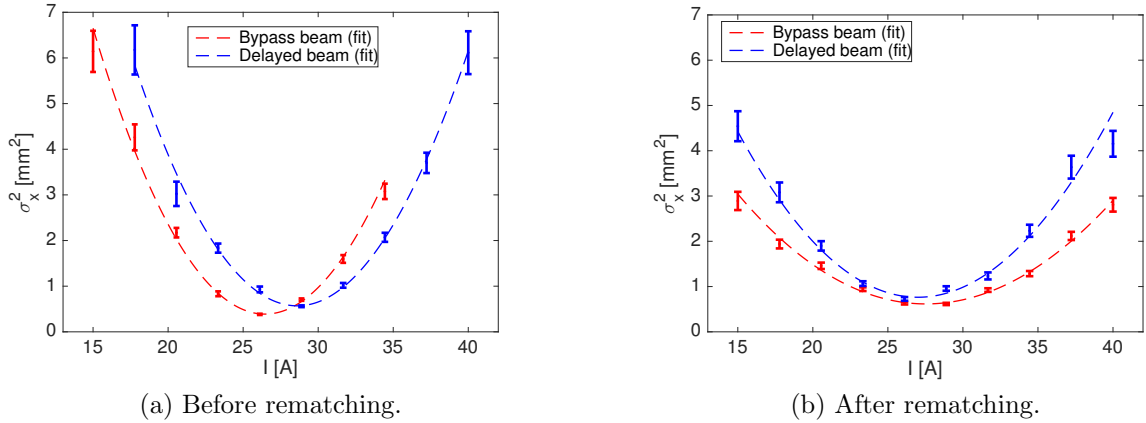


Figure 5.14: Horizontal beam variance measured at the screen CT.MTV0550 in the CTS dump line as a function of the quadrupole current used to perform quadrupole scan measurements before (a) and after (b) a first optics rematching at the end of the CTF3 linac. The error bars are computed from the Gaussian fits to the profiles measured at the screen. The dashed lines are the fits to the data corresponding to the Twiss parameters that are reported in Table 5.2. In blue are the measurements performed on a beam being delayed in the DL, while red represents the beam bypassing the DL.

adjust the quadrupoles before the DL such that the beam would arrive at the DL injection with the expected closed solution of the ring. The Twiss parameters obtained for the two beams before and after the rematching are shown in Table 5.2. Note that in Figure 5.14(a) the minimum beam size is obtained for different values of the quadrupole used for the scan, while in Figure 5.14(b) both parabolas are centred around the same minimum. This is reflected in a better matching of the β and α parameters reported in Table 5.2. The measured emittance reduction was unexpected, especially for the bypassing beam. From Figure 5.14 the emittance reduction is naively caused by the overall smaller beam variance measured during the scan.

The parameters measured and reported in Table 5.2 were not compatible a priori with

	Before correction			After correction		
	β_x [m]	α_x	ϵ_{Nx} [μm]	β_x [m]	α_x	ϵ_{Nx} [μm]
Nominal values	8.4	-0.8	-	8.4	-0.8	-
Bypass beam	13.2 ± 0.6	-0.9 ± 0.1	117 ± 3	5.9 ± 0.3	-0.6 ± 0.1	84 ± 2
Delayed beam	10.5 ± 0.4	-1.3 ± 0.1	138 ± 3	6.8 ± 0.5	-0.5 ± 0.1	120 ± 4

Table 5.2: Summary of the horizontal Twiss parameters measured in the CTS dump line for a beam bypassing the DL and one delayed in it. The first macro column contains the values before any optics correction, while the second macro column contains the values after a transverse optics matching between delayed and bypassing beams.

the desired nominal values. A second iteration of re-matching was attempted. This time also the vertical plane was considered. Figure 5.15 shows similar quadrupole scan measurement obtained after the last correction iteration. The final Twiss parameters for the different

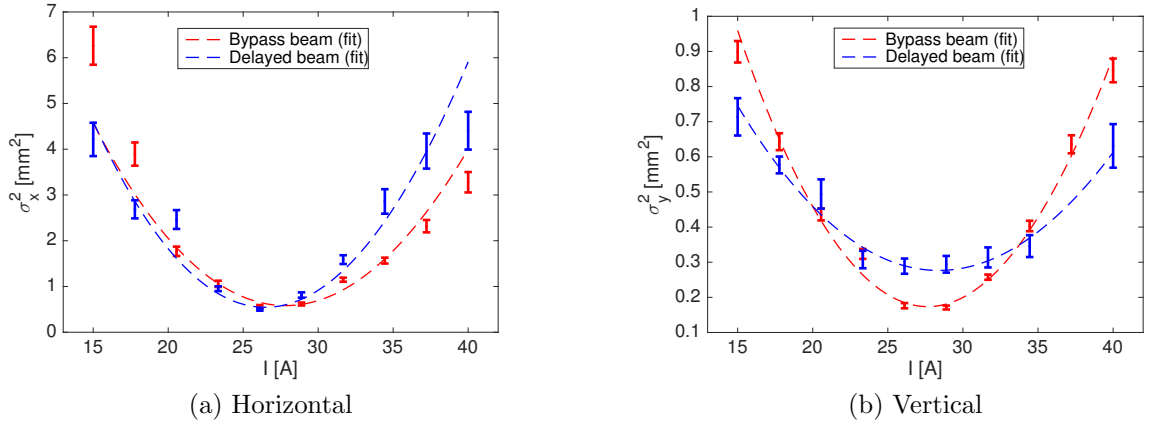


Figure 5.15: Beam variance measured at the screen CT.MTV0550 in the CTS dump line as a function of the quadrupole current used to perform quadrupole scan measurements in the horizontal (a) and vertical (b) plane after optics rematching between bypass (red) and delayed (blue) beams. The error bars are computed from the Gaussian fits to the profiles measured at the screen. The dashed lines are the fits to the data corresponding to the Twiss parameters that are reported in Table 5.3.

beams and planes are summarised in Table 5.3. One can see that in the horizontal plane the two beams seem to be reasonably matched with respect to each other and close to the nominal values. However in the vertical plane the results differ from the matching goal.

In order to better investigate what was happening it is useful to use the tomography technique presented in Section 3.4.1. The same profiles acquired to perform the quadrupole scan measurements shown in Figure 5.15 are used to produce the phase-space beam distribution reconstruction presented in Figure 5.16. Indeed from the tomography view, especially in the vertical plane, it seems that the beam was far from being Gaussian. This leads to a difficult interpretation of the β and α parameters measured with a conventional quadrupole scan. However the tomography reconstruction of the phase space suggests that the two beams are pretty well matched with respect to each other, and the vertical β parameter difference noted

	β_x [m]	α_x	ϵ_{Nx} [μm]	β_y [m]	α_y	ϵ_{Ny} [μm]
Nominal values	8.4	-0.8	-	13.5	-0.4	-
Bypass beam	7.6 ± 1.0	-0.8 ± 0.1	102 ± 6	4.6 ± 0.3	0.0 ± 0.1	65 ± 2
Delayed beam	8.9 ± 1.1	-0.6 ± 0.1	111 ± 7	2.7 ± 0.3	0.1 ± 0.1	61 ± 5

Table 5.3: Summary of the transverse Twiss parameters of the bypassing and delayed beams fitted from the quadrupole scan measurements presented in Figure 5.15.

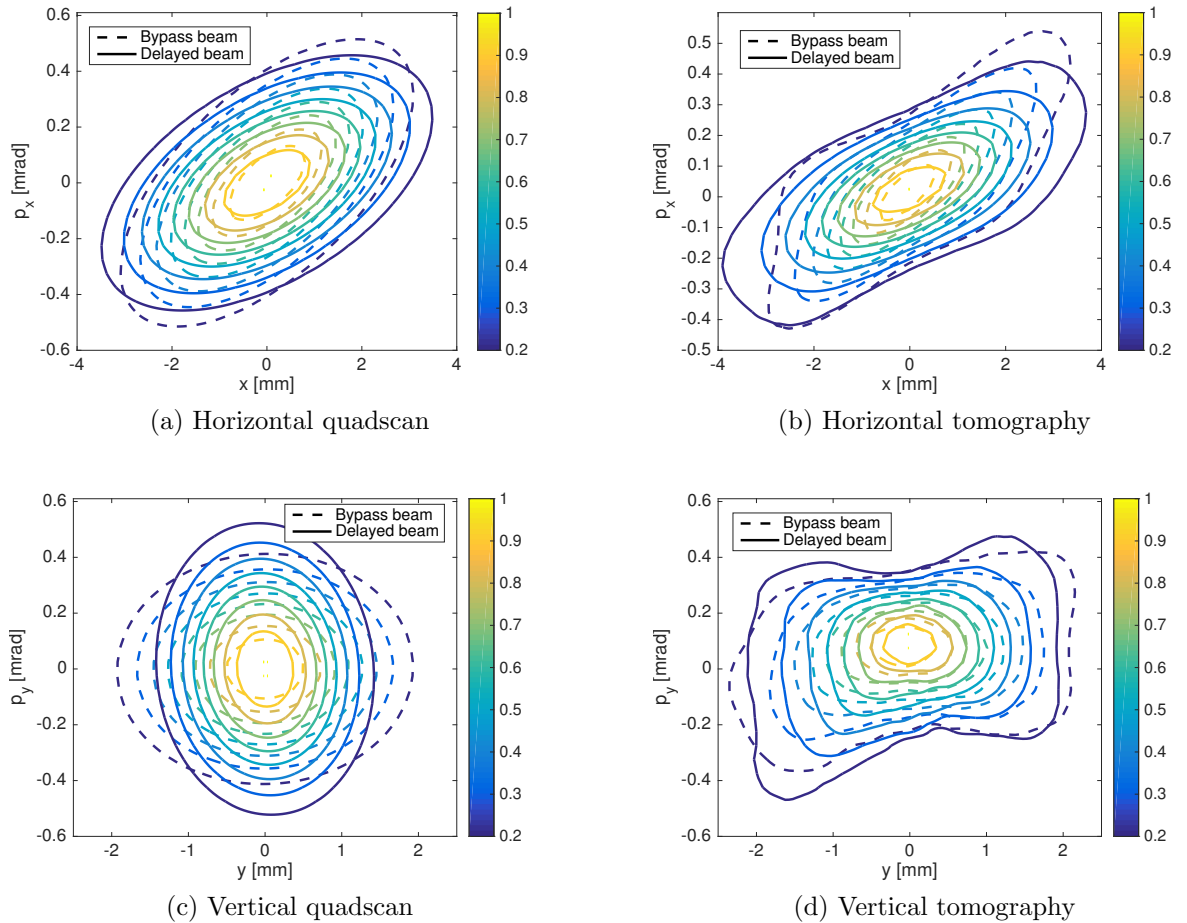


Figure 5.16: Horizontal ((a) and (b)) and vertical ((c) and (d)) phase-space distributions of the delayed and bypassing beams as measured by simple quadrupole scan ((a) and (c)) and tomographic ((b) and (d)) techniques. For both kinds of representation the same measured profile are used. The dashed contours represent the beam bypassing the DL, while the continuous ones are the distributions of the delayed beam. The colour code is the density distribution, which has been normalised to have a peak value equal to 1.

in Table 5.3 might actually be harmless. Still the non-Gaussian shape of the phase space might be a limiting factor for the overall performance of the DBRC. A dedicated study would be needed to verify the accuracy and precision of the tomographic measurements, which has not been performed yet.

5.5 Matching between different turns in CR

The next step in the beam recombination process at CTF3 is the factor-4 recombination that takes place in the Combiner Ring (CR). Here a set of measurements and corrections with the aim of improving the quality of a pure factor-4 recombination in the CR are reported. This means that all the results presented in this section have been obtained with a beam that was bypassing the DL using magnetic correctors instead of the RF deflector normally used for the factor-2 recombination. The beam generated from the linac was at 3 GHz, which was then not suitable for the full factor-8 recombination.

Note that the reported experiments were not performed in chronological order. Even in the chronological case, the facility could have been set up for different experiment from day to day, so earlier corrections and performance might not be preserved between different experiments.

5.5.1 Measurement of the transverse matching

At CTF3 it is possible to measure the transverse matching between different turns in the CR only by extracting the beam from the CR after a different number of turns, and hence measuring the Twiss parameters by means of quadrupole scans in the following transfer line (TL2).

Figure 5.17 shows a measurement performed in the early stage of the beam set-up in the late 2015 run of CTF3. Each dashed-contour curve represents the FWHM of the beam distribution after being stored in the CR for different turns. In order to be more precise, note that the “1st turn” beam is actually travelling only through half of the CR ring and immediately extracted in the following transfer line. Similarly the “2nd turn” beam is the one that does one full turn and one half in the CR, and so on. The measured Twiss parameters used for the reconstructions in Figure 5.17 are summarised in Table 5.4. Note that the location where the measurement was performed is known to measure vertical emittances that are not consistent with measurements in other parts of the facility. So far no convincing explanation has been found for this underestimation of the emittance, and further investigations are ongoing. Even if the absolute values are likely to be wrong, the relative comparison between different beam set-ups can be useful for improving the performance of the DBRC.

The phase-space representation in Figure 5.17 and the Twiss parameters reported in Table 5.4 underline a degradation of the beam quality the longer the beam is stored in the CR. Notable is the horizontal emittance after 4 turns in the CR. From Figure 5.17 one can see that the beam after 4 turns seems to be far off centre compared with the beams extracted

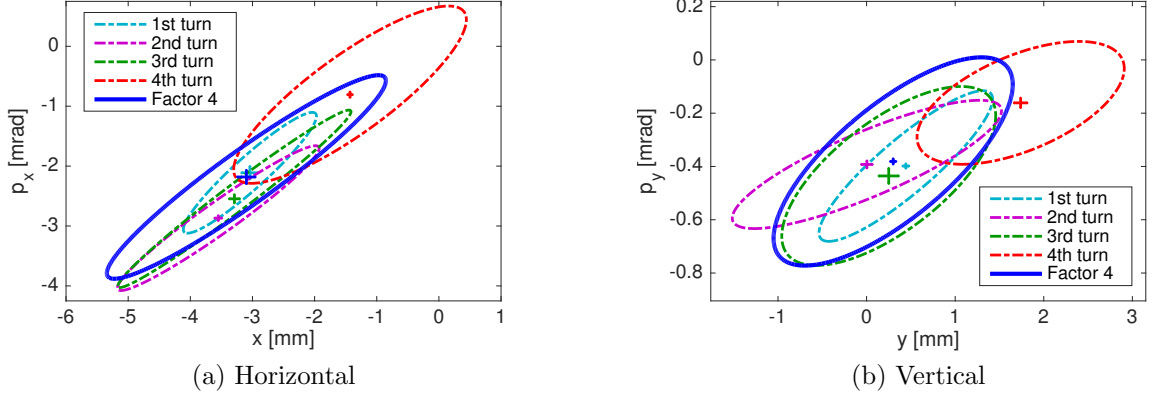


Figure 5.17: Reconstruction of the horizontal (a) and vertical (b) phase-space beam distributions after extraction from the CR (measurements performed at MTV CC.MTV0253). Each line represents the FWHM border of a reconstructed Gaussian beam based on the Twiss parameters measured by means of a quadrupole scan. The dashed lines represent measurements of beams that made different numbers of turns in the CR. The continuous-blue lines are the measurements performed on a factor-4 recombined beam. The cross at the centre of each curve represents the measured centre of the fitted Gaussian beam, and the size of the cross is the error of this measurement.

	β_x [m]	α_x	ϵ_{Nx} [μm]	β_y [m]	α_y	ϵ_{Ny} [μm]
Nominal values	8.9	-7.2	-	4.8	0	-
1 st turn beam	3.0 ± 0.7	-2.7 ± 0.6	72 ± 7	7.5 ± 0.4	-1.9 ± 0.1	24 ± 7
2 nd turn beam	5.1 ± 0.5	-3.6 ± 0.4	99 ± 4	11.5 ± 1.2	-1.5 ± 0.2	38 ± 2
3 rd turn beam	6.9 ± 0.6	-5.3 ± 0.5	98 ± 3	4.9 ± 0.4	-0.9 ± 0.1	57 ± 2
4 th turn beam	2.4 ± 0.2	-1.6 ± 0.2	281 ± 8	6.1 ± 0.7	-0.7 ± 0.2	43 ± 7
Factor-4 beam	4.1 ± 0.4	-2.9 ± 0.3	234 ± 9	5.1 ± 0.5	-1.1 ± 0.2	68 ± 3

Table 5.4: Summary of the transverse optics matching for beams stored from one to four turns in the CR and then extracted in the following transfer line. Measurement performed using screen CC.MTV0253.

earlier from the CR. In the vertical plane it might be worrying the different orientation of the ellipses representing the second and fourth turns, which might be the sign of a vertical optics mismatch. In general however the overall emittance increase experienced by the beams stored longer in the CR seems to hide most of the transverse optics mismatches.

The combined factor-4 beam can be seen as the sum of the 4 beams that travelled through different numbers of turns in the CR. The measurement performed on such a beam seems to represent well the single-turn measurements. By considering the covariance matrices of each beam (see Eq. 2.15) one can compute the expected covariance matrix for the recombined beam (see Appendix D). Assuming no error the theoretical overall emittance turns out to be $196 \mu\text{m}$ (horizontal) and $54 \mu\text{m}$ (vertical) which are values slightly below the respective measurements shown in the last row of Table 5.4.

No attempt was made in the latest CTF3 run to improve the transverse matching. Instead more effort was put into trying to work on the orbit closure of the ring between different turns, and to studying the dispersion effects which might affect also the quadrupole scan measurements presented here.

5.5.2 Orbit matching

The transverse optics measurements presented in the previous sections show a possible orbit mismatch in the CR, which is clearly visible in Figure 5.17 between the beam stored in the CR for a single turn and the one stored for 4 turns. In order to inject the beam into the closed orbit of the ring one has two possibilities:

- Modify the incoming orbit such that the beam is injected onto the natural closed orbit of the ring.
- Modify the closed orbit of the ring by acting on the correctors installed in the ring itself, and so match the closed orbit of the ring with the incoming orbit.

The first method is probably the cleanest: one could measure the closed orbit of the ring by taking the average orbit of a beam circulating for many turns, hence steer the incoming beam such that the first turn orbit equals the closed orbit previously measured. On the other hand this requires one to have a beam already circulating for many turns into the ring, and have BPMs able to measure precisely the orbit for several turns. Normally this is not the case at CTF3. From experience at CTF3 it turns out that the most effective approach is the second. The orbit closure correction is performed by acting on the correctors of the CR while minimising the difference between the orbits of the first and second turns in the ring.

Figure 5.18 shows an example of such a correction. Not all the BPMs of the CR were used, but only those in dispersion-free areas of the ring. This was an attempt to minimise the energy effects observed in BPMs that are normally in regions with high dispersion. The strengths of the correctors that were used for the correction are shown in Figure 5.19. For the vertical plane it is important to point out that the feedback tool was able not only to

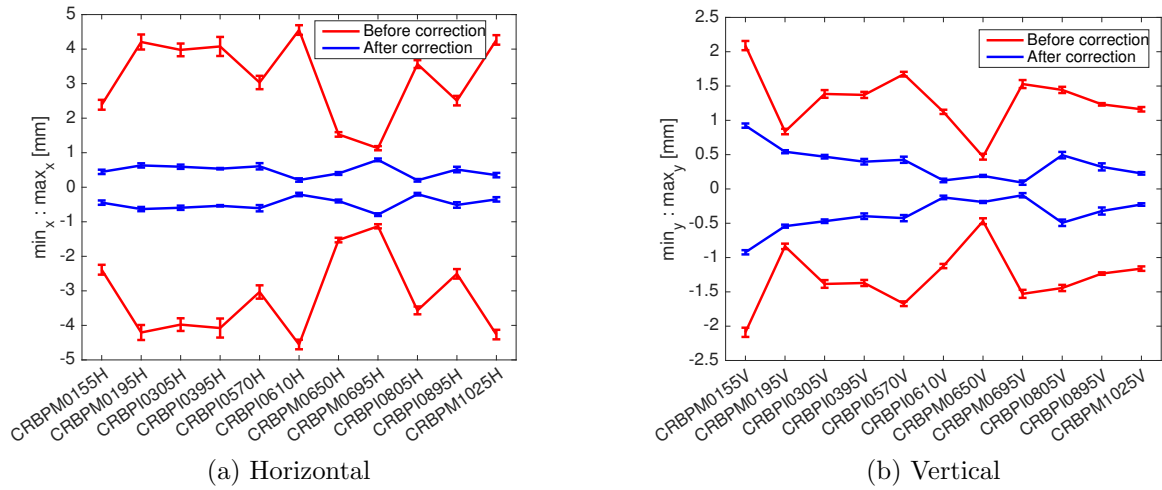


Figure 5.18: Horizontal (a) and vertical (b) orbit corridors within which the orbit of a beam circulating for 4 turns in the CR are confined before (red) and after (blue) an orbit closure correction.

heavily reduce the orbit mismatch, but also to remove the unnecessary power of the last three correctors in the ring. At the BPMs shown in Figure 5.18 the orbit difference between different turns was reduced to below 1 mm in the horizontal plane and 0.5 mm in the vertical. The result obtained should be compared with the tolerances for an ideal machine that were presented in Section 4.2.3 (Figure 4.13). Note that for the vertical plane the statistical emittance growth one should expect should be below 30%, while in the horizontal plane things are more critical, being close to the 70% envelope of Figure 4.13(a).

Unfortunately there was not enough time to systematically measure the initial and final Twiss parameters of the different turns before and after the orbit correction presented in Figure 5.18. Only for the vertical plane a measurement of the Twiss parameters of a factor-4 combined beam was taken right before and after the orbit correction presented here, while for the horizontal plane this measurement was performed only after the orbit correction. For

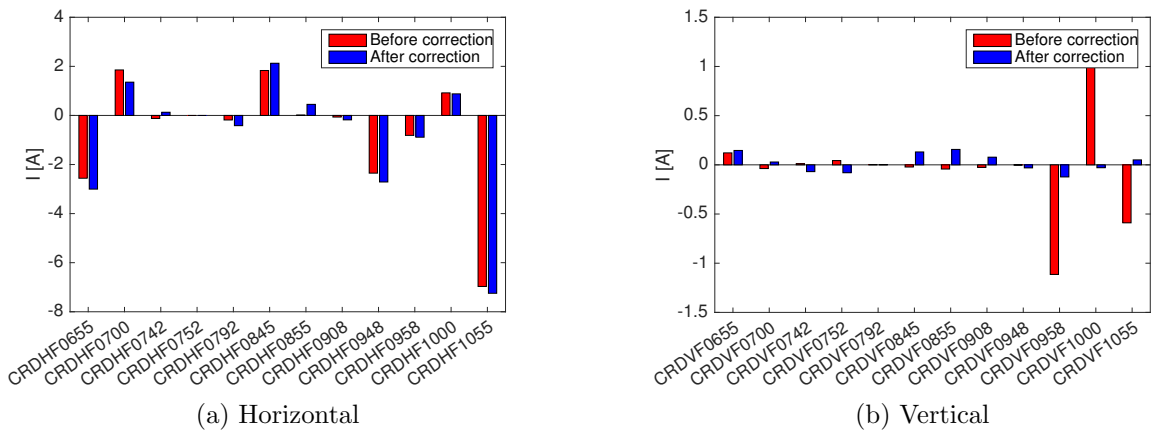


Figure 5.19: Strength of the horizontal (a) and vertical (b) correctors in the CR before (red) and after (blue) an orbit closure correction.

	β_x [m]	α_x	ϵ_{Nx} [μm]	β_y [m]	α_y	ϵ_{Ny} [μm]
Nominal values	8.9	-7.2	-	4.8	0	-
Before correction	4.1 ± 0.4	-2.9 ± 0.3	234 ± 9	7.2 ± 0.7	-1.4 ± 0.2	66 ± 3
After correction	7.1 ± 0.3	-5.3 ± 0.3	173 ± 4	6.7 ± 1.3	-1.5 ± 0.4	37 ± 3

Table 5.5: Comparison between Twiss parameters of a factor-4 beam measured at screen CC.MTV0253 before and after orbit closure in the CR. Note that for the horizontal plane the measurement was performed a few days before the correction.

the horizontal plane one can consider as a reference the latest measurement presented in the previous section. Figure 5.20 shows the comparison between the beam variance for the different scans, while the fitted Twiss parameters are reported in Table 5.5. In the vertical plane the effect of the orbit correction is clear, and it results in almost a factor-2 reduction of the overall emittance. For the horizontal plane, as already stated, no measurement right before the correction is available, so it is possible that many parameters could have changed between the quadrupole scan measurements. Still a 25% emittance reduction is visible and also the Twiss parameters α_x and β_x seem to get closer to the nominal values.

In general one can state that the orbit closure correction brings an evident benefit in the combined beam quality, which is still believed to be one of the main source of emittance growth in the CR.

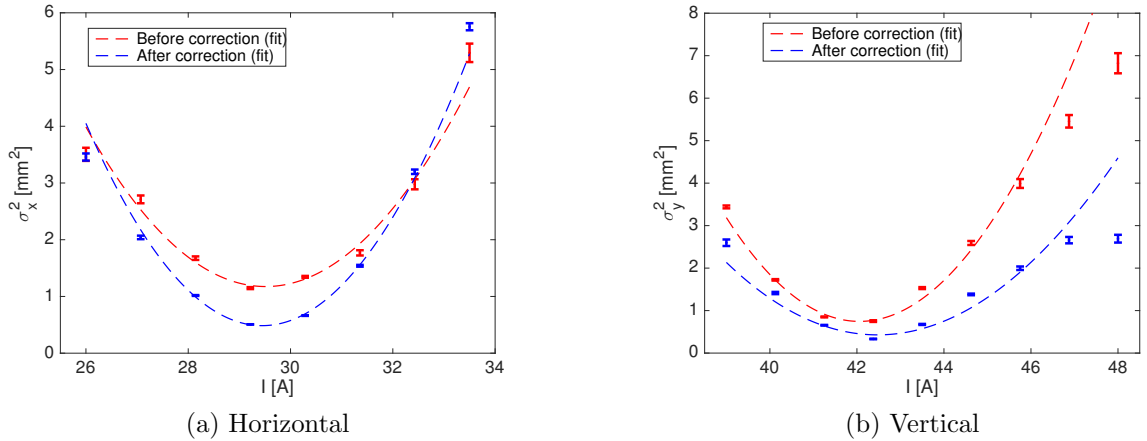


Figure 5.20: Beam variance measured at the screen CC.MTV0253 in TL2 as a function of the quadrupole current used to perform quadrupole scan measurements in the horizontal (a) and vertical (b) plane. The red points are relative to a combined factor-4 beam before orbit closure correction, while in blue is the same scan after the correction presented in Figure 5.18. The error bars are computed from the Gaussian fits to the profiles measured at the screen. The dashed lines are the fits to the data corresponding to the Twiss parameters that are reported in Table 5.5. Note that the red scan in the horizontal plane was performed a few days before the orbit correction.

5.5.3 Dispersion Target Steering in the CR

A possible further step with respect to the orbit closure could be to verify and eventually correct the horizontal dispersion in the CR by means of Dispersion Target Steering (DTS). By definition the dispersion is the difference between orbits of beams (or particles) with different energies. If the wanted dispersion is zero, i.e. DFS, one has not to worry too much about BPM calibrations and/or to know with precision the energy variation induced: the aim of the correction is to see no orbit variation for any reasonable beam-energy change. Clearly things are more complicated for Dispersion Target Steering (DTS) and a simple calibration issue can easily lead to unsuccessful results. In order to apply DTS the strategy adopted at CTF3 is to measure first the “nominal” dispersion expected by measuring the orbit response after scaling all the bending magnets in the line under consideration. As seen in Section 2.4 this is equivalent to measure the *first-order* dispersion generated by the bending magnets, which are assumed to be the only sources of dispersion in an ideal machine. This kind of measurement can serve as a calibration of the BPMs³, and also to verify that the quadrupoles in a line are properly set for the actual energy of the beam.

Figure 5.21 shows a measurement of the nominal dispersion pattern measured by scaling the bending magnet of the CR. The measured dispersion is in agreement with the expected design dispersion. The big discrepancy at CR.BPI0925 is probably due to faulty electronics, as well as some unexpected dispersion at the last BPM CR.BPI1070⁴. It has to be stressed that the measured value is *not* the actual dispersion of the ring, but the dispersion generated by the presence of the bending magnets. This measurement, to first approximation, is blind to element misalignments, correctors and non-zero incoming orbit. The fact that no dispersion is measured in this way, where one should expect zero dispersion, is a sign of the correct setting of the quadrupoles in the line. If the quadrupoles were set incorrectly for the beam energy, a clear discrepancy would be visible in the middle of the ring, where a long straight section with no dispersion is present.

Confident of the nominal dispersion measurement, a dispersion measurement and correction using all the correctors available in the ring was performed. The outcome of the correction is shown in Figure 5.22. By changing the beam current generated by the thermionic gun of the CTF3 Drive Beam one obtains beams with different energies. The orbit difference reveals the actual dispersion, which now includes both the nominal dispersion and the additional contributions of any undesired kicks (e.g. element misalignments). Note in Figure 5.22 that a non-zero dispersion is actually injected into the ring probably due to an error in the upstream transfer line TL1. The DTS was performed by using only the correctors installed in the ring. For this reason one cannot expect to be able to correct dispersion in the first part of the ring, but only in the second part. In this region the correction is indeed effective, and one is able to obtain a dispersion that is close to the nominal value.

However this turned out to be the wrong approach: first because the correction, by

³Note that here no normalisation is necessary: scaling the magnets by +1% is equivalent at first order to scale the energy by -1%. The only source of systematic error is the knowledge of the behaviour of the bending magnet as a function of the current provided to it.

⁴This discrepancy was observed only at the time of analysing the data, further investigation will be needed to understand its source.

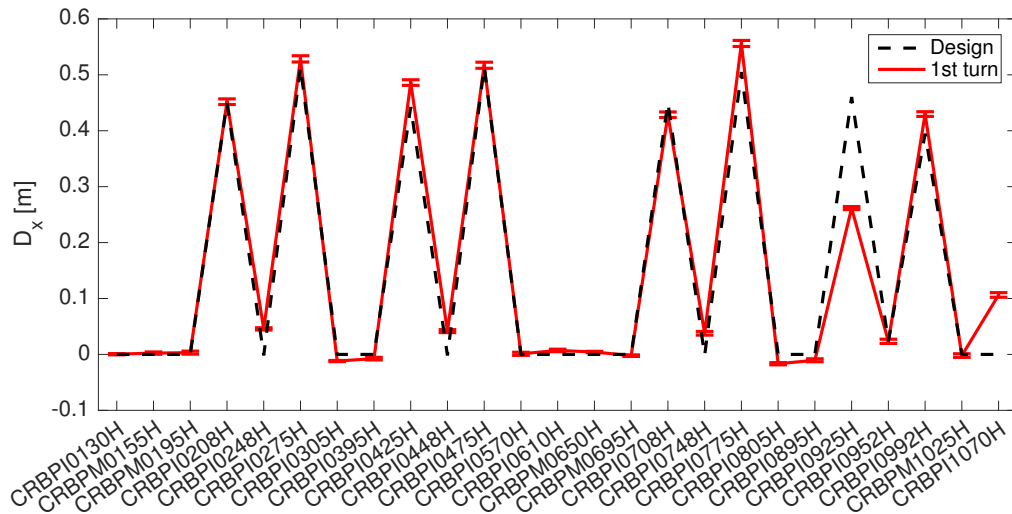


Figure 5.21: In red is the measured “nominal” dispersion at the BPMs installed in the CR. The measurement was performed by scaling the main bending magnets in the ring. The dispersion shown is the one for the first turn in the ring. Dashed-black is the dispersion expected for an ideal CR.

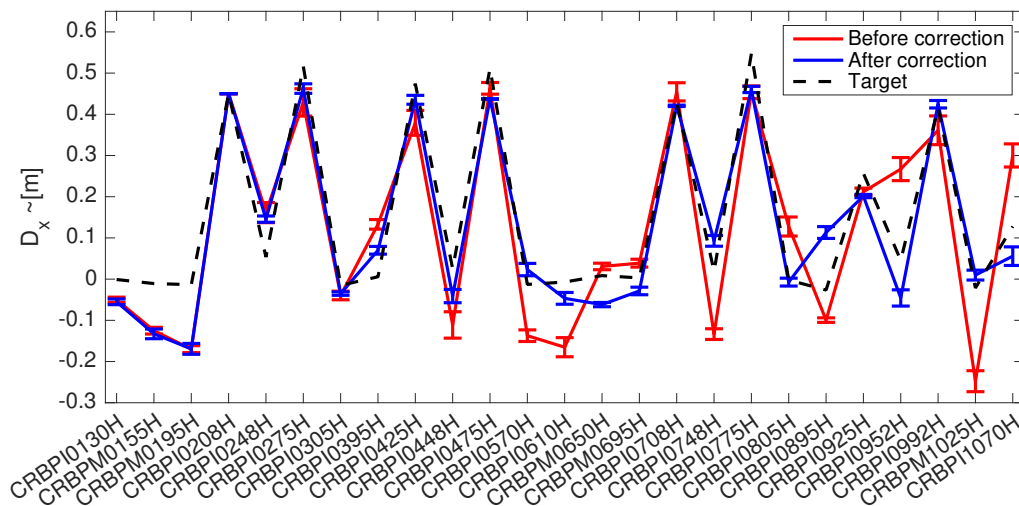
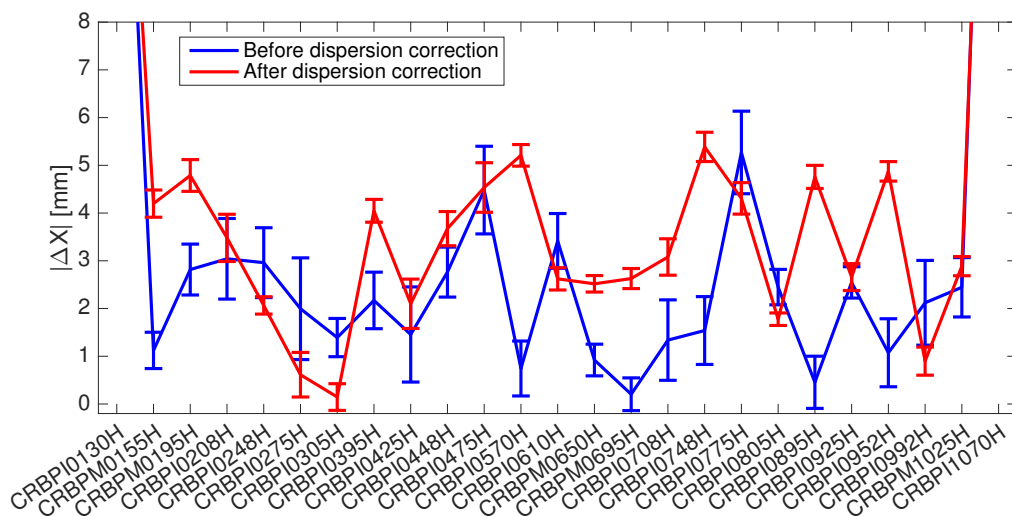


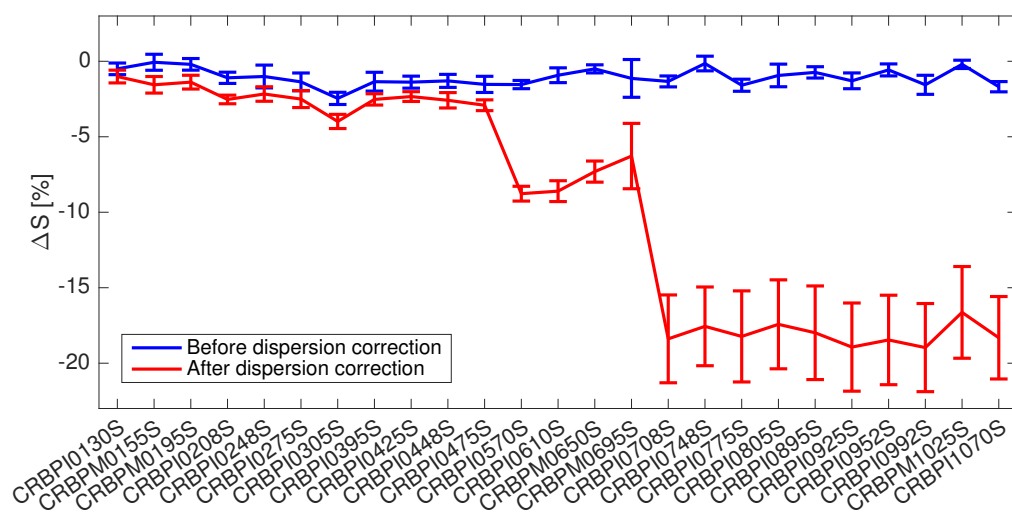
Figure 5.22: First turn horizontal dispersion measurement before (red) and after (blue) DTS at the BPMs installed in the CR. Dashed-black is the target dispersion sought during the correction that was measured before by scaling the bending magnets of the ring. The measurement was performed by varying the beam current at the source of the linac and by normalising the response with BPM CR.BPI0208.

definition, could not change the dispersion in the first part of the ring; second because it turned out that the actual orbit of the beam, which was not considered during the correction, was not suitable for storing the beam for more than one turn. Figure 5.23 shows the effect of the correction on the orbit closure and beam current transmission from the first turn to the second. Though the starting orbit was already not optimum in terms of closure, after the correction the orbit closure was even worse. Moreover the beam transport was heavily affected in turns later than the first. Conceptually this is not a surprise since the correction was targeting a different observable.

A second attempt was made by targeting both dispersion and orbit matching. This time, instead of looking at only the first turn in the CR, 4 turns were considered. The optimum



(a)



(b)

Figure 5.23: Difference between the first- and second-turn horizontal beam orbit (a) and beam current (b) at the BPMs in the CR. In blue are the values before DTS in the CR, while in red are those after DTS.

would be to match orbit and dispersion for all four turns for all 25 BPMs installed in the ring. This gives $25 \times 2 \times 3$ observables (i.e. orbit and dispersion differences between the first and later turns). Due to the high number of observables and small number of correctors (24) one can simplify the problem by requiring only the matching for the 4 BPMs installed near the extraction from the ring. The result of this attempt is presented in Figure 5.24. The result is not excellent, but an overall reduction of orbit and dispersion closure on those 4 BPMs is visible. Moreover a new quadrupole scan measurement at screen CC.MTV0253 for a factor-4 beam gave a final emittance of $112 \mu\text{m}$ to be compared with the $173 \mu\text{m}$ achieved with the simpler orbit closure correction between first and second turns in the ring presented in the previous section.

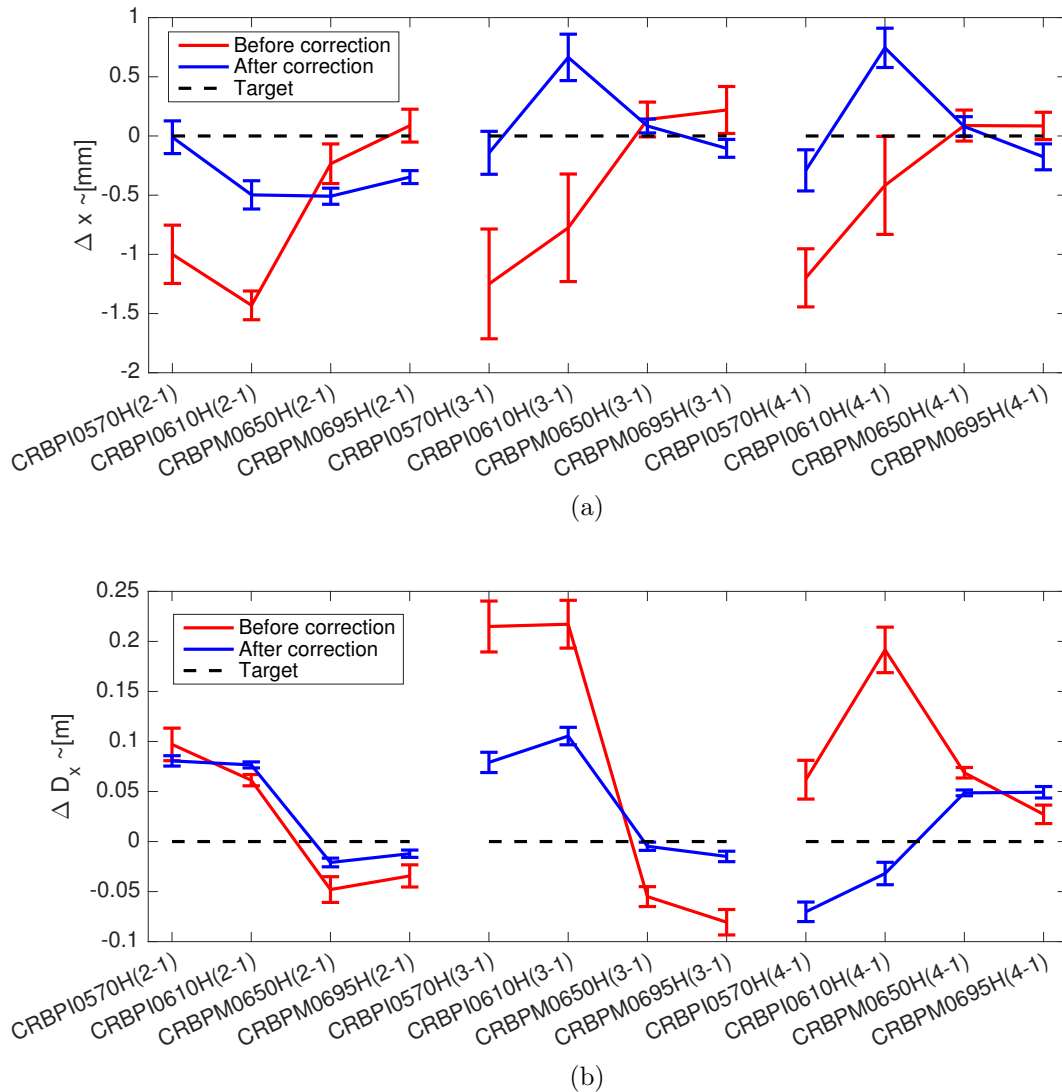


Figure 5.24: Results of the dispersion and orbit matching in the 4 BPMs near the extraction from the CR for a beam circulating for 4 turns. (a) the orbit difference between the 2nd, 3rd and 4th and the 1st turn; (b) the dispersion differences. In red are the values before the correction while in blue are those after the correction. Dashed-black lines represent the targets that in this case are all zero.

All these tests were conducted in a limited amount of time and probably not enough care was put on the stability of the beam generated in the linac. One should bear in mind that the study presented in Section 4.2 revealed strong non-linear dispersion effects that can play an important role also here. In order to better understand, Figure 5.25 shows the expected modelled behaviour of the non-linear dispersion at some BPMs for 4 consecutive turns. For each BPM it shows the simple energy dependence of the orbit and the point-by-point tangent to the curve, i.e. the linear dispersion one would measure if the average beam momentum were different than the set-up of all the magnetic elements. Note that for a mean energy deviation of less than 1%, which is comparable with a machine drift, one should expect a separation of the orbits for different turns up to 1 mm (see for example Figure 5.25(a) and (e)). The behaviour of the linear dispersion is similar: here a variation of 10 cm is easily expected. These values should be compared with the orbit and dispersion closure reported in Figure 5.24.

In general the results achieved demonstrate the ability to control a series of effects up to the level where the natural stability of the machine might start to play the dominant role. The next step would require a better knowledge of the accuracy of the beam instrumentation and more refined control of the long-term stability of the beam, which is being addressed at CTF3 by complementary work [103, 104].

5.6 Latest beam quality

The set-up and tuning of the Drive Beam recombination at CTF3 requires generally a few weeks of operation. Many corrections are necessary, and most of them are coupled with each other. It is then difficult to say which correction contributed the most to the final recombination quality. However an interesting measurement was performed on the last day of CTF3 operation of 2015: a factor-8 beam was finally set up for RF power production in the later CLEX experimental area. Quadrupole scan measurements were then performed at the end of the TL2 line using the screen CC.MTV0970. In order to verify the quality of the recombination, at least partially, the measurements were also performed after dumping all the bunches going via the DL, and so generating an unnatural factor-4 recombination in the CR. The measured Twiss parameters for the horizontal and vertical plane and both set-ups are reported in Table 5.6, while a graphical representation of the data collected is shown in Figure 5.26.

Note that these measurements were taken after the beam was empirically optimised to

	β_x [m]	α_x	ϵ_{Nx} [μm]	β_y [m]	α_y	ϵ_{Ny} [μm]
Factor-8 beam	9.9 ± 1.1	0.7 ± 0.1	467 ± 27	27.8 ± 2.2	-6.1 ± 0.5	199 ± 7
Without DL bunches	9.0 ± 0.5	0.6 ± 0.1	371 ± 10	26.4 ± 2.2	-5.9 ± 0.5	195 ± 7

Table 5.6: Comparison of the measured Twiss parameter between the final factor-8 beam of 2015 and the same beam without the bunches going via the DL. The measurements were performed with the screen CC.MTV0970 at the end of DBRC.

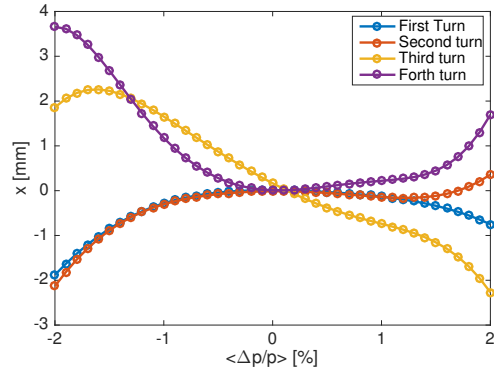
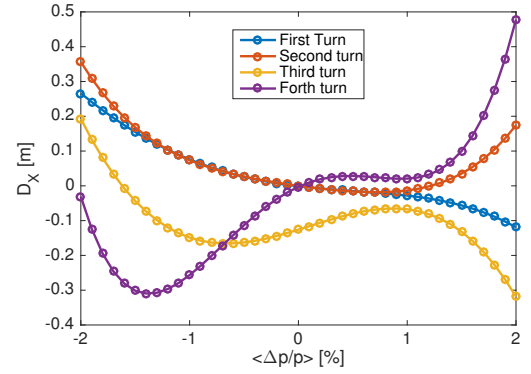
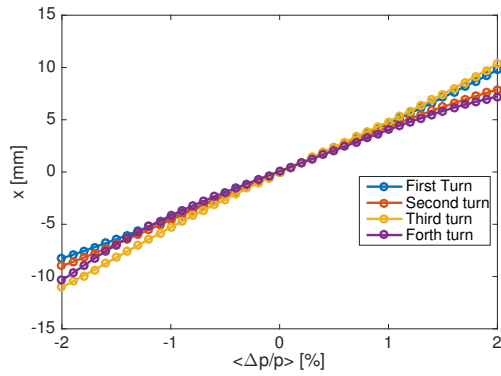
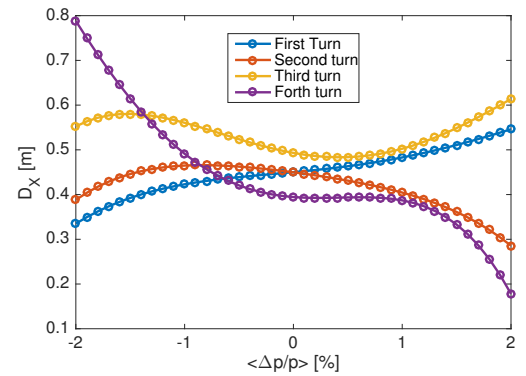
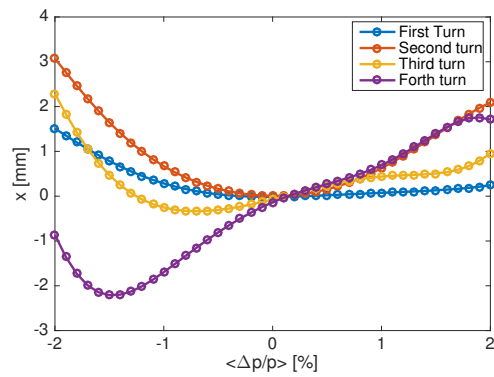
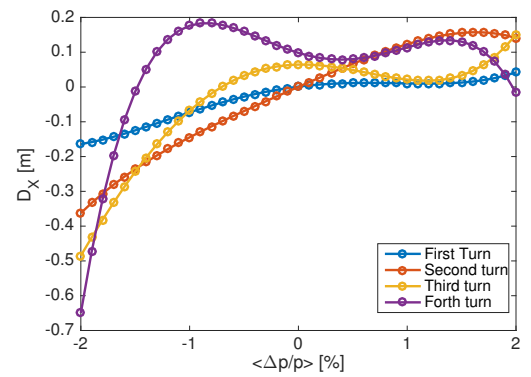
(a) CRBPM0155H ($\langle x \rangle$)(b) CRBPM0155H ($\frac{dx}{d\Delta p/p_0}$)(c) CRBPI0208H ($\langle x \rangle$)(d) CRBPI0208H ($\frac{dx}{d\Delta p/p_0}$)(e) CRBPI0248H ($\langle x \rangle$)(f) CRBPI0248H ($\frac{dx}{d\Delta p/p_0}$)

Figure 5.25: Expected orbit (first column of plots) and linear dispersion (second column of plots) as a function of a hypothetical mean beam-momentum error. Behaviour obtained by means of MAD-X simulations for an ideal CR. Each row shows the behaviour in a different BPM in the CR. Each colour representst a different turn in the CR.

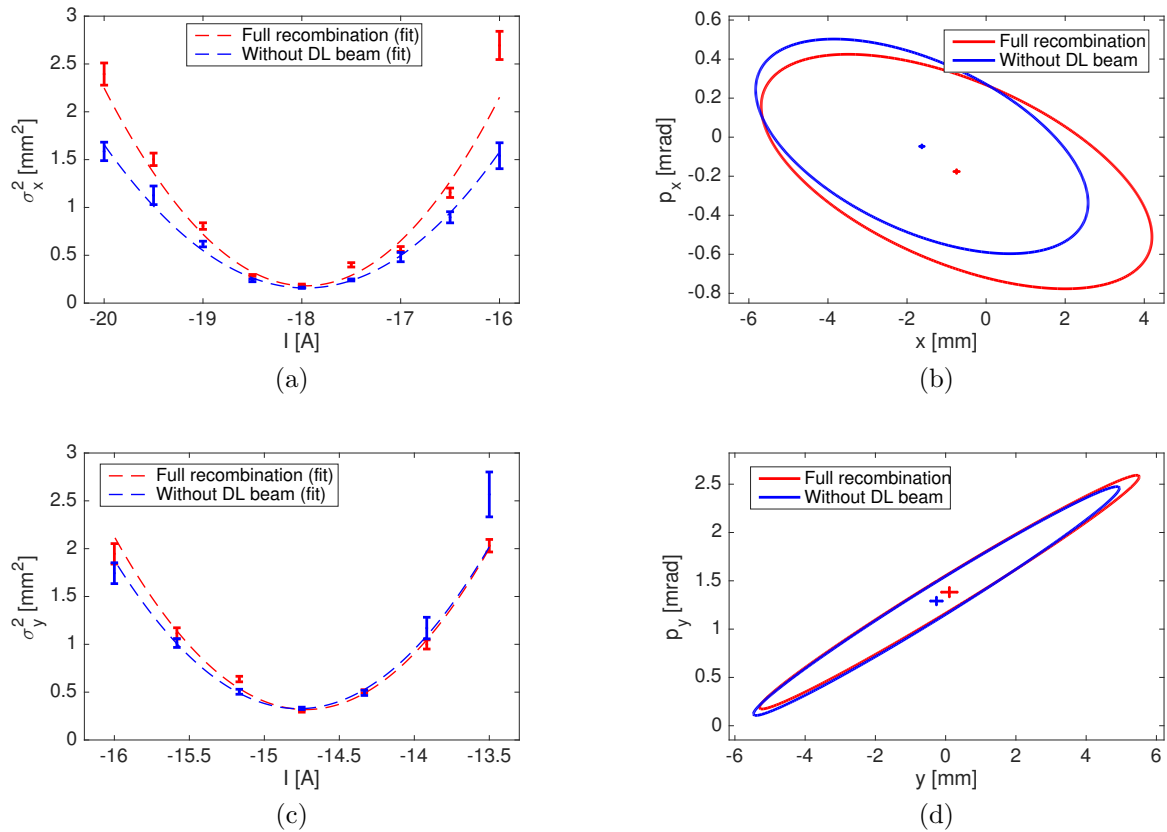


Figure 5.26: Beam variance measured at the screen CC.MTV0970 in TL2 as a function of the quadrupole current used to perform quadrupole scan measurements in the horizontal (a) and vertical (c) planes. The measured Twiss parameters, reported in Table 5.6, are used to construct the contour plots in Figures (b) and (d). These represents in phase space the FWHM borders of a hypothetical Gaussian beam with covariance given by the measured Twiss parameters. The red traces are relative to a fully combined factor-8 beam, while in blue are the equivalent quadrupole scans but dumping earlier the bunches that normally go via the DL.

obtain the optimum power production in the CLEX area. This means that the length of the DL and CR could have been adjusted by acting on the wiggler magnets installed in the two rings, and also the beam setup could have been manipulated at the injector. This might have spoiled part of the optimisation performed earlier, but it is interesting to see that in the vertical plane, normally the plane less affected by energy and ring length variations, there is no substantial difference with or without the DL bunches. For the horizontal plane things are not as good, but still an increase of only 25% in ϵ_x between the beam without the DL component and the full factor-8 beam is a sign of good recombination quality. Moreover from Figure 5.26(b) one can see that the increase in ϵ_x seems to be due to an orbit error of the order of 2 mm in the DL recombination. This could be easily explained by the empirical optimisations that were performed to maximise the power production.

5.7 Other Applications of the Generic Feedback

The possible application of the feedback tool developed at CTF3 and described in Section 3.3 are not restricted to orbit and dispersion corrections. Due to generality of the question and the abstract implementation of the “linearFeedback” tool, it was possible to apply the same software to completely different scenarios. The feedback helped to further improve not only the beam at CTF3, but it was possible to even implement an orbit correction at the Proton Synchrotron at CERN. In this section a few additional examples of use of the feedback are presented.

5.7.1 Optimisation of the Bunching System

The RF used to produce and accelerate the Drive Beam at CTF3 is generated by 3 GHz klystrons that produce 5.5 μs RF pulses of about 30 MW. Each RF pulse is then compressed by a special RF pulse compressor cavity [105] down to the required 1.4 μs pulse length and roughly doubling the pulse power. Such a pulse is then used to feed two accelerating structures in the Drive Beam linac. This RF gymnastic increases the efficiency of the system and allows one to quickly accelerate the 4 A Drive Beam up to the nominal energy of about 130 MeV at the end of the linac. The drawback is that the phase along the produced 1.4 μs RF pulse is not constant, but has typically a parabolic shape with a maximum phase variation along the pulse of about 10 degrees at 3 GHz. The RF used for the bunching of the DC beam is actually not compressed, so it naturally does not have this specific phase variation along the pulse. In order to ensure a homogenous acceleration and bunch quality all along the pulse also the bunching has to be performed with the same phase variation. Such a phase variation along the pulse is then programmed by means of a waveform generator installed in the Low Level RF (LLRF) production chain of the buncher klystron.

An indirect measurement of the matching between the produced bunch frequency variation and the first accelerating RF is measurable by an RF pickup (BPR) [106, 107] installed right after the injector. This device, referred to as CL.BPR0475, provides a measurement of the variation of a combination of bunch length and bunch charge along the pulse. Any

mismatch in phase or amplitude between the RF used for the bunching and the RF used for the first beam acceleration results in a non-uniform bunching quality and so a non-flat BPR signal.

Figure 5.27 shows a typical correction of the flatness of the BPR Waveguide signal (CL.BPR0475W) by acting on the waveform programmed for the buncher klystron (MKS02). For this result a 3GHz beam was set-up. The correction used all the features of the devel-

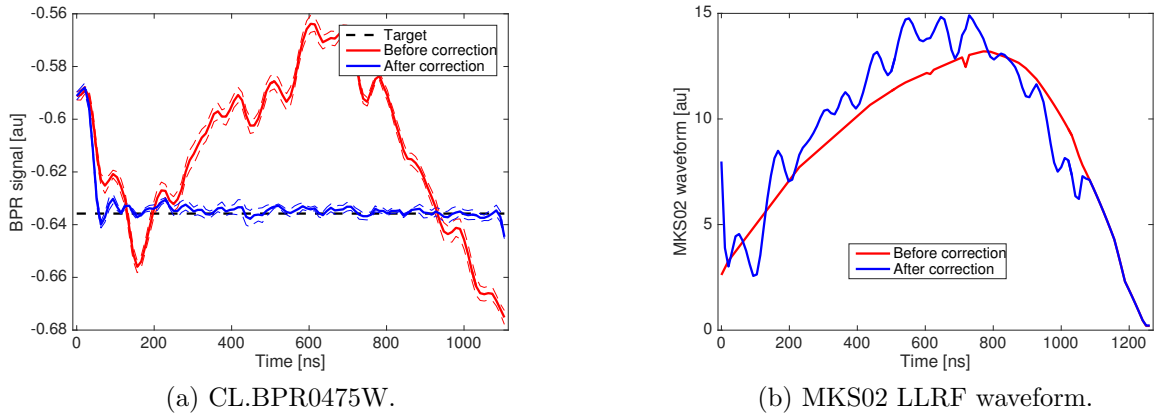


Figure 5.27: Typical result of an optimisation of the BPR CL.BPR0475W signal at CTF3. (a) shows the BPR signal along the beam pulse in time domain. The dashed-black line in (a) is the target signal requested to the feedback application. The dashed-red and dashed-blue lines are the statistical variation of the BPR signal. (b) shows part of the LLRF waveform setting as a function of time for klystron MKS02. In red are the measurements and settings before correction, while in blue are after the correction.

oped linearFeedback tool. First the variation of the BPR signal induced by a variation of the LLRF waveform was measured. Afterwards the waveform was altered as little as possible to obtain the desired flatness of the BPR signal. Practically it is difficult to demonstrate the benefits of such a correction. However from experience a flatter BPR signal finally turns into a smaller beam-energy spread of the produced beam, which is then easier to transport and recombine in the DBRC.

5.7.2 Energy Stabilisation Along the Pulse

At the end of the Drive Beam linac one would like to obtain a flat mean energy distribution along the $1.2 \mu\text{s}$ beam pulse. This might not be the case due to the RF pulse compression adopted at CTF3 and consequent variations along the pulse of RF power and phase, or more simply due to non-uniformity of the bunch charge. Similar to the BPR correction presented in the previous section, a possible feedback implemented at CTF3 is to modify the Low Level RF (LLRF) waveform programmed for the last klystron (MKS15) in order to obtain flat beam energy afterwards. The horizontal beam orbit along the pulse at the first dispersive BPM (CT.BPI0680H) is used as beam energy profile monitor by normalising the orbit with the expected dispersion ($D_x = 0.605 \text{ m}$).

Figure 5.28 shows a typical result obtained with a 1.5 GHz beam, i.e. a beam normally

setup for a factor-8 recombination. The eight 140 ns sub-trains are easily visible along the 1.3 μs -long pulse in Figure 5.28(a). The long transient at the head of each sub-train is due to the “too slow” phase switching of the TWTs used in the injector to flip by 180 degrees at 1.5 GHz the pre-bunching of the beam. The bandwidth of the RF distribution and of the accelerating cavities does not allow one to correct this long transient, so the correction is operated only on the central part of each sub-train, i.e. where a target is defined in Figure 5.28(a). Note in Figure 5.28(b) that the new waveform tries to compensate part of

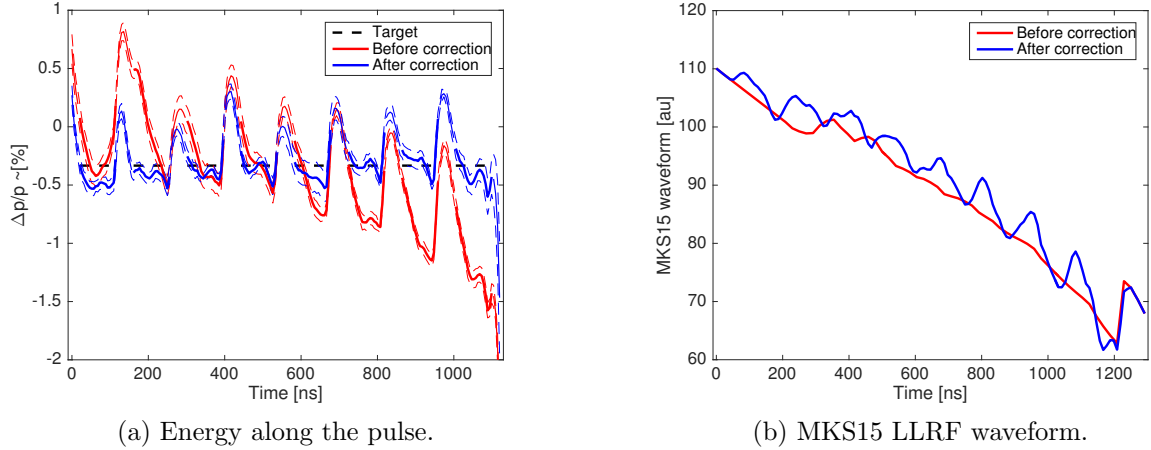


Figure 5.28: Typical result of beam energy flattening along a 1.5GHz beam at CTF3. (a) shows the energy variation along the beam pulse measured at the first dispersive BPM in TL1 (CT.BPI0680H) assuming nominal dispersion. The dashed-black line in (a) is the target momentum requested of the feedback application. The dashed-red and dashed-blue lines are the statistical variation of the BPM signal. (b) shows part of the LRF waveform setting as a function of time for klystron MKS15. In red are the measurements and settings before correction, while in blue are those after the correction.

the long transient between one sub-train and the other. Finally all the sub-trains lie on the same energy in Figure 5.28(a), and also the excursion of the transient is reduced.

Such a correction is clearly beneficial for the quality of the finally-combined beam because it heavily reduces the overall energy spread of the beam. The simulations presented in Section 4.3 predict that the overall beam-energy spread has an effect on the emittance due to the non-linear dispersion arising in the DBRC. Improvements could be measured on the factor-8 combined beam by means of quadrupole scan measurements. Figure 5.29 shows the improvement in beam variance while performing a quadrupole scan of the combined beam before and after the correction. The fitted Twiss parameters are reported in Table 5.7.

5.7.3 Injection bump closure at the CERN Proton Synchrotron

The result presented here shows the power of the developed feedback tool by demonstrating its ability to be easily adapted to a different accelerator of the CERN accelerator complex, in particular at the Proton Synchrotron (PS).

In order to inject the hadron beam into the PS the closed orbit of the ring is *locally*

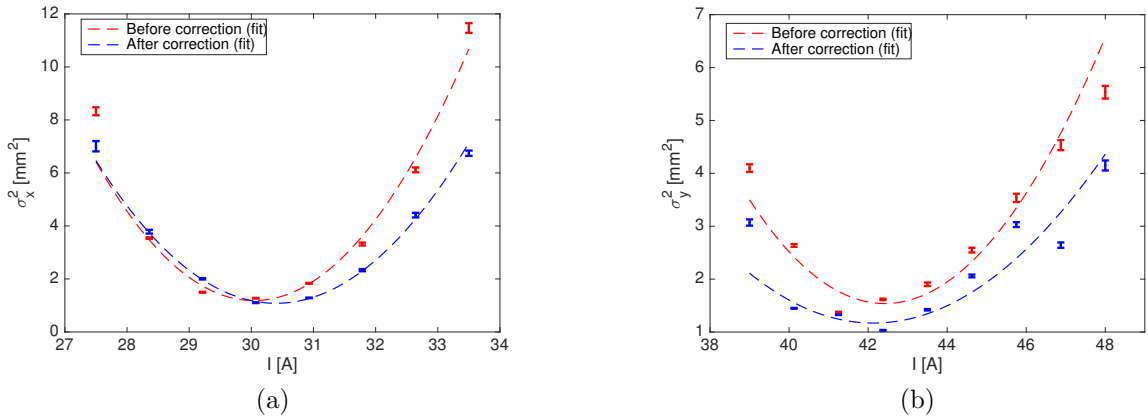


Figure 5.29: Beam variance measured at the screen CC.MTV0253 in TL2 as a function of the quadrupole current used to perform quadrupole scan measurements in the horizontal (a) and vertical (b) planes. These represent in phase space the FWHM borders of a hypothetical Gaussian beam with covariance given by the measured Twiss parameters. In red are the measurements performed before the energy flattening correction presented in Figure 5.28, while in blue are the measurements after the correction.

	β_x [m]	α_x	ϵ_{Nx} [μm]	β_y [m]	α_y	ϵ_{Ny} [μm]
Nominal values	8.9	-7.2	-	4.8	0	-
Before correction	6.5 ± 0.6	-5.3 ± 0.5	446 ± 18	4.0 ± 0.7	-0.8 ± 0.2	76 ± 5
After correction	5.5 ± 0.2	-4.8 ± 0.2	380 ± 6	3.5 ± 0.9	-0.6 ± 0.2	50 ± 5

Table 5.7: Twiss parameters measured using screen CC.MTV0253 for a factor-8 combined beam before and after energy flattening correction shown in Figure 5.29.

adjusted in order to make the circulating beam approach the injection septa [108]. This adjustment is performed by using orbit bumpers that should create an orbit bump only at the injection location without altering the orbit elsewhere in the ring. This bump is then reduced and finally removed right after injection in order to increase the acceptance during beam acceleration and final extraction. The usual approach at the PS was to set-up the bump mainly according to the MAD-X model of the injection area, and afterwards perform empirical corrections by hand. Clearly any error in the bumper strength or imperfections in the model of the machine could result in a leakage of orbit outside the injection location, eventually leading to phase-space filamentation and consequent beam quality degradation.

LinearFeedback provides all the tools necessary to attack the problem. The ability to measure the response matrix on the real machine allows one to drop any model-driven assumption. Moreover in a storage ring this kind of correction is easier than at CTF3, because the time the beam is stored into the ring is much longer, and the measurement of the beam orbit over many turns is more accurate. The solution proposed is similar to that performed in the CR at CTF3 for the closed orbit. The idea was first to measure the closed orbit as the orbit of the beam much later after injection, when no injection bump was active anymore, and any residual orbit oscillation is already dumped by other effects. Afterwards the injection bump correction consisted of varying the 4 bumpers' strengths until the orbit

during injection was the same as the orbit of the steady circulating beam, except for the single BPM that is actually installed within the injection bump itself.

Figure 5.30 shows a typical result of such a correction performed in mid 2015. For the correction the closed orbit was measured as the orbit average of a few turns around turn 1000, while the bumped orbit was measured over an average of a few turns around turn 100. The bump was completely switched off around turn 500. Note how only one BPM trace is affected by the bump after the correction (Figure 5.30(b)), while all the other traces are only slightly perturbed. The fast oscillation which is still visible even after the correction on each trace is still a sign of a small injection error, which is translated into additional betatron motion [109]. In order to achieve the closed bump of Figure 5.30(b) the first and last bumpers had to be changed by almost 10%, while the other two inner bumpers were basically untouched.

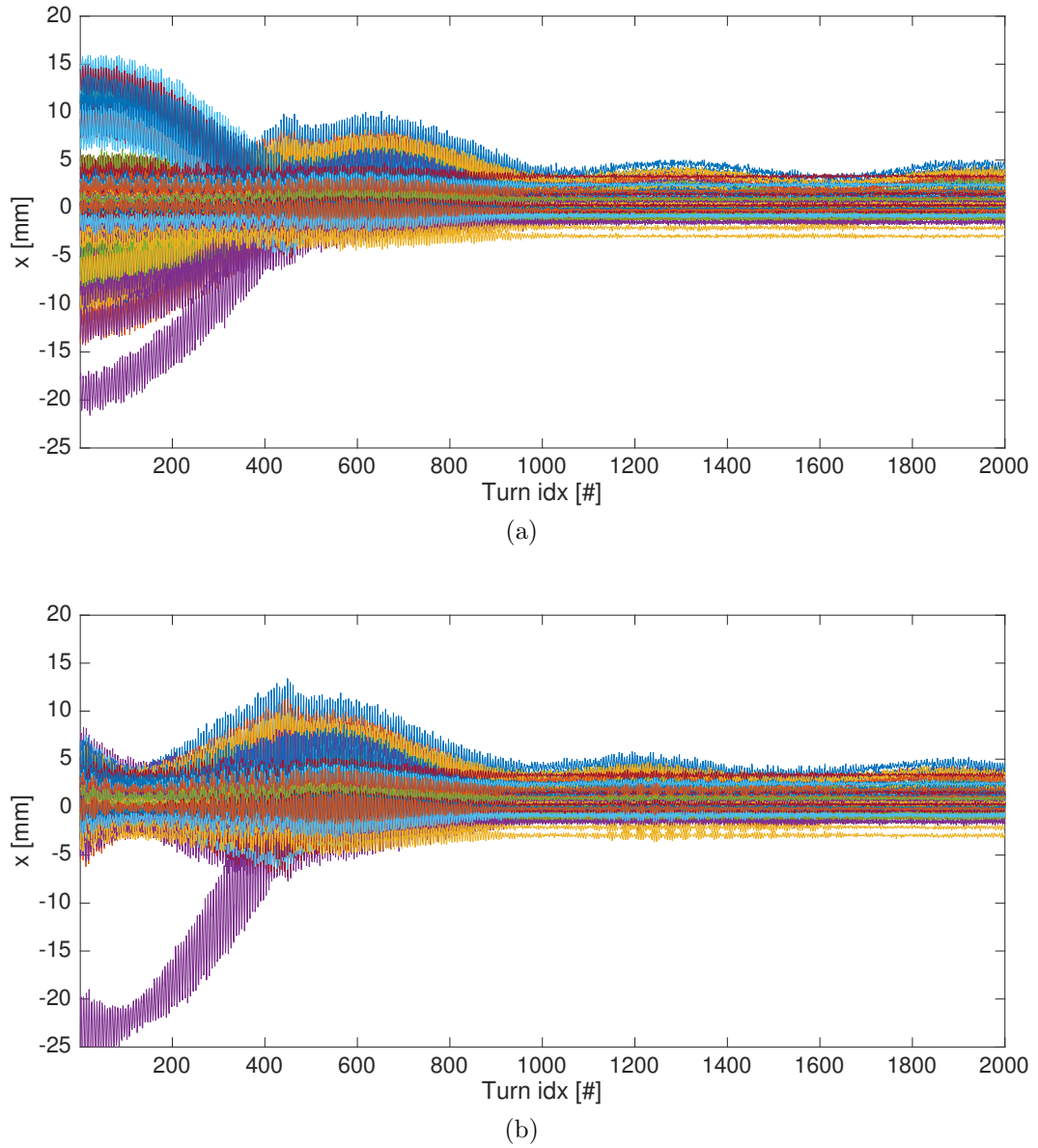


Figure 5.30: Result of orbit bump closure correction at injection in the CERN Proton Synchrotron. (a) the orbit measured at each BPM installed in the ring as a function of the number of turns performed by the beam before the orbit correction. (b) the situation after the correction. Each coloured line represents a different BPM.

Chapter 6

Conclusions

6.1 Summary

The CLIC design is one of the leading alternatives for a future lepton collider. The Drive Beam and its recombination in the DBRC is one of the key components of the design. One of the requirements for the DBRC is to produce a recombined beam with $150 \mu\text{m}$ normalised emittance in both horizontal and vertical phase spaces and an intensity stability of 0.75×10^{-3} [3]. CTF3 aims to prove the feasibility of the recombination process with the same requirements [5].

The initial goal of this thesis was to optimise the Drive Beam recombination at CTF3 by controlling the orbit of the beam for the different paths through the DBRC, and hence limit the emittance growth due to unclosed orbits. This required a deep understanding of CTF3 and its recombination process, and the development of a custom strategy suitable for this unique problem.

In order to operate the machine efficiently, the knowledge of the accelerator control system architecture was fundamental. A generic slow-feedback framework has been developed in MATLAB. It allows one to optimise any desired signal that is available in the CERN accelerator control system by acting on the chosen actuators. The ease of use of this tool allows one to set-up a feedback to optimise and stabilise any parameter that (quasi-)linearly responds to some controllable excitation. In this framework an orbit and dispersion correction tool has been developed. The existing tools and procedures for measuring the transverse properties of the beam have been further developed. A novel strategy and tool for measuring the nominal and actual dispersion in any beamline of CTF3 and the tomographic reconstruction of the beam phase spaces have been introduced.

A custom definition of emittance has been proposed to study the effect of the orbit mismatch between bunches that arrive at the end of the DBRC after taking different paths. This allowed one to specify tolerances on the main measurable quantities available, i.e. beam orbit and transverse phase-space measurements at specific locations.

The main sources of emittance growth in the DBRC due to the high energy-spread of the beam have been identified and analysed. MAD-X simulations showed that the strong optics

of the DBRC induces non-linear distortions of the transverse optics and dispersion. The DL optics was found to be the main source of non-linear horizontal dispersion, which leads to the generation of tails in transverse phase space. Such tails make the set-up of the beam in the DL challenging and they can affect the beam-current stability. This is in agreement with the experienced difficulties of the operators in transporting the beam through the DL without losses.

A new DL optics has been proposed to cure the emittance growth due to non-linear dispersion. It is based only on linear elements (i.e. quadrupoles), which makes it easier to implement than the previous corrections based on sextupoles. The new optics has been successfully implemented and tested. Preliminary results show that the new optics allows one to improve the operability and tunability of the DBRC, with positive effects on the combined-beam current stability.

A campaign of orbit and dispersion measurement and correction has been performed in the key parts of the DBRC. As a verification of the correction method and tools, the horizontal and vertical dispersion in the linac has been corrected leading to a remarkable improvement of the beam quality as measured at the entrance of the DBRC. DFS was also successfully applied in the vertical plane in the TL1 transfer line.

The ability to close the orbit mismatch between the bunches delayed in the DL and the ones bypassing it has been demonstrated within ± 0.2 mm, which would correspond to an emittance growth of less than 30% for an ideal monochromatic beam. In the CR a similar correction has been performed. Here the final orbit closure between the 4 circulating trains of bunches was $\approx \pm 0.5$ mm in the vertical and $\approx \pm 1$ mm in the horizontal. This result was not fully satisfactory because it would correspond to a horizontal emittance increase of about 70 % if the beam were monochromatic. In order to further improve the performance of the recombination in the CR, horizontal DTS was attempted. Even though the correction was successful in itself, the recombination performance was degraded due to beam losses. This suggested a more global approach where both dispersion and orbit were closed in the extraction line of the CR, which eventually gave the best recombined beam. Further investigations using the MAD-X model of the CR revealed that even for an ideal machine the orbit and dispersion distortions due to small beam-energy errors are comparable with the measured mismatches.

Transverse optics verifications have also been conducted and presented. In general no major issues have been found, however the quadrupole scan technique used for the measurements is particularly affected by the residual dispersion that might reach the screen used to measure the beam size. The developed tomographic technique proved to be useful in the qualitative analysis of the beam phase-space distribution.

The developed feedback tool has proved to be helpful also for a wider range of applications. At CTF3 it has been used to adjust the bunching in the Drive Beam injector and to correct the energy variation along the pulse at the end of the linac. A custom application has also been developed for correcting the injection orbit of the PS at CERN.

6.2 Suggestions for further work

At the time of writing the record normalised emittance measured at the end of TL2, i.e. right before the CLEX experimental area, is about $500 \mu\text{m}$ in the horizontal and $150 \mu\text{m}$ in the vertical planes. The required $150 \mu\text{m}$ horizontal emittance seems still far from being achieved. The main difference between vertical and horizontal planes is the presence in the latter of all the bends and kicks that are imposed on the beam during the recombination process. In this plane are then concentrated most of the energy-related effects, and non-linear dispersion seems to be the predominant effect as shown by all simulations and experimental observations presented in this thesis. The optimisation of the DL optics was a positive experience. One could try to further optimise not only the DL, but also the optics of TL1 and CR. Even though they seem to contribute less to the overall emittance growth, one might be able to gain in dynamic aperture, which could be extremely useful for reaching the beam-current stability goals of CTF3. Moreover the simulations presented in this work do not take into account any machine imperfections. In reality it is well known that the alignment of the beamline at CTF3 is not ideal, and it might be interesting to quantify the effects on the beam quality.

The discrepancies between MAD-X and PTC simulations has also to be understood and addressed. If PTC_TWISS is most accurate one might better consider the results presented in Figure 4.39. The strong chromatic aberration of the vertical phase space might be one of the main sources of beam losses that are experienced in the DL. In that case one might want to repeat the optimisation procedure for the DL optics specifically targeting a less pronounced chromaticity in this plane.

From the point of view of the beam-based correction, all the developed tools seem to cover all the needs for which they have been developed. One should now invest more resources in improving the accuracy of the instrumentation and measurement procedures. For example, from Figure 5.25 it is evident that a 1% error in determining the energy of the beam has a strong impact on the orbit and dispersion closure in the CR. BPMs are the main sources of information for all orbit- and energy-related measurements, and so they should be the first devices to be better characterised. Unfortunately the diversity of the BPM types installed in CTF3 does not facilitate this task. The transverse optics measurements have also shown accuracy limitations. There are still inconsistencies between different measurement locations, and uncorrected dispersion seems to spoil any absolute measurement not carefully performed. New procedures and new ideas to verify such a measurements should be evaluated.

Another aspect that has not yet been fully analysed is the presence of the RF deflectors necessary to the recombination process. These also act on the beam in the horizontal plane, and they may couple the longitudinal and horizontal phase spaces. Preliminary simulations presented in Section 4.3 show a remarkable lengthening of the off-energy tails of the bunches that could support this hypothesis. However there are still strong discrepancies between MAD-X and PTC simulations (see Figure 4.24) which may completely change the full picture. As a cross check it might be interesting to simulate the beam recombination process using the newly available PLACET2 [87] code, which can fully simulate the behaviour of the RF deflectors.

Appendix A

Periodic Lattice Solution

In a ring, or in general in any periodic transfer line, one is often interested in finding the closed solution, i.e. the α , β and so γ .

From Eq. 2.7 one knows how a Σ matrix evolves knowing the transfer matrix \mathbf{R}_{0S} , and so how to evolve the Twiss parameters. Written in the form of Eq. 2.20, the problem of finding the periodic solution where initial and final Twiss parameters are identical is equivalent to finding an eigenvector of the 3×3 matrix of Eq. 2.20 with eigenvalue equal to 1. One needs then to solve the problem:

$$\begin{aligned} \begin{pmatrix} A^2 & -2AB & B^2 \\ -AC & AD + BC & -BD \\ C^2 & -2CD & D^2 \end{pmatrix} \begin{pmatrix} \beta \\ \alpha \\ \gamma \end{pmatrix} - \begin{pmatrix} 1 & 0 & 0 \\ 0 & 1 & 0 \\ 0 & 0 & 1 \end{pmatrix} \begin{pmatrix} \beta \\ \alpha \\ \gamma \end{pmatrix} = 0 \\ \begin{pmatrix} A^2 - 1 & -2AB & B^2 \\ -AC & AD + BC - 1 & -BD \\ C^2 & -2CD & D^2 - 1 \end{pmatrix} \begin{pmatrix} \beta \\ \alpha \\ \gamma \end{pmatrix} = 0 \end{aligned} \quad (\text{A.1})$$

that has a non trivial solution if and only if the determinant of the 3×3 matrix of Eq. A.1 is equal to 0. Taking into account Eq. 2.19 one can also write the relation

$$AD - BC = 1 \quad (\text{A.2})$$

and so:

$$D = \frac{1 + BC}{A} \quad \text{if } A \neq 0 \quad (\text{A.3})$$

$$C = -\frac{1}{B} \quad \text{if } A = 0 \quad (\text{A.4})$$

In the case of $A = 0$ the determinant of the matrix of Eq. A.1 becomes

$$\begin{aligned} \det \begin{pmatrix} -1 & 0 & B^2 \\ 0 & -2 & -BD \\ 1/B^2 & 2D/B & D^2 - 1 \end{pmatrix} = \\ = 2(D^2 - 1) + 2 - 2D^2 = 0. \end{aligned} \quad (\text{A.5})$$

In the case of $A \neq 0$ one can also verify that:

$$\det \begin{pmatrix} A^2 - 1 & -2AB & B^2 \\ -AC & 2BC & -\frac{B(1+BC)}{A} \\ C^2 & -2\frac{C(1+BC)}{A} & \frac{(1+BC)^2}{A^2} - 1 \end{pmatrix} = 0 \quad (\text{A.6})$$

Eqs. A.5 and A.6 say that it always exists a solution of the matrix in Eq. A.1.

It is possible to compute analytically the solution of the system, but one needs to distinguish between different cases:

$$\begin{pmatrix} \beta \\ \alpha \\ \gamma \end{pmatrix} = k \begin{pmatrix} -\frac{B}{C} \\ -\frac{A-D}{2C} \\ 1 \end{pmatrix} \quad \text{if } A \neq 0; C \neq 0 \quad (\text{A.7})$$

$$= k \begin{pmatrix} \frac{2AB}{A^2-1} \\ 1 \\ 0 \end{pmatrix} \quad \text{if } A \neq 0; C = 0 \quad (\text{A.8})$$

$$= k \begin{pmatrix} B^2 \\ -\frac{BD}{2} \\ 1 \end{pmatrix} \quad \text{if } A = 0; (B \neq 0; C = -\frac{1}{B}) \quad (\text{A.9})$$

where k is a free scalar constant $\neq 0$. Not every solution can be physically acceptable. The solution has to be compatible with the definition of γ , Eq. 2.13, and $\beta > 0$. Solution A.8 is excluded because from Eq. 2.13 it must also be $\gamma > 0$. For the solution A.7 one can write the relation:

$$k = \sqrt{\frac{-4C^2}{(A+D)^2 - 4}} \quad (\text{A.10})$$

that has a real solution only if

$$(A+D)^2 - 4 < 0. \quad (\text{A.11})$$

For the solution A.9 it must be

$$k = \frac{2}{B} \sqrt{\frac{1}{4-D^2}} \quad (\text{A.12})$$

that has a real solution only if

$$D^2 < 4. \quad (\text{A.13})$$

To summarise, one has the following cases:

- if $A \neq 0; C \neq 0; (A+D)^2 - 4 < 0$; then

$$\begin{pmatrix} \beta \\ \alpha \\ \gamma \end{pmatrix} = k \begin{pmatrix} -\frac{B}{C} \\ -\frac{A-D}{2C} \\ 1 \end{pmatrix} \quad k = \sqrt{\frac{-4C^2}{(A+D)^2 - 4}} \quad (\text{A.14})$$

- if $A = 0$; $(B \neq 0; C = -1/B)$ ¹; $D^2 < 4$; then

$$\begin{pmatrix} \beta \\ \alpha \\ \gamma \end{pmatrix} = k \begin{pmatrix} B^2 \\ \frac{-BD}{2} \\ 1 \end{pmatrix} \quad k = \frac{2}{B} \sqrt{\frac{1}{4 - D^2}} \quad (\text{A.15})$$

and no acceptable periodic solution otherwise. Note that in general a periodic solution exists only if:

$$|\text{Tr}(\mathbf{R}_{0S})| < 2 \quad \text{and } C \neq 0. \quad (\text{A.16})$$

In the literature this is also referred as the *stability criterion* [44, 39].

¹These conditions follow by the condition of $\det(\mathbf{R}_{0S}) = 1$.

Appendix B

Verification of the main assumptions

In this work many assumptions have been made in order to simplify the treatment of the physics behind the DBRC at CTF3. This appendix provides some justification by giving the order of magnitude of the main effects considering the Drive Beam parameters.

B.1 Ideal, Gaussian initial beam

For all simulations a perfectly Gaussian beam in all transverse and longitudinal phase spaces without coupling is assumed. The aim of the simulations is not to represent the real beam, but to understand and optimise the performance of the DBRC from an ideal point of view. Of course a detailed optimisation would imply a better modelling of the incoming beam, and a detailed investigation on all *higher* order effects that can only be achieved by intensive and extensive tracking simulations.

B.2 Synchrotron radiation

One of the main reasons to justify the study of a linear lepton collider instead of a circular one is the effect of synchrotron radiation that limits the maximum beam energy reachable in rings. In the DBRC rings are still necessary to perform the Drive Beam recombination, but the beam energy is much lower compared to the colliding main beams. Let us consider the case of the DL at CTF3. In practical units the energy loss by an electron after a single turn in a ring of radius ρ is [39]:

$$\Delta E_{electron}[\text{keV}] = 88.46 \frac{(E[\text{GeV}])^4}{\rho[\text{m}]} \quad (\text{B.1})$$

The energy of the beam is < 140 MeV. The bending radius of the DL bending magnets is $\rho \approx L_{bend}/\theta_{bend} \approx 0.56/(\pi/6) \approx 1[\text{m}]$. This leads to an energy loss per turn of $\approx 34[\text{eV}]$. The energy spread of the beam is about $\sigma_{\Delta p/p} \approx 0.6\% \approx 840\text{keV}$, hence there are a few order of magnitude difference between the natural energy spread and the additional spread eventually induced by synchrotron radiation.

A more serious effect could be the Coherent Synchrotron Radiation (CSR) which is the enhancement of the synchrotron radiation power that can be emitted by short and dense bunches¹. Simulations for this effect have been carried out during the design of CTF3 [5] and for CLIC in [3]. CSR effects depends on the bunch intensity, length and on the geometry and properties of the vacuum chamber that are difficult to simulate. In order to avoid CSR effects in the DBRC, a magnetic chicane to elongate the bunch length before the DBRC and to re-compress it after the recombination have been studied and implemented at CTF3. In the present work the assumption is that the bunch length is or can be made long enough not to encounter this problem. Still, as reported in [3], a final verification and optimisation of CSR effects will need to be addressed for the final CLIC design.

B.3 Betatron linearity

In this work the transfer lines are assumed to be perfectly linear for monochromatic beams, even when sextupoles are powered.

Even though non-linearities might arise from magnet fringe fields and imperfections, these are normally relevant only for long lattices and in particular storage rings where the beam crosses the same element many times. The DBRC at CTF3 is mainly made of quadrupoles and bending magnets, and the maximum length traveled by the beam is about 350 m.

In order to be sure that such non-linearities are negligible compared to the effects presented in Section 4.3, a simple PTC_TRACK of a few particles representing the envelope of a typical monochromatic beam has been performed. The worst scenario is presented here by considering a beam taking the longest path in the DBRC (1 turn in the DL, 3¹/₂ turns in the CR) and with the DL sextupoles powered as in Table 4.5. The simulated beam parameters are summarised in the following table:

Nominal beam momentum	140 [MeV/c]
Energy offset	0.6 [%]
Energy spread (σ_p)	0 [%]
Normalised horizontal emittance (ϵ_{Nx})	60 [μm]
Normalised vertical emittance (ϵ_{Ny})	100 [μm]

Note the non-zero beam energy offset with respect to the nominal beam momentum.

Figure B.1 shows the outcome of the simulation. Each ellipse represents the border at one, two and three sigma with respect to the simulated beam parameters. One can clearly observe that there is a difference between the response matrices computed with standard MAD-X TWISS and PTC_TWISS, as seen already in Chapter 4. On the other hand the PTC_TWISS and PTC_TRACK results are consistent. The only difference is driven by the non-linearities that are taken into account only by PTC_TRACK. The deformations are more pronounced for the outer ellipses as expected.

¹A recent introduction and reference about CSR can be found in [110].

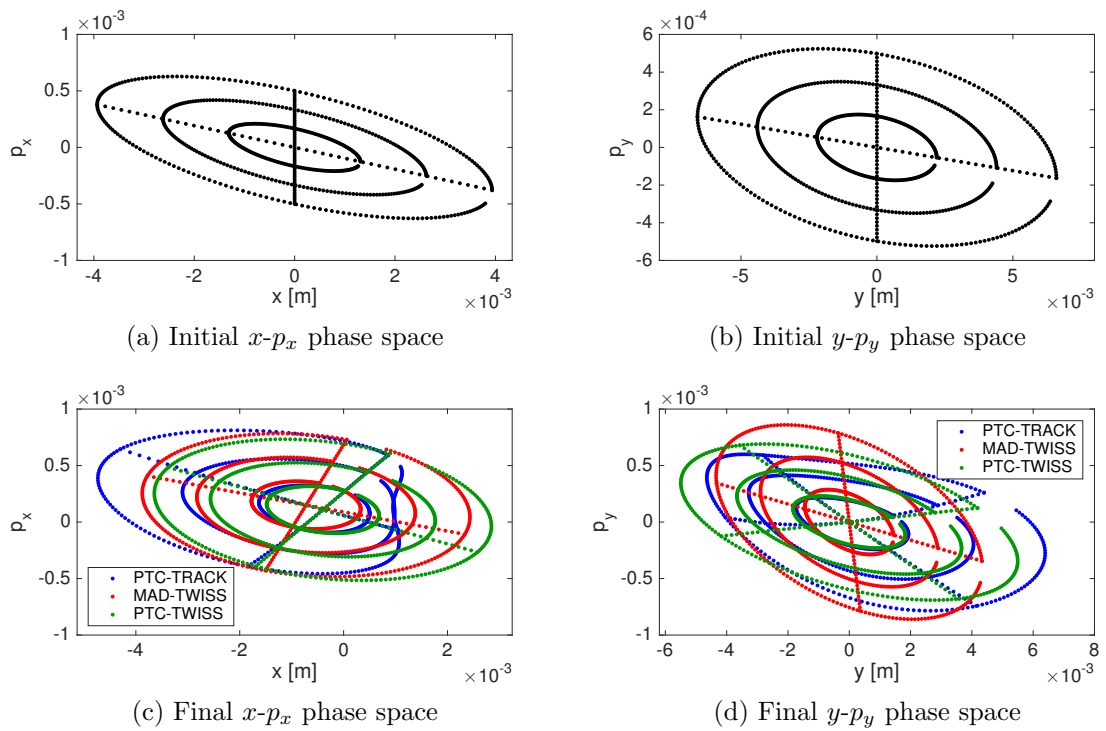


Figure B.1: Horizontal ((a) and (c)) and vertical ((b) and (d)) phase space at the entrance ((a) and (b)) and at the exit ((c) and (d)) of the DBRC computed by means of PTC_TRACK (blue), or simple linear matrix multiplication (red and green). The transport matrices are computed by means of MAD-X TWISS (red) or PTC_TWISS (green).

In order to give an order of magnitude of the deformation, a Gaussian beam of 100000 particles has been tracked with PTC_TRACK along the same path. The final statistical emittance growth computed at the end of the line resulted to be $< 3\%$ in the horizontal and $< 1.5\%$ in the vertical phase spaces. Such an effect is then at least of one order of magnitude smaller than the non-linear effect due to energy spread studied in Section 4.3.

Appendix C

Useful Taylor Series

The following truncated Taylor series are reported for convenience. Equations C.2 and C.4 are expanded around $x = 0$, while Eq. C.5 is expanded in a generic point x_0 .

$$\frac{1}{(1+x)^n} = \sum_{k=0}^{\infty} (-1)^k \frac{(n-1+k)!}{(n-1)!k!} x^k \quad (\text{C.1})$$

$$= 1 - nx + \frac{n(n+1)}{2}x^2 - \frac{n(n+1)(n+2)}{6}x^3 + o(x^4). \quad (\text{C.2})$$

$$(1+x)^n = \sum_{k=0}^n \frac{n!}{(n-k)!k!} x^k \quad (\text{C.3})$$

$$= 1 + nx + \frac{n(n-1)}{2}x^2 + \frac{n(n-1)(n-2)}{6}x^3 + o(x^4). \quad (\text{C.4})$$

$$\begin{aligned} \sin x &= \sin x_0 + \cos x_0(x - x_0) + \\ &\quad - \frac{1}{2} \sin x_0(x - x_0)^2 - \frac{1}{6} \cos x_0(x - x_0)^3 + o(x^4). \end{aligned} \quad (\text{C.5})$$

Appendix D

Combining Covariance Matrices

Following the mathematical definition, the covariance between two random variables is defined as:

$$\sigma(\mathbf{x}, \mathbf{y}) = \langle \mathbf{xy} \rangle - \langle \mathbf{x} \rangle \langle \mathbf{y} \rangle \quad (\text{D.1})$$

where $\langle \cdot \rangle$ identifies the operation of *mean* of the enclosed variable. In the simplest case of 2 random variables (\mathbf{x}, \mathbf{y}) their covariance matrix is then defined as:

$$\Sigma = \begin{bmatrix} \sigma(\mathbf{x}, \mathbf{x}) & \sigma(\mathbf{x}, \mathbf{y}) \\ \sigma(\mathbf{y}, \mathbf{x}) & \sigma(\mathbf{y}, \mathbf{y}) \end{bmatrix}. \quad (\text{D.2})$$

In some cases one knows the covariance matrices of two (or more) subsets of the given variables (e.g. $\Sigma_1; \Sigma_2$), and one might want to compute the covariance matrix of the entire ensemble. By knowing the number of elements in each subset ($n_1; n_2$) and mean values ($\langle \mathbf{x}_1 \rangle; \langle \mathbf{x}_2 \rangle; \langle \mathbf{y}_1 \rangle; \langle \mathbf{y}_2 \rangle$), and by applying the definition of Eq. D.2 one can easily find the following relations:

$$\langle \mathbf{x} \rangle = \frac{n_1 \langle \mathbf{x}_1 \rangle + n_2 \langle \mathbf{x}_2 \rangle}{n_1 + n_2} \quad (\text{D.3})$$

$$\langle \mathbf{y} \rangle = \frac{n_1 \langle \mathbf{y}_1 \rangle + n_2 \langle \mathbf{y}_2 \rangle}{n_1 + n_2} \quad (\text{D.4})$$

$$\langle \mathbf{xy} \rangle = \frac{n_1 (\sigma(\mathbf{x}_1, \mathbf{y}_1) + \langle \mathbf{x}_1 \rangle \langle \mathbf{y}_1 \rangle) + n_2 (\sigma(\mathbf{x}_2, \mathbf{y}_2) + \langle \mathbf{x}_2 \rangle \langle \mathbf{y}_2 \rangle)}{n_1 + n_2}. \quad (\text{D.5})$$

From Eq. D.5 one can then compute the elements matrix of the overall covariance matrix Σ without directly handling the original random variables.

Bibliography

- [1] O. S. Brüning, P. Collier, P. Lebrun, et al., LHC Design Report, Tech. Rep. CERN-2004-003-V1, CERN, Geneva (2004). URL <https://cds.cern.ch/record/782076>
- [2] Future Circular Collider (FCC) study. URL <http://cern.ch/fcc>
- [3] M. Aicheler, P. Burrows, M. Draper, et al., A Multi-TeV Linear Collider Based on CLIC Technology: CLIC Conceptual Design Report, Tech. Rep. CERN-2012-007, CERN, Geneva (2012). URL <https://cds.cern.ch/record/1500095>
- [4] T. Behnke, J. E. Brau, B. Foster, et al., The International Linear Collider - Volume 1: Executive Summary, Tech. Rep. CERN-ATS-2013-037, CERN, Geneva (2013). URL <http://cds.cern.ch/record/1601966>
- [5] G. Geschonke, A. Ghigo, CTF3 Design Report, Tech. Rep. CERN-PS-2002-008-RF, CERN, Geneva (2002). URL <http://cds.cern.ch/record/559331>
- [6] H. Grote, F. Schmidt, MAD-X: An Upgrade from MAD8, in: Proceedings of the 2003 Particle Accelerator Conference, PAC2003, Portland, 2003.
- [7] W. N. Cottingham, D. A. Greenwood, An Introduction to the Standard Model of Particle Physics, Cambridge University Press, 2007.
- [8] H. J. Lipkin, New possibilities for exotic hadrons – anticharmed strange baryons, Physics Letters B 195 (1987) 484–488.
- [9] R. Aaij, B. Adeva, M. Adinolfi, et al., Observation of $J/\psi p$ Resonances Consistent with Pentaquark States in $\Lambda_b^0 \rightarrow J/\psi K^- p$ Decays, Phys. Rev. Lett. 115 (2015) 072001.
- [10] P. W. Higgs, Broken symmetries and the masses of gauge bosons, Phys. Rev. Lett. 13 (1964) 508–509.
- [11] F. Englert, R. Brout, Broken symmetry and the mass of gauge vector mesons, Phys. Rev. Lett. 13 (1964) 321–323.
- [12] G. S. Guralnik, C. R. Hagen, T. W. B. Kibble, Global conservation laws and massless particles, Phys. Rev. Lett. 13 (1964) 585–587.
- [13] G. Aad, T. Abajyan, B. Abbott, et al., Observation of a new particle in the search for the Standard Model Higgs boson with the ATLAS detector at the LHC, Physics Letters B 716 (2012) 1–29.

- [14] S. Chatrchyan, V. Khachatryan, A. Sirunyan, et al., Observation of a new boson at a mass of 125 GeV with the CMS experiment at the LHC, *Physics Letters B* 716 (2012) 30–61.
- [15] Search for new physics in high mass diphoton events in proton-proton collisions at $\sqrt{s} = 13$ TeV, Tech. Rep. CMS-PAS-EXO-15-004, CERN, Geneva (2015). URL <https://cds.cern.ch/record/2114808>
- [16] Search for resonances decaying to photon pairs in 3.2 fb^{-1} of pp collisions at $\sqrt{s} = 13$ TeV with the ATLAS detector, Tech. Rep. ATLAS-CONF-2015-081, CERN, Geneva (2015). URL <http://cds.cern.ch/record/2114853>
- [17] T. A. collaboration, Search for scalar diphoton resonances with 15.4 fb^{-1} of data collected at $\sqrt{s}=13$ TeV in 2015 and 2016 with the ATLAS detector, Tech. Rep. ATLAS-CONF-2016-059, CERN, Geneva (2016). URL <https://cds.cern.ch/record/2206154>
- [18] Search for resonant production of high mass photon pairs using 12.9 fb^{-1} of proton-proton collisions at $\sqrt{s} = 13$ TeV and combined interpretation of searches at 8 and 13 TeV, Tech. Rep. CMS-PAS-EXO-16-027, CERN, Geneva (2016). URL <https://cds.cern.ch/record/2205245>
- [19] The European Strategy for Particle Physics – Update 2013. URL <https://cds.cern.ch/record/1567258>
- [20] LEP Design Report: Vol.2. The LEP Main Ring, Tech. Rep. CERN-LEP-84-01, CERN, Geneva (1984). URL <http://cds.cern.ch/record/102083>
- [21] V. Shiltsev, When will we know a muon collider is feasible? Status and directions of muon accelerator R&D, *Mod. Phys. Lett. A*25 (2010) 567–577.
- [22] Future Circular Collider (FCC-ee) study. URL <http://cern.ch/fcc-ee>
- [23] C.-S. S. Group, CEPC-SPPC Preliminary Conceptual Design Report. 2. Accelerator, Tech. Rep. IHEP-CEPC-DR-2015-01, IHEP, Beijing (2015). URL <http://cepc.ihep.ac.cn/preCDR/volume.html>
- [24] Executive summary of ITRP Report. URL <http://www.fnal.gov/directorate/icfa/index.html>
- [25] S. Stapnes, Linear Collider Studies, in: Proceedings of the 27th Linear Accelerator Conference, LINAC2014, Geneva, 2014, paper MOIOA01.
- [26] F. Zimmermann, M. Benedikt, K. Oide, et al., Status and Challenges for FCC-ee, Tech. Rep. CERN-ACC-2015-111, CERN, Geneva (2015). URL <http://cds.cern.ch/record/2057706>
- [27] J. W. et al., Future Circular Collider Study – Lepton Collider Parameters, Tech. Rep. FCC-ACC-SPC-0003, CERN, Geneva (2014). URL <https://edms5.cern.ch/document/1346081/2.0>

- [28] CLIC study. URL <http://cern.ch/clic-study>
- [29] A. Grudiev, S. Calatroni, W. Wuensch, New local field quantity describing the high gradient limit of accelerating structures, *Phys. Rev. ST Accel. Beams* 12 (2009) 102001.
- [30] E. Adli, A Study of the Beam Physics in the CLIC Drive Beam Decelerator, Tech. Rep. CERN-THESIS-2010-024, Oslo U. (2009). URL <http://inspirehep.net/record/887068/files/CERN-THESIS-2010-024.pdf>
- [31] J.-P. Delahaye, et al., CLIC: A Two beam multi-TeV e^{+-} linear collider, in: Proceedings of the 20th Linear Accelerator Conference, LINAC2000, Monterey, 2000, paper MO201.
- [32] H. H. Braun, R. Corsini, S. Doebert, et al., Efficient long-pulse fully-loaded CTF3 linac operation, in: Proceedings of the 23rd Linear Accelerator Conference, LINAC2006, Knoxville, 2006, paper MOP002.
- [33] J. L. Navarro Quirante, R. Corsini, A. Degiovanni, et al., Effect of Beam-Loading on the Breakdown Rate of High Gradient Accelerating Structures, in: Proceedings of the 27th Linear Accelerator Conference, LINAC2014, Geneva, 2014, paper TUPP033.
- [34] A. Ghigo, D. Alesini, G. Benedetti, et al., Commissioning and first measurements on the CTF3 chicane, in: Proceedings of the 2005 Particle Accelerator Conference, PAC2005, Knoxville, 2005, paper RPPP001.
- [35] P. K. Skowronski, A. Andersson, A. Ghigo, et al., Design of Phase Feed Forward System in CTF3 and Performance of Fast Beam Phase Monitors, in: Proceedings of the 4th International Particle Accelerator Conference, IPAC2013, Shanghai, 2013, paper WEOBB203.
- [36] J. Roberts, A. Andersson, P. Burrows, et al., First Results From Beam Tests of the CLIC Drive Beam Phase Feedforward Prototype at CTF3, in: Proceedings of the 6th International Particle Accelerator Conference, IPAC2015, Richmond, 2015, paper MOPWI001.
- [37] J. L. Navarro Quirante, et al., CALIFES: A Multi-Purpose Electron Beam for Accelerator Technology Tests, in: Proceedings of the 27th Linear Accelerator Conference, LINAC2014, Geneva, 2014, paper MOPP030.
- [38] S. Y. Lee, *Accelerator physics*; 3rd ed., World Scientific, Singapore, 2012.
- [39] H. Wiedemann, *Particle accelerator physics*; 3rd ed., Springer, Berlin, 2007.
- [40] K. Wille, *The physics of particle accelerators: an introduction*, Oxford Univ. Press, Oxford, 2000.
- [41] M. Reiser, *Theory and design of charged particle beams*, Wiley series in beam physics and accelerator technology, Wiley, New York, 1994.

- [42] D. Alesini, F. Marcellini, C. Biscari, A. Ghigo, R. Corsini, Beam instability induced by RF deflectors in the combiner ring of the CLIC test facility and mitigation by damped deflecting structures, *Phys. Rev. Spec. Top. Accel. Beams* 14 (2011) 022001.
- [43] H. Grote, F. Schmidt, L. Deniau, G. Roy, The MAD-X Program (Methodical Accelerator Design) Version 5.02.04 User's Reference Manual. URL <http://madx.web.cern.ch/madx/releases/5.02.04/madxuguide.pdf>
- [44] E. D. Courant, H. S. Snyder, Theory of the alternating gradient synchrotron, *Annals Phys.* 3 (1958) 1–48.
- [45] J. Buon, Beam phase space and emittance; rev. version, Tech. Rep. LAL-RT-90-15-REV, LAL, Orsay (1992). URL <http://cours.lal.in2p3.fr/ecoles/accelerateurs/Jbuon2.pdf>
- [46] F. Schmidt, MAD-X PTC integration, in: Proceedings of the 2005 Particle Accelerator Conference, PAC2005, Knoxville, 2005, paper MPPE012.
- [47] F. Schmidt, E. Forest, E. McIntosh, Introduction to the polymorphic tracking code: Fibre bundles, polymorphic taylor types and exact tracking, Tech. Rep. CERN-SL-2002-044-AP, CERN, Geneva (2002). URL <https://cds.cern.ch/record/573082>
- [48] V. B. et al., JAPC - the Java API for Parameter Control, in: Proceedings of the 10th International Conference on Accelerator and Large Experimental Physics Control Systems, ICALEPCS2005, Geneva, 2005, paper TH15-80.
- [49] S. Deghaye, D. Jacquet, I. Kozsar, J. Serrano, OASIS: A new system to acquire and display the analog signals for LHC, in: Proceedings of the 9th International Conference on Accelerator and Large Experimental Physics Control Systems, ICALEPCS2003, Gyeongju, 2003, paper WP502.
- [50] A. J. Campbell, A. Gagnaire, R. Garoby, et al., A VME-based measurement system for RF parameters in the CERN PS, in: Proceedings of the 5th European Particle Accelerator Conference, EPAC1996, Sitges, 1996, paper TUP017L.
- [51] T. Persson, Fighting beam instabilities at CTF3, Master's thesis, Chalmers University of Technology, Göteborg (2011).
- [52] P. K. Skowronski, T. Persson, Beam Stability at CTF3, in: Proceedings of the 3rd International Particle Accelerator Conference, IPAC2012, New Orleans, 2012, paper TUPPR032.
- [53] T. Persson, P. Skowronski, R. Corsini, Drive beam stability studies and stabilization algorithms in CLIC Test Facility 3, *Nuclear Instruments and Methods in Physics Research Section A: Accelerators, Spectrometers, Detectors and Associated Equipment* 735 (2014) 152–156.
- [54] A. Dubrovskiy, L. Malina, P. K. Skowronski, F. Tecker, T. Persson, Review of the Drive Beam Stabilization in the CLIC Test Facility CTF3, in: Proceedings of the

- 4th International Particle Accelerator Conference, IPAC2013, Shanghai, 2013, paper WEPEA069.
- [55] MATLAB, version 8.4 (R2014b), The MathWorks Inc., Natick, Massachusetts, 2014.
- [56] M. G. Minty, F. Zimmermann, Measurement and control of charged particle beams, Particle acceleration and detection, Springer, Berlin, 2003.
- [57] A. Latina, D. Pellegrini, J. Pfingstner, D. Schulte, E. Adli, Toolbox for Applying Beam-Based Alignment to Linacs, in: Proceedings of the 27th Linear Accelerator Conference, LINAC2014, Geneva, 2014, paper THPP034.
- [58] A. Latina, J. Pfingstner, D. Schulte, E. Adli, Tests of Beam-based Alignment at FACET, in: Proceedings of the 5th International Particle Accelerator Conference, IPAC2014, 2014, paper TUPRO065.
- [59] J. Shlens, A Tutorial on Principal Component Analysis, CoRR abs/1404.1100. URL <http://arxiv.org/abs/1404.1100>
- [60] L. Trefethen, D. Bau, Numerical Linear Algebra, Society for Industrial and Applied Mathematics, 1997.
- [61] C. Lawson, R. Hanson, Solving Least Squares Problems, Society for Industrial and Applied Mathematics, 1995.
- [62] MATLAB lsqin function. URL <http://it.mathworks.com/help/optim/ug/lsqin.html>
- [63] Y. Chung, G. Decker, K. Evans, Closed Orbit Correction Using Singular Value Decomposition of the Response Matrix, in: Proceedings of the 1993 Particle Accelerator Conference, PAC93, Washington, 1993, p. 2263.
- [64] F. Lohl, Measurements of the transverse emittance at the VUV-FEL, Master's thesis, University of Hamburg (2005).
- [65] E. Prat, M. Aiba, Four-dimensional transverse beam matrix measurement using the multiple-quadrupole scan technique, Phys. Rev. Spec. Top. Accel. Beams 17 (2014) 052801.
- [66] P. Urschütz, H.-H. Braun, R. Corsini, et al., Beam dynamics studies and emittance optimization in the CTF3 linac at CERN, in: Proceedings of the 10th European Particle Accelerator Conference, EPAC2016, Edinburgh, 2006, paper MOPLS102.
- [67] P. Skowronski, Private Communication.
- [68] B. Constance, Private Communication.
- [69] N. Čutić, E. Mansten, Emittance and Beta Functions Measurements for the MAX IV Linac, in: Proceedings of the 4th International Particle Accelerator, IPAC2013, Shanghai, 2013, paper MOPME070.

- [70] P. Tenenbaum, Emittance measurements in CTF-2 drive beam, Tech. Rep. CERN-CLIC-NOTE-326, CERN, Geneva (1997). URL <https://cds.cern.ch/record/321551>
- [71] H.-H. Braun, F. Chautard, P. Tenenbaum, Nulling emittance measurement technique for CLIC Test Facility, in: Proceedings of the 17th IEEE Particle Accelerator Conference, PAC97, Vancouver, 1997, pp. 479–484.
- [72] M. Oivegøard, V. Ziemann, Effect of large momentum spread on emittance measurements, Nuclear Instruments and Methods in Physics Research Section A: Accelerators, Spectrometers, Detectors and Associated Equipment 707 (2013) 114–119.
- [73] M. Castellano, A. Cianchi, V. A. Verzilov, Emittance and dispersion measurements at TTF, in: Proceedings of the 4th European Workshop on Diagnostics and Instrumentation for Particle Accelerators, DIPAC1999, Chester, 1999, paper PT10.
- [74] C. McKee, P. O’Shea, J. Madey, Phase space tomography of relativistic electron beams, Nuclear Instruments and Methods in Physics Research Section A: Accelerators, Spectrometers, Detectors and Associated Equipment 358 (1995) 264–267.
- [75] K. Hock, M. Ibison, D. Holder, A. Wolski, B. Muratori, Beam tomography in transverse normalised phase space, Nuclear Instruments and Methods in Physics Research Section A: Accelerators, Spectrometers, Detectors and Associated Equipment 642 (2011) 36–44.
- [76] A. Rollings, Private Communication.
- [77] L. Martin, Private Communication.
- [78] J. Radon, Über die Bestimmung von Funktionen durch ihre Integralwerte längs gewisser Mannigfaltigkeiten, Akad. Wiss. 69 (1917) 262–277.
- [79] J. Radon, On the determination of functions from their integral values along certain manifolds, IEEE Transactions on Medical Imaging MI-5 (1986) 170–176.
- [80] MATLAB iradon function. URL <http://it.mathworks.com/help/images/ref/iradon.html>
- [81] A. Kak, Principles of computerized tomographic imaging, Society for Industrial and Applied Mathematics, Philadelphia, 2001.
- [82] C. Biscari, R. Corsini, T. E. D’Amico, et al., CTF3: Design of Driving Beam Combiner Ring, Tech. Rep. CERN-OPEN-2001-018, CERN, Geneva (2001). URL <https://cds.cern.ch/record/488603>
- [83] R. Corsini, A. Ferrari, L. Rinolfi, P. Royer, F. A. Tecker, Experimental results on electron beam combination and bunch frequency multiplication, Phys. Rev. Spec. Top. Accel. Beams 7 (2004) 040101.

- [84] S. Bettoni, E. Bravin, R. Corsini, et al., Measuring the Bunch Frequency Multiplication at CTF3, in: Proceedings of the 1st International Particle Accelerator Conference, IPAC2010, Kyoto, 2010, paper MOPE058.
- [85] A. Dabrowski, S. Bettoni, E. Bravin, et al., Measuring the bunch frequency multiplication at the 3rd CLIC Test Facility, *J. Instrum.* 7 (2012) P01005.
- [86] J. Barranco Garcia, P. Skowronski, F. Tecker, C. Biscari, Design of the CLIC Drive Beam Recombination Complex, in: Proceedings of the 2nd International Particle Accelerator Conference, IPAC2011, San Sebastian, 2011, paper TUPC022.
- [87] D. Pellegrini, A. Latina, D. Schulte, PLACET2: a Novel Code for Beam Dynamics in Recirculating Machines, in: Proceedings of the 6th International Particle Accelerator Conference, IPAC2015, Richmond, 2015, paper MOPJE068.
- [88] E. Welzl, Smallest enclosing disks (balls and ellipsoids), in: Proceedings of the New Results and New Trends in Computer Science Symposium, Springer-Verlag, Graz, 1991, pp. 359–370.
- [89] C. A. Lindstrøm, E. Adli, Design of general apochromatic drift-quadrupole beam lines, *Phys. Rev. Accel. Beams* 19 (2016) 071002.
- [90] V. Balandin, R. Brinkmann, W. Decking, N. Golubeva, Third-Order Apochromatic Drift-Quadrupole Beamline, in: Proceedings of the 2nd International Particle Accelerator Conference, IPAC2012, New Orleans, 2012, paper TUPPC069.
- [91] V. Balandin, W. Decking, N. Golubeva, Large Energy Acceptance Dogleg for the XFEL Injector, in: Proceedings of the 2nd International Particle Accelerator Conference, IPAC2011, San Sebastian, 2011, paper WEPC007.
- [92] M. Gasior, An Inductive Pick-Up for Beam Position and Current Measurements, in: Proceedings of the 6th European Workshop on Beam Diagnostics and Instrumentation for Particle Accelerators, DIPAC2003, Mainz, 2003, paper CT01.
- [93] M. Gasior, A current mode inductive pick-up for beam position and current measurement, in: Proceedings of the 7th European Workshop on Beam Diagnostics and Instrumentation for Particle Accelerators, DIPAC2005, Lyons, 2005, paper POT014.
- [94] A. Stella, A. Ghigo, F. Marcellini, A. Zolla, Design of a beam position monitor for the CTF3 combiner ring, Tech. Rep. CTFF3-008,2002, INFN, Frascati (2002). URL <http://www.lnf.infn.it/acceleratori/ctf3/ctff3notes/CTFF3-008.pdf>
- [95] J. Jacquemier, J.-M. Nappa, J. Tassan, S. Vilalte, Acquisition chain for CTF3 pick-ups read-out, Tech. Rep. LAPP-TECH-2009-01, LAPP, Annecy-le-Vieux (2009). URL <http://hal.in2p3.fr/in2p3-00412457>
- [96] A. Benot-Morell, B. P. Bielawski, L. Bobb, et al., Status of the CLIC/CTF Beam Instrumentation R&D, in: Proceedings of the 5th International Particle Accelerator Conference, IPAC2015, Dresden, 2014, paper THPME178.

- [97] F. J. Cullinan, S. T. Boogert, W. Farabolini, et al., Long bunch trains measured using a prototype cavity beam position monitor for the Compact Linear Collider, *Phys. Rev. Spec. Top. Accel. Beams* 18 (2015) 112802.
- [98] T. Dobers, Private Communication.
- [99] E. Adli, R. Corsini, A. Dabrowski, et al., Status of an automatic Beam Steering for the CLIC Test Facility 3, in: *Proceedings of the 24th International Linear Accelerator Conference, LINAC2008, Victoria, 2008*, paper TUP016.
- [100] A. Latina, J. Pfingstner, D. Schulte, et al., Experimental demonstration of a global dispersion-free steering correction at the new linac test facility at SLAC, *Phys. Rev. Spec. Top. Accel. Beams* 17 (2014) 042803.
- [101] J. Pfingstner, D. Schulte, On-Line Dispersion Free Steering for the Main Linac of CLIC, in: *Proceedings of the 26th International Linear Accelerator Conference, LINAC2012, Tel Aviv, 2012*, paper SUPB007.
- [102] T. Raubenheimer, R. Ruth, A dispersion-free trajectory correction technique for linear colliders, *Nuclear Instruments and Methods in Physics Research Section A: Accelerators, Spectrometers, Detectors and Associated Equipment* 302 (1991) 191–208.
- [103] T. Persson, Private Communication.
- [104] L. Malina, Private Communication.
- [105] R. Bossart, P. Brown, J. Mourier, I. V. Syratchev, L. Tanner, High-power Microwave Pulse Compression of Klystrons by Phase-Modulation of High-Q Storage Cavities, *Tech. Rep. CERN-OPEN-2004-015*, CERN, Geneva (2004). URL <http://cds.cern.ch/record/741401>
- [106] A. Dabrowski, H. Braun, R. Corsini, et al., Non-destructive Single Shot Bunch Length Measurements for the CLIC Test Facility 3, in: *Proceedings of the 22nd Particle Accelerator Conference, PAC2007, Albuquerque, 2007*, paper FRPMS045.
- [107] A. E. Dabrowski, E. Adli, S. Bettoni, et al., Measuring the longitudinal bunch profile at CTF3, in: *Proceedings of the 25th Linear Accelerator Conference, LINAC2010, Tsukuba, 2010*, paper TUP100.
- [108] M. J. Barnes, J. Borburgh, B. Goddard, M. Hourican, Injection and extraction magnets: septa, in: *Proceedings of the 2009 CAS-CERN Accelerator School: Specialised course on Magnets, Geneva, 2010*, pp. 167–184.
- [109] G. Sterbini, Private Communication.
- [110] W. Chou, C. Biscari, ICFA Beam Dynamics Newsletter, No 35 (2004). URL http://icfa-usa.jlab.org/archive/newsletter/icfa_bd_nl_35.pdf